Geochronology and Source of Metals and Fluids in Iron Oxide – Apatite and Iron Oxide – Copper – Gold Mineral Deposits

by

María Alejandra Rodríguez Mustafa

A dissertation submitted in partial fulfillment
of the requirements for the degree of
Doctor of Philosophy
(Earth and Environmental Sciences)
in the University of Michigan
2022

Doctoral Committee:

Professor Adam C. Simon, Chair
Professor Joel D. Blum
Assistant Professor Robert Holder
Professor Emeritus Stephen Kesler
Professor Kyger C. Lohmann
Professor Sally Oey

María Alejandra Rodríguez Mustafa

maalromu@umich.edu

ORCID iD: 0000-0001-5434-5045

Dedication

To Lela, who should have been the first doctor in the family.

Acknowledgements

This dissertation would not have been possible without the guidance and patience of my committee members, Drs. Adam Simon, Stephen Kesler, Joel Blum, Kyger Lohmann, Robert Holder, and Sally Oey. I want to thank them for their time and valuable feedback. Steve, thank you for all the exploration lessons and the thoughtful questions. Robert, thank you for believing in magnetite geochronology from day one and for always be willing to answer any question. Joel and Kacey, thank you for helping me understand the world of isotopes. Sally, thanks for seeing the hidden star in me. Finally, I want to thank my advisor, Adam Simon, for his patience and encouragement, and for constantly supporting and mentoring me in my academic and professional endeavors. I am also incredibly grateful with Drs. Larry Cathles and John Thompson for their wonderful and constant mentorship and for believing in me from early on. They have been instrumental throughout my PhD, and I will always be honored to have worked with them.

I would also like to thank my collaborators, Drs. Ilya Bindeman, Holly Stein, Brian Jicha, Ryan Mathur, and Andrew Kylander-Clark for helping me produce high-quality isotope data and Dr. Dominique Weiss for hosting me in her exceptional labs at UBC. I am also very grateful with Dr. Owen Neill for training me in the SEM and the microprobe and for *always* being available to help.

Funding for this dissertation was provided by the Society of Economic Geologists Student Research Grants and Graduate Fellowship, the Scott Turner Award, the Rackham Graduate School, Marcobre S.A, and the National Science Foundation (including the AGeS grant).

My project in Chile would have not been possible without my Chilean collaborators, Drs. Irene del Real, Martin Reich, and Fernando Barra and without access to Candelaria and Quince provided by Lundin Mining and David Cadwell, respectively. I want to thank Marcobre for hosting me at Mina Justa and allowing me to research this intriguing deposit in Peru. I want to thank the Mine Geology and Exploration teams and support staff for all their assistance during

and after the field visit. In particular, I want to thank Edson L.B Machado, José Luis Silva, Julio Adco, Helbert Flores, Miguel Núñez, Juan Carlos Bazán, Rothny Valeriano, and Percy Salazar.

I am glad I got to meet so many wonderful people in Ann Arbor who helped me in many ways during my PhD. My time in Ann Arbor would have also not been the same without my friends from GRIN and from MSE. I want to thank the EARTH department faculty and staff as well as the staff at Rackham for all the troubleshooting and support. I am also honored to have been part of the 2017 cohort: Molly, Brie, Tariq, Elizabeth, Sooyeon, Guolei, Prithvi, and Marlon. It was a pleasure to be part of your grad school journey and I will always cherish our memories together. Huge thanks to Juliana Mesa and Laura Motta for all their support and kindness and to Sam, Sha, Kirk, Nik, Meg, Alex T., Sophie, Daeun, Jing Ci, Olivia and many others for being great friends and role model educators.

Enormous gratitude to my lab family, Drs. Laura Bilenker, Tristan Childress, Nikita La Cruz, Brian Konecke, José Tomás Ovalle, and soon to be Drs. Jackie Kleinsasser, Justin Casaus, Daniel Blakemore, Chris Emproto, Andrés González, and Allyson Murray for all the mentoring, support, help, time, and solidarity. I have learned from and with you and I would not be where I am without you.

Finally, I want to express my greatest gratitude to Duncan, friends, and family who have always believed in me and encouraged me to chase my dreams. Thanks to my GV and UNAL friends and to all the Nexitos for being the best friends and cheerleaders. Gracias a mi padre, Miguel Alberto, a mi madre, María Clara, a mi hermana, Mariana, a mi tía Mabel Elisa, a mis abuelas Graciela y Adelia (que en paz descansen) por su infinito apoyo y por infundir en mi la fortaleza que hoy me permite culminar este logro.

Table of Contents

List of Tables

List of Figures

List of Appendices

Abstract

As the human population increases and shifts towards low-carbon technologies such as solar panels and electric vehicles, the demand for metals will keep escalating. In consequence, new sources of these materials need to be discovered to develop the infrastructure for the production and storage of renewable energy to meet carbon reduction targets. Iron oxide deposits, in particular iron oxide – apatite (IOA) and iron oxide – copper – gold (IOCG) deposits, contain important amounts of energy-critical elements such as Fe, Cu, U, V, Ni, and Co. Due to their spatial and temporal association with each other, it has been hypothesized that both deposit types are part of the same mineralizing system. To find new mineral deposits, an understanding of how they form must be developed to increase the efficiency of the discovery process. This work integrates innovative geochemical tools to improve our knowledge of the processes that result in the formation of iron oxide deposits.

To constrain the sources of the fluids and metals in IOA and IOCG deposits, I focused on the characterization of the mineral magnetite from the Candelaria IOCG deposit and the Quince IOA prospect in Chile and from the Mina Justa IOCG deposit and the Marcona IOA deposit in Peru, as well as the copper sulfides from Mina Justa. The textural characterization and copper isotopes of sulfides are consistent with a high-temperature, magmatic-hydrothermal origin for copper mineralization. Iron, hydrogen, and oxygen isotope data from magnetite support an igneous to magmatic-hydrothermal source for the iron mineralization. Magnetite textures present igneous and magmatic-hydrothermal affinities, and the trace element concentrations indicate more than one generation of magnetite in IOCG deposits and a cooling trend for magnetite at Candelaria, where the deeper portion of the system corresponds to a transitional phase between the shallower IOCG deposit and deeper IOA mineralization. The combined chemical and textural data are consistent with an igneous/magmatic-hydrothermal origin for the fluids and metals that result in IOCG and IOA deposits in the Andes.

To understand the timing of iron and copper mineralization and to test the link between IOA and IOCG deposits, I dated ore minerals (including pioneering *in-situ* dating of magnetite)

from the neighboring Mina Justa IOCG and Marcona IOA deposits. The data indicate that copper mineralization at Mina Justa occurred at ca. 160 Ma, approximately 70 million years earlier than previously proposed, and that iron mineralization at Mina Justa and at Marcona occurred within the same timeframe and is older than copper mineralization. These results indicate that Mina Justa is an IOCG deposit that overprints IOA-style mineralization, linking IOA and IOCG deposits in Peru and providing insights into their geologic setting.

Detailed mineral characterization combined with innovative geochronology can decipher the ingredients and processes that form iron oxide mineral deposits. This knowledge can be applied to develop effective exploration strategies to find these deposits to supply the increasing demand of metals that are necessary for the development of green energy technologies.

Chapter 1 : Introduction

Mining has been a crucial activity for humanity since prehistoric times. Materials extracted from the Earth have allowed humans to progress and create tools to improve their quality of life. In particular, iron and copper have been essential elements for the development of modern civilization. Both elements are widely used in construction and as components in everyday objects, from electronics to automobiles. More recently, with the need to transition to environmentally friendly energy sources, the demand for iron, copper, and other elements has substantially increased due to the need for these to develop infrastructure and storage solutions for the low-carbon energy future. For example, iron, copper, and other critical elements are the most abundant materials in steel and electronic components used in wind turbines and electric vehicles. To secure the resources needed to fulfill the expected demand, new mineral deposits need to be discovered. However, success in exploration has decreased as the deposits that outcrop on the surface have been already identified. To improve this rate, geologists need to understand how and where mineral deposits form in order to generate new exploration methods and techniques to find them.

My dissertation investigates the origin of iron oxide – copper – gold (IOCG) and iron oxide – apatite (IOA) mineral deposits. These deposits are major sources of iron, copper, and gold, and are enriched in other elements that are critical for the development of a post-carbon infrastructure. Even though these deposit types have been studied separately, their close spatiotemporal association has led to the suggestion that they have the same origin. I use the geochemistry of the mineral magnetite to find the source of the metals and fluids that form these deposits. I also apply novel geochronological techniques to establish the timing of different mineralization stages to constrain a unifying, conceptual model for mineralization. The results of my dissertation will allow for the development of geophysical and geochemical exploration techniques to find new deposits that will optimize the exploration process and maintain the supply of resources for future generations.

1.1 Iron Oxide Deposits

Iron oxide deposits comprise a wide range of mineral deposits rich in iron oxide minerals like magnetite and hematite and can contain several other elements such as Cu, Au, Ag, U, P, V, Co, Ni, and rare earth elements in different proportions. Iron oxide deposits are found worldwide and have formed throughout the last 2 billion years. They are structurally and sometimes stratigraphically controlled and are associated with extensive sodic-calcic alteration. However, they are not restricted to a single tectonic setting or host rock and are not always associated with intrusions, which has led to several hypotheses for their origin (Hitzman, 2000; Williams et al., 2005; Groves et al., 2010; Barton, 2014).

Iron oxide deposits are commonly grouped as either iron oxide – copper – gold (IOCG) or iron oxide – apatite (IOA) deposits depending on their mineralogy. Traditionally, separate models of formation have been proposed for IOCG and IOA deposits. In general, it is accepted that IOCG deposits form by hydrothermal processes where the hydrothermal ore fluid has been proposed to be a non-magmatic brine that leaches metals from the crust (Barton and Johnson, 1996; Haynes, 2000; Benavides et al., 2007), a magmatic-hydrothermal fluid that extracts the metals from a silicate magma (Pollard, 2006), or a combination of both (Hitzman, 2000; Chiaradia et al., 2006; Groves et al., 2010; Rieger and Marschik, 2012). The major hypotheses for IOA formation are: 1) a purely magmatic origin in which a silicate melt unmixes into a silica-rich melt and an iron-volatiles-rich melt that ascends and gets emplaced in the crust (Nyström and Henriquez, 1994; Naslund et al., 2002; Chen et al., 2010; Tornos et al., 2017; Hou et al., 2018); 2) a magmatic-hydrothermal origin in which the fluid extracts the metals from a silicate magma (Hildebrand, 1986; Jonsson et al., 2013; Westhues et al., 2017); 3) a combined igneous and magmatic-hydrothermal model in which primary igneous microscopic magnetite grains attach to bubbles and ascend and around which hydrothermal magnetite precipitates as the fluid cools down (Knipping et al., 2015; Knipping et al., 2019). In order to test the different models, I look at the geochemical signals (minor element and isotopic compositions) of the ore minerals to fingerprint the sources of the fluids and the metals and to estimate the temperature of formation of the deposits.

1.2 Magnetite geochemistry

Magnetite is an iron oxide mineral with the formula $Fe^{2+}{}_1Fe^{3+}{}_2O_4$. It has an inverse spinel crystal structure in which the octahedral sites are occupied by ferric (Fe^{3+}) and ferrous iron (Fe^{2+}), while tetrahedral sites are only occupied by ferric ions. Depending on their charge and ionic radii, numerous cations may substitute for iron. Trivalent cations that may substitute for Fe^{3+} are Cr, V, Mn, Al, and Ga, while divalent cations that may substitute for Fe^{2+} are Mg, Ni, and Mn. Other ions like Ti^{4+} can be incorporated in magnetite if the substitution is coupled with another divalent ion. The incorporation of ions is also controlled by oxygen fugacity (fO2) and temperature. The concentration of iron tends to be lower and the concentration of other elements tends to be higher at higher temperatures and lower fO2. Therefore, magnetite composition can be used to estimate the physicochemical conditions under which it formed (Nadoll et al., 2014).

Isotope studies are powerful tools to evaluate the sources of metals and the fluids that transport them and are proxies for the temperature at which the minerals of interest formed. Because the concentration of certain isotopes can be very low, normalized isotopic ratios are used instead. The delta notation expresses the ratio of the studied sample and a standard as:

$$\delta^{a}X_{sample}(‰) = \left[\frac{({}^{a}X/{}^{b}X)_{measured}}{({}^{a}X/{}^{b}X)_{standard}} - 1\right] \times 1000$$

where X is the element of interest, a is the mass of the more abundant isotope, and b is the mass of the less abundant isotope.

Magnetite oxygen isotope compositions are well constrained for igneous rocks, and more recently, for IOA and IOCG deposits. Pioneering studies that have paired oxygen and iron studies in these deposits have been able to fingerprint the source of the metals, and the degree of contribution of different sources to the fluids that transport them. (Bilenker et al., 2016; Childress et al., 2016; Troll et al., 2019; Childress et al., 2020b; Childress et al., 2020a). Other metal isotopes such as copper have also been used to trace the source and the relative timing of occurrence of copper mineralization in a deposit, this is, to identify if the copper minerals are primary or if they resulted from secondary, supergene processes (Mathur et al., 2010; Mathur et al., 2012).

1.3 Ore geochronology

Geochronology is the branch of geology that utilizes the rate of radioactive decay of certain elements to calculate the age of formation of the mineral that contains them. Traditionally, mineralization ages have been determined by dating zircon and apatite grains from igneous rocks that have a clear cross-cutting relationship with mineralization. However, they represent only a maximum or a minimum age and are restricted to deposits that show such relationships. Biotite, K-feldspar and other minerals that occur in the same alteration stage as the ore minerals can also be used for indirectly dating mineralization, but only where the paragenetic sequence has been clearly interpreted. However, there is a risk that such minerals could have been reset due to posterior hydrothermal pulses, indicating ages of alteration rather than of mineralization (Hames, 2021). More recently, bulk techniques such as Re–Os dating in sulfides have provided a direct determination of ore mineralization and have become increasingly popular (Stein, 2014), However, suitable sulfides for Re–Os geochronology do not occur in IOA deposits and only in a few IOCG deposits, whereas magnetite is a ubiquitous mineral in these and other mineral deposits.

The first published attempt to use magnetite as a geochronometer was performed by Özdemir and York (1990) using the Ar–Ar step heating method. Following researchers used sequential leaching methods to obtain U–Pb dates from Banded Iron Formations and IOA deposits (Erel et al., 1997; Frei et al., 1999; Gelcich et al., 2005; Stendal et al., 2006). In the past 15 years, magnetite thermo and geochronology has been developed using the (U – Th)/He system (Blackburn et al., 2007; Cooperdock and Stockli, 2016) and the first LA-ICP-MS U–Pb magnetite date with application to economic geology was presented by Courtney-Davies et al. (2020). New advances in U–Pb in-situ geochronology, pioneered in this dissertation, paired with a detailed chemical and textural characterization of ore minerals, can help resolve different mineralization events in a single deposit maintaining the sample within its spatial and geological context.

1.4 Applications to the understanding of IOCG and IOA deposits

I focus on unveiling the processes that result in IOA and IOCG deposits in the Andes as these deposits are the youngest of their kind. As they have not been subject to major deformation events or metamorphism, the chemistry (elemental and isotopic) of their minerals preserve

information about the conditions under which they formed. Given that magnetite is a ubiquitous mineral in both deposits, I use geochemical analyses to unveil the sources of the metals and the fluids and the conditions of formation of this mineral to understand the broader geological origins of these deposits. I also develop the potential for magnetite to be a geochronometer, thus, directly dating the timing of mineralization and opening the door for this mineral to be used in several other geological applications.

Chapter 2 presents geochemical data for magnetite from the Candelaria IOCG deposit and the Quince IOA prospect in Chile. Several magnetite types were identified based on their textural features and their chemical composition and magmatic and magmatic-hydrothermal characteristics were observed in both deposits. Ilmenite exsolution and granules were identified in Quince and in the deeper part of Candelaria and indicate that original titanomagnetite was present in both deposits. Minor and trace elements decrease from deep to shallow samples and from cores to rims within single grains, demonstrating an overall cooling trend and features like triple junctions indicate that dissolution-reprecipitation processes took place. Iron, oxygen, and hydrogen isotopes fingerprint a magmatic-hydrothermal source for the metals and the fluids at both deposits. Oxygen isotopes and actinolite composition were used as proxies for temperature and both agree with a high-temperature origin for both deposits consistent with an igneous to hydrothermal origin, where the shallow part of Candelaria is the typical IOCG deposit, whereas its deeper part represents a transition to a deeper IOA mineralization equivalent to Quince and other IOA deposits in Chile. This chapter is published in Economic Geology 2020 (v. 115, 7).

Chapter 3 focuses on understanding the processes that resulted in the mineralization at the Mina Justa IOCG deposit in Peru. I used magnetite geochemistry to characterize samples from different mineralization styles in the deposit, the “manto” in the shallow part of the system consisting of massive magnetite with disseminated sulfides (mainly pyrite and chalcopyrite), and the deeper disseminated to massive magnetite hydrothermal breccia that hosts most of the copper mineralization. Backscattered electron imaging documents the presence of mushketovite, which was originally hematite that was reduced to magnetite, and reveals textures of hydrothermal affinity in magnetite grains. Electron probe microanalyzer data reveal that trace element concentrations in magnetite are higher in the “manto” samples, especially in magnetite grains that contain abundant inclusions. These data agree with previous geochronological results that differentiate two magnetite mineralizing events. The first event resulted in the “manto” that

formed at a higher temperature as indicated by its higher trace element content. The second event consisted of lower temperature magnetite that is associated with the breccia and the Cu mineralization. Isotopic studies on magnetite and sulfides indicate a silicate magmatic reservoir for the ore fluids at Mina Justa. I also measured 17O in some magnetite samples and used Δ17O and δ18O values to assess the input (or lack of) of meteoric water and basinal brines. This holistic isotopic approach reveals the source of ore fluids at the Mina Justa IOCG deposit and helps to clarify the processes associated with the formation of the multi-stage Mina Justa deposit. This chapter is published in Economic Geology 2022 (v. 117, 3).

Chapter 4 tests the relative timing proposed in chapter 3 for mineralization at Mina Justa by using novel geochronological methods to date ore minerals directly. Previous workers used Ar–Ar geochronology to date alteration minerals (actinolite and microcline) from Mina Justa. The samples yielded dates ranging between 157 and 95 Ma and the authors interpreted magnetite to have formed at around 110 Ma and Cu sulfides at around 100 Ma, suggesting two separate mineralization events in the deposit. However, the relationships between the alteration minerals and the mineralization stages are poorly constrained hence, the proposed ages do not provide direct information about the timing of mineralization.

I characterized samples from the manto and breccia units at Mina Justa via scanning electron microscopy and identified magnetite, apatite, and titanite grains for U–Pb isotope measurements via in situ multi-collector inductively coupled plasma mass spectrometry (MC-ICP-MS). This innovative technique allows to perform spot analyses for detailed geochronological studies. Additionally, its application for dating magnetite opens the door to date mineralization in ore deposits that lack “traditional datable minerals” like molybdenite. I also prepared sulfide separates for Re–Os geochronology.

Our results are the first to date ore minerals at Mina Justa and indicate that magnetite, titanite, apatite, and sulfides in the deposit are older than previously published, inferred ages of mineralization, and that are temporally associated with the giant, neighboring Marcona IOA deposit. The results of this project contributed to understand the timescales of iron and copper mineralization at Mina Justa. This knowledge will help to identify the tectonic setting propitious for the occurrence of IOCG deposits in the Andes and elsewhere, allowing for the refinement of geophysical and geochemical exploration techniques to find new prospects that will optimize the

exploration process and maintain the supply of resources for future generations. This chapter will be submitted to a peer-reviewed journal in 2022.

1.5 References

Barton, M.D., 2014, Iron Oxide(–Cu–Au–REE–P–Ag–U–Co) Systems, in Holland, H.D. and Turekian, K.K. eds., Treatise on Geochemistry (Second Edition): Oxford, Elsevier, p. 515–541.

Barton, M.D., and Johnson, D.A., 1996, An evaporitic-source model for igneous-related Fe oxide(-REE – Cu-Au-U) mineralization: Geology, v. 24, p. 259–262.

Benavides, J., Kyser, T.K., Clark, A.H., Oates, C.J., Zamora, R., Tarnovschi, R., and Castillo, B., 2007, The Mantoverde Iron Oxide – copper – gold District, III Región, Chile: The Role of Regionally Derived, Nonmagmatic Fluids in Chalcopyrite Mineralization: Economic Geology, v. 102, no. 3, p. 415–440.

Bilenker, L.D., Simon, A.C., Reich, M., Lundstrom, C.C., Gajos, N., Bindeman, I., Barra, F., and Munizaga, R., 2016, Fe–O stable isotope pairs elucidate a high-temperature origin of Chilean iron iron oxide – apatite deposits: Geochimica et Cosmochimica Acta, v. 177, p. 94–104.

Blackburn, T.J., Stockli, D.F., and Walker, J.D., 2007, Magnetite (U–Th)/He dating and its application to the geochronology of intermediate to mafic volcanic rocks: Earth and Planetary Science Letters, v. 259, no. 3, p. 360–371.

Chen, H., Clark, A.H., and Kyser, T.K., 2010, The Marcona Magnetite Deposit, Ica, South-Central Peru: A Product of Hydrous, Iron Oxide-Rich Melts? Economic Geology, v. 105, no. 8, p. 1441–1456.

Chiaradia, M., Banks, D., Cliff, R., Marschik, R., and de Haller, A., 2006, Origin of fluids in iron oxide–copper–gold deposits: constraints from δ37Cl, 87Sr/86Sri and Cl/Br: Mineralium Deposita, v. 41, no. 6, p. 565–573.

Childress, T., Simon, A.C., Reich, M., Barra, F., Bilenker, L.D., Cruz, N.L.L., Bindeman, I.N., and Ovalle, J.T., 2020a, Triple Oxygen (δ18O, Δ17O), Hydrogen (δ2H), and Iron (δ56Fe) Stable Isotope Signatures Indicate a Silicate Magma Source and Magmatic-Hydrothermal Genesis for Magnetite Orebodies at El Laco, Chile: Economic Geology, v. 115, no. 7, p. 1519–1536.

Childress, T.M., Simon, A.C., Day, W.C., Lundstrom, C.C., and Bindeman, I.N., 2016, Iron and Oxygen Isotope Signatures of the Pea Ridge and Pilot Knob Magnetite – apatite Deposits, Southeast Missouri, USA: Economic Geology, v. 111, no. 8, p. 2033–2044.

Childress, T.M., Simon, A.C., Reich, M., Barra, F., Arce, M., Lundstrom, C.C., and Bindeman, I.N., 2020b, Formation of the Mantoverde iron oxide – copper – gold (IOCG) deposit, Chile: insights from Fe and O stable isotopes and comparisons with iron iron oxide – apatite (IOA) deposits: Mineralium Deposita, v. 55, no. 7, p. 1489–1504.

Cooperdock, E.H.G., and Stockli, D.F., 2016, Unraveling alteration histories in serpentinites and associated ultramafic rocks with magnetite (U-Th)/He geochronology: Geology, v. 44, no. 11, p. 967–970.

Courtney-Davies, L., Ciobanu, C.L., Verdugo-Ihl, M.R., Cook, N.J., Ehrig, K.J., Wade, B.P., Zhu, Z.-Y., and Kamenetsky, V.S., 2020, ~1760 Ma magnetite-bearing protoliths in the Olympic Dam deposit, South Australia: Implications for ore genesis and regional metallogeny: Ore Geology Reviews, v. 118, p. 103337.

Erel, Y., Harlavan, Y., Stein, M., and Blum, J.D., 1997, U–Pb dating of Fe-rich phases using a sequential leaching method: Geochimica et Cosmochimica Acta, v. 61, no. 8, p. 1697–1703.

Frei, R., Bridgwater, D., Rosing, M., and Stecher, O., 1999, Controversial Pb-Pb and Sm-Nd isotope results in the early Archean Isua (West Greenland) oxide iron formation: preservation of primary signatures versus secondary disturbances: Geochimica et Cosmochimica Acta, v. 63, no. 3, p. 473–488.

Gelcich, S., Davis, D.W., and Spooner, E.T.C., 2005, Testing the apatite – magnetite geochronometer: U–Pb and 40Ar/39Ar geochronology of plutonic rocks, massive magnetite – apatite tabular bodies, and IOCG mineralization in Northern Chile: Geochimica et Cosmochimica Acta, v. 69, no. 13, p. 3367–3384.

Groves, D.I., Bierlein, F.P., Meinert, L.D., and Hitzman, M.W., 2010, Iron Oxide Copper-Gold (IOCG) Deposits through Earth History: Implications for Origin, Lithospheric Setting, and Distinction from Other Epigenetic Iron Oxide Deposits: Economic Geology, v. 105, p. 641–654.

Hames, W.E., 2021, K/Ar and 40Ar/39Ar Dating Methods, in Encyclopedia of Geology: Elsevier, p. 50–65.

Haynes, D.W., 2000, Iron Oxide Copper (-Gold) Deposits: Their Position In The Ore Spectrum And Modes of Origin, in Porter, T.M. ed., Hydrothermal Iron Oxide Copper-Gold & Related Deposits: A Global Perspective: Adelaide, PGC Publishing, p. 71–90.

Hildebrand, R.S., 1986, Kiruna-type deposits; their origin and relationship to intermediate subvolcanic plutons in the Great Bear magmatic zone, Northwest Canada: Economic Geology, v. 81, no. 3, p. 640–659.

Hitzman, M.W., 2000, Iron Oxide – cu-Au Deposits: What, Where, When, and Why, in Porter, T.M. ed., Hydrothermal Iron Oxide Copper-Gold & Related Deposits: A Global Perspective 1: Adelaide, PGC Publishing, p. 9–25.

Hou, T., Charlier, B., and Namur, O., 2018, Immiscible hydrous Fe – ca – P melt and the origin of iron iron oxide – apatite ore deposits: Nature Communications, v. 9, p. 1–8.

Jonsson, E., Troll, V.R., Högdahl, K., Harris, C., Weis, F., Nilsson, K.P., and Skelton, A., 2013, Magmatic origin of giant "Kiruna-type" apatite-iron-oxide ores in Central Sweden: Scientific Reports, v. 3, p. 1–8.

Knipping, J.L., Bilenker, L.D., Simon, A.C., Reich, M., Barra, F., Deditius, A.P., Lundstrom, C., Bindeman, I., and Munizaga, R., 2015, Giant Kiruna-type deposits form by efficient flotation of magmatic magnetite suspensions: Geology, v. 43, no. 7, p. 591–594.

Knipping, J.L., Webster, J.D., Simon, A.C., and Holtz, F., 2019, Accumulation of magnetite by flotation on bubbles during decompression of silicate magma: Scientific Reports, v. 9, no. 1, p. 3852.

Mathur, R., Dendas, M., Titley, S., and Phillips, A., 2010, Patterns in the Copper Isotope Composition of Minerals in Porphyry Copper Deposits in Southwestern United States: Economic Geology, v. 105, no. 8, p. 1457–1467.

Mathur, R., Ruiz, J., Casselman, M.J., Megaw, P., and van Egmond, R., 2012, Use of Cu isotopes to distinguish primary and secondary Cu mineralization in the Cañariaco Norte porphyry copper deposit, Northern Peru: Mineralium Deposita, v. 47, no. 7, p. 755–762.

Nadoll, P., Angerer, T., Mauk, J.L., French, D., and Walshe, J., 2014, The chemistry of hydrothermal magnetite: A review: Ore Geology Reviews, v. 61, p. 1–32.

Naslund, H.R., Henriquez, F., Nyström, J.O., Vivallo, W., and Dobbs, F.M., 2002, Magmatic Iron Ires and Associated Mineralisation: Examples from the Chilean High Andes and Coastal Cordillera, in Porter, T.M. ed., Hydrothermal Iron Oxide Copper-Gold & Related Deposits: A Global Perspective 2: Adelaide, PGC Publishing, p. 207–226.

Nyström, J.O., and Henriquez, F., 1994, Magmatic features of iron ores of the Kiruna type in Chile and Sweden; ore textures and magnetite geochemistry: Economic Geology, v. 89, no. 4, p. 820–839.

Özdemir, Ö., and York, D., 1990, 40Ar/39Ar laser dating of a single grain of magnetite: Tectonophysics, v. 184, no. 1, p. 21–33.

Pollard, P.J., 2006, An intrusion-related origin for Cu–Au mineralization in iron oxide–copper–gold (IOCG) provinces: Mineralium Deposita, v. 41, no. 2, p. 179–187.

Rieger, A.A., and Marschik, R., 2012, The evolution of the hydrothermal IOCG system in the Mantoverde district, northern Chile: new evidence from microthermometry and stable isotope geochemistry: Mineralium Deposita, v. 47, p. 359–369.

Stein, H.J., 2014, Dating and Tracing the History of Ore Formation, in Treatise on Geochemistry: Elsevier, p. 87–118.

Stendal, H., Secher, K., and Frei, R., 2006, 207Pb-206Pb dating of magnetite, monazite and allanite in the central and northern Nagssugtoqidian orogen, West Greenland: GEUS Bulletin, v. 11, p. 101–114.

Tornos, F., Velasco, F., and Hanchar, J.M., 2017, The Magmatic to Magmatic-Hydrothermal Evolution of the El Laco Deposit (Chile) and Its Implications for the Genesis of Magnetite – apatite Deposits: Economic Geology, v. 112, p. 1595–1628.

Troll, V.R., Weis, F.A., Jonsson, E., Andersson, U.B., Majidi, S.A., Högdahl, K., Harris, C., Millet, M.-A., Chinnasamy, S.S., Kooijman, E., and Nilsson, K.P., 2019, Global Fe–O isotope correlation reveals magmatic origin of Kiruna-type apatite-iron-oxide ores: Nature Communications, v. 10, no. 1, p. 1712.

Westhues, A., Hanchar, J.M., LeMessurier, M.J., and Whitehouse, M.J., 2017, Evidence for hydrothermal alteration and source regions for the Kiruna iron oxide–apatite ore (northern Sweden) from zircon Hf and O isotopes: Geology, v. 45, no. 6, p. 571–574.

Williams, P., Barton, M.D., Johnson, D.A., Fontboté, L., De Haller, A., Mark, G., Oliver, N.H.S., and Marschik, R., 2005, Iron Oxide Copper-Gold Deposits: Geology, Space-Time Distribution, and Possible Modes of Origin: Economic Geology, v. 100, p. 371–405.

Chapter 2 : A Continuum from Iron Oxide – copper – gold (IOCG) to Iron Iron oxide – apatite (IOA) Deposits: Evidence from Fe and O Stable Isotopes and Trace Element Chemistry of Magnetite

Co-authors: Maria A. Rodriguez-Mustafa, Adam C. Simon, Irene del Real, John F.H. Thompson, Laura D. Bilenker, Fernando Barra, Ilya Bindeman

Published in *Economic Geology* (2020) v. 115, 7.

2.1 Abstract

Iron oxide – copper – gold (IOCG) and iron iron oxide – apatite (IOA) deposits are major sources of Fe, Cu and Au. Magnetite is the modally dominant and commodity mineral in IOA deposits, whereas magnetite and hematite are predominant in IOCG deposits with copper sulfides being the primary commodity minerals. It is generally accepted that IOCG deposits formed by hydrothermal processes, but there is a lack of consensus for the source of the ore fluid(s). There are multiple competing hypotheses for the formation of IOA deposits with models that range from purely magmatic to purely hydrothermal. In the Chilean Iron Belt, the spatial and temporal association of IOCG and IOA deposits has led to the hypothesis that IOA and IOCG deposits are genetically connected, where S – Cu – Au -poor magnetite-dominated IOA deposits represent the stratigraphically deeper levels of S – Cu – Au -rich magnetite- and hematite-dominated IOCG deposits. Here we report minor element and Fe and O stable isotope abundances for magnetite, and H stable isotope abundances for actinolite from the Candelaria IOCG deposit and Quince IOA prospect in the Chilean Iron Belt. Backscattered electron imaging reveals textures of igneous and magmatic-hydrothermal affinities and the exsolution of Mn-ilmenite from magnetite in Quince and deep levels of Candelaria (>500 m below the bottom of the open pit). Trace element concentrations in magnetite systematically increase with depth in both deposits, and decrease from core to rim within magnetite grains in shallow samples from Candelaria. These results are consistent with a cooling trend for magnetite growth from deep to shallow levels in both systems. Iron isotope concentrations of magnetite range from δ^{56}Fe values of 0.11 ± 0.07‰ to 0.16 ± 0.05‰ for Quince, and between 0.16 ± 0.03‰ and 0.42 ± 0.04‰ for Candelaria. Oxygen isotope concentrations of magnetite range from δ^{18}O values of 2.65 ± 0.07‰

to 3.33 ± 0.07‰ for Quince, and between 1.16 ± 0.07‰ and 7.80 ± 0.07‰ for Candelaria. For cogenetic actinolite, δD values range from -41.7 ± 2.10‰ to -39.0 ± 2.10‰ for Quince, and from -93.9 ± 2.10‰ to -54.0 ± 2.10‰ for Candelaria, and $\delta^{18}O$ values range between 5.89 ± 0.23‰ and 6.02 ± 0.23‰ for Quince, and between 7.50 ± 0.23‰ and 7.69 ± 0.23‰ for Candelaria. The paired Fe and O isotope compositions of magnetite and the H isotope signature of actinolite fingerprint a magmatic source reservoir for ore fluids at Candelaria and Quince. Temperature estimates from O-isotope thermometry and Fe # of actinolite are consistent with high-temperature mineralization (600 – 860 °C). The re-integrated composition of primary Ti-rich magnetite is consistent with igneous magnetite and supports magmatic conditions for the formation of magnetite in the Quince prospect and the deep portion of the Candelaria deposit. The trace element variations and zonation in magnetite from shallower levels of Candelaria are consistent with magnetite growth from a cooling magmatic-hydrothermal fluid. The combined chemical and textural data are consistent with a combined igneous and magmatic-hydrothermal origin for Quince and Candelaria, where the deeper portion of Candelaria corresponds to a transitional phase between the shallower IOCG deposit and a deeper IOA system analogous to the Quince IOA prospect, providing evidence for a continuum between both deposit types.

2.2 Introduction

Iron oxide – copper – gold (IOCG) and iron oxide – apatite (IOA) mineral deposits are major sources of Fe, Cu and Au, and are commonly enriched in other elements (e.g., Ag, Mo, Co, As, U, and REE) (Hitzman et al., 1992; Hitzman, 2000; Williams et al., 2005; Groves et al., 2010; Barton, 2014; Corriveau et al., 2016). Both deposit types are structurally and/or stratigraphically controlled, are associated with extensive Na-Ca and more localized K alteration, and contain abundant Fe-oxides; magnetite in IOAs, and magnetite and/or hematite in IOCGs. These deposit types are distributed globally and occur sporadically over a considerable age range from the Archean to the Pliocene (Hitzman, 2000; Williams et al., 2005; Groves et al., 2010; Barton, 2014).

Traditionally, distinct and separate genetic models have been proposed for IOCG and IOA deposits. In general, it is accepted that IOCG deposits form by hydrothermal processes where the hydrothermal ore fluid has been proposed to be a basinal brine that leaches metals

from the crust (Barton and Johnson, 1996; Haynes, 2000; Benavides et al., 2007), a magmatic-hydrothermal fluid that extracts the metals from a silicate magma (Pollard, 2006), or a combination of both (Hitzman, 2000; Chiaradia et al., 2006; Groves et al., 2010; Rieger and Marschik, 2012). However, there is no consensus regarding the origin of IOA deposits. The four competing genetic models for IOA deposits are: 1) a purely magmatic origin that invokes the unmixing of an intermediate silicate melt into coexisting Fe-P-rich melt and Si-rich melt where volatiles such as F, Cl and H_2O are hypothesized to preferentially partition into the Fe-P-melt making it less dense and allowing it to ascend from the source magma into the upper crust where it crystallizes to form an IOA deposit (Nyström and Henriquez, 1994; Naslund et al., 2002; Chen et al., 2011; Tornos et al., 2017; Hou et al., 2018); 2) a magmatic-hydrothermal origin in which the fluid extracts the metals from a silicate magma (Hildebrand, 1986; Jonsson et al., 2013; Westhues et al., 2017a; Westhues et al., 2017b); 3) a hydrothermal metasomatic origin involving a magmatic-hydrothermal fluid (Ménard, 1995) or a mixed ore fluid that consisted of magmatic-hydrothermal and basinal brines (Rhodes and Oreskes, 1999); 4) a combined igneous and magmatic-hydrothermal model in which primary igneous magnetite nano- and micro-lites serve as nucleation sites for an exsolving hypersaline magmatic-hydrothermal fluid, with hydrothermal magnetite growing from the fluid as it cools during ascent and emplacement (Knipping et al., 2015a; Knipping et al., 2019).

In the Chilean Iron Belt, the spatial and temporal association of IOCG and IOA deposits has led some to suggest a genetic connection between the two deposit types, where S – Cu – Au -poor magnetite-dominated IOA deposits represent the deeper levels of S – Cu – Au -rich magnetite- and/or hematite-dominated IOCG deposits (Espinoza et al., 1996; Naslund et al., 2002; Sillitoe, 2003; Knipping et al., 2015a; Reich et al., 2016; Barra et al., 2017; Simon et al., 2018).

In this study, we investigate the geochemistry of magnetite and actinolite from drill core samples from the world-class Candelaria IOCG deposit and the Quince IOA prospect, both in the Chilean Iron Belt. Importantly, these two ore bodies are spatially separate and did not form from the same mineralizing event. The purpose of the current study is to use the geochemistry of magnetite, the modally dominant mineral in both deposits, and actinolite to assess the hypothesis that IOCG and IOA deposit types are products of a single evolving ore system. The chemistry and textures of magnetite in samples from drill cores from both deposits were investigated using

an electron probe microanalyzer (EPMA) and a scanning electron microscope (SEM) in order to evaluate the conditions and processes under which magnetite formed. Additionally, we provide the first analyses of Fe and O stable isotopes of magnetite and H stable isotopes of actinolite from these deposits to fingerprint the source of the ore fluids. Temperatures of mineralization at both deposits were estimated by using two methods: the oxygen isotope compositions of cogenetic magnetite and actinolite, and the Fe # of actinolite.

2.3 Geological background

The Chilean Iron Belt extends for over 800 km in the Coastal Cordillera of northern Chile and southern Peru (Figure 2-1) and contains ~50 Jurassic – Cretaceous IOA and IOCG mineral deposits hosted in Jurassic – Cretaceous volcanic sequences. In general, IOA and IOCG deposits are temporally and spatially associated, and occur along curvatures and intersections of faults with different orientations (NNE and NW) within the strike-slip Atacama Fault System (AFS) (Nyström and Henriquez, 1994; Barra et al., 2017; Veloso et al., 2017). The AFS evolved between 132 and 125 Ma from a purely extensional back-arc setting to a transtensional setting as a response to a change in the plate interactions (Brown et al., 1993; Charrier et al., 2007).

2.3.1 Quince

Quince is an IOA prospect located ~40 km east of Chañaral, Chile (Figure 2-1). It was discovered in 1998 by an aeromagnetic survey. Geophysical data and drill core assaying were used to estimate a total resource of 2300 million tonnes at 30% Fe and 325.8 million tonnes at 0.39% V_2O_5. (Quince Iron Chile Website, 2019). The mineralization is hosted in the Late Jurassic volcanic La Negra Formation and the Cretaceous Sierra Aspera Diorite, and is covered by Quaternary sediments (SRK Consulting, 2014). The Quince prospect consists mainly of massive magnetite lenses and banded magnetite – calcite – quartz veins and magnetite – actinolite veins, indicating an initial mineralization event within a ductile shear zone belonging to the Atacama Fault System (SRK Consulting, 2014). Stockwork-style mineralization with magnetite-rich breccias and magnetite veinlets distal to the ductile shear zone suggest a transition to a brittle regime where mineralization is mostly controlled by faulting. Magnetite is cogenetic with actinolite, and apatite, diopside, calcite, quartz, and pyrite occur as modally minor phases. Sodic-calcic alteration dominated by albite and epidote is pervasive within the ore body and host

rocks. Moderate potassic (K-feldspar and biotite) and quartz – chlorite – serricite alteration have also been reported in the prospect (SRK Consulting, 2014). Late-stage fractures filled with calcite and chlorite cut the main mineralization.

2.3.2 Candelaria

The Candelaria IOCG deposit has been in production for over 20 years, and is located near the city of Copiapó, Chile, in the Candelaria – Punta del Cobre District (Figure 2-2). Mineral reserves as of 2018 for the Candelaria open pit and the Española project were 415 Mt at 0.48% Cu and 0.11 g/t of Au (Couture et al., 2018). Mineralization consists of Fe-oxides (magnetite, mushketovite and hematite) and sulfides (pyrite, chalcopyrite and minor pyrrhotite) and is mostly hosted in the Cretaceous volcanic to volcaniclastic Punta del Cobre Formation, which consists of the Lower Andesite, Dacite, Volcanic sediments, and Upper Andesite members (del Real et al., 2018). The Punta del Cobre Formation is overlain by the marine sedimentary Chañarcillo Group, which was deposited in a shallow-marine environment associated with the development of the Chañarcillo back-arc basin (Marschik et al., 1997) and contains carbonate-bearing horizons (Marschik and Fontboté, 2001b; Mourgues, 2004; del Real et al., 2018).

Mineralization is stratigraphically and/or structurally controlled. Stratigraphically controlled bodies (commonly called “mantos”) are characterized by magnetite – actinolite zones, pervasive magnetite – actinolite with potassic (biotite, K-feldspar) ± quartz alteration and disseminated sulfides (chalcopyrite, pyrrhotite ± pyrite), and overprinting biotite, magnetite (± mushketovite), chalcopyrite, pyrrhotite ± pyrite and sphalerite veins and disseminations (del Real et al., 2018). Structurally controlled veins and breccias consist of chalcopyrite ± pyrite, actinolite, magnetite ± mushketovite, with intense Na-Ca (albite – epidote), potassic (biotite, K-feldspar) ± quartz alteration (del Real et al., 2018).

The mineralization spanned between 118 – 112 Ma (del Real et al., 2018), with an early magnetite – actinolite event (del Real et al., 2018) overprinted by a main chalcopyrite – magnetite Cu mineralization event at 115 Ma (Marschik and Fontboté, 2001a; Mathur et al., 2002) accompanied by actinolite and potassic (biotite and K-feldspar) alteration (del Real et al., 2018). A comprehensive description of the geology, alteration, and mineralization styles of this deposit can be found in del Real et al. (2018).

Marschik and Fontboté (2001a) proposed three main stages for the formation of Candelaria based on their investigation of samples from the shallow levels of the deposit. Those authors report fluid inclusion homogenization temperatures that indicate magnetite formed between 600 °C and 500 °C followed by sulfide-rich mineralization between 470 °C and 328 °C, and a later hematite dominated mineralization at temperatures <300 °C. The $\delta^{18}O$ values for quartz reported by Marschik et al. (2000), $\delta^{34}S$ data for anhydrite, chalcopyrite, pyrite, pyrrhotite and sphalerite reported by Marschik and Fontboté (2001a), and in situ $\delta^{34}S$ of pyrite reported by del Real et al. (in review) support a magmatic-derived fluid as the primary ore fluid responsible for IOCG mineralization at Candelaria, and mixing of the ore fluid with external (meteoric or basinal) fluid(s) during the late (low-temperature; <250 °C) stage of mineralization.

2.4 Sampling and Methods

Three core samples were collected from drill hole AQ-19 located in the southern portion of the Quince prospect. This 496 m long drill hole traverses the magnetite veinlet-rich breccia, the massive magnetite mineralization, and the stockwork zone. Sixteen core samples from the Candelaria – Punta del Cobre District were collected from drill holes in the Santos underground mine (DH703), the Candelaria mine (LD0987, LD1111, and LD1687B), and nearby exploration targets (ES032, ES064) (Figure 2-2). Ten of the samples were collected from drill hole LD1687B, which was collared in the Candelaria open pit and was drilled to 1147 m at an azimuth of 245° and a plunge of 60 °.

2.4.1 Sample preparation

Three samples from Quince and six samples from the Candelaria – Punta del Cobre District were mounted in epoxy resin for EPMA and SEM analyses. Eight thin sections spanning the whole length of the LD1687B Candelaria drill core were made for microscopy and EPMA studies. For isotopic analyses, magnetite was sampled from the massive magnetite horizons, or from magnetite veins where available, from the Candelaria – Punta del Cobre District and the Quince prospect. Each sample was crushed using an agate mortar and pestle, which was rinsed with ethanol and put through an ultrasonic cleaner between each sample to prevent contamination. The magnetic fraction was obtained by using a hand magnet wrapped in weighing paper, and individual, visibly un-weathered magnetite grains were handpicked using a binocular microscope at ~40x magnification. Actinolite separates were obtained using a Frantz magnetic

separator, followed by lithium metatungstate heavy liquid separation, and handpicking of individual grains under the microscope to minimize the presence of other mineral phases. For samples where the intergrown minerals had a very small grain size, the resulting actinolite separates may have contained a small fraction of fine intergrown minerals including magnetite. Aliquots of actinolite analyzed for O isotopes, described below, were pre-fluorinated to remove impurities such as chlorite.

2.4.2 EPMA and FE-SEM

Backscattered electron (BSE) images were obtained to characterize textures by using a JEOL 7800FLV field emission-scanning electron microscope (FE-SEM) in the Electron Microbeam Analysis Laboratory at the University of Michigan. Point and line transect analyses were performed by using a Cameca SX-100 electron microprobe with a focused beam, a voltage of 20 keV and a current of 30 nA for magnetite and ilmenite grains, and a 2 μm beam, 15 keV and 20 nA for actinolite samples. Counting times, standards and detection limits are listed in the Supplementary Materials (Table A-1). We measured Mg, Al, Si, P, Ca, Ti, V, Cr, Mn, and Fe in magnetite and ilmenite grains avoiding inclusions and exsolution lamellae, and executed a TiKα - VKβ interference correction. For actinolite grains, concentrations of Si, Ti, Al, Fe, Mn, Mg, Ca, Na, K and P oxides were calculated from raw X-ray intensities using a ZAF intensity correction.

2.4.3 Iron isotopes

Ion chromatography was performed on magnetite grains to isolate pure Fe from each sample. To fully dissolve each sample, approximately 2.0 mg were first digested in HF and HNO_3 for $\geq$24 hours, dried on a hot plate, re-fluxed in aqua regia, and dried once more. In preparation for column chemistry, samples were dissolved in 0.5 mL 8N HCl, dried, and dissolved in 0.4 mL 8N HCl at ~120 °C. The conditioning and elution procedure were completed following the procedure of Huang et al. (2011) using Biorad AG1-X8 Ion Exchange Resin (200 – 400 mesh). All reactants (HNO_3, HCl, HF) were Optima Grade and H_2O was ultrapure. The stable Fe isotope analyses were performed at the Pacific Centre for Isotopic and Geochemical Research, University of British Columbia using a Nu Plasma 1700 multi collector-inductively coupled plasma-mass spectrometer (MC-ICP-MS) in dry plasma mode with a DSN-100 Desolvating Nebulizer System. All analyses were performed in true high-resolution mode as isobaric interferences (i.e., Ar complexes) were fully resolved from the Fe isotopes (^{54}Fe, ^{56}Fe,

^{57}Fe). Minor Cr corrections were done online for each analysis by monitoring ^{52}Cr. Every sample was measured between 2 and 4 times, and was bracketed immediately before and after analysis by the measurement of standard 14 from the Institute for Reference Materials and Measurements (IRMM-14). The concentration of the samples was adjusted to be within 10% of the bracketing standard solution.

2.4.4 Oxygen and hydrogen isotopes

The isotopic ratio of δ^{18}O SMOW of magnetite and actinolite separates (1.5 – 2.1 mg each) was measured at the University of Oregon using BrF_5 in a laser fluorination line connected to a Thermo-Finnigan MAT 253 gas isotope ratio mass spectrometer (IRMS) in dual inlet mode. The Gore Mountain garnet (GMG) standard (6.52‰) and UWG-2 garnet (5.8‰) were measured prior, during, and after the sample analyses to quantify them onto a SMOW scale (Loewen and Bindeman, 2016). Yields (μmol/mg of extracted O_2 gas) were monitored by a Barathron gauge. The water content and stable δD isotope ratios of actinolite samples were measured by thermal pyrolysis using thermal conversion elemental analyzer attached to a MAT 253 IRMS by a continuous flow method also at the University of Oregon. We used a glassy carbon reactor held at 1450 °C following the analytical procedures described in Bindeman et al. (2012). For standards we used new USGS57 and 58 micas (Qi et al., 2017), and our analyses had a precision of ±0.03 wt% water and ±2‰ δD.

2.4.5 Reintegration of ilmenite exsolution lamellae and granules in magnetite

We selected 6 BSE images from 3 samples from Quince and 7 BSE images from 3 Candelaria samples that contain magnetite and ilmenite. We used the difference in grayscale between magnetite and ilmenite to do a supervised image classification and estimate the fraction of magnetite and ilmenite in each image by using the Python programming language. We then normalized the mineral fractions with their respective average Ti, V, Al and Mn concentrations to a single magnetite phase.

2.5 Results

2.5.1 Core Sample Descriptions

Candelaria: The upper part of drill core LD1687B intersects layered sedimentary rocks replaced by magnetite, traverses the manto massive magnetite (± mushketovite) mineralization, and then cuts through magnetite and actinolite-rich horizons at greater depth (Figure 2-3 a-f). Pyrite, chalcopyrite and minor pyrrhotite are present disseminated or in veins, and decrease in abundance with depth. Sodic-calcic (actinolite, albite, epidote) and potassic (K-feldspar ± biotite) are the dominant alteration assemblages. Late-stage quartz and anhydrite veins cross-cut primary mineralization, and secondary chlorite is also present (Figure 2-3f). Other accessory minerals in the Candelaria – Punta del Cobre District only identified in thin section include apatite, calcite, ilmenite, and titanite. Detailed hand sample descriptions are provided in Table 2-1.

Quince: Representative scans of drill core samples of the magnetite veintlet-rich breccia, massive magnetite, and magnetite from the stockwork zone are shown in Figure 2-3g, h and i, respectively. Magnetite (modal abundance of ~95%) and actinolite (modal abundance of ~5%) are intergrown with each other and occur in the groundmass and as veinlets (Figure 2-3i). Apatite and diopside are minor accessory phases. Disseminated pyrite is present, but is modally insignificant. The main alteration in the deposit is sodic-calcic (albite±scapolite±epidote). Late-stage quartz (± chlorite) veins cross-cut the main mineralization. Detailed hand sample descriptions are provided in Table 2-1.

2.5.2 Magnetite textures and associated minerals

The BSE images of magnetite from the Candelaria – Punta del Cobre District reveal two magnetite textures (Table 2-2). Type C is characterized by euhedral magnetite lacking visible exsolution lamellae and few or no visible aluminosilicate or other inclusions (Figure 2-4a,e). Type D refers to both mushketovite (hematite that has been replaced by magnetite) that exhibits patchy zonation and magnetite that exhibits concentric (core and rim) zonation between relatively dark and light areas, where the dark areas are locally inclusion-rich (Figure 2-4b-c). Magnetite type C is present throughout the entire LD1687B hole. Magnetite type D was only identified in shallower samples (i.e., <500 m deep). Magnetite grains with ilmenite exsolution lamellae, type B at Quince as described below, were not observed in any Candelaria samples. Magnetite grains from the deep samples (>500 m below the bottom of the open pit) in the

Candelaria drill hole LD1687B, however, are intimately related with ilmenite that occurs as fracture infill (Figure 2-4d), or as granules adjacent to magnetite grains (Figure 2-4f).

The BSE images from Quince reveal three magnetite textures (Table 2-2): magnetite rich in Fe – mg silicate and aluminosilicate inclusions (type A), magnetite that contains abundant ilmenite exsolution lamellae forming trellis and cloth textures (type B), and euhedral magnetite without visible inclusions or exsolution lamellae (type C) (Figure 2-4g-i). All three textures are observed throughout the entire length of the sampled drill hole and there is no textural zonation observed within grains. In magnetite type B, trellis texture is predominant in the deepest sample (404 m), while cloth-textured exsolution lamellae are visibly more abundant than trellis-textured lamellae in the shallowest sample (68 m). The sample from intermediate depth (334 m) shows both textures in similar proportions. Magnetite grains of all textural types commonly meet at triple junctions (Figure 2-4g-i). Ilmenite, and rutile to a lesser extent, are present along grain boundaries and fill interstices among magnetite (mostly type C) grains. Interstitial ilmenite and rutile are more abundant in shallower samples, and their occurrence is inversely proportional to the quantity of exsolution lamellae in magnetite (Figure 2-4g).

2.5.3 Trace element compositions of magnetite

All EPMA data for magnetite and ilmenite are provided in Table A-2 and Table A-3. Magnetite from Quince contains 71.8 ± 0.8 wt% Fe. Iron, Si, and Cr in magnetite generally increase with depth throughout the drill hole, while Al, Ti and Mn generally decrease. Vanadium and Ca show no significant variation with depth, and Mg fluctuates non-systematically. Interstitial ilmenite is enriched in Mn, containing an average Mn concentration of 5.1 ± 2.4 wt%. Magnetite from the Candelaria – Punta del Cobre District contains 71.3 ± 1.06 wt% Fe. The concentrations of Mg, Al, Ca, V, and Cr in magnetite generally increase with depth, whereas Mn generally decreases. Iron, Si, and Ti concentrations in magnetite do not show systematic variations with depth, but the concentration of Ti in magnetite is higher in samples where ilmenite is present. The rims of zoned magnetite grains (Type D) from shallow samples are enriched in Fe (71.8 wt% Fe) and depleted in trace elements (0.01 wt% Cr, 0.04 wt% Ca, 0.05 wt% Al, 0.05 wt% Mn, 0.08 wt% Ti, 0.09 wt% Mg, 0.19 wt% Si) relative to cores (70.1 wt% Fe, 0.03 wt% Cr, 0.16 wt% Ca, 0.12 wt% Al, 0.07 wt% Mn, 0.11 wt% Ti, 0.22 wt% Mg, 0.73 wt% Si). Ilmenite granules are Mn-rich (average 4.3 ± 2.6 wt% Mn; maximum 10.9 wt% Mn).

2.5.4 Ilmenite reintegration in magnetite

The EPMA Ti, V, Mn and Al contents of individual ilmenite and magnetite grains from the analyzed BSE images, and the results for the mineral fraction estimations and the reintegration of ilmenite into host magnetite are summarized in Table A-5. After the reintegration, the calculated concentrations of Ti, V, Al and Mn (wt.%) vary between 0.53 – 2.92, BDL – 0.03, BDL – 0.03, and 0.05 – 0.35, respectively, for the samples of Candelaria, and between 0.56 – 3.03, 0.15 – 0.17, 0.03 – 0.05, and 0.10 – 0.70 for the Quince samples.

2.5.5 Actinolite chemistry

All EPMA data for actinolite are provided in Table A-4. Average compositions for three Candelaria samples at progressively greater depth downhole: 43 (617.8 m), 52 (731.3 m) and 58 (846.5 m) in drill hole LD1687B, and Quince sample 2 (down hole depth = 404.3m) are summarized in Table 2-3. On average, the actinolite from Candelaria is enriched in FeO (11.3 – 13.2 wt%) and CaO (12.2 wt.%) and depleted in TiO_2 (0.12 – 0 .27 wt.%), Al_2O_3 (3.21 – 4.14 wt.%), MgO (15.5 – 16.5 wt.%), and Na_2O (0.36 – 0.50 wt.%) with respect to the actinolite from Quince (8.94 FeO wt.%, 11.6 CaO wt.%, 0.38 TiO_2 wt.%, 4.35 Al_2O_3 wt.%, 18.9 MgO wt.%, and 0.73 Na_2O wt.%). The average Ca (a.p.f.u) content of actinolite in the Candelaria samples was 2.03, and 1.90 for the Quince sample (Table 2-3). For the same samples, the Fe number of actinolite (Fe # = [molar Fe]/([molar Fe]+[molar Mg])) was calculated by following the methodology by Lledo and Jenkins (2008). The actinolite grains yielded an average Fe number ± 2σ of 0.29 ± 0.11, 0.28 ± 0.05, 0.32 ± 0.05, and 0.21 ± 0.05, respectively.

2.5.6 Iron isotope compositions of magnetite separates

Table 2-4 summarizes the Fe isotope data for the 16 magnetite samples relative to the IRMM-14. Analyses of the reference material BCR-2 yielded an average value of 0.09 ± 0.03‰ (n=12), which is consistent with the value of 0.09 ± 0.01‰ (n=8) recommended by Craddock and Dauphas (2011). The $\delta^{56}Fe$ ± 2σ (2 standard deviation) values for magnetite from Quince range between 0.11 ± 0.07‰ and 0.16 ± 0.05‰ and yield an average value of 0.13 ± 0.03‰ (n=3). The samples from Candelaria range between 0.16 ± 0.03‰ and 0.42 ± 0.04‰ and yield an average of 0.23 ± 0.04‰ (n=13).

2.5.7 Oxygen and hydrogen isotope compositions of magnetite and actinolite separates

Oxygen isotope data for 15 magnetite and 5 actinolite samples (Table 2-4) are reported relative to the international Vienna Standard Mean Ocean Water (VSMOW) standard. Analyses of the standard GMG yielded $\delta^{18}O \pm 2\sigma$ values of 6.24 ± 0.07‰ and 6.42 ± 0.23‰ over two days of measurements for the magnetite samples, and 6.48 ± 0.23‰ for the actinolite samples. The analytical values were corrected by using the difference between the measured and the expected value for the standard for each day.

The $\delta^{18}O \pm 2\sigma$ values for magnetite from Quince range between 2.65 ± 0.07‰ and 3.33 ± 0.07‰ and have an average $\delta^{18}O \pm 2\sigma$ value of 3.04 ± 0.4‰ (n=3). The samples from Candelaria yielded $\delta^{18}O \pm 2\sigma$ values that range from 1.16 ± 0.07‰ to 7.80 ± 0.07‰, and have an average $\delta^{18}O \pm 2\sigma$ value of 3.52 ± 0.94‰ (n=12). The average $\delta^{18}O \pm 2\sigma$ values for actinolite are 5.96 ± 0.13‰ (n=2) and 7.57 ± 0.12‰ (n=3) for Quince and Candelaria, respectively.
Hydrogen isotope values of actinolite samples relative to VSMOW are compiled in Table 2-4. The $\delta D \pm 2\sigma$ values for actinolite from Quince average -40.4 ± 2.7‰ (n=2), and from Candelaria average -67.3 ± 18.0‰ (n=4), with the lightest value corresponding to the shallowest sample. The water content (wt.% $H_2O \pm 2\sigma$) of actinolite from Quince averages 2.00 ± 0.03 wt% (n=2), and actinolite from Candelaria averages 1.97 ± 0.89 wt% (n=4). The low H_2O concentration and the light δD value measured for sample 6 from the LD1687B drill hole may reflect the presence of some chlorite and magnetite identified in hand sample (Table 2-1).

2.6 Discussion

2.6.1 Constraints on magnetite and actinolite formation

The inclusion-rich magnetite (type A) from Quince (Figure 2-4h,i) is similar to magnetite reported in drill core from the El Laco (Ovalle et al., 2018), Los Colorados (Knipping et al., 2015b) and El Romeral (Rojas et al., 2018) IOA deposits in Chile. Those authors concluded that El Laco, Los Colorados and El Romeral formed by a combination of igneous and magmatic-hydrothermal processes based on the stability of the magnetite-hosted mineral inclusions (all three deposits) and the presence of ilmenite exsolution lamellae (El Laco and El Romeral) in magnetite. Magnetite grains with trellis and cloth textured ilmenite exsolution lamellae, as observed in type B magnetite in Quince, are common in igneous rocks and Fe-Ti oxide deposits hosted in mafic intrusions (Buddington and Lindsley, 1964; Carmichael, 1966; Haggerty, 1976;

Pang et al., 2008; Tan et al., 2016; Arguin et al., 2018), but to our knowledge have only been reported in a few studies of IOA deposits (e.g., Malmberget: Lund, 2013; El Laco: Ovalle et al., 2018; El Romeral: Rojas et al., 2018; Gushan: Sun et al., 2019) and in the Sossego IOCG deposit (Huang and Beaudoin, 2019). The presence of trellis and cloth texture exsolution lamellae results from oxyexsolution of primary Ti-rich magnetite. The process of oxyexsolution was first described by Buddington and Lindsley (1964) who experimentally demonstrated that at 550 – 1000 °C in the FeO-Fe_2O_3-TiO_2 system, a solid solution exists between magnetite and ulvöspinel (Fe_2TiO_4). If magnetite–ulvöspinel$_{SS}$ cools in a water-rich system, the ulvöspinel component of the solid solution is directly oxidized to magnetite and ilmenite, where the latter exsolves along the (111) planes of magnetite (Buddington and Lindsley, 1964; Haggerty, 1976). Trellis and cloth textures can coexist in a single magnetite grain, but cloth texture is generated at lower temperatures than trellis texture (Neybergh et al., 1980; Gruenewaldt et al., 1985). In Quince, the transition from trellis dominated to cloth dominated textures in magnetite grains from deep to shallow levels indicates cooling of the system, and correlates with increasing proportions of interstitial ilmenite and inclusion-free magnetite (type C) at shallower levels (Figure 2-4g-i). The presence of ilmenite exsolution lamellae in magnetite grains and coating grain boundaries in samples from Quince is evidence for primary Ti-rich magnetite growth at magmatic or near-magmatic temperatures.

The Al_2O_3 and TiO_2 compositions of actinolite are directly proportional to the temperature and pressure conditions at which they formed (Mark and Foster, 2000 and references therein). The elevated content of these oxides in actinolite from the deeper samples at Candelaria and Quince are consistent with mineralization at high-temperature conditions (Table 2-3 and Table A-4). The temperature of mineralization for Quince was estimated using the Fe # of actinolite, which is coeval with magnetite, following Lledo and Jenkins (2008). Those authors experimentally demonstrated the upper stability of natural actinolite from the Pleito Melón IOA deposit in Chile (Fe # = 0.22 and Ca a.p.f.u = 1.97) to be ~780 °C at 100 MPa and 850 °C at 400 MPa. The Ca a.p.f.u. of actinolite from Quince is similar to that reported by Lledo and Jenkins (2008), which allows us to use their model to estimate the temperature of actinolite crystallization. The Fe # of actinolite of the Quince samples yields a formation temperature of 795 °C at 100 MPa and 830 °C at 400 MPa (Table 2-3). These temperatures are within the range of 610 – 820 °C estimated by Bilenker et al. (2016) for actinolite from the Los Colorados IOA

deposit, Chile and 735 – 840 °C estimated by Rojas et al. (2018) for actinolite from the El Romeral IOA deposit, Chile by using the Fe # method. The textural association of actinolite and magnetite in samples from Quince is similar to that reported for Los Colorados (Bilenker et al., 2016), El Romeral (Rojas et al., 2018) and Cerro Negro Norte (Salazar et al., 2019). The composition of actinolite from Quince is also similar to that reported from actinolite from the aforementioned studies and indicates mineral growth at magmatic to magmatic-hydrothermal conditions, which is consistent with the conclusions reported for mineralization at Los Colorados, El Romeral and Cerro Negro Norte. We note that the δD values of actinolite cogenetic with magnetite in Quince and the deeper samples from Candelaria (Table 2-4) are consistent with a high-temperature, magmatic source when paired with their O isotope values (Taylor, 1974; Hedenquist and Lowenstern, 1994), as has been reported for actinolite from Los Colorados IOA deposit (Bilenker et al. 2016).

We also estimated the temperature of mineralization at Quince by using the oxygen isotope fractionation factor between actinolite and magnetite using the equation 1:

$$\delta^{18}O_{actinolite} - \delta^{18}O_{magnetite} = \Delta^{18}O_{actinolite-magnetite}$$

$$\sim 1000 \ln \alpha = 10^6 \times \frac{A}{T^2}$$

where $\Delta^{18}O_{actinolite\ -\ magnetite}$ was calculated using the measured isotopic compositions of sample AQ-19 2. An A factor of 3.54 for diopside (a close analogue to actinolite; Chiba et al., 1989) was used as a proxy for actinolite as no direct experimental data for actinolite are available. We highlight that the analyzed magnetite grains contain ilmenite exsolution lamellae, and that the bulk magnetite – ilmenite oxygen isotope ratios are likely representative of the primary Ti-rich magnetite and not affected by exsolution, as magnetite is the dominant phase and is buffered (cf. Valley, 2001). The magnetite – actinolite pairs from the deepest level of Quince yield calculated temperatures of 835 °C and 860 °C. These model temperatures for magnetite are consistent with the high temperatures estimated from actinolite chemistry and indicate formation of primary igneous magnetite–ulvöspinel$_{SS}$ that unmixed during cooling and subsequent oxidation to magnetite and ilmenite, where the latter is present as exsolution lamellae in magnetite and interstitially coating grain boundaries among magnetite grains (Figure 2-4g-i). The agreement between temperatures of mineralization estimated by using the Fe # of actinolite and $\Delta^{18}O_{actinolite}$

$_{\text{– magnetite}}$ suggests that the two phases crystallized in equilibrium with one another (cf. Farquhar et al., 1993; Valley, 2001).

We did not observe ilmenite exsolution lamellae in any magnetite grains from Candelaria as described above for magnetite type B in Quince. However, the presence of ilmenite granules intimately associated with magnetite in the deepest Candelaria samples (e.g., Figure 2-4f, >800 m below the bottom of the open pit) and the interstitial ilmenite in Quince samples are consistent with the granule oxyexsolution process described by Buddington and Lindsley (1964). Those authors report that granular ilmenite is produced by fluid-mediated oxyexsolution of primary magnetite–ulvöspinel$_{SS}$ that results in complete exsolution of ilmenite from magnetite. Granular oxyexsolution occurs by subsolidus oxidation of magnetite–ulvöspinel$_{SS}$ by reaction with intergranular fluid. The presence of triple junctions among magnetite grains in both deposits (Figure 2-4e,g-i), and of interstitial ilmenite in the Quince samples (Figure 2-4g,h), are evidence for re-equilibration of primary Ti-rich magnetite and re-precipitation of pristine, hydrothermal magnetite (Type C) and interstitial ilmenite in the presence of a high-temperature fluid (Hu et al., 2014; Heidarian et al., 2016; Ovalle et al., 2018). The decrease in ilmenite exsolution lamellae in magnetite coupled with the increase in interstitial ilmenite from deep to shallow levels in Quince, and the ilmenite granules in deeper samples from Candelaria are consistent with migration of exsolved ilmenite outside of the magnetite crystal structure by reaction with high-temperature hydrothermal fluid potentially during the ore forming mineralization process. The presence of interstitial rutile with ilmenite and magnetite is also evidence for re-equilibration of original Ti-rich magnetite under hydrothermal conditions at temperatures ranging from 400 °C to 700 °C as reported in studies of porphyry copper deposits (Rabbia et al., 2009; Rabbia and Hernández, 2012).

The temperatures of crystallization for actinolite in Candelaria samples LD1987B 43, 52, and 58 estimated following Lledo and Jenkins (2008) at 100 MPa are 752°C, 756°C, and 741°C, respectively (Table 2-3). The actinolite – magnetite pair ($\Delta^{18}O_{\text{actinolite – magnetite}}$) approach yielded minimum temperatures of formation of 591°C, 665 °C, and 595 °C for samples LD1987B 43, 61 and 74 (Table 2-4). The lack of agreement for temperatures at Candelaria estimated using the Fe # of actinolite and $\Delta^{18}O_{\text{actinolite – magnetite}}$ pairs likely reflects uncertainties in the thermodynamic model of Lledo and Jenkins (2008) used to calculate model temperatures from the Fe # of actinolite, and possibly O-isotope resetting of magnetite and/or actinolite during cooling. The

actinolite composition for the Candelaria samples LD1987B 43, 52, and 58 yields an average Ca a.p.f.u. of 2.03, which is slightly higher than the Ca a.p.f.u value of 1.8 that Lledo and Jenkins (2008) used to derive the thermodynamic model from their experimental data. According to Lledo and Jenkins (2008), increasing the Ca a.p.f.u by 0.3 overestimated the temperature of actinolite crystallization in their experiments by 25 °C. Thus, the model temperatures calculated from the Fe # of Candelaria actinolite may similarly be overestimated when considering the Ca content of actinolite. If mineralization at Candelaria occurred at a pressure <100 MPa, and if we assume a linear relationship for Fe # and temperature from 100 – 400 MPa as experimentally determined by Lledo and Jenkins (2008), extrapolating to pressures < 100 MPa would also result in overestimation of Fe # temperatures by approximately 20 °C / 100MPa.

For the temperatures estimated by using the $\Delta^{18}O_{actinolite\ -\ magnetite}$ method, Edwards and Valley (1998) reported that variable $f(H_2O)$ during cooling promotes faster diffusion and resetting of $\delta^{18}O$ in diopside (a proxy for actinolite) from granulite facies marbles, and Kohn (1999) reports similar findings for diopside in amphibolites and pelites. It has also been reported that diffusive exchange of oxygen isotopes during complete granular exsolution of ilmenite from originally Ti-rich magnetite (i.e., where Ti is completely exsolved from magnetite) occurring at variable $f(H_2O)$ during cooling can lower the closure temperature of magnetite and allow for oxygen isotope resetting (Cartwright et al., 1993; Farquhar and Chacko, 1994; Valley, 2001). The results of the aforementioned studies indicate that the temperatures estimated from the Fe # of actinolite overestimate the temperature of mineralization, and O-isotope partitioning between magnetite and actinolite underestimate the temperature of mineralization at Candelaria. Considering the uncertainties inherent in each of the two methods used to estimate temperatures, we suggest that magnetite – actinolite mineralization likely occurred over a temperature range in between the estimations by both methods.

At shallow levels, Marschik and Fontboté, 2001a estimated temperatures of 600 – 500 °C for the magnetite – actinolite first stage, and ~500 – ~300 °C for the Cu-rich second stage at Candelaria based on fluid inclusions. Pyrite – anhydrite and pyrite – chalcopyrite geothermometry at Candelaria indicate a temperature gradient between 600 and 300 °C for the sulfide mineralization though the whole deposit (del Real et al., in review). Therefore, our estimated temperatures for actinolite and magnetite formation at Candelaria, representing the magnetite – actinolite first stage at deeper levels, are consistent with the temperature differences

for sulfide mineralization between shallow and deep (hotter) portions of the system. The temperatures reported here for samples from the deeper zones of Candelaria are also consistent with temperatures reported for IOA deposits. For example, temperatures of 600 – 900 °C were reported for massive magnetite mineralization in the Grängesberg mining district, Sweden (Weis, 2013), 610 °C – >850 °C for massive magnetite mineralization at Los Colorados, Chile (Knipping et al., 2015b; Bilenker et al., 2016), up to 840 °C at El Romeral, Chile (Rojas et al., 2018), up to 800 °C at Cerro Negro Norte, Chile (Salazar et al., 2019), >800 °C at el Laco, Chile (Nyström et al., 2008; Tornos et al., 2016), and >800 °C for early-stage magnetite at the Gushan deposit, China (Sun et al., 2019). The temperature overlap between the deeper samples from Candelaria and IOA deposits from districts globally provides evidence to support the hypothesis that IOCG mineralization transitions to IOA mineralization with increasing depth.

Additional insight into the temperature(s) of mineralization is provided by the concentrations of trace elements such as Al, Mn, Ti and V in magnetite that can be used to assess the temperature of magnetite growth by using the discriminant diagram developed by Nadoll et al. (2014) after Dupuis and Beaudoin (2011). Those authors compiled data for magnetite samples with well-constrained temperatures of formation from ore deposit types that include banded iron formations (BIF), IOCG, IOA, porphyry and Fe-Ti, V deposits. High-temperature, magmatic and magmatic-hydrothermal magnetite growth correspond to samples rich in [Ti+V] and [Al+Mn], whereas low-temperature magnetite growth results in lower concentrations of the same trace elements.

The Al, Mn, Ti and V concentrations in magnetite from Quince and Candelaria are plotted in Figure 2-5a. The chemistry of magnetite samples from Quince plot, on average, in the IOA field, and the deeper magnetite samples from Candelaria partially overlap the Quince and shallower Candelaria samples. This suggests that, at depth, the magnetite at Candelaria has a transitional composition between the IOCG and IOA classifications and the temperatures associated with them, which is consistent with the isotope thermometry and actinolite geochemistry previously discussed. The average [Ti+V] and [Al+Mn] values for shallower magnetite samples from Candelaria plot mostly in the IOCG field with data points extending to higher trace element concentrations that plot in the porphyry and IOA fields and lower trace element concentrations that plot in the BIF field. The shallow Candelaria data yield an average composition that plots on the boundary between IOCG and IOA deposits (Figure 2-5a).

Importantly, samples from Quince contain abundant Mn-rich ilmenite exsolution lamellae and interstitial ilmenite, and the deep samples from Candelaria contain Mn-rich ilmenite granules. EPMA analyses were carefully performed to avoid analyzing any exsolved ilmenite lamellae when analyzing magnetite. Similarly, we carefully analyzed interstitial and ilmenite exsolution lamellae to avoid hitting magnetite. The original trace element content of magnetite in these samples that now contain exsolved ilmenite was approximated by reintegrating the exsolved ilmenite composition into the host magnetite. The reconstructed original magnetite composition of the deep samples from Candelaria and the samples from Quince plot predominantly in the Fe-Ti, V field (igneous magnetite) (Figure 2-5b). This result is consistent with Sun et al. (2019) who reintegrated exsolved ilmenite to calculate the Ti concentration of primary magnetite in the Gushan IOA deposit and report that primary magnetite plots in the Fe-Ti, V field. The originally Ti-rich magnetite at Quince and the deep portion of Candelaria is associated with high-temperature formation conditions as discussed above. When combined with the magnetite chemistry from the Candelaria shallow samples, the data are interpreted to define a cooling trend (Figure 2-5b) from the deep to the shallow samples of Candelaria, suggesting that the deep portion of the Candelaria IOCG deposit is chemically analogous to the Quince IOA prospect.

In the zoned magnetite grains (type D) in the shallow part of Candelaria, rims are depleted in Ti, V, Al, and Mn with respect to the cores (Figure 2-4b, Figure 2-5c). This observation is consistent with textures and chemistry from hydrothermal magnetite from the Los Colorados (Knipping et al., 2015b; Deditius et al., 2018) and El Romeral (Rojas et al., 2018) IOA deposits in the Chilean Iron Belt, and the Pliocene El Laco IOA deposit in northern Chile (Ovalle et al., 2018). Deditius et al. (2018) used transmission electron microscopy (TEM) to identify nanoparticle – sized minerals (diopside, clinoenstatite, amphibole (tremolite – actinolite), phlogopite, ulvöspinel and Ti-rich magnetite) hosted in the darker areas of zoned, late-stage, low-temperature, hydrothermal magnetite from the Los Colorados IOA deposit. Those authors reported that the magnetite zones that host nanoparticles are also enriched in trace elements and concluded that the nanoparticles formed owing to supersaturation from a hydrothermal fluid, followed by entrapment during continuous growth of the magnetite host, similar to our observations for zoned magnetite (type D).

2.6.2 Iron and oxygen isotope constraints on the source of ore fluids

Previous compilations of Fe and O isotope data for igneous settings and different ore deposit types have allowed the determination of ranges of $\delta^{56}Fe$ and $\delta^{18}O$ that can be associated with particular fluid reservoirs (Taylor, 1967; Taylor, 1968; Heimann et al., 2008; Jonsson et al., 2013; Weis, 2013; Wawryk and Foden, 2015; Bilenker et al., 2016; Childress et al., 2016; Wawryk and Foden, 2017; Troll et al., 2019). The coupled interpretation of Fe – O isotope pairs has proven successful for fingerprinting the provenance of magnetite in IOA deposits worldwide (Weis, 2013; Bilenker et al., 2016; Childress et al., 2016; Troll et al., 2019). All of the $\delta^{56}Fe$ and $\delta^{18}O$ values from Quince and all but two $\delta^{18}O$ values from Candelaria are within the field defined for magmatic/magmatic-hydrothermal magnetite (Figure 2-6). A magmatic/magmatic-hydrothermal origin for Fe and O in magnetite from Candelaria is consistent with conclusions based on noble gas and halogen data (Marschik and Kendrick, 2015), fluid-inclusion and stable isotope data (Marschik and Fontboté, 2001a; Del Real et al., in review) and Re–Os isotope data (Mathur et al., 2002).

The two slightly elevated $\delta^{18}O$ values belong to the shallowest samples at Candelaria, where magnetite is replacing layered, sedimentary rocks. These samples come from the volcanic-sedimentary levels of the Punta del Cobre Formation, or from the base of the Chañarcillo Group, which contains carbonate-bearing rocks (Marschik and Fontboté, 2001b; Mourgues, 2004; del Real et al., 2018). We performed a mass balance calculation to simulate interaction of a magmatic-hydrothermal fluid (initial $\delta^{18}O$ ~5 to 8‰) with carbonates ($\delta^{18}O$ of ~28‰, Price et al., 2008) in the host rocks. The range of $\delta^{18}O$ for the fluid was based on the fractionation factor between magnetite and water between 500 °C and 650 °C, temperatures associated with the shallow levels of the deposit. As the fluid dissolves the carbonates, the O coming from them mixes with the O in the magmatic-hydrothermal fluid, shifting the value of $\delta^{18}O$ of the ore fluid values towards more positive values. Magnetite that precipitates from such fluid would preserve the heavier $\delta^{18}O$ value of the fluid isotopically buffered by carbonate-bearing host rocks. A rock/water volume of 0.2 – 0 .3 produces a magmatic-hydrothermal fluid from which magnetite with $\delta^{18}O$ ~5 to 8‰ precipitates. The host rocks are not reported to contain any ferroan carbonate mineral phases (cf. Marschik and Fontboté, 2001b; del Real et al., 2018) thus, we cannot model the possible effect of water-rock interactions with carbonate host rocks on the values of $\delta^{56}Fe$. Alternatively, the elevated $\delta^{18}O$ could have resulted from fluid mixing between a magmatic-hydrothermal fluid and a fluid in equilibrium with the carbonate in the host rock.

Besides fluid-rock interaction, the spread in the $\delta^{18}O$ values in the shallow Candelaria samples may reflect redox changes in the system associated with the formation of mushketovite. The increased $\delta^{56}Fe$ values at Candelaria with respect to Quince probably reflect a temperature control in the fractionation of Fe isotopes, suggesting that Quince formed at a higher temperature compared to Candelaria.

2.6.3 A model that explains IOA and IOCG deposits as part of a genetic continuum

A genetic link between IOA and IOCG deposits was first hypothesized by Hitzman et al. (1992) based on their global assessment of Proterozoic iron oxide (Cu – U – Au – REE) deposits, and subsequently by Espinoza et al. (1996) based on observations of the spatial and temporal relationships among these classes of deposits in the Chilean Iron Belt. Our results show that magnetite from the deep portion of the Candelaria IOCG system is very similar — texturally and compositionally — to magnetite from the Quince occurrence (this study) and that the compositions define an interpreted cooling trend in trace element space (Figure 2-5b). The compositions of magnetite from Candelaria and Quince are also similar to those reported for the Los Colorados (Knipping et al., 2015b; Knipping et al., 2015a), El Romeral (Rojas et al., 2018) and Cerro Negro Norte (Salazar et al., 2019) IOA deposits in the Chilean Iron Belt and the El Laco IOA deposit in northern Chile (Ovalle et al., 2018). The overlap of magnetite geochemical data for these deposits supports the hypothesized genetic link between IOA and IOCG deposits (Huang and Beaudoin, 2019). A continuum from IOA to IOCG mineralization within individual systems has been suggested for Olympic Dam (Apukhtina et al., 2017), the Great Bear Magmatic Zone (Corriveau et al., 2016), the Mesoproterozoic St. Francois Mountains Terrane, Southeast Missouri (Day et al., 2016), and several deposits in the Chilean Iron Belt (Naslund et al., 2002; Sillitoe, 2003; Barra et al., 2017; Childress et al., 2020).

2.7 Conclusions

The Fe and O stable isotope data for magnetite and H isotope data for actinolite support a magmatic/magmatic-hydrothermal origin for the Candelaria IOCG and the Quince IOA mineral deposits in the Chilean Iron Belt. The trellis and cloth textures, triple junctions and zonation in magnetite grains are consistent with oxy-exsolution of a primary magnetite – ulvöspinel solid solution to magnetite that contains ilmenite exsolution lamellae. This process was enhanced by

syn- or post-mineralization dissolution-reprecipitation and re-equilibration processes of originally Ti-rich magnetite caused by the interaction with a cooling hypogene magmatic-hydrothermal fluid. Such interaction is also reflected in the geochemical zonation of trace elements, which systematically decrease from core to rim in individual (zoned) magnetite grains, and between deep and shallow samples.

The geochemical and textural characterization of magnetite and actinolite from Candelaria and Quince indicate a magmatic to magmatic-hydrothermal origin for these mineral deposits, and suggest that the deep part of Candelaria represents the transition between shallow IOCG and deeper IOA mineralization. The flotation model as proposed by Knipping et al. (2015a) can explain the origin of both Quince and Candelaria, supporting the hypothesis that IOA and IOCG deposits are parts of a single genetic continuum.

The observations at Candelaria reveal a clear transition with depth from an IOCG deposit to IOA mineralization (Figure 2-7). This is consistent with the genetic model proposed by Knipping et al. (2015a) that explains IOCG and IOA mineralization as parts of a single continuum resulting from the combination of igneous and magmatic-hydrothermal processes. In their unifying model, microlites of Ti-rich magnetite (i.e., type A with inclusions, and type B with exsolved ilmenite) crystallize from a silicate melt and serve as nucleation sites for magmatic-hydrothermal fluid that is exsolved from silicate melt during decompression. Continued degassing of magmatic-hydrothermal fluid that nucleates as bubbles on magnetite microlites results in the formation of a magnetite-fluid suspension that is more buoyant than the surrounding magma, allowing this magnetite-bearing ore fluid to ascend and carry Ti-rich magnetite (Knipping et al., 2019). During ascent and emplacement, the ore fluid will react with Ti-rich magnetite, promoting local dissolution-reprecipitation reactions along grain boundaries, catalyzing the exsolution of Ti from the lamellae into ilmenite granules (Buddington and Lindsley, 1964), and the precipitation of exsolution- and inclusion-free magnetite (type C). The presence of triple junctions among magnetite grains, as well as the trace element zonation between cores and rims within single grains preserve evidence for such processes. Experimental data (Hezarkhani et al., 1999; Ulrich et al., 2001; Williams-Jones and Migdisov, 2014; Hurtig and Williams-Jones, 2014) demonstrate that the exsolved magmatic-hydrothermal fluid continues to transport Fe, Cu, Au, and S after forming IOA mineralization at depth. The fluid continues to cool during ascent and emplacement, and precipitates oxides and sulfides in the

shallower levels of the system to form an IOCG deposit (Knipping et al., 2015a; Reich et al., 2016; Simon et al., 2018). Type D magnetite (and mushketovite), which are only present in the shallow zone of Candelaria, are purely hydrothermal minerals that precipitated from the ascending fluid after it produced IOA mineralization at deeper levels of the system. Marschik and Fontboté (2001a) report that type D magnetite precipitated at temperatures between 500 – 600 °C, and was followed by chalcopyrite and pyrite mineralization as the fluid cooled below 500 °C.

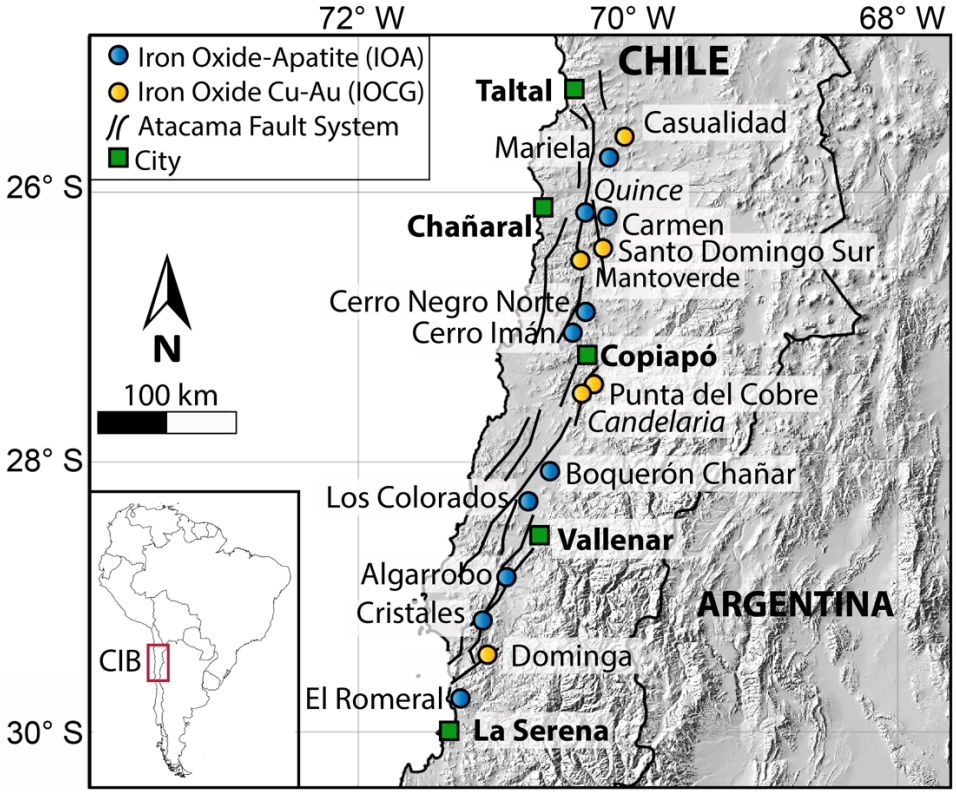

Figure 2-1: Location of major IOA and IOCG deposits in the Chilean Iron Belt (CIB) along the Atacama Fault System. The deposits studied are in italics. (Modified from Barra et al., 2017; Palma et al., 2019.)

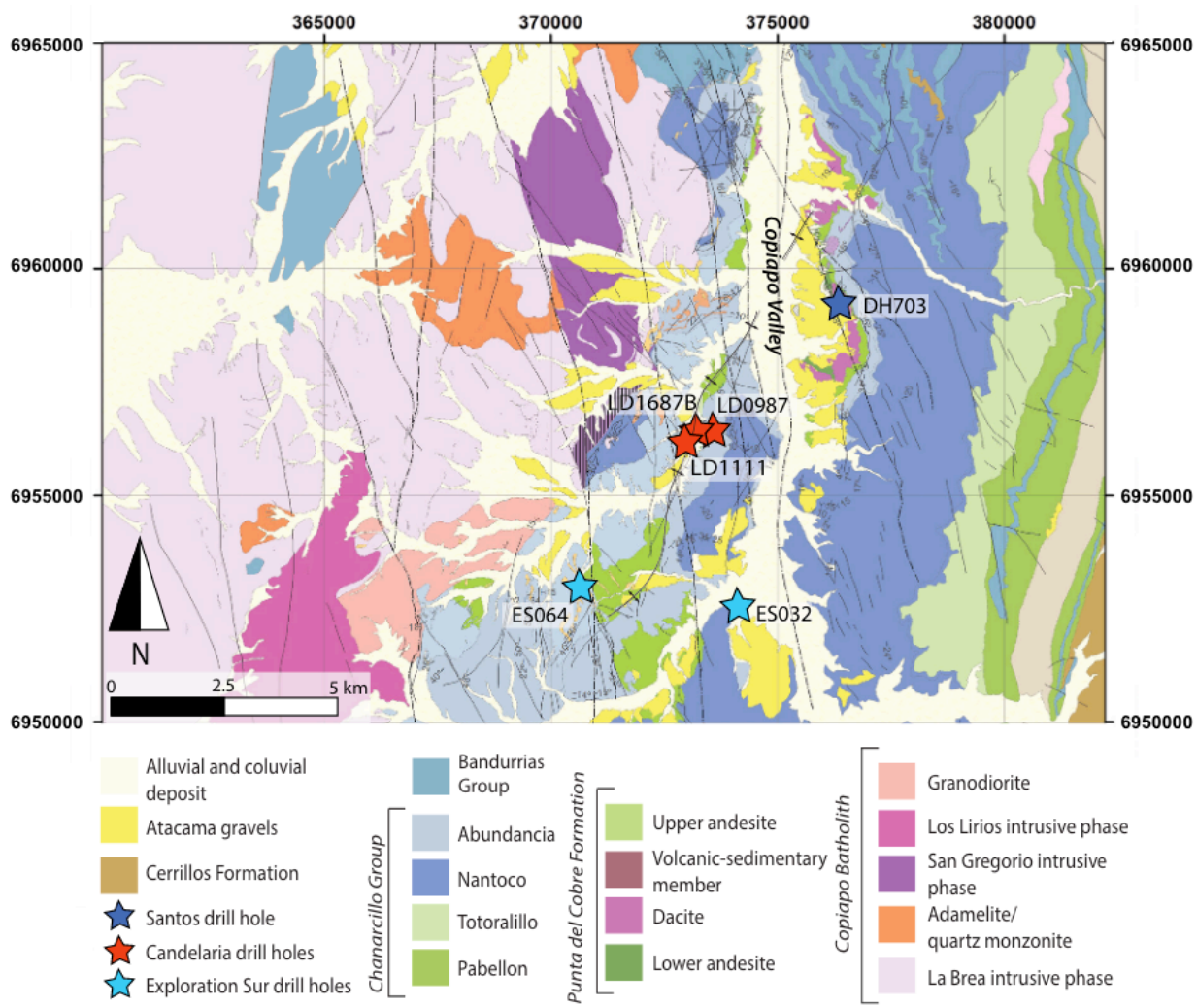

Figure 2-2: Geologic map with the location of the drill holes from the Candelaria – Punta del Cobre District. (Modified from del Real et al., 2018.)

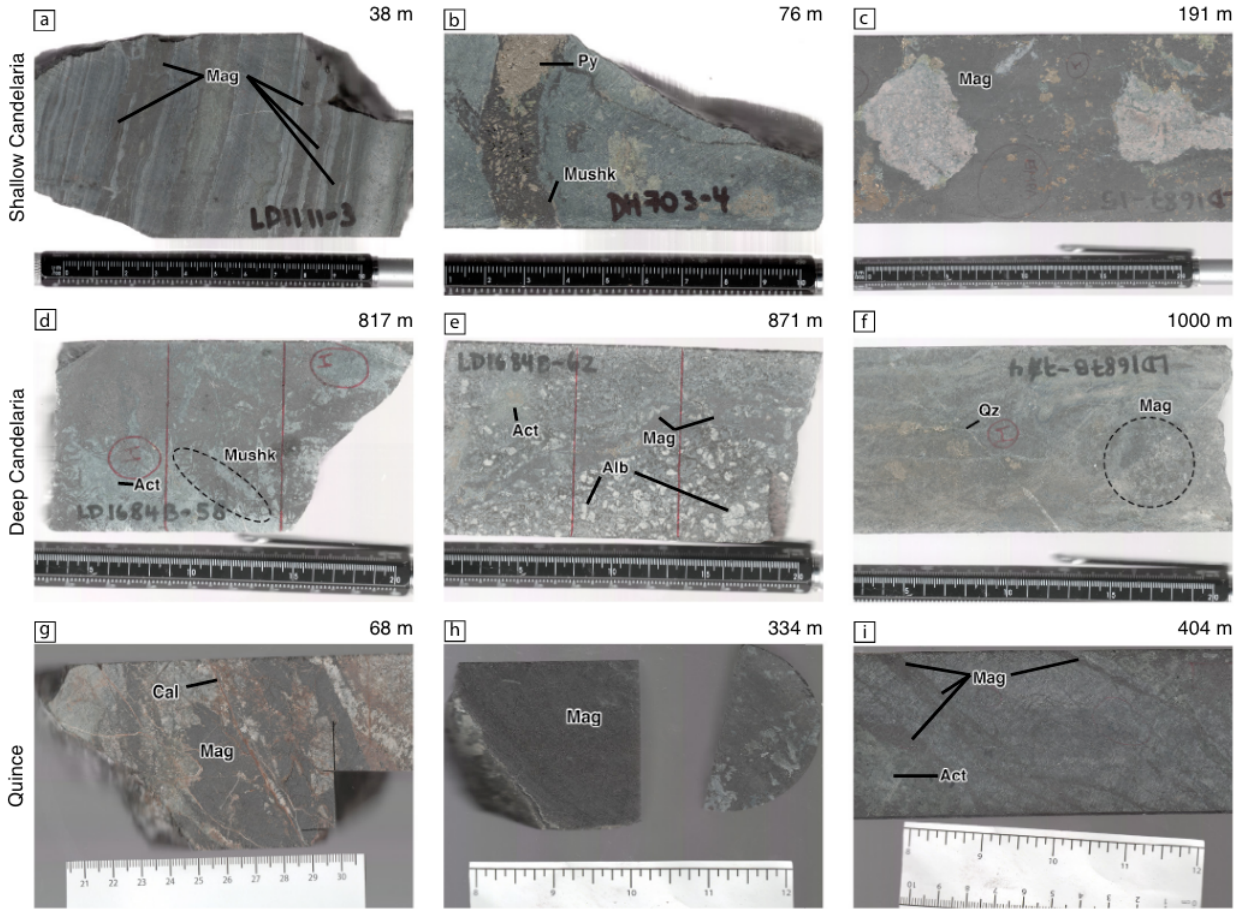

Figure 2-3: Representative drill core samples divided as follows: shallow Candelaria, deep Candelaria and Quince. Sample depths are indicated in the top right corner of each picture, and increase from left to right. Detailed sample descriptions are in Table 2-1. a) Sample LD1111 3 showing intercalation of magnetite-rich and -poor bands. b) Sample DH703 4 showing mushketovite plus sulfide vein. c) Sample LD1687B 15 with magnetite matrix, disseminated pyrite and chalcopyrite, and altered andesitic clasts. d) Sample LD1687B 58 showing intergrown actinolite and mushketovite. e) Sample LD1687B 62 showing albitization, fine-grained actinolite and magnetite in the matrix, and magnetite veins with less pyrite and chalcopyrite compared to the veins at shallower levels. f) Sample LD1687B 74 with disseminated magnetite and minor pyrite and chalcopyrite. A late-stage quartz veinlet cuts the main mineralization. g) Sample AQ-19 4 showing brecciated magnetite vein with later calcite – siderite veinlets. h) Massive magnetite from sample AQ-19 3. i) Sample AQ-19 2 with magnetite intergrown with actinolite in matrix. Act=actinolite, Alb=albitization, Cal=calcite/siderite, Mag=magnetite, Mushk=mushketovite, Qz=quartz.

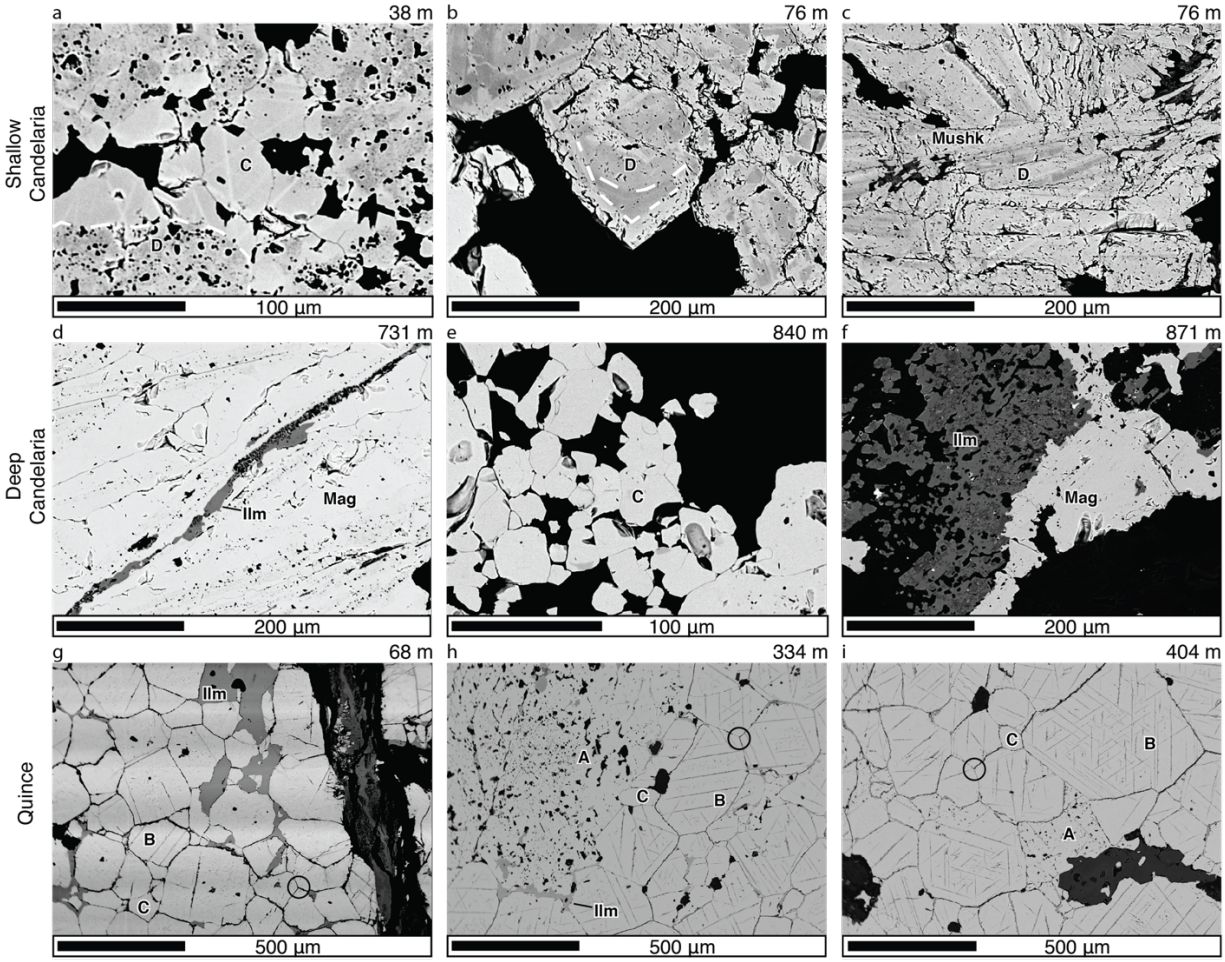

Figure 2-4: Back scattered electron images from selected samples. Organization as in Figure 2-3. a) Sample LD1111 3 showing magnetite type C (center) and D (lower left), where the dashed line shows the boundary between the dark, inclusion-rich core and the lighter, inclusion-free rim. b) Sample DH7034 showing magnetite type D with core-rim zonation and sulfides (bright grains in lower, left corner). The dashed lines separate the darker core from the lighter rim. c) Sample DH 703 4 showing mushketovite grains with darker and light areas (magnetite type D with patchy zonation). d) Sample LD1687B 52 showing ilmenite and rutile filling fractures between magnetite grains. e) Sample LD1687 61 showing magnetite type C. f) Sample LD1687 62 where magnetite is intimately related to ilmenite granules. Note the absence of exsolution textures in magnetite. g) Sample AQ-19 4 with triple junctions (in circle), interstitial ilmenite and magnetite types C and B with predominantly cloth texture and lesser trellis texture. h) Sample AQ-19 3 showing triple junctions, and magnetites type A, C, and B with trellis and cloth textures. Ilmenite filling interstices but in less proportion relative to the shallower sample AQ-19 4. i) Sample AQ-19 2 with magnetite types A, C, and B with abundant exsolution lamellae forming trellis textures and minor cloth texture. Interstitial ilmenite is less abundant than at shallower levels.

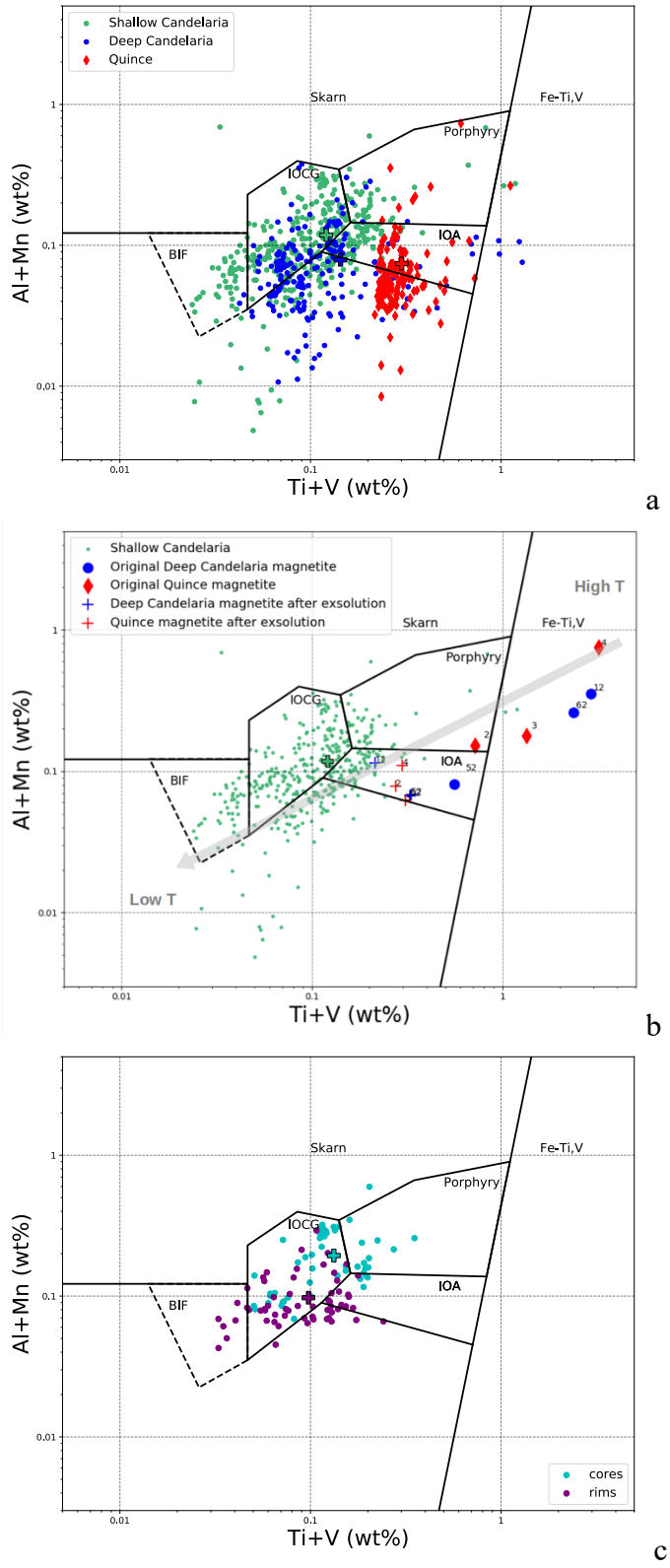

Figure 2-5: Magnetite discriminant diagram from Nadoll et al. (2014) after Dupuis and Beaudoin (2011). Crosses indicate the average composition for each category. a. The shallow Candelaria samples (green dots) plot on

average in the IOCG field, while the deep Candelaria samples (blue dots) and the Quince samples (red diamonds) plot in the IOA field on average. The partial overlap of the deep Candelaria samples with the shallow Candelaria and the Quince samples suggests a transitional composition and temperature between IOCG and IOA for this part of the system. b. Plus signs represent the average trace element concentration of the magnetite samples that contain ilmenite, where blue is for the deep Candelaria samples and red is for Quince samples. Blue circles show the calculated original composition of the magnetite after reintegrating the ilmenite granules at Candelaria, and the red diamonds correspond to the calculated original magnetite from Quince after reintegrating the interstitial ilmenite and the exsolution lamellae. The samples are identified by the number next to the symbol. The arrow is based on the composition-temperature data presented in Nadoll et al. (2014) for the expected trend of the trace element chemistry of magnetite that grows from a cooling magmatic-hydrothermal fluid. c. Dots represent EPMA data from Type D magnetite with core to rim zonation in the shallow Candelaria samples. A transition is observed between high-temperature, Al, Mn, Ti, V enriched cores and low-temperature, trace element depleted rims.

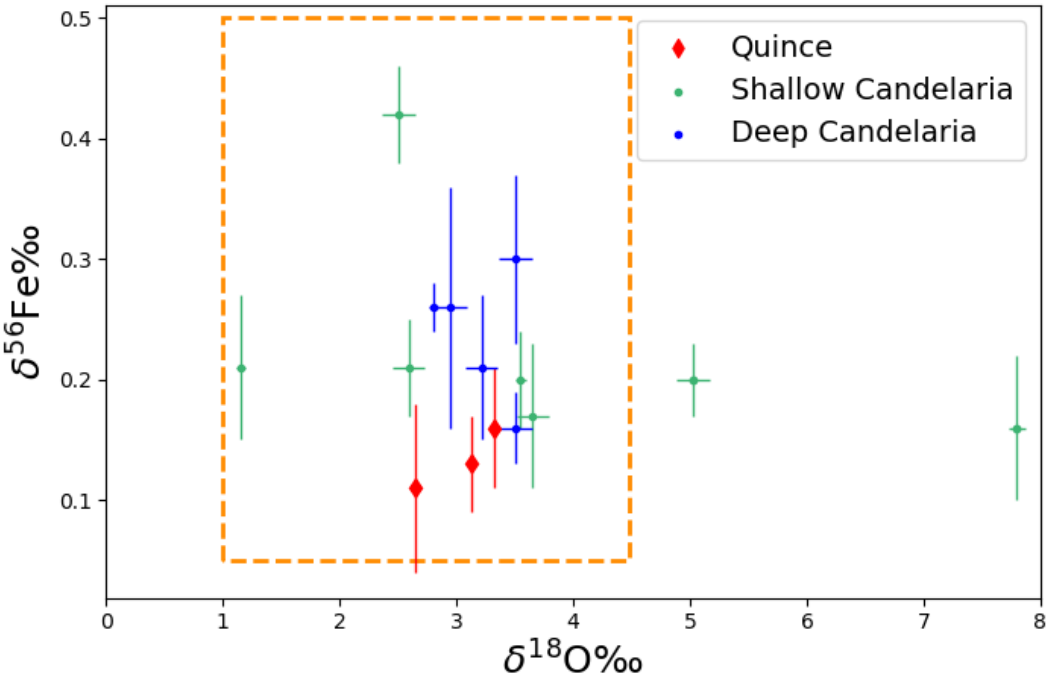

Figure 2-6: Magnetite Fe – O isotope pairs for Quince (red) and Candelaria (green = shallow Candelaria; blue = deep Candelaria) with 2σ error bars. The orange box outlines the range for oxygen (Taylor, 1967, 1968) and iron (Heimann et al, 2008; Bilenker et al., 2016; Troll et al., 2019) isotopes for magmatic and magmatic-hydrothermal magnetite. The two samples that plot outside the magmatic-magmatic hydrothermal range (orange dashed lines) are discussed in the main text.

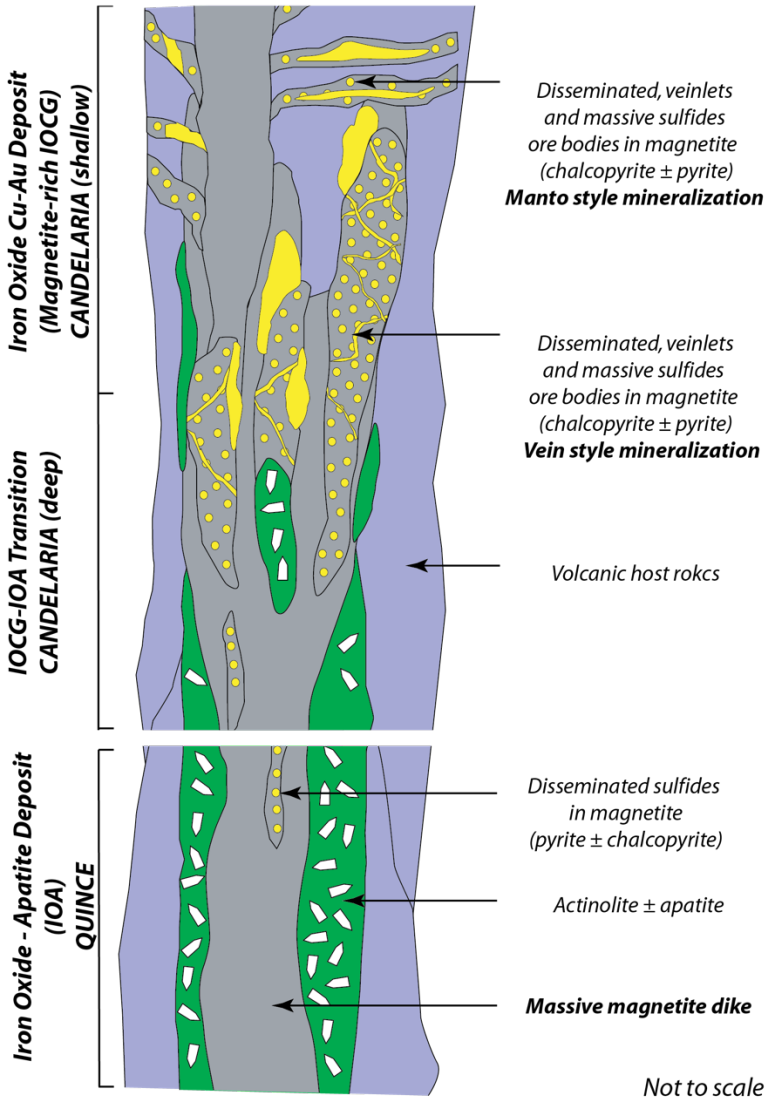

Figure 2-7: Schematic representation of the IOA-IOCG continuum and characteristic mineralizations of each section, where Quince is the IOA mineral deposit, shallow Candelaria is the IOCG mineral deposit, and deep Candelaria represents the transition between both. (Modified from Barra et al., 2017.)

Table 2-1: Sample descriptions

Area	Drill core	Sample	Vertical depth from collar (m)	Elevation from sea level (m)	Macroscopic highlights
Quince	AQ-19	4	68	631	Brecciated magnetite veins in sodic-calcic altered groundmass with calcite – siderite veins.
Quince	AQ-19	3	334	362	Massive magnetite with disseminated sulfides, and chlorite product of alteration.

Quince	AQ-19	2	404	294	Sodic-calcic altered groundmass with magnetite – actinolite ductile bands. Late, chlorite – calcite veins cross-cut.
Santos	DH703	4	76	549	Altered andesitic rock with potassic alteration (biotite and k-feldspar) and a mushketovite vein that contains massive pyrite.
Candelaria	LD1111	3	38	394	Volcano-sedimentary unit with bands that have been replaced by magnetite and subsequently microfaulted. Pervasive sodic-calcic alteration in the rest of the layers was affected by subsequent silicification.
Candelaria	LD1111	18	398	34	Magnetite – actinolite breccia with veins of massive pyrite and calcite accompanied by secondary epidote.
Candelaria	LD0987	9	493	29	Andesitic rock with potassic alteration (k-feldspar) and chlorite. Veins of pyrite and chalcopyrite. Minor, fine, disseminated magnetite.
Exploration Sur	ES032	12	743	-35	Sample from the manto mineralization. Massive magnetite aggregates and actinolite. Abundant disseminated pyrite. Potassic alteration and scattered secondary epidote.
Exploration Sur	ES064	19	1091	-299	Pervasively albitized groundmass with patches and veinlets of magnetite. Posterior K-feldspar veins contain massive, euhedral pyrite.
Candelaria	LD1687B	6	80	395	Volcano-sedimentary unit with bands that have been replaced by magnetite. Subsequent chloritization and silicification.
Candelaria	LD1687B	12	133	342	Undifferentiated matrix with magnetite fragments. Sulfides present in their borders and fractures.
Candelaria	LD1687B	15	191	284	Disseminated sulfides (py, cpy) and massive magnetite in breccia with potassic-altered andesitic clasts.
Candelaria	LD1687B	34	486	-11	Abundant sulfides (py, cpy, po) in magnetite breccia with clasts pervasively altered to chlorite.
Candelaria	LD1687B	43	618	-143	Breccia with sodic-calcic altered groundmass with few disseminated sulfides and massive magnetite clasts.
Candelaria	LD1687B	52	731	-256	Mushketovite and potassic feldspar veins in fine, undifferentiated matrix.

Candelaria	LD1687B	58	817	-342	Massive mushketovite and minor actinolite in altered volcanic matrix.
Candelaria	LD1687B	61	840	-365	Albitized volcanic rock with a massive magnetite vein cross-cut by a chlorite vein. Posterior K-feldspar veins contain sulfides.
Candelaria	LD1687B	62	871	-396	Porphyritic rock with k-feldspar veins cutting magnetite veins.
Candelaria	LD1687B	74	1000	-525	Disseminated magnetite in volcanic rock. Minor sulfides and late-stage quartz veins.

Table 2-2: Magnetite types

Type	Occurrence	Inclusion	Zoning	Other features
A	Quince	Rich	Absent	
B	Quince	Poor	Absent	Ilmenite exsolution lamellae
C	Quince and Candelaria	Absent	Absent	Associated to ilmenite (interstitial or as granules)
D	Shallow Candelaria	Localized	Concentric or patchy	

Table 2-3: Actinolite chemistry. Average per sample; in wt.%

															Estimated T (°C ± 2σ)	
Drill core	Sample	Points per sample	SiO_2	TiO_2	Al_2O_3	FeO	MnO	MgO	CaO	Na_2O	K_2O	Total	Ca a.p.f.u	Fe #	100 MPa	400 MPa
LD 1687B	43	23	51.2	0.14	4.14	12.1	0.22	16.2	12.2	0.36	0.15	96.7	2.03	0.29	752 ± 36	
LD 1687B	52	10	51.9	0.27	3.21	11.3	0.23	16.5	12.2	0.50	0.18	96.3	2.03	0.28	756 ± 18	
LD 1687B	58	5	51.4	0.12	3.74	13.2	0.25	15.5	12.2	0.43	0.24	97.0	2.03	0.32	741 ± 18	
AQ -19	2	9	51.8	0.38	4.35	8.94	0.24	18.9	11.6	0.73	0.20	97.0	1.90	0.21	782 ± 18	830 ± 18

Table 2-4: Isotopic results. n refers to the number of measurements per sample

		Magnetite								**Actinolite**						**Esti-mated T**
Drill core	**Sample**	**$\delta^{56}Fe$ (‰)**	**2sd**	**n56**	**$\delta^{57}Fe$ (‰)**	**2sd**	**n57**	**$\delta^{18}O$ (‰)**	**2sd**	**δD (‰)**	**2sd**	**wt% H_2O**	**2sd**	**$\delta^{18}O$ (‰)**	**2sd**	**(°C ± 2sd)**
AQ-19	4	0.16	0.05	4	0.26	0.08	3	3.33	0.07							
AQ-19	3	0.11	0.07	3	0.27	0.05	3	2.65	0.07							
AQ-19	2	0.13	0.04	4	0.18	0.14	4	3.13	0.07	-39.0	2.10	2.01	0.08	5.89	0.23	835 ± 20

AQ-19	2									-41.7	2.10	1.98	0.08	6.02	0.23	860 ± 20
DH703	4	0.21	0.06	3	0.33	0.06	2	1.16	0.07							
LD1111	3	0.16	0.06	3	0.22	0.08	3	7.80	0.07							
LD1111	18	0.20	0.04	3	0.18	0.05	3	3.55	0.07							
ES064	19	0.23	0.05	3	0.35	0.15	3									
LD1687 B	6	0.20	0.03	4	0.28	0.06	4	5.03	0.23	-93.9	2.10	0.81	0.08			
LD1687 B	12	0.17	0.06	3	0.32	0.24	3	3.65	0.23							
LD1687 B	15	0.21	0.04	3	0.33	0.09	3	2.59	0.23							
LD1687 B	34	0.42	0.04	3	0.65	0.25	3	2.50	0.23							
LD1687 B	43	0.26	0.10	4	0.40	0.23	4	2.95	0.23	-57.4	2.10	2.84	0.08	*7.69*	0.23	591 ± 20
LD1687 B	58	0.21	0.06	4	0.25	0.05	4	3.21	0.23							
LD1687 B	61	0.16	0.03	3	0.30	0.21	3	3.50	0.23	-64.0	2.10	1.75	0.08	*7.53*	0.23	665 ± 20
LD1687 B	62	0.30	0.07	3	0.45	0.13	3	3.50	0.23							
LD1687 B	74	0.26	0.02	3	0.39	0.09	3	2.81	0.07	-54.0	2.10	2.47	0.08	*7.50*	0.23	595 ± 20
Avera-ges																
Cande-laria		0.23	0.04		0.34	0.07		3.52	0.94	-67.3	18.2	1.97	0.89	7.57	0.12	
Quince		0.13	0.03		0.24	0.06		3.04	0.40	-40.4	2.70	2.00	0.03	5.96	0.13	
sd: Standard deviation					Blank cell: No data					Single crystal				*Pre-fluorinated*		

2.8 References

Apukhtina, O. B., Kamenetsky, V. S., Ehrig, K., Kamenetsky, M. B., Maas, R., Thompson, J., McPhie, J., Ciobanu, C. L., and Cook, N. J., 2017, Early, deep magnetite-fluorapatite mineralization at the Olympic Dam Cu-U-Au-Ag deposit, South Australia: Economic Geology, v. 112, p. 1531–1542.

Arguin, J.-P., Pagé, P., Barnes, S.-J., Girard, R., and Duran, C., 2018, An Integrated Model for Ilmenite, Al-Spinel, and Corundum Exsolutions in Titanomagnetite from Oxide-Rich Layers of the Lac Doré Complex (Québec, Canada): Minerals, v. 8, p. 476.

Barra, F., Reich, M., Selby, D., Rojas, P., Simon, A., Salazar, E., and Palma, G., 2017, Unraveling the origin of the Andean IOCG clan: A Re–Os isotope approach: Ore Geology Reviews, v. 81, p. 62–78.

Barton, M. D., 2014, Iron Oxide(–Cu–Au–REE–P–Ag–U–Co) Systems, in Holland, H. D. and Turekian, K. K. eds., Treatise on Geochemistry (Second Edition): Oxford, Elsevier, p. 515–541.

Barton, M. D., and Johnson, D. A., 1996, An evaporitic-source model for igneous-related Fe oxide(-REE – Cu-Au-U) mineralization: Geology, v. 24, p. 259–262.

Benavides, J., Kyser, T. K., Clark, A. H., Oates, C. J., Zamora, R., Tarnovschi, R., and Castillo, B., 2007, The Mantoverde Iron Oxide – copper – gold District, III Región, Chile: The Role of Regionally Derived, Nonmagmatic Fluids in Chalcopyrite Mineralization: Economic Geology, v. 102, p. 415–440.

Bilenker, L. D., Simon, A. C., Reich, M., Lundstrom, C. C., Gajos, N., Bindeman, I., Barra, F., and Munizaga, R., 2016, Fe–O stable isotope pairs elucidate a high-temperature origin of Chilean iron iron oxide – apatite deposits: Geochimica et Cosmochimica Acta, v. 177, p. 94–104.

Brown, M., Diáz, F., and Grocott, J., 1993, Displacement history of the Atacama fault system 25°00′S-27° 00′S, northern Chile: GSA Bulletin, v. 105, p. 1165–1174.

Buddington, A. F., and Lindsley, D. H., 1964, Iron-Titanium Oxide Minerals and Synthetic Equivalents: Journal of Petrology, v. 5, p. 310–357.

Carmichael, I. S. E., 1966, The iron-titanium oxides of salic volcanic rocks and their associated ferromagnesian silicates: Contributions to Mineralogy and Petrology, v. 14, p. 36–64.

Cartwright, I., Valley, J. W., and Hazelwood, A.-M., 1993, Resetting of oxybarometers and oxygen isotope ratios in granulite facies orthogneisses during cooling and shearing, Adirondack Mountains, New York: Contributions to Mineralogy and Petrology, v. 113, p. 208–225.

Charrier, R., Pinto, L., and Rodríguez, M. P., 2007, Tectonostratigraphic evolution of the Andean Orogen in Chile, in Moreno, T. and Gibbons, W. eds., The Geology of Chile: The Geological Society of London, p. 21–114.

Chen, H., Kyser, T. K., and Clark, A. H., 2011, Contrasting fluids and reservoirs in the contiguous Marcona and Mina Justa iron oxide – cu (-Ag-Au) deposits, south-central Perú: Mineralium Deposita, v. 46, p. 677–706.

Chiaradia, M., Banks, D., Cliff, R., Marschik, R., and de Haller, A., 2006, Origin of fluids in iron oxide–copper–gold deposits: constraints from δ37Cl, 87Sr/86Sri and Cl/Br: Mineralium Deposita, v. 41, p. 565–573.

Chiba, H., Chacko, T., Clayton, R. N., and Goldsmith, J. R., 1989, Oxygen isotope fractionations involving diopside, forsterite, magnetite, and calcite: Application to geothermometry: Geochimica et Cosmochimica Acta, v. 53, p. 2985–2995.

Childress, T. M., Simon, A. C., Day, W. C., Lundstrom, C. C., and Bindeman, I. N., 2016, Iron and Oxygen Isotope Signatures of the Pea Ridge and Pilot Knob Magnetite – apatite Deposits, Southeast Missouri, USA: Economic Geology, v. 111, p. 2033–2044.

Childress, T. M., Simon, A. C., Reich, M., Barra, F., Arce, M., Lundstrom, C. C., and Bindeman, I. N., 2020, Formation of the Mantoverde iron oxide – copper – gold (IOCG) deposit, Chile: insights from Fe and O stable isotopes and comparisons with iron iron oxide – apatite (IOA) deposits: Mineralium Deposita.

Corriveau, L., Montreuil, J. F., and Potter, E. G., 2016, Alteration facies linkages among iron oxide copper-gold, iron iron oxide – apatite, and affiliated deposits in the great bear magmatic zone, Northwest Territories, Canada: Economic Geology, v. 111, p. 2045–2072.

Couture, J.-F., Cole, G., Zhang, B., Scott, C. C., Kautzman, S., Nilsson, J., Dance, A., and Vidal, M. I., 2018, Technical Report for the Candelaria Copper Mining Complex, Atacama Region, Region III, Chile: SRK Consulting 3CL014.002, accessed January 15, 2019, at https://www.lundinmining.com/site/assets/files/3641/candelaria_2018_tr.pdf.

Craddock, P. R., and Dauphas, N., 2011, Iron Isotopic Compositions of Geological Reference Materials and Chondrites: Geostandards and Geoanalytical Research, v. 35, p. 101–123.

Day, W. C., Slack, J. F., Ayuso, R. A., and Seeger, C. M., 2016, Regional geologic and petrologic framework for iron oxide ± apatite ± rare earth element and iron oxide copper-gold deposits of the mesoproterozoic St. Francois Mountains Terrane, Southeast Missouri, USA: Economic Geology, v. 111, p. 1825–1858.

Deditius, A. P., Reich, M., Simon, A. C., Suvorova, A., Knipping, J., Roberts, M. P., Rubanov, S., Dodd, A., and Saunders, M., 2018, Nanogeochemistry of hydrothermal magnetite: Contributions to Mineralogy and Petrology, v. 173, p. 46.

Dupuis, C., and Beaudoin, G., 2011, Discriminant diagrams for iron oxide trace element fingerprinting of mineral deposit types: Mineralium Deposita, v. 46, p. 319–335.

Edwards, K. J., and Valley, J. W., 1998, Oxygen isotope diffusion and zoning in diopside: the importance of water fugacity during cooling: Geochimica et Cosmochimica Acta, v. 62, p. 2265–2277.

Espinoza, S., Veliz, H., Esquivel, J., Arias, J., and Moraga, A., 1996, The Cupriferous Province of the Coastal Range, Northern Chile, in Camus, F., Sillitoe, R. H., and Petersen, R. eds., Andean Copper Deposits: New discoveries, mineralization, styles and metallogeny: Society of Economic Geologists Special Publication, p. 19–32.

Farquhar, J., and Chacko, T., 1994, Exsolution-enhanced oxygen exchange: Implications for oxygen isotope closure temperatures in minerals: Geology, v. 22, p. 751–754.

Farquhar, J., Chacko, T., and Frost, B. R., 1993, Strategies for high-temperature oxygen isotope thermometry: a worked example from the Laramie Anorthosite Complex, Wyoming, USA: Earth and Planetary Science Letters, v. 117, p. 407–422.

Groves, D. I., Bierlein, F. P., Meinert, L. D., and Hitzman, M. W., 2010, Iron Oxide Copper-Gold (IOCG) Deposits through Earth History: Implications for Origin, Lithospheric Setting, and Distinction from Other Epigenetic Iron Oxide Deposits: Economic Geology, v. 105, p. 641–654.

Gruenewaldt, G. V., Klemm, D. D., Henckel, J., and Dehm, R. M., 1985, Exsolution features in titanomagnetites from massive magnetite layers and their host rocks of the upper zone, eastern Bushveld Complex: Economic Geology, v. 80, p. 1049–1061.

Haggerty, S., 1976, Opaque mineral oxides in terrestrial igneous rocks, in Rumble III, D. ed., Short Course Notes. Oxide Minerals: Mineralogical Society of America, p. 101–300.

Haynes, D. W., 2000, Iron Oxide Copper (-Gold) Deposits: Their Position In The Ore Spectrum And Modes of Origin, in Porter, T. M. ed., Hydrothermal Iron Oxide Copper-Gold & Related Deposits: A Global Perspective: Adelaide, PGC Publishing, p. 71–90.

Hedenquist, J. W., and Lowenstern, J. B., 1994, The role of magmas in the formation of hydrothermal ore deposits: Nature, v. 370, p. 519–527.

Heidarian, H., Lentz, D., Alirezaei, S., Peighambari, S., and Hall, D., 2016, Using the chemical analysis of magnetite to constrain various stages in the formation and genesis of the Kiruna-type chadormalu magnetite – apatite deposit, Bafq district, Central Iran: Mineralogy and Petrology, v. 110, p. 927–942.

Heimann, A., Beard, B. L., and Johnson, C. M., 2008, The role of volatile exsolution and sub-solidus fluid/rock interactions in producing high 56Fe/54Fe ratios in siliceous igneous rocks: Geochimica et Cosmochimica Acta, v. 72, p. 4379–4396.

Hezarkhani, A., Williams-Jones, A. E., and Gammons, C. H., 1999, Factors controlling copper solubility and chalcopyrite deposition in the Sungun porphyry copper deposit, Iran: Mineralium Deposita, v. 34, p. 770–783.

Hildebrand, R. S., 1986, Kiruna-type deposits; their origin and relationship to intermediate subvolcanic plutons in the Great Bear magmatic zone, Northwest Canada: Economic Geology, v. 81, p. 640–659.

Hitzman, M. W., 2000, Iron Oxide – cu-Au Deposits: What, Where, When, and Why, in Porter, T. M. ed., Hydrothermal Iron Oxide Copper-Gold & Related Deposits: A Global Perspective 1: Adelaide, PGC Publishing, p. 9–25.

Hitzman, M. W., Oreskes, N., and Einaudi, M. T., 1992, Geological characteristics and tectonic setting of proterozoic iron oxide (Cu – U – Au – REE) deposits: Precambrian Research, v. 58, p. 241–287.

Hou, T., Charlier, B., and Namur, O., 2018, Immiscible hydrous Fe – ca – P melt and the origin of iron iron oxide – apatite ore deposits: Nature Communications, v. 9, p. 1–8.

Hu, H., Li, J.-W., Lentz, D., Ren, Z., Zhao, X.-F., Deng, X.-D., and Hall, D., 2014, Dissolution–reprecipitation process of magnetite from the Chengchao iron deposit: Insights into ore genesis and implication for in-situ chemical analysis of magnetite: Ore Geology Reviews, v. 57, p. 393–405.

Huang, F., Zhang, Z., Lundstrom, C. C., and Zhi, X., 2011, Iron and magnesium isotopic compositions of peridotite xenoliths from Eastern China: Geochimica et Cosmochimica Acta, v. 75, p. 3318–3334.

Huang, X.-W., and Beaudoin, G., 2019, Textures and Chemical Compositions of Magnetite from Iron Oxide Copper-Gold (IOCG) and Kiruna-Type Iron Iron oxide – apatite (IOA) Deposits and Their Implications for Ore Genesis and Magnetite Classification Schemes: Economic Geology, v. 114, p. 953–979.

Hurtig, N. C., and Williams-Jones, A. E., 2014, An experimental study of the transport of gold through hydration of AuCl in aqueous vapour and vapour-like fluids: Geochimica et Cosmochimica Acta, v. 127, p. 305–325.

Jonsson, E., Troll, V. R., Högdahl, K., Harris, C., Weis, F., Nilsson, K. P., and Skelton, A., 2013, Magmatic origin of giant "Kiruna-type" apatite-iron-oxide ores in Central Sweden: Scientific Reports, v. 3, p. 1–8.

Knipping, J. L., Bilenker, L. D., Simon, A. C., Reich, M., Barra, F., Deditius, A. P., Lundstrom, C., Bindeman, I., and Munizaga, R., 2015a, Giant Kiruna-type deposits form by efficient flotation of magmatic magnetite suspensions: Geology, v. 43, p. 591–594.

Knipping, J. L., Bilenker, L. D., Simon, A. C., Reich, M., Barra, F., Deditius, A. P., Wälle, M., Heinrich, C. A., Holtz, F., and Munizaga, R., 2015b, Trace elements in magnetite from massive iron iron oxide – apatite deposits indicate a combined formation by igneous and magmatic-hydrothermal processes: Geochimica et Cosmochimica Acta, v. 171, p. 15–38.

Knipping, J. L., Webster, J. D., Simon, A. C., and Holtz, F., 2019, Accumulation of magnetite by flotation on bubbles during decompression of silicate magma: Scientific Reports, v. 9, p. 3852.

Kohn, M. J., 1999, Why most dry rocks should cool wet: American Mineralogist, v. 84, p. 570–580.

Loewen, M. W., and Bindeman, I. N., 2016, Oxygen isotope thermometry reveals high magmatic temperatures and short residence times in Yellowstone and other hot-dry rhyolites compared to cold-wet systems: American Mineralogist, v. 101, p. 1222–1227.

Lund, C., 2013, Mineralogical, Chemical and Textural Characterisation of the Malmberget Iron Ore Deposit for a Geometallurgical Model: Sweden, Lulea University of Technology.

Marschik, R., and Fontboté, L., 2001a, The Candelaria – Punta del Cobre Iron Oxide Cu-Au(-Zn-Ag) Deposits, Chile: Economic Geology, v. 96, p. 1799–1826.

Marschik, R., and Fontboté, L., 2001b, The Punta del Cobre Formation, Punta del Cobre – candelaria area, northern Chile: Journal of South American Earth Sciences, v. 14, p. 401–433.

Marschik, R., and Kendrick, M. A., 2015, Noble gas and halogen constraints on fluid sources in iron oxide – copper – gold mineralization: Mantoverde and La Candelaria, Northern Chile: Mineralium Deposita, v. 50, p. 357–371.

Marschik, R., Singer, B. S., Munizaga, F., Tassinari, C., Moritz, R., and Fontboté, L., 1997, Age of Cu(-Fe)-Au mineralization and thermal evolution of the Punta del Cobre district, Chile: Mineralium Deposita, v. 32, p. 531–546.

Marschik, R., Leveille, R. A., and Martin, W., 2000, La Candelaria and the Punta del Cobre district, Chile: Early Cretaceous iron oxide Cu–Au(–Zn–Ag) mineralization, in Porter, T. M. ed., Hydrothermal Iron-Oxide Copper-Gold & Related Deposits: A Global Perspective: Adelaide, Australian Mineral Foundation, p. 163–175.

Mathur, R., Marschik, R., Ruiz, J., Munizaga, F., Leveille, R., and Martin, W., 2002, Age of Mineralization of the Candelaria Fe Oxide Cu-Au Deposit and the Origin of the Chilean Iron Belt, Based on Re–Os Isotopes: Economic Geology, v. 97, p. 59–71.

Ménard, J.-J., 1995, Relationship between altered pyroxene diorite and the magnetite mineralization in the Chilean Iron Belt, with emphasis on the El Algarrobo iron deposits (Atacama region, Chile): Mineralium Deposita, v. 30, p. 268–274.

Mourgues, F. A., 2004, Advances in ammonite biostratigraphy of the marine Atacama basin (Lower Cretaceous), northern Chile, and its relationship with the Neuquén basin, Argentina: Journal of South American Earth Sciences, v. 17, p. 3–10.

Nadoll, P., Angerer, T., Mauk, J. L., French, D., and Walshe, J., 2014, The chemistry of hydrothermal magnetite: A review: Ore Geology Reviews, v. 61, p. 1–32.

Naslund, H. R., Henriquez, F., Nyström, J. O., Vivallo, W., and Dobbs, F. M., 2002, Magmatic Iron Ires and Associated Mineralisation: Examples from the Chilean High Andes and Coastal Cordillera, in Porter, T. M. ed., Hydrothermal Iron Oxide Copper-Gold & Related Deposits: A Global Perspective 2: Adelaide, PGC Publishing, p. 207–226.

Neybergh, H., Laduron, D., Martin, H., and Verkaeren, J., 1980, The vanadiferous magnetite deposits of the Oursi region, Upper-Volta: Economic Geology, v. 75, p. 1042–1052.

Nyström, J. O., and Henriquez, F., 1994, Magmatic features of iron ores of the Kiruna type in Chile and Sweden; ore textures and magnetite geochemistry: Economic Geology, v. 89, p. 820–839.

Nyström, J. O., Billström, K., Henríquez, F., Fallick, A. E., and Naslund, H. R., 2008, Oxygen isotope composition of magnetite in iron ores of the Kiruna type in Chile and Sweden: GFF, v. 130, p. 177–188.

Ovalle, J. T., La Cruz, N. L., Reich, M., Barra, F., Simon, A. C., Konecke, B. A., Rodriguez-Mustafa, M. A., Deditius, A. P., Childress, T. M., and Morata, D., 2018, Formation of massive iron deposits linked to explosive volcanic eruptions: Scientific Reports, v. 8, p. 14855.

Palma, G., Barra, F., Reich, M., Valencia, V., Simon, A. C., Vervoort, J., Leisen, M., and Romero, R., 2019, Halogens, trace element concentrations, and Sr-Nd isotopes in apatite from iron iron oxide – apatite (IOA) deposits in the Chilean iron belt: Evidence for magmatic and hydrothermal stages of mineralization: Geochimica et Cosmochimica Acta, v. 246, p. 515–540.

Pang, K.-N., Zhou, M.-F., Lindsley, D., Zhao, D., and Malpas, J., 2008, Origin of Fe–Ti Oxide Ores in Mafic Intrusions: Evidence from the Panzhihua Intrusion, SW China: Journal of Petrology, v. 49, p. 295–313.

Pollard, P. J., 2006, An intrusion-related origin for Cu–Au mineralization in iron oxide–copper–gold (IOCG) provinces: Mineralium Deposita, v. 41, p. 179–187.

Price, G. D., Dashwood, B., Taylor, G. K., Kalin, R. M., and Ogle, N., 2008, Carbon isotope and magnetostratigraphy of the Cretaceous (Barremian – Aptian) Pabellón Formation, Chañarcillo Basin, Chile: Cretaceous Research, v. 29, p. 183–191.

Qi, H., Coplen, T. B., Gehre, M., Vennemann, T. W., Brand, W. A., Geilmann, H., Olack, G., Bindeman, I. N., Palandri, J., Huang, L., and Longstaffe, F. J., 2017, New biotite and muscovite isotopic reference materials, USGS57 and USGS58, for δ2H measurements–A replacement for NBS 30: Chemical Geology, v. 467, p. 89–99.

Quince Iron Chile Website, 2019, Quince Iron Chile (https://www.quinceironchile.com/).

Rabbia, O. M., and Hernández, L. B., 2012, Mineral Chemistry and Potential Applications of Natural-Multi-Doped Hydrothermal Rutile from Porphyry Copper Deposits, in Low, I.-M. (Jim) ed., Rutile: Properties, Synthesis and Applications: Nova Science Publishers, Inc., p. 209–228.

Rabbia, O. M., Hernández, L. B., French, D. H., King, R. W., and Ayers, J. C., 2009, The El Teniente porphyry Cu–Mo deposit from a hydrothermal rutile perspective: Mineralium Deposita, v. 44, p. 849.

del Real, I., Thompson, J. F. H., and Carriedo, J., 2018, Lithological and structural controls on the genesis of the Candelaria – Punta del Cobre Iron Oxide Copper Gold district, Northern Chile: Ore Geology Reviews, v. 102, p. 106–153.

del Real, I., Thompson, J.F.H., Simon, A.C., Reich, M., Geochemical and isotopic signature of pyrite as a proxy for fluid source and evolution in the Candelaria – Punta del Cobre IOCG district, Chile: Geochimica et Cosmochimica Acta, in review.

Reich, M., Simon, A. C., Deditius, A. P., Barra, F., Chryssoulis, S., Lagas, G., Tardani, D., Knipping, J., Bilenker, L., Sánchez-Alfaro, P., Roberts, M., and Munizaga, R., 2016, Trace Element Signature of Pyrite from the Los Colorados Iron Iron oxide – apatite (IOA) Deposit, Chile: A Missing Link Between Andean IOA and IOCG Systems? Economic Geology, v. 111, p. 743–761.

Rhodes, A., and Oreskes, N., 1999, Oxygen Isotope Composition of Magnetite Deposits at El Laco, Chile: Evidence of Formation from Isotopically Heavy Fluids, in Skinner, B. ed., Geology and Ore Deposits of the Central Andes: Society of Economic Geologists Special Publication, 7, p. 333–351.

Rieger, A. A., and Marschik, R., 2012, The evolution of the hydrothermal IOCG system in the Mantoverde district, northern Chile: new evidence from microthermometry and stable isotope geochemistry: Mineralium Deposita, v. 47, p. 359–369.

Rojas, P. A., Barra, F., Deditius, A., Reich, M., Simon, A., Roberts, M., and Rojo, M., 2018, New contributions to the understanding of Kiruna-type iron iron oxide – apatite deposits revealed by magnetite ore and gangue mineral geochemistry at the El Romeral deposit, Chile: Ore Geology Reviews, v. 93, p. 413–435.

Salazar, E., Barra, F., Reich, M., Simon, A., Leisen, M., Palma, G., Romero, R., and Rojo, M., 2019, Trace element geochemistry of magnetite from the Cerro Negro Norte iron oxide–apatite deposit, northern Chile: Mineralium Deposita.

Sillitoe, R. H., 2003, Iron oxide – copper – gold deposits: an Andean view: Mineralium Deposita, v. 38, p. 787–812.

Simon, A., Knipping, J., Reich, M., Barra, F., Deditius, A., Bilenker, L., and Childress, T., 2018, A holistic model that combines igneous and magmatic-hydrothermal processes to explain Kiruna-type iron oxide - apatite deposits and iron oxide - copper - gold deposits as products of a single evolving ore system: Society of Economic Geologists Special Publication, v. 21, p. 89–114.

SRK Consulting, 2014, Quince Sur Iron Project Preliminary Economic Assessment: SRK Consulting 05-2501–11, 11–31 p.

Sun, W., Yuan, F., Jowitt, S. M., Zhou, T., Liu, G., Li, X., Wang, F., and Troll, V. R., 2019, In situ LA–ICP–MS trace element analyses of magnetite: genetic implications for the Zhonggu orefield, Ningwu volcanic basin, Anhui Province, China: Mineralium Deposita, v. 54, p. 1243–1264.

Tan, W., Liu, P., He, H., Wang, C. Y., and Liang, X., 2016, Mineralogy and Origin of Exsolution in Ti-rich Magnetite from Different Magmatic Fe-ti Oxide-bearing Intrusions: The Canadian Mineralogist, v. 54, p. 539–553.

Taylor, H. P., 1967, Oxygen Isotope Studies of Hydrothermal Mineral Deposits, in Barnes, H. L. ed., Geochemistry of Hydrothermal Ore Deposits: New York, Holt, Rinehart and Winston, p. 109–142.

Taylor, H. P., 1968, The oxygen isotope geochemistry of igneous rocks: Contributions to Mineralogy and Petrology, v. 19, p. 1–71.

Taylor, H. P., 1974, The Application of Oxygen and Hydrogen Isotope Studies to Problems of Hydrothermal Alteration and Ore Deposition: Economic Geology, v. 69, p. 843–883.

Tornos, F., Velasco, F., and Hanchar, J. M., 2016, Iron-rich melts, magmatic magnetite, and superheated hydrothermal systems: The El Laco deposit, Chile: Geology, v. 44, p. 427–430.

Tornos, F., Velasco, F., and Hanchar, J. M., 2017, The Magmatic to Magmatic-Hydrothermal Evolution of the El Laco Deposit (Chile) and Its Implications for the Genesis of Magnetite – apatite Deposits: Economic Geology, v. 112, p. 1595–1628.

Troll, V. R., Weis, F. A., Jonsson, E., Andersson, U. B., Majidi, S. A., Högdahl, K., Harris, C., Millet, M.-A., Chinnasamy, S. S., Kooijman, E., and Nilsson, K. P., 2019, Global Fe–O isotope correlation reveals magmatic origin of Kiruna-type apatite-iron-oxide ores: Nature Communications, v. 10, p. 1712.

Ulrich, T., Günther, D., and Heinrich, C. A., 2001, The Evolution of a Porphyry Cu-Au Deposit, Based on LA-ICP-MS Analysis of Fluid Inclusions: Bajo de la Alumbrera, Argentina: Economic Geology, v. 96, p. 1743–1774.

Valley, J. W., 2001, Stable Isotope Thermometry at High Temperatures: Reviews in Mineralogy and Geochemistry, v. 43, p. 365–413.

Veloso, E., Cembrano, J., Arancibia, G., Heuser, G., Neira, S., Siña, A., Garrido, I., Vermeesch, P., and Selby, D., 2017, Tectono-metallogenetic evolution of the Fe–Cu deposit of Dominga, northern Chile: Mineralium Deposita, v. 52, p. 595–620.

Wawryk, C. M., and Foden, J. D., 2015, Fe-isotope fractionation in magmatic-hydrothermal mineral deposits: A case study from the Renison Sn–W deposit, Tasmania: Geochimica et Cosmochimica Acta, v. 150, p. 285–298.

Wawryk, C. M., and Foden, J. D., 2017, Iron-isotope systematics from the Batu Hijau Cu-Au deposit, Sumbawa, Indonesia: Chemical Geology, v. 466, p. 159–172.

Weis, F., 2013,Oxygen and Iron Isotope Systematics of the Grängesberg Mining District (GMD), Central SwedenPhD Dissertation: Sweden, Uppsala universitet: 1–83 p.

Westhues, A., Hanchar, J. M., LeMessurier, M. J., and Whitehouse, M. J., 2017a, Evidence for hydrothermal alteration and source regions for the Kiruna iron oxide–apatite ore (northern Sweden) from zircon Hf and O isotopes: Geology, v. 45, p. 571–574.

Westhues, A., Hanchar, J. M., Voisey, C. R., Whitehouse, M. J., Rossman, G. R., and Wirth, R., 2017b, Tracing the fluid evolution of the Kiruna iron oxide apatite deposits using zircon, monazite, and whole rock trace elements and isotopic studies: Chemical Geology, v. 466, p. 303–322.

Williams, P., Barton, M. D., Johnson, D. A., Fontboté, L., De Haller, A., Mark, G., Oliver, N. H. S., and Marschik, R., 2005, Iron Oxide Copper-Gold Deposits: Geology, Space-Time Distribution, and Possible Modes of Origin: Economic Geology, v. 100, p. 371–405.

Williams-Jones, A. E., and Migdisov, A. A., 2014, Experimental Constraints on the Transport and Deposition of Metals in Ore-Forming Hydrothermal Systems (K. D. Kelley & H. C. Golden, Eds.): Society of Economic Geologists Special Publication, v. 18, p. 77–95.

Chapter 3 : The Mina Justa Iron Oxide Copper Gold (IOCG) Deposit, Peru: Constraints on Metal and Ore Fluid Sources

Co-authors: Maria A. Rodriguez-Mustafa, Adam C. Simon, Laura Bilenker, Ilya Bindeman, Ryan Mathur, Edson L.B Machado

Published in *Economic Geology* (2022) v. 117, 3.

3.1 Abstract

Iron oxide – copper – gold (IOCG) deposits are major sources of Cu, contain abundant Fea – Poxides and may contain Au, Ag, Co, rare earth elements (REE), U and other metals as economically important byproducts in some deposits. They form by hydrothermal processes, but the source of the metals and ore fluid(s) is still debated. We investigated the geochemistry of magnetite from the hydrothermal unit and manto ore bodies at the Mina Justa IOCG deposit in Peru to assess the source of the iron oxides and their relationship with the economic Cu mineralization. We identified three types of magnetite: Magnetite with inclusions (type I) is only found in the manto, is the richest in trace elements, and crystallized between 459 – 707 °C; type Dark (D) has no visible inclusions and formed at around 543 °C; and type Bright (B) has no inclusions, has the highest Fe content, and formed at around 443 °C. Temperatures were estimated using the Mg content in magnetite. Magnetite samples from Mina Justa yielded an average $\delta^{56}Fe \pm 2\sigma$ value of 0.28 ± 0.05‰ (n=9), an average $\delta^{18}O \pm 2\sigma$ value of 2.19 ± 0.45‰ (n=9), and $\Delta'^{17}O$ values that range between -0.075‰ and -0.047‰. Sulfide separates yielded $\delta^{65}Cu$ values that range from -0.32‰ to -0.09‰. The trace element compositions and textures of magnetite, along with temperature estimations for magnetite crystallization, are consistent with the manto magnetite belonging to an iron iron oxide – apatite (IOA) style mineralization that was overprinted by a younger, structurally controlled IOCG event that formed the hydrothermal unit ore body. Altogether, the stable isotopic data fingerprint a magmatic-hydrothermal source for the ore fluids carrying the Fe and Cu at Mina Justa and preclude significant input from meteoric water and basinal brines.

3.2 Introduction

Iron oxide – copper – gold (IOCG) mineral deposits are found worldwide and have a wide age range spanning from the Archean to the Cretaceous. These deposits are enriched in Fe and Cu, and can contain economically important amounts of Au, Ag, Co, U and rare earth elements (REE). They contain abundant magnetite and/or hematite, are structurally and/or stratigraphically controlled, and are usually associated with extensive Na-Ca alteration and more localized K alteration (Hitzman et al., 1992; Hitzman, 2000; Williams et al., 2005; Groves et al., 2010; Barton, 2014; Corriveau et al., 2016). It is generally accepted that IOCG deposits form by hydrothermal processes. However, the source of metals and ore fluid(s) remains controversial. Hitzman et al. (1992) and Pollard (2006) suggested a fluid of magmatic origin. Barton and Johnson (1996) proposed that a basinal brine would leach metals from the country rocks. Others have argued that IOCG deposits can be formed by a mix of both types of fluids (Hitzman et al., 1992; Hitzman, 2000; Chiaradia et al., 2006; Groves et al., 2010; Rieger and Marschik, 2012). At the Raúla – PCondestable and Mina Justa IOCG deposits in Peru and the Candelaria IOCG deposit in Chile, sulfur isotope data indicate mixing of a magmatic fluid with a later, external fluid source (seawater or brine). However, mixing with the external fluid is not required for ore deposition (de Haller and Fontboté, 2009; Li et al., 2018; del Real et al., 2020).

Based on the spatial and temporal relationship between iron iron oxide – apatite (IOA) and IOCG deposits in Chile, it has been suggested that in this region IOCG deposits might represent the shallower, lower temperature manifestations of IOA deposits (Espinoza et al., 1996; Naslund et al., 2002; Sillitoe, 2003; Knipping et al., 2015a; Reich et al., 2016; Barra et al., 2017; Simon et al., 2018).

Rodriguez-Mustafa et al. (2020) showed that in the Candelaria IOCG deposit in Chile, the transition from shallower IOCG mineralization to a deeper IOA mineral assemblage is recorded by the geochemistry of magnetite. In Peru, several IOA and IOCG occurrences, including important deposits such as Raúla – PCondestable, Marcona, and Mina Justa show a similar spatial distribution to the deposits found in Chile (Atkin et al., 1985; Clark et al., 1990; Vidal et al., 1990; Hawkes et al., 2002; Injoque, 2002; de Haller et al., 2006; de Haller and Fontboté, 2009; Chen et al., 2010) (Figure 3-1), but no genetic link between IOA and IOCG deposits has been established there yet.

In this study, we characterize magnetite from drill core samples from the Mina Justa IOCG deposit in Peru to assess the source of the iron oxides and their relationship with the economic Cu mineralization to better understand the evolution of the deposit. We investigated the textures and chemistry of magnetite by using a scanning electron microscope (SEM) and an electron probe microanalyzer (EPMA) to constrain the conditions under which magnetite formed, and we used the Mg content of magnetite grains to calculate magnetite crystallization temperatures. Furthermore, we measured Fe and O stable isotope abundances in magnetite, Cu isotope abundances in sulfides, and O and H isotope abundances in actinolite to fingerprint the source of the metals and ore fluids and to evaluate the potential input of meteoric and basinal fluids in the mineralization process.

3.3 Geologic Background

The Mina Justa IOCG deposit is located within the IOA-IOCG Belt in southern Peru, about 5 km NW from the Marcona IOA deposit described by Chen et al. (2010) (Figure 3-1). Basement rocks in the area consist of high-grade metamorphic rocks from the Paleo-Mesoproterozoic Arequipa Massif (Atkin et al., 1985; Wasteneys et al., 1995). The basement is overlain by a Paleozoic meta-sedimentary sequence that includes the Marcona Formation, which hosts most of the Fe mineralization in the Marcona IOA deposit (Hawkes et al., 2002; Injoque, 2002; Chen et al., 2010). The overlying Mesozoic volcano-sedimentary sequence comprises the Río Grande, Jahuay, Yauca and Copará formations (Caldas Vidal, 1978). The Mina Justa deposit is hosted in the upper member of the ~4000m thick Río Grande Formation, which dips 40° to 60° to the NW, and is composed mainly of intercalations of porphyritic andesites, andesitic volcaniclastic rocks, fossiliferous limestones, arkoses, and mudstones (Caldas Vidal, 1978; Chen et al., 2010). A recently identified diorite intrudes the Rio Grande Formation in the mine area. The Tunga Andesite Unit contains several 20 – 50 m thick post-mineralization porphyritic andesitic dykes with glomerophyric plagioclase crystals that cut the Río Grande Formation and the diorite, and are referred to as ocöites due to their similarity to the Ocoa Formation near Copiapó, Chile (Hawkes et al., 2002; Chen et al., 2010).

The NW trending Treinta Libras Fault System is the major regional structure (Injoque, 2002), and locally, the main fault systems in the area are: Repetición/Mina Justa and Huaca/Tunga (Hawkes et al., 2002) (Figure 3-2). The Repetición faults developed in the Jurassic

as a result of compression and sinistral shearing of the Treinta Libras Fault System, and are older than Cu mineralization at Mina Justa (Chen et al., 2010). They controlled the emplacement of the magnetite mantos at Marcona (Chen et al., 2010), and could have controlled the magnetite mantos at Mina Justa as well (Fonseca, 2016). The Mina Justa normal faults are interpreted to represent a reactivation of the Repetición faults due to a change to dextral transtension of the Treinta Libras Fault System (Chen et al., 2010). The Huaca/Tunga normal faults were a major structural control for the SE dipping main ore body that hosts most of the Cu mineralization (Hawkes et al., 2002). They are the youngest faults and the porphyritic andesitic dykes in the area follow their orientation (Hawkes et al., 2002; Chen et al., 2010). Displacements in these dykes caused by faults from all systems evidence a more recent reactivation of all of them (Fonseca, 2016).

The Mina Justa deposit has a combined measured, indicated, and inferred oxide resource of 219 Mt at 0.51% Cu and sulfide resource of 213 Mt at 1.00% Cu, 8.0 g/t Ag and 0.06 g/t Au (Fowler and Stephenson, 2016). The deposit consists of a main SE plunging, structurally controlled ore body (Figure 3-3, Figure 3-4) dominated by magnetite, mushketovite, sulfides, and actinolite (±apatite) that occur as massive aggregates or as clasts and matrix in hydrothermal breccias (Figure 3-5a,b). As the intensity of alteration commonly precludes the identification of primary lithologies within the ore body, and as textures vary between clearly breccia-hosted mineralization and wholesale replacement by hydrothermal minerals (where a breccia host cannot be confirmed), we use the term "hydrothermal unit" to reference intense replacement by hydrothermal minerals coincident with the main ore bodies. The hydrothermal unit has the highest Cu grades in the deposit, but Cu mineralization is also hosted in the surrounding Río Grande Formation presenting an outward zonation of hypogene sulfides from bornite – chalcocite (Figure 3-5c) through chalcopyrite – bornite to chalcopyrite>pyrite (Figure 3-5d,e), and to pyrite>chalcopyrite (Sillitoe, 2002; Hawkes, 2003). Fine-grained magnetite-dominated mantos (20 – 30 m thick) dip to the NW (Figure 3-2, Figure 3-3, Figure 3-4), are parallel to bedding in the Río Grande Formation, and are interpreted to have replaced limestone-rich horizons in that unit (Figure 3-5f-h) (Sillitoe, 2002). They host localized Cu mineralization with similar sulfide assemblages as the main hydrothermal unit. The deposit hosts a supergene Cu-oxide zone (chrysocolla, atacamite) that extends on average to 200 m below the surface (Chen et al., 2010).

A 7-stage paragenetic sequence for the Mina Justa deposit was presented by Chen et al. (2010). Those authors described an early-stage massive magnetite body associated with microcline (Ar/Ar 142.4 ± 6.7 Ma) and cross-cut by actinolite (Ar/Ar 110.9 ± 0.7 Ma), and younger main and upper bodies consisting of magnetite – pyrite (associated with microcline, Ar/Ar 103.7 ± 0.6 Ma and 101.5 ± 0.7 Ma). The magnetite – pyrite bodies host most of the overprinting Cu mineralization (microcline envelopes, Ar/Ar 99.1 ± 0.9 Ma and 95.0 ± 0.6 Ma), but Cu sulfides also overprint the massive magnetite body. In our study, the massive magnetite body corresponds to the NW dipping manto and the magnetite – pyrite bodies relate to the hydrothermal unit. Chen et al. (2010) presented and used geochronological data to conclude that the manto is a distinct, older event probably associated with the formation of the neighboring Marcona IOA deposit and is not related to the IOCG mineralization hosted in the Mina Justa hydrothermal unit. However, the Cu mineralization hosted in the manto belongs to the same mineralizing event identified in the hydrothermal unit (Sillitoe, 2002).

More recently, Hu et al. (2020), summarized the paragenesis of the hydrothermal unit ore body into 4 stages: 1. Magnetite – actinolite – K feldspar – albite ± apatite early alteration stage; 2. Hematite stage; 3. Magnetite + pyrite ± titanite ± quartz ± chlorite stage that includes mushketovite (specular hematite from stage 2 that has been converted to magnetite retaining the original morphology) and granular magnetite; 4. Copper mineralization stage dominated by chalcopyrite and other copper sulfides (bornite, chalcocite, and digenite) that incorporate Ag in their structure and occur as veins cutting the previous stages (Chen et al., 2010). Chalcopyrite partially or completely replaces pyrite from stage 3 (Chen et al., 2010; Li et al., 2018) (Figure 3-5d, Figure 3-6a), occurs with chalcocite and bornite (Figure 3-6b,c), and presents rims of covellite (Figure 3-6d). Hematite coexists with bornite and chalcocite, which present symplectitic textures (Figure 3-6e). Minor, later sphalerite – galena, calcite – quartz (Figure 3-5e), and hematite (Figure 3-6c) are present as veins or filling cracks (Chen et al., 2010).

Hu et al. (2020) studied stage 3 magnetite and mushketovite from the hydrothermal unit and concluded that they formed from a cooling hydrothermal fluid. For the same stage, Chen et al. (2011) reported $\delta^{18}O$ values for magnetite (2.7 – 4.7‰) and $\delta^{34}S$ values for pyrite (1.1 and 1.6‰), and interpreted those as being associated with a magmatic fluid. The authors also reported results of thermometry on fluid inclusions of unknown origin in quartz from Stage 3 and calcite from stage 4, and interpreted that external fluids were involved in the Cu mineralization.

Furthermore, Li et al. (2018) reported in-situ $\delta^{34}S$ values and Co/Ni and Se/S ratios of Stage 3 pyrite (-0.5 to 6.4‰) and stage 4 chalcopyrite (-0.6 to 4.6‰). The authors concluded that the fluids involved in stage 3 were primarily magmatic with an incursion of a later, external fluid, whereas the fluids for stage 4 were mainly external fluids that leached the andesitic host rocks, but they do not rule out input from magmatic fluids in this stage.

3.4 Methods

3.4.1 Sample collection

We selected 19 core samples from 5 drill holes (Table 3-1) to investigate the lateral and vertical variations in the geochemistry of the mineralization in the Mina Justa deposit (Figure 3-2b, Figure A-1 to Figure A-5). The samples come from between 87 m and 472 m down-hole to avoid the Cu oxide zone and are classified as coming from the manto or the hydrothermal unit.

3.4.2 Sample preparation

The samples from Mina Justa were either mounted in epoxy resin or sent for thin section fabrication in order to perform EPMA and SEM analyses on polished grains. For isotopic analyses, 9 representative samples of magnetite and 6 representative samples of sulfides (chalcopyrite, chalcocite, and bornite) from the hydrothermal unit and manto bodies were selected. Each sample was crushed using an agate mortar and pestle, which was rinsed with ethanol and put through an ultrasonic cleaner between each sample to prevent contamination. The magnetic fraction was obtained by using a hand magnet wrapped in weighing paper, and individual, visibly unweathered magnetite/mushketovite and sulfide grains were handpicked using a binocular microscope at ~40x magnification. Actinolite separates were obtained from two samples using a Frantz magnetic separator, and handpicking individual grains under the microscope to eliminate the presence of other mineral phases. Aliquots of actinolite and magnetite analyzed for O isotopes, described below, were pre-fluorinated for 4 hours to remove impurities and alteration products such as chlorite and other reactive phases.

3.4.3 EPMA and FE-SEM

Backscattered electron (BSE) images and energy-dispersive X-ray spectroscopy (EDS) maps were obtained to characterize textures and elemental variations by using a JEOL 7800FLV field emission-scanning electron microscope (FE-SEM) in the Electron Microbeam Analysis Laboratory at the University of Michigan. In the same facility, point and line transect analyses were performed by using a Cameca SX-100 electron microprobe with a focused beam, a voltage of 20 keV and a current of 40 nA for magnetite grains. Counting times, standards and detection limits are listed in the Supplementary Materials (Table A-6). We measured Mg, Al, Si, Ca, Ti, V, Cr, Mn, Co, Ni and Fe in magnetite grains and carefully avoided inclusions. We executed TiKα - VKβ and FeKα - CoKβ interference corrections.

3.4.4 Iron isotopes

To obtain pure Fe from each sample, dissolution and ion chromatography were performed on magnetite/mushketovite grains. Approximately 2.0 mg of sample were first digested in HF and HNO_3 for ≥24 hours, dried on a hot plate, refluxed in aqua regia, and dried once more to completely dissolve each sample. In preparation for column chemistry, samples were dissolved in 0.5 mL 8N HCl, dried, and dissolved in 0.4 mL 8N HCl at ~120 °C. The conditioning and elution procedures were completed following the procedure of Huang et al. (2011) using Biorad AG1-X8 Ion Exchange Resin (200 – 400 mesh). All reactants (HNO_3, HCl, HF) were Optima Grade and H_2O was ultrapure. The stable Fe isotope analyses were performed at the Pacific Centre for Isotopic and Geochemical Research, University of British Columbia using a Nu Plasma 1700 multi collector-inductively coupled plasma-mass spectrometer (MC-ICP-MS) in dry plasma mode with a DSN-100 Desolvating Nebulizer System. All analyses were performed in true high-resolution mode and isobaric interferences (i.e., Ar complexes) were fully resolved from the Fe isotopes (^{54}Fe, ^{56}Fe, ^{57}Fe). Minor Cr corrections were done online for each analysis by monitoring ^{52}Cr. Every sample was measured between 3 and 6 times and was bracketed immediately before and after each analysis by the measurement of standard 14 from the Institute for Reference Materials and Measurements (IRMM-14). The concentration of Fe in the samples was adjusted to be within 10% of the bracketing standard solution. Analyses of the reference material BCR-2 yielded an average value of $\delta^{56}Fe$ 0.08 ± 0.05‰ (n=11), which is consistent with the value of 0.09 ± 0.01‰ (n=8) recommended by Craddock and Dauphas (2011).

3.4.5 Oxygen and hydrogen isotopes

Oxygen isotope abundances (^{16}O and ^{18}O) of magnetite/mushketovite and actinolite separates (2.0 – 2.2 mg each) were measured at the University of Oregon using BrF_5 in a laser fluorination line connected to a Thermo-Finnigan MAT 253 gas isotope ratio mass spectrometer (IRMS) in dual inlet mode. Laser power was slowly increased to minimize jumping movements of the grains during fluorination with BrF_5. Yields (μmol/mg of extracted O_2 gas) were monitored by a Barathron gauge. For samples that did not experience grain jumping, O_2 yields were close to the theoretical 100%, demonstrating that analyzed magnetite grains were not weathered. The Gore Mountain garnet (GMG, 6.52‰) and San Carlos Olivine (SCO, 5.25‰) standards were measured prior, during, and after the sample analyses to quantify the data onto a SMOW scale (Loewen and Bindeman, 2016). Analyses of the standard GMG yielded $\delta^{18}O \pm 2\sigma$ values of 6.17 ± 0.15‰ for the magnetite and actinolite samples. The analytical values were corrected to VSMOW scale by using the difference between the measured and the expected value for the standard for each day.

The abundance of ^{17}O was measured in 4 magnetite samples and capital delta values were calculated using Equation 1:

$$\Delta^{17}O_{sample} = \delta^{17}O_{sample} - \delta^{18}O_{sample} \times 0.5305$$

where 0.5305 is the slope of the reference line for minerals formed at high temperatures (Pack et al., 2016; Sharp et al., 2018; Miller et al., 2020). Triple oxygen isotopes were measured in a single session with O_2 gas as analyte run against calibrated reference gas, with an additional gas chromatographic purification step in a controlled He flow using a 6 ft long zeolite column that was added to the University of Oregon fluorination line (Bindeman et al., 2018). This procedure is needed to minimize potential ^{17}O contaminants such as NF and organics. The average San Carlos Olivine during $\Delta^{17}O$ analyses was -0.05 ± 0.012‰ (2σ, n = 3).

The water content and stable δD isotope ratios of actinolite samples were measured over 2 days by thermal pyrolysis using a thermal conversion elemental analyzer attached to a MAT 253 IRMS by a continuous flow method also at the University of Oregon. We used a glassy carbon reactor held at 1450 °C following the analytical procedures described in Bindeman et al. (2012). For standards we used USGS57 biotite and USGS58 muscovite (Qi et al., 2017). Our analyses yielded average $\delta D \pm 2\sigma$ (n=10) values of -90.9 ± 2.5‰ and -27.3 ± 1.0‰, and calculated wt.% $H_2O \pm 2\sigma$ (n=10) contents of 2.5 ± 0.1% and 1.0 ± 0.1%, respectively. Water

was determined by peak integration of H and D areas relative to that of the standards NBS30 and USGS57 micas (nominal H_2O = 3.5 wt%). The results are reported relative to VSMOW.

3.4.6 Copper isotopes

Approximately 10 to 30 mg of Cu sulfide samples were hand separated. The samples were dissolved by 3mL of heated ultrapure aqua regia. Solutions were dried and Cu was purified with the ion exchange chromatography described in Mathur et al. (2009). Solutions were measured at Rutgers University on the Neptune plus MC-ICP-MS. Solutions were measured in low resolution mode with a jet cone to enhance sensitivity, and were measured at 100ppb Cu and generated 5V on the ^{63}Cu. Mass bias was corrected for by standard sample bracketing. All values are reported as per mil relative to the NIST 976 standard. On peak blank corrections were applied to each value and the blank was measured 8 times during each session. Samples and standards matched within 15% of the ^{63}Cu voltage. Samples were measured in duplicate and errors are within 0.08‰ which is the 2σ variation of the NIST 976 throughout the measuring session. We assume 0.08‰ as the estimate for the error on all measurements. To verify the accuracy of the measurements, a USA penny from 1838 (first reported in Mathur et al., 2009) overlapped with the published value of $\delta^{65}Cu = 0.05 \pm 0.06$‰, n=4.

3.5 Results

3.5.1 Magnetite textures

Magnetite and mushketovite (hematite that has been replaced by magnetite preserving the original tabular shape) occur as massive aggregates, disseminations, veins, and clasts. Actinolite is fine-grained and intergrown with magnetite, or massive, fibrous and associated with apatite. The fibrous actinolite presents zonation in BSE and contains titanite inclusions.

Based on morphology, BSE grey-scale tone and inclusion content, three main textures of Fe-oxides were identified in the Mina Justa samples (Table 3-2). Magnetite with inclusions (type I) consists of cores in euhedral to subhedral magnetite grains and bands that contain numerous sub-micron, rounded to elongated inclusions of titanite and a Ca-Mg silicate (probably actinolite) (Figure 3-7a-c). Type I magnetite presents a medium to dark tone in BSE, and was only

identified in the manto. Types Dark (D) and Bright (B) were identified in both the manto and the hydrothermal unit. Type D consists of patches in mushketovite (Figure 3-7, Figure 3-8a) and in granular magnetite that present a dark tone in BSE images but no visible mineral inclusions (Figure 3-8b,c). Type Bright (B) refers to the lighter-BSE bands in mushketovite (Figure 3-7d, Figure 3-8a), patches in granular magnetite (Figure 3-8b,c) and anhedral granular magnetite grains that are inclusion-free (Figure 3-8d). In the manto, type B is also found meeting at triple junctions, surrounding type I magnetite grains (Figure 3-7b-c), and locally associated with chlorite and interstitial titanite (Figure 3-9). In the hydrothermal unit, mushketovite grains of type B are porous and contain scheelite inclusions (inset in Figure 3-8a).

3.5.2 Trace element compositions of magnetite

The EPMA data are compiled in Table A-7. Summary statistics of element concentrations for samples from the manto and the hydrothermal unit, as well as for each magnetite type are presented in Table 3-3. Cobalt was below detection limit for more than 50% of the analyses and no statistics for Co are reported.

All magnetite grains from the manto are enriched in Mn (0.09 ± 0.03 wt.%), Cr (0.03 ± 0.01 wt.%), V (0.96 ± 0.17 wt.%), and Ni (0.01 ± 0.01 wt.%) with respect to magnetite from the hydrothermal unit (Mn (0.05 ± 0.02 wt.%), Cr (0.01 ± 0.01 wt.%), and V (0.21 ± 0.19 wt.%)) (Figure 3-10). Magnetite grains from the manto overlap with but are slightly depleted in Fe (70.7 ± 1.10 wt.%) relative to the hydrothermal unit grains Fe (71.8 ± 0.83 wt.%), and magnetite type B is the richest in Fe in both the manto and hydrothermal unit. Magnetite type I, only found in the manto, is also enriched in Si (0.97 ± 0.55 wt.%), Mg (0.22 ± 0.15 wt.%), Ti (0.11 ± 0.06 wt.%), and Ca (0.41 ± 0.19 wt.%) compared to types D (Si (0.54 ± 0.41 wt.%), Mg (0.11 ± 0.08 wt.%), Ti (0.05 ± 0.04 wt.%), Ca (0.19 ± 0.16 wt.%)) and B (Si (0.14 ± 0.07 wt.%), Mg (0.03 ± 0.04 wt.%), Ti (0.04 ± 0.03), Ca (0.04 ± 0.07 wt.%)) (Figure 3-10). Aluminum is slightly enriched in type D magnetite grains in the hydrothermal unit, but has a similar concentration in the other magnetite types.

3.5.3 Temperature estimations

We calculated formation temperatures of individual magnetite grains by implementing the Mg in magnetite empirical geothermometer

$$T_{Mg-mag}(℃) = \frac{-8344(\pm 320)}{\ln X_{Mg} - 4.1(\pm 0.28)} - 273$$

developed by Canil and Lacourse (2020). Where Mg was below detection limit, we used half of that value to estimate the minimum formation temperature, which corresponds to 371 °C. The number of analyses below detection limit were 87 out of 195 for type B and 9 out of 37 for type D. Table 3-3 provides the summary statistics for the temperatures for the manto and the hydrothermal unit and for the different magnetite types. Magnetite from the manto crystallized over a temperature range between 372 and 707 °C, and magnetite from the hydrothermal unit crystallized over the range 371 to 657 °C. Magnetite types D and B have an average ± 1sd estimated formation temperature of 543 ± 106 °C and 443 ± 74 °C, respectively. The latter value is influenced by the number of analyses below the detection limit. The higher magnetite crystallization temperatures of the manto are associated with magnetite type I (not present in the hydrothermal unit), which records the highest temperatures (>700 °C) (Figure 3-11) and has an average ± 1sd estimated formation temperature of 628 ± 95 °C.

Hu et al. (2020) report that the process of reducing hematite to mushketovite produces a change of the crystal lattice of the latter, which results in the re-equilibration of the new phase with the fluid so that the Mg content of mushketovite reflects the temperature at which mushketovite formed. We note that we chose spots for EPMA analysis to avoid inclusions visible in BSE. We recognize that this cannot eliminate inclusions that may have existed within the penetration volume of the electron beam, which is approximately 1500nm deep by 1500nm wide based on Monte Carlo simulations for the EPMA conditions reported above. The effect of Mg-bearing inclusions will depend on the mass ratio of Mg-inclusions to Mg-in-magnetite, which we cannot quantitatively constrain. We scrutinized the magnetite compositional data and concluded that the model temperatures reported in our manuscript accurately reflect changes in the crystallization temperature among different generations of magnetite.

3.5.4 Iron isotope compositions of magnetite separates

Iron isotope data for magnetite samples are summarized in Table 3-4. The $\delta^{56}Fe \pm 2\sigma$ values relative to the IRMM-14 standard for magnetite from Mina Justa range between 0.17 ± 0.03‰ and 0.40 ± 0.10‰ and yield an average value of 0.28 ± 0.05‰ (n=9).

3.5.5 Oxygen and hydrogen isotope compositions of magnetite and actinolite separates

Oxygen isotope data for magnetite and actinolite are summarized in Table 3-4. The $\delta^{18}O \pm 2\sigma$ values for magnetite from Mina Justa range between 0.74 ± 0.15‰ and 3.16 ± 0.15‰ and have an average $\delta^{18}O \pm 2\sigma$ value of 2.19 ± 0.45‰ (n=9). The $\Delta^{17}O$ values from 4 magnetite samples range between -0.075‰ and -0.047‰. The $\delta^{18}O \pm 2\sigma$ values for actinolite are 8.16 ± 0.15‰ and 8.14 ± 0.15‰. The $\delta D \pm 2\sigma$ values for actinolite from Mina Justa are -35.2 ± 1.86‰ and -43.14 ± 1.86‰ (Table 3-4). The water content (wt.% H_2O) of the same actinolite samples is 2.03 wt.% and 2.24 wt.%.

3.5.6 Copper isotope compositions of sulfide separates

Copper isotope data are summarized in Table 3-4. The $\delta^{65}Cu$ values for sulfides from Mina Justa range between -0.32 ± 0.08‰ and -0.09 ± 0.08‰, with the most negative values coming from samples that present covellite replacing chalcopyrite (Figure 3-6d) or symplectitic bornite – chalcocite intergrowths (Figure 3-6e).

3.6 Discussion

3.6.1 Evolution of the Mina Justa deposit

The magnetite in the manto and hydrothermal unit correspond to two separate events as supported by the paragenesis and Ar/Ar geochronology reported by Chen et al. (2010). Those authors associate the magnetite of the manto to the early stage of alteration in Mina Justa (stage 1) and relate it to the magnetite mineralization at the nearby Marcona IOA deposit, therefore being older than the hydrothermal unit and Cu mineralization. The geochemical and textural characteristics of the magnetite from Mina Justa allow us to identify two generations of magnetite in the deposit. Magnetite with inclusions (type I), found only in the manto, has the highest concentrations of trace elements (V, Ti, Si, Ni, Mn, Mg, Cr, and Ca) in Mina Justa (Figure 3-10). As the amount of trace elements that magnetite can host in its structure increases with temperature, magnetite type I is interpreted to have formed at a higher temperature than magnetite from the second generation (types Dark (D) and Bright (B)). This is consistent with the temperature estimations from the Mg content in magnetite, where type I yields a higher average temperature than magnetite types B and D (Figure 3-11). Magnetite with characteristics similar to type I has been described in other IOA deposits in Chile (e.g., Los Colorados:

Knipping et al., (2015b)), and the estimated temperature for magnetite type I at Mina Justa is consistent with estimations for hydrothermal magnetite formation from other Chilean IOA deposits (Bilenker et al., 2016; Rojas et al., 2018; Salazar et al., 2019; Rodriguez-Mustafa et al., 2020) and from the estimations for magnetite from the Marcona IOA deposit (Chen et al., 2011). We do not see the high temperature (magnetite type I) in the hydrothermal unit, only in the manto. If the manto had been emplaced in its current position after the hydrothermal unit had formed, we would see this magnetite type in both geologic units. Therefore, magnetite type I represents the high temperature, first generation of magnetite that formed the manto at Mina Justa.

Stage 2 specular hematite formed along the Mina Justa fault system from a more oxidized fluid (above the hematite – magnetite redox buffer) driven by the sulfur buffer (SO_2-H_2S-H_2SO_4) and was later reduced as it cooled to form pyrite and stage 3 mushketovite (Giggenbach, 1987; Einaudi, 2003; de Haller and Fontboté, 2009), causing a volume decrease reflected in the porosity of this mineral (Figure 3-8a) (Hu et al., 2020). Hu et al. (2020) also assigned the formation of granular magnetite to that stage. We found Stage 3 mushketovite and granular magnetite in the hydrothermal unit and in the manto, suggesting that the fluids responsible for stages 2 and 3 also flowed through existing fractures associated with the manto.

The fluid responsible for stage 3 precipitated the second generation of magnetite (types D and B) and pyrite. In the manto, this fluid reacted and equilibrated with magnetite type I, as demonstrated by annealing textures such as triple junctions in type B magnetite that is surrounding type I grains (Figure 3-7b-c), and precipitated types B and D that contain higher concentrations of V, Ni, Cr and Mn compared to the same magnetite types in the hydrothermal unit. Those elements are highly compatible in magnetite, whereas Ti, Ca, Si and Mg formed interstitial titanite and chloritized actinolite (Figure 3-9). The significant differences in the concentrations of V, Mn, and Cr clearly discriminate magnetite associated with the manto from magnetite from the hydrothermal unit (Figure 3-10).

Type D magnetite is equivalent to types T_{M1-2} (mushketovite) and T_{M2-1} (granular magnetite) described by Hu et al. (2020), while type B magnetite is equivalent to types T_{M1-3} (mushketovite) and T_{M2-2} (granular magnetite) described by those authors. Magnetite type D enrichment in Si, Mg and Ca when compared to type B (Figure 3-10) suggests that magnetite type D precipitated from the hydrothermal fluid at a higher temperature than magnetite type B, as

indicated by the lower concentrations of those elements in magnetite B. The estimations of magnetite formation temperature based on its Mg content suggest that type D precipitated from the fluid at around 550 °C, while type B precipitated at around 450 °C. These temperatures suggest precipitation from a cooling fluid for these magnetite types as suggested by Hu et al. (2020) for their equivalent magnetite types. Our estimations are also consistent with magnetite temperatures reported by Chen et al. (2011) for that same stage based on oxygen isotope thermometry, and are comparable to magnetite formation temperatures from the Candelaria IOCG deposit in Chile (e.g., Marschik and Fontboté, 2001; Rodriguez-Mustafa et al., 2020).

Stage 4 fluid flowed through the same conduits as stage 3 fluid and precipitated the Cu-sulfides mostly in the hydrothermal unit and to a lesser extent in the manto. This is supported by the similarity between the Cu mineralization assemblage in the hydrothermal unit and the manto and the proportionality between Cu content and amount of stage 3 magnetite (Sillitoe, 2002). The symplectitic texture between chalcocite and bornite (Figure 3-6e) has also been observed at the Olympic Dam (Roberts and Hudson, 1983; Ciobanu et al., 2017) and Salobo (de Melo et al., 2017) IOCG deposits. This texture is a result of exsolution from an initial bornite – chalcocite solid solution (Bn_{ss}), and is not indicative of a particular temperature or cooling rate (Brett, 1964). A close examination of the phase diagrams in the Cu-Fe-S system indicates that the Bn_{ss} is stable between 300 and 700 °C, and exsolves into distinct phases ≤300 °C under hydrothermal conditions (Yund and Kullerud, 1966; Sugaki et al., 1975). In the Cu-Fe-S-O system, the assemblage bornite – chalcocite – hematite is stable at 500 °C and 1 kbar (Hemley et al., 1992). Additionally, the outward zonation of the hypogene sulfides (bornite, chalcocite → chalcopyrite, bornite → chalcopyrite > pyrite) combined with the progressive replacement of chalcopyrite by bornite and later by chalcocite (Figure 3-6b,c) is consistent with a cooling fluid between ~600 and ~100 °C and log aS_2 (S activity coeff) -1 to -15 (Barton, Jr., 1970; Einaudi et al., 2003). Therefore, the hypogene sulfides at Mina Justa formed by a stage 4 fluid that precipitated chalcopyrite followed by Bn_{ss} and hematite at high temperature (~500 °C). As the Bn_{ss} cooled down to 300 °C, it exsolved and generated the symplectitic texture between chalcocite and bornite, which supports a hypogene origin for chalcocite in the deposit.

The temperatures indicated by the sulfide phase assemblage for stage 4 at Mina Justa are consistent with the estimations for similar sulfide mineralization at other IOCG deposits. Based on detailed textural and chemical analysis of similar sulfide assemblages, Ciobanu et al. (2017)

concluded that at Olympic Dam, the Bn_{ss} formed at temperatures over 300 °C and cooled to below 120 °C. Marschik and Fontboté (2001) presented fluid inclusion and sulfide-sulfate fractionation data to establish a temperature of mineralization of 340 to >470 °C for the sulfide (pyrite – chalcopyrite) stage at the Candelaria IOCG deposit in Chile. The temperature range reported by those authors is consistent with the zonation of sulfides in Mina Justa, with sulfides crystallizing from a cooling fluid between ~500 and ~300 °C.

Chen et al. (2011) used fluid inclusions in calcite veins that cross-cut stage 1 to infer a temperature range of 88 – 220 °C for the Cu-sulfide mineralization (stage 4). However, those inclusions are of unknown origin and could be secondary. We also found late-stage quartz-calcite veins that cross-cut stage 4 that must be younger than the Cu mineralization (Figure 3-5e); thus, the veins and temperatures reported by Chen et al. (2011) could also be part of this late stage. Temperatures from fluid inclusions in late-stage calcite in the Mantoverde (Rieger and Marschik, 2012) and Candelaria IOCG deposits (Marschik and Fontboté, 2001) are 250 °C and ≤ 236 °C respectively, and are consistent with the temperatures reported by Chen et al. (2011) for Mina Justa.

3.6.2 Source of fluids and metals

The source of the ore fluids and metals remains one of the most controversial aspects in IOCG systems. Hypotheses cover a diverse range of ideas, with some arguing that the metals are sourced from the host rock and mobilized by basinal brines (Barton and Johnson, 1996; Haynes, 2000; Benavides et al., 2007), others favoring a magmatic source for the metals and the fluids (Pollard, 2006), and others supporting a combination of magmatic and basinal fluids (Hitzman et al., 1992; Hitzman, 2000; Chiaradia et al., 2006; Groves et al., 2010; Rieger and Marschik, 2012). Traditional stable isotopic systems (H, C, O, S) have been widely used to assess the source of ore fluids, however, non-traditional, stable transition metals isotopic systems (i.e. Cu, Fe, Zn, Ag) offer a direct tool to determine the origin of the metals themselves.

A global compilation of stable Fe and O isotope data from IOA deposits and igneous rocks has constrained a field for magmatic and high-temperature magmatic-hydrothermal magnetite (Troll et al., 2019). All the Fe – O isotope pairs from the samples from Mina Justa fall within the magmatic and magmatic-hydrothermal field and fingerprint a magmatic/magmatic-hydrothermal source for the magnetite and mushketovite in the deposit (Figure 3-12). The $\delta^{18}O$

values reported here for magnetite from Mina Justa are also consistent with the range (2.7 – 4.7‰) reported by Chen et al. (2011), which fall within the range for magmatic and magmatic-hydrothermal magnetite (Taylor, 1968; Troll et al., 2019). The overall higher $\delta^{18}O$ values of magnetite from the manto compared to the hydrothermal unit are consistent with cooling and with a greater proportion of O being sourced from the wall rock, as the manto magnetite replaced carbonate-rich horizons from the Río Grande Formation (Hawkes et al., 2002; Sillitoe, 2002). At the Candelaria IOCG deposit in Chile, magnetite that replaced carbonate-bearing layers also yields elevated $\delta^{18}O$ values (Rodriguez-Mustafa et al., 2020). Those authors calculated a rock/water volume of 0.2 – 0 .3 that resulted in the hydrothermal fluid from which such magnetite precipitated. The higher $\delta^{56}Fe$ values in the hydrothermal unit indicate that there was more fractionation than in the manto, indicating that magnetite formed at a lower temperature in the hydrothermal unit, which is consistent with the temperature estimations from the Mg content of magnetite. The $\delta^{18}O$ values for actinolite from the Mina Justa hydrothermal unit overlap the $\delta^{18}O$ values reported for actinolite from the Quince IOA prospect (Rodriguez-Mustafa et al., 2020) in Chile and the Murdie Murdie IOCG prospect in the Olympic Dam district in Australia (Bastrakov et al., 2007), and are also consistent with a magmatic source.

In order to assess the possible role of meteoric water or basinal brines as oxygen source reservoirs, the calculated $\Delta'^{17}O$ values for magnetite from the manto and the hydrothermal unit at Mina Justa are plotted against their respective $\delta^{18}O$ values (Pack et al., 2016; Zakharov et al., 2019; Peters et al., 2020), and compared with data from the El Laco IOA deposit in Chile (Childress et al., 2020) and the Bafq and Sirjan IOA deposits in Iran (Peters et al., 2020) (Figure 3-12). Our data do not overlap the fields modeled by Peters et al. (2020) for magnetite in equilibrium with seawater (150 – 600 °C) or with meteoric water (400 °C) and mostly coincide with the field for magmatic and magmatic-hydrothermal magnetite, indicating a magmatic or magmatic-hydrothermal reservoir for oxygen incorporated into magnetite, consistent with the Fe isotope data. Peters et al. (2020) calculated the isotopic composition of end member magnetite that had equilibrated at high temperature (~800 °C) with fluids that had exchanged oxygen with sulfate from evaporites. They interpret the variable $\Delta'^{17}O$ values in their data to indicate that magnetite crystallized from a magmatic fluid that had interacted with evaporites. The data reported here for Mina Justa magnetite do not show such a range in $\Delta'^{17}O$ space (Figure 3-12), precluding a considerable input from evaporitic sources in the oxygen reservoir for magnetite.

Overall, the O isotopes from Mina Justa support a magmatic or magmatic-hydrothermal reservoir and disallow the predominance of meteoric, seawater, and basinal brines as oxygen sources for magnetite.

Published S isotope data for pyrite from stage 3 ($\delta^{34}S$ range from -0.5 to 6.4‰) and chalcopyrite from stage 4 ($\delta^{34}S$ range from -0.6 to 4.6‰) from Mina Justa cluster around 1‰ and show a slight bimodal distribution (Li et al., 2018). Those authors suggested that the stage 3 fluids were mainly of magmatic origin with a later incursion of an external fluid and acknowledged the possibility of a magmatic-hydrothermal source for the S in the chalcopyrite from stage 4 (Li et al., 2018).

The new $\delta^{65}Cu$ data reported here, which range from -0.09 to -0.32‰, are close to the bulk silicate Earth $\delta^{65}Cu$ average (0.06 ± 0.20 (2SD); Liu et al., 2015) and are within the range for hypogene sulfides in porphyry copper deposits (Figure 3-13) (Mathur et al., 2009; Mathur et al., 2012; Cooke et al., 2014). Thus, the $\delta^{65}Cu$ values for sulfides from Mina Justa corroborate the hypogene nature of the chalcopyrite, bornite, and chalcocite, and are consistent with an igneous source for Cu. The two samples with the lowest Cu isotope values from the Mina Justa hydrothermal unit present chalcopyrite being replaced by covellite (Figure 3-6d), which is a typical weathering product (Craig and Vaughan, 1994). Such an oxidative process evidenced by the considerable amount of Cu-oxides at Mina Justa would cause a loss of heavy Cu isotopes, resulting in a shift to lower $\delta^{65}Cu$ values in the original hypogene sulfides (chalcopyrite, bornite, and chalcocite) (Mathur et al., 2012).

3.7 Conclusions

The study of magnetite from the manto and hydrothermal unit at the Mina Justa IOCG deposit revealed two generations of Fe oxides that predate the Cu mineralization. Magnetite from the first generation is found in the manto only and its high trace element content indicates a high temperature of crystallization and is consistent with geochemistry of magnetite from IOA deposits in Chile. Magnetite from the second generation is found mainly in the structurally controlled hydrothermal unit but is also present in the manto. It consists of mushketovite and granular magnetite and yields lower crystallization temperatures than magnetite from the first generation. The Cu mineralization is hosted mainly in the hydrothermal unit and its zonation in

the deposit, alongside with its mineral textures, are consistent with a cooling fluid. The temperature estimations coupled with the novel $\Delta'^{17}O$ isotope results disallow the input of significant meteoric or basinal brines as ore fluids, and our Fe, O and Cu isotope data are consistent with published O and S data and fingerprint a magmatic-hydrothermal source for the ore fluids and metals in the deposit.

Mina Justa is a multi-stage mineral deposit that records an older IOA mineralization hosted in the manto ore bodies that could be related to the neighboring Marcona IOA deposit. The manto bodies at Mina Justa were overprinted by structurally controlled IOCG mineralization (hydrothermal unit) consisting of an initial Fe stage (hematite to magnetite/mushketovite + pyrite) and a following Cu sulfide stage. This paragenetic sequence from oxidized to reduced assemblages has been reported at other IOCG deposits in the Andean Belt (Marschik and Fontboté, 2001; de Haller and Fontboté, 2009; del Real et al., 2018) and results from the interaction and cooling of the oxidized magmatic-hydrothermal ore fluid with the reduced volcano-sedimentary host lithologies (Giggenbach, 1987; de Haller and Fontboté, 2009).

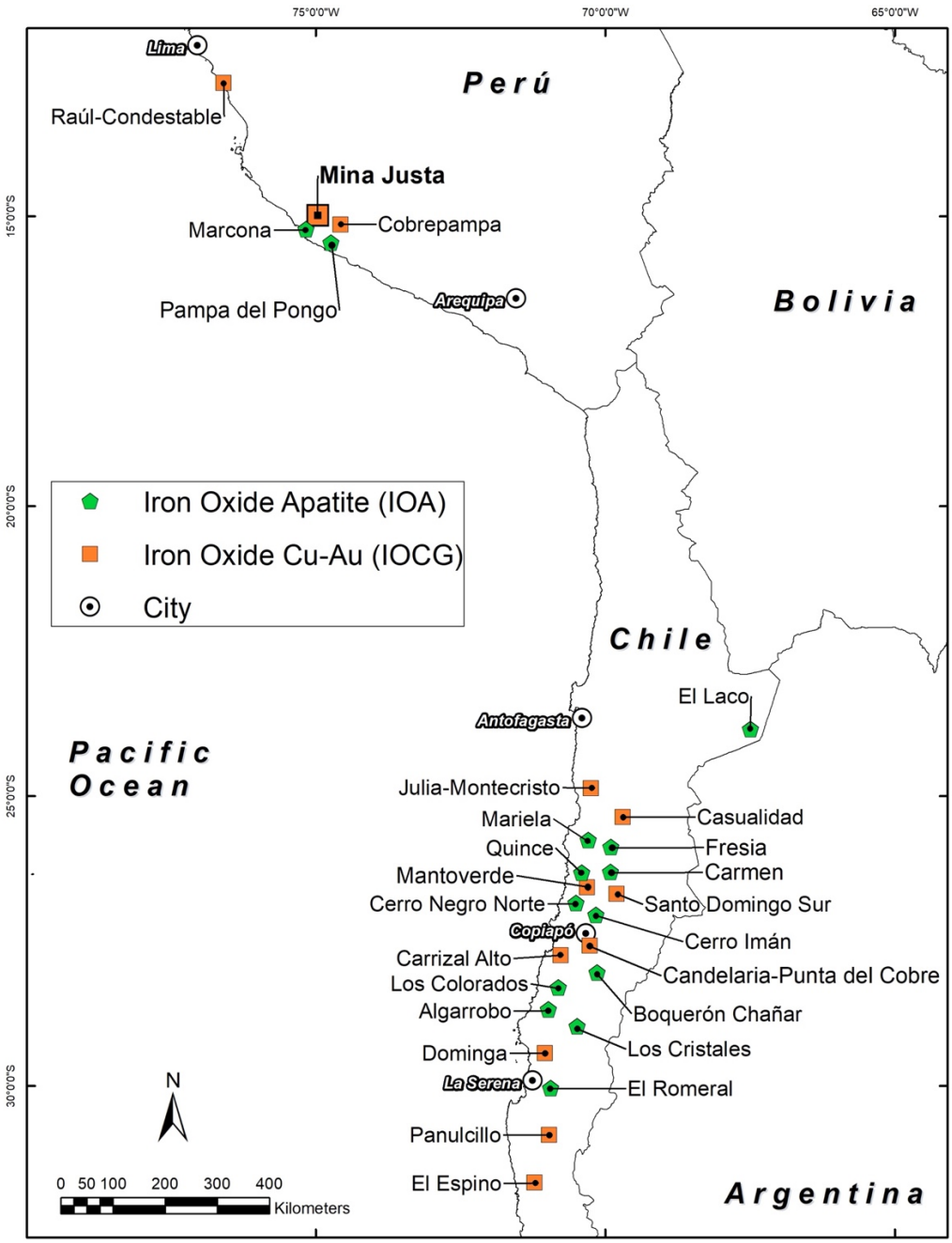

Figure 3-1 Regional map of the western margin of South America highlighting the main IOA and IOCG deposits in Chile and Peru:

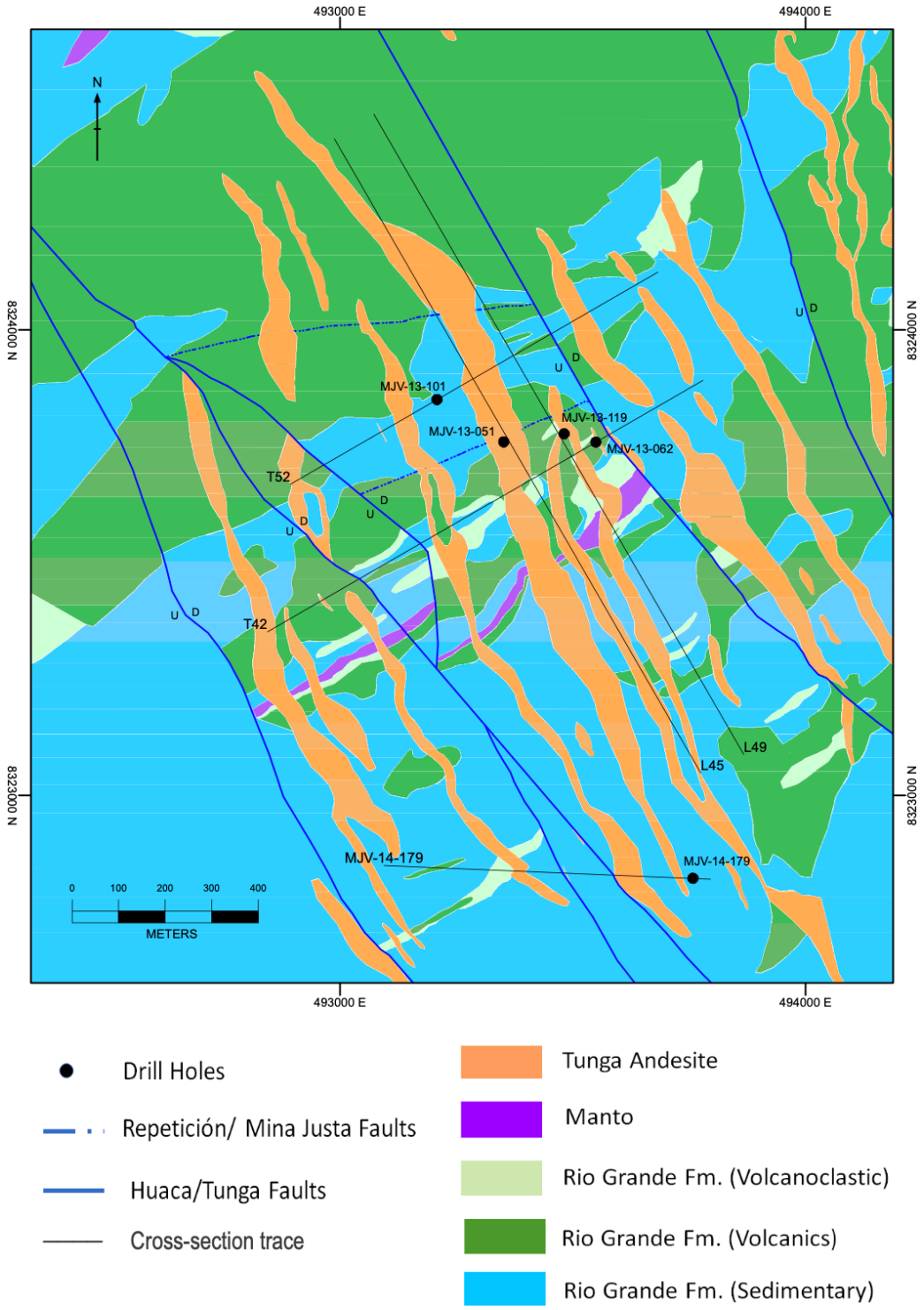

Figure 3-2: Simplified geological map (at 1:7500 scale) of the Mina Justa deposit with the location of the sampled drill cores. Coordinate system: WGS84, UTM Zone 18L. The manto is hosted in and follows the bedding of the volcano-sedimentary Río Grande Formation. The porphyritic andesitic dykes are post-mineralization, structurally controlled features. (Map provided by Marcobre). The cross-sections are shown in Figure A-1to Figure A-5.

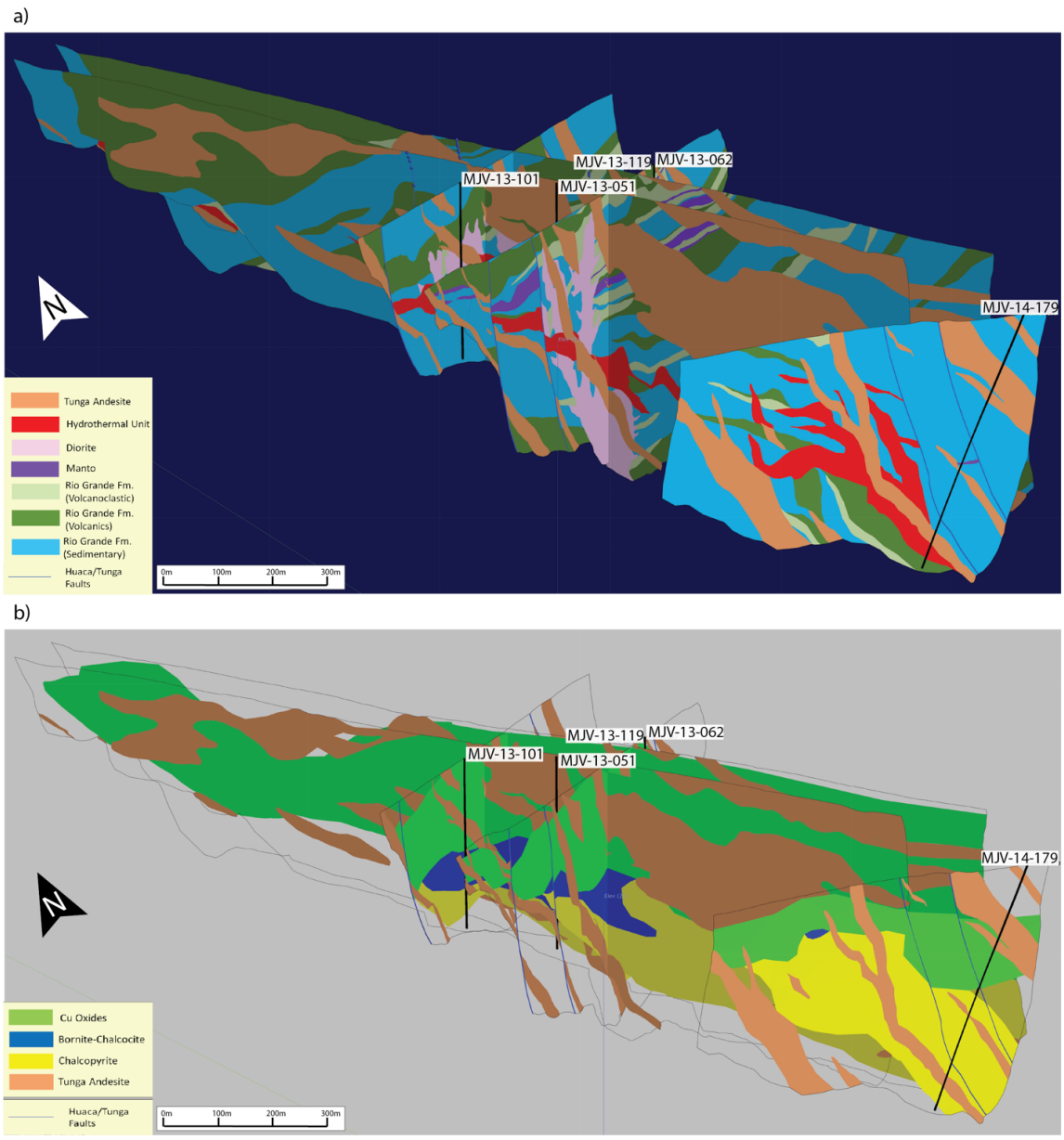

Figure 3-3: Perspective view of sections and drill traces in a 3D model of the Mina Justa deposit highlighting the longitudinal sections. The manto ore body dips to the NW while the structurally controlled hydrothermal unit dips to the SE. The black lines correspond to the sampled drill holes. a). Distribution of lithological units. b) Distribution of Cu mineralization. (Diagrams provided by Marcobre).

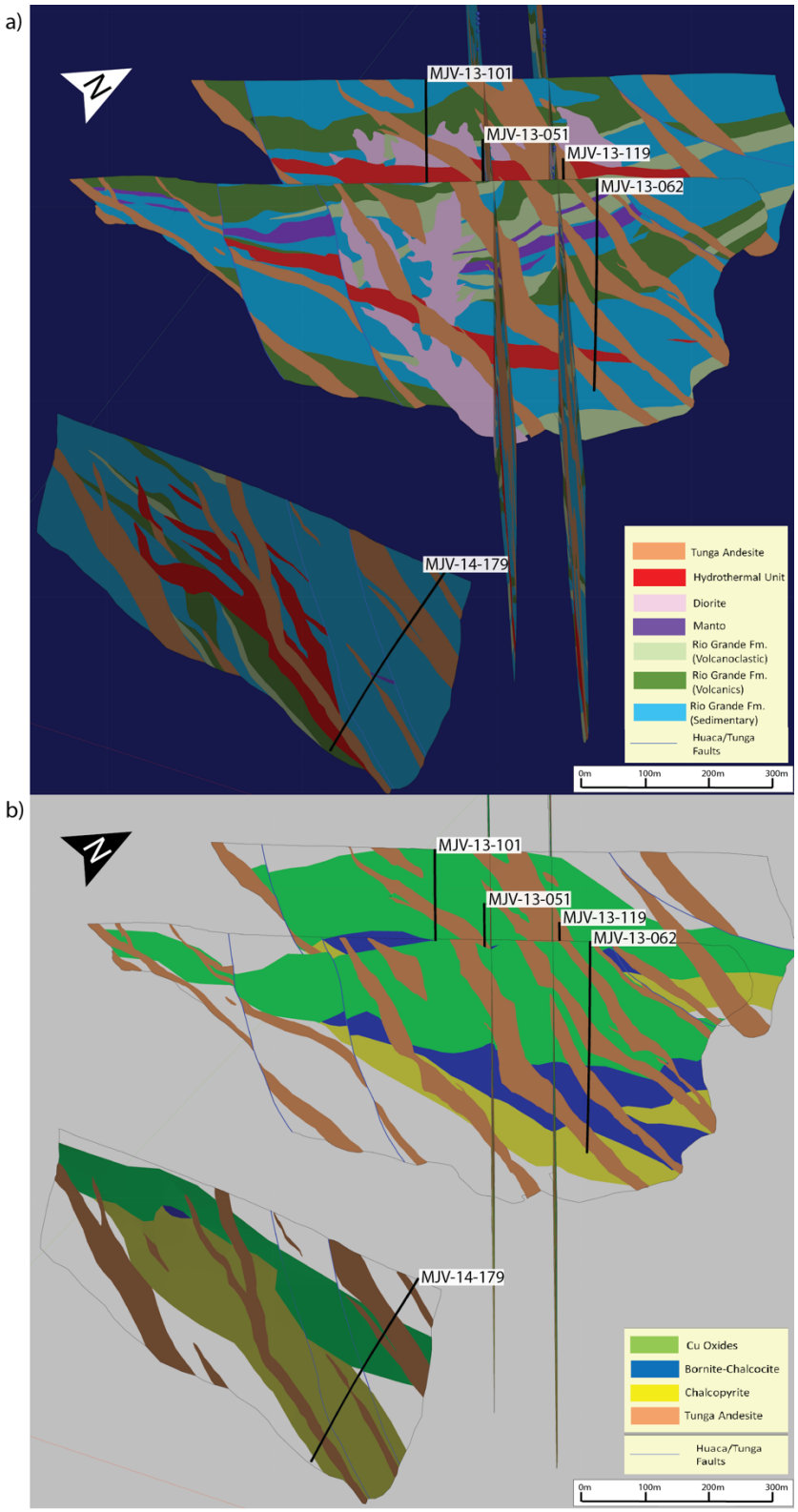

Figure 3-4: Perspective view of sections and drill traces in a 3D model of the Mina Justa deposit highlighting the transverse sections. The manto ore body dips to the NW while the structurally controlled hydrothermal unit dips to the SE. The black lines correspond to the sampled drill holes. a) Distribution of lithological units. b) Distribution of Cu mineralization. (Diagrams provided by Marcobre).

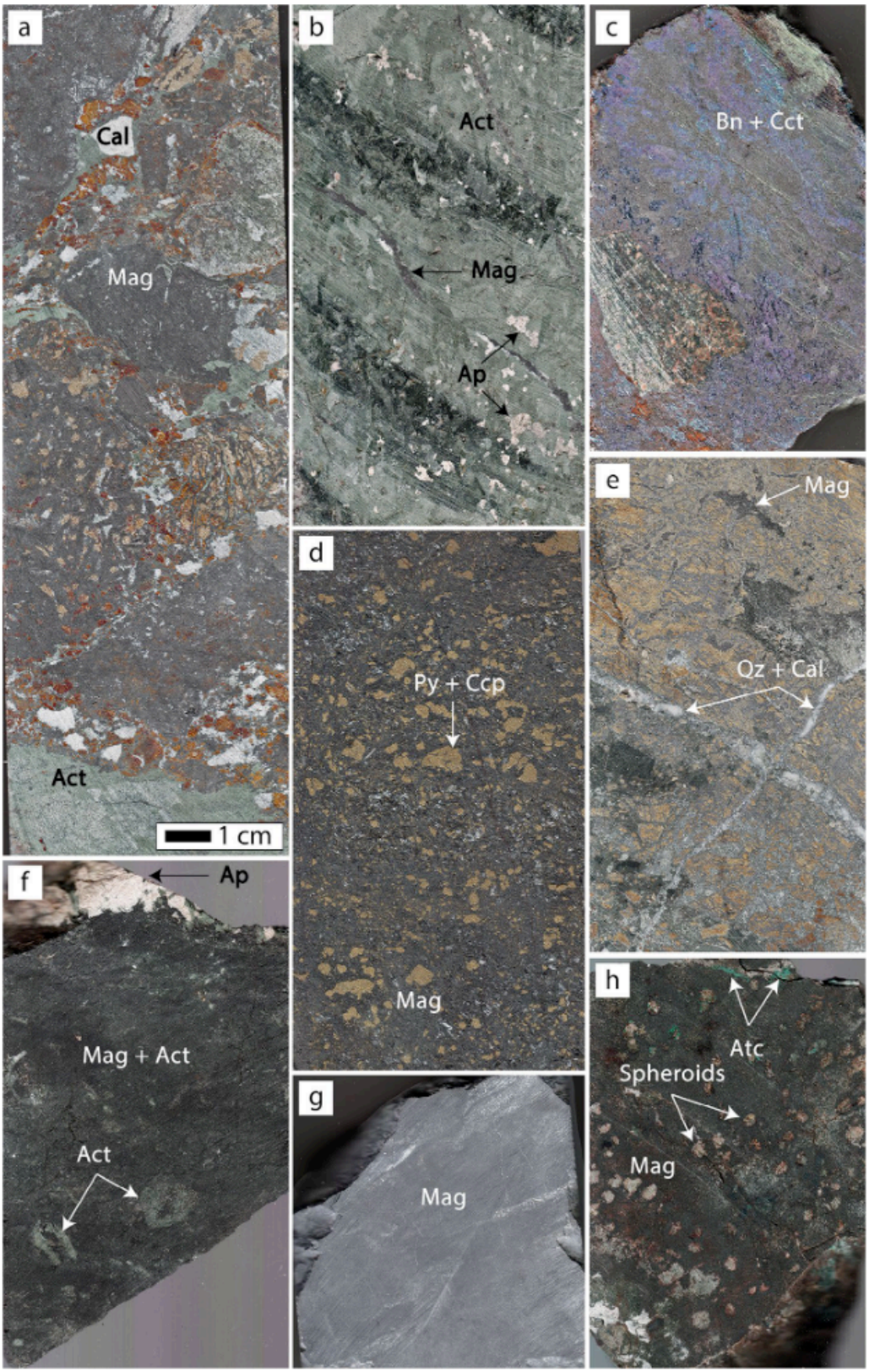

Figure 3-5: Representative hand samples from the Mina Justa deposit. Samples a-e come from the hydrothermal unit, and samples f-h from the manto. All samples have the same scale (a). Act=actinolite, Ap=apatite, Atc=atacamite,

Bn=bornite, Cal=calcite, Cct=chalcocite, Mag=magnetite, Qz=quartz. a. Sample GM13: Hydrothermal unit. Hydrothermal breccia with clasts of magnetite, actinolite, calcite, and altered host rock in a magnetite (mushketovite) and mixed sulfide matrix. b. Sample NN58: Massive actinolite intergrown with apatite, cross-cut by magnetite veinlets. c. Sample NN53: Sample from the sulfide mineralization in the hydrothermal unit. Bornite and chalcocite in magnetite matrix with an altered volcanic clast. d. Sample NN06: Massive magnetite (mushketovite) with disseminated chalcopyrite replacing pyrite. e. Sample NN16: Hydrothermal breccia with magnetite – chloritized actinolite matrix with quartz, apatite and pyrite clasts. Most of the pyrite has been replaced by chalcopyrite, galena and sphalerite. Quartz-calcite veins cross-cut the breccia. f. Sample NN50: Fine grained magnetite and actinolite. The latter is also replacing marine fossils. Part of a later apatite, fibrous actinolite, and mushketovite vein is visible in the top. g. Sample NN52: Very fine-grained, massive magnetite. h. Sample NN04: Fine-grained magnetite matrix with spheroids composed of calcite, quartz, and potassium feldspar. The spheroids are surrounded by a coarser magnetite halo. Supergene atacamite replacing covellite is also present.

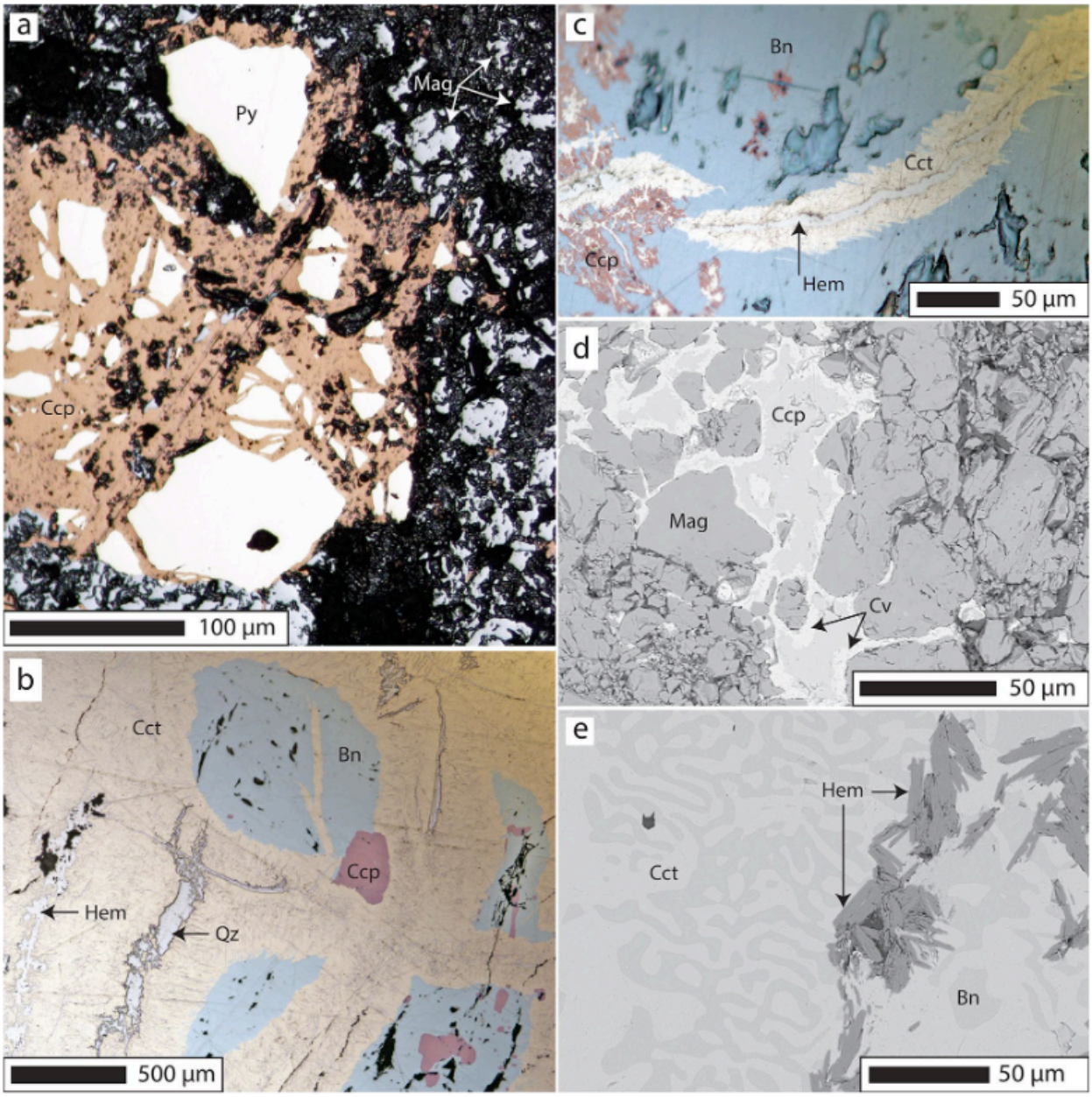

Figure 3-6: Reflected light photographs (A-C) and BSE images (D-E) of: A. Disseminated magnetite and chalcopyrite replacing pyrite (sample NN59). B. Chalcocite, which exhibits flame texture, is replacing bornite. The latter is replacing chalcopyrite. Hematite and quartz are also present filling interstices and fractures (sample NN51). C. Lateral slip en-echelon hematite vein that resulted from local extension. The vein has a chalcocite halo replacing bornite (Sample NN01). D. Massive magnetite grains with interstitial chalcopyrite with covellite rims (sample NN06). E. Hematite co-existing with chalcocite and bornite that display a symplectitic texture (sample NN53). Bn=bornite, Cct=chalcocite, Ccp=chalcopyrite, Hem=hematite, Mag=magnetite, Py=pyrite, Qz=quartz.

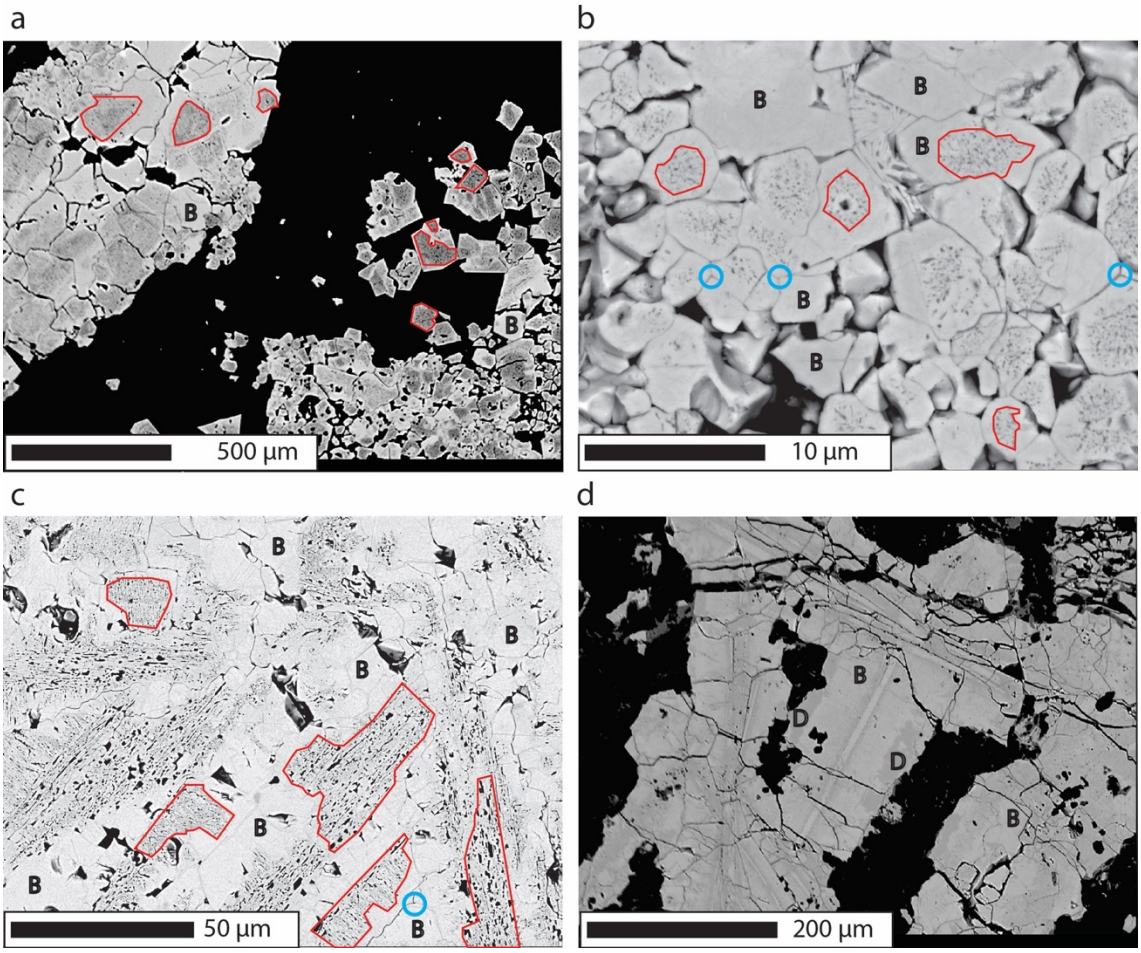

Figure 3-7: Magnetite and mushketovite textures from the manto at Mina Justa. Magnetite with inclusions (type I) is outlined in red, and types Dark (D) and Bright (B) are identified with the letters D and B, respectively. Triple junctions are circled in blue. a. Type I magnetite euhedral to subhedral cores surrounded by magnetite type B (sample NN51). b. Another example of magnetite type B surrounding magnetite type I. Note the difference in scale with a. The sub-micron inclusions are visible only in magnetite type I. The platy mineral in the top, center is hematite (sample NN01). c. Type I magnetite bands containing elongated inclusions. Type B surrounds type I (sample NN01). d. Mushketovite showing patches of magnetite types B and D. Type D magnetite shows a darker color in BSE, but no visible inclusions (sample NN04).

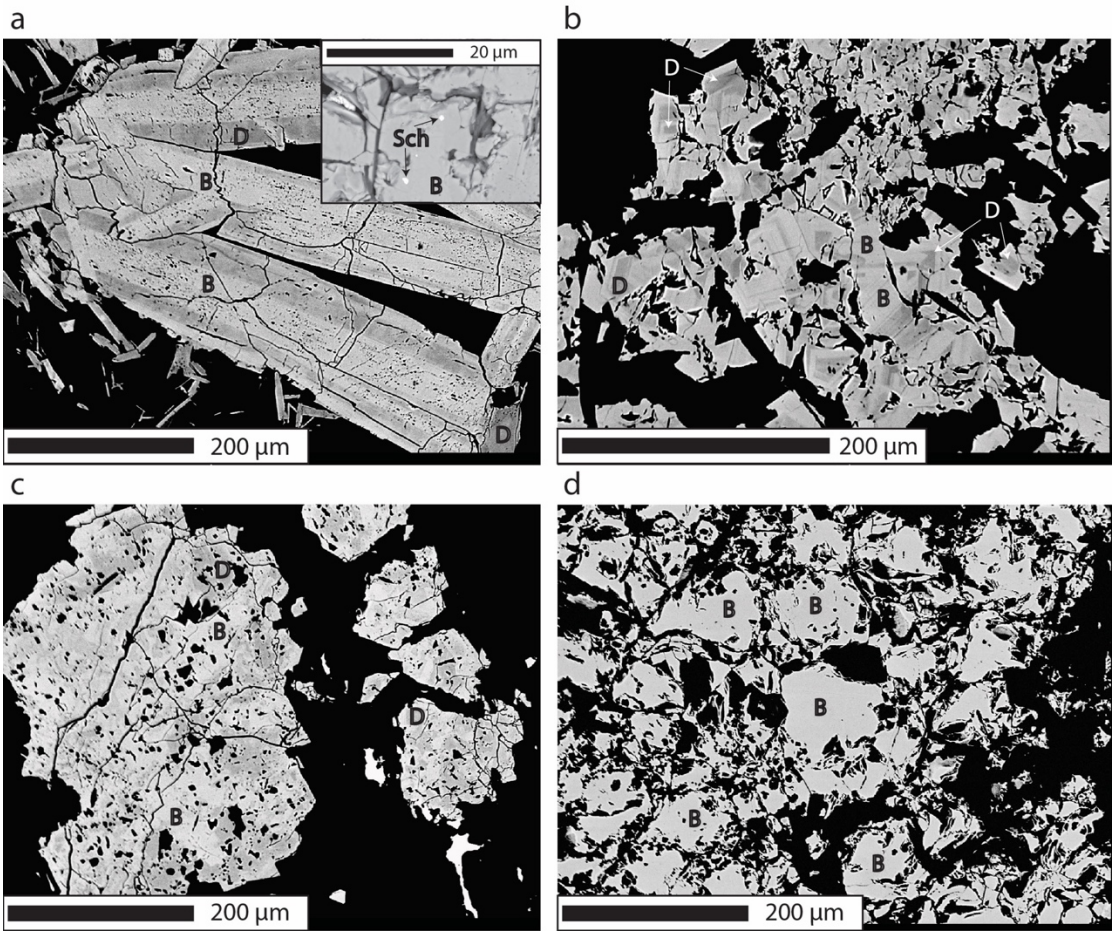

Figure 3-8:Magnetite and mushketovite textures from the hydrothermal unit at Mina Justa. Magnetite types Dark (D) and Bright (B) are identified with the letters D and B, respectively. a. Mushketovite showing patches of magnetite types B and D. Type D magnetite shows a darker color in BSE, but no visible inclusions. Type B is porous and has scheelite inclusions (Sch in inset) (sample NN54). b. Granular magnetite showing zoning of magnetite types D and B (sample NN57). c. Fractured granular magnetite with patches of type D and B magnetite (sample NN54). d. Granular magnetite type B grains. Note absence of zonation (sample NN59).

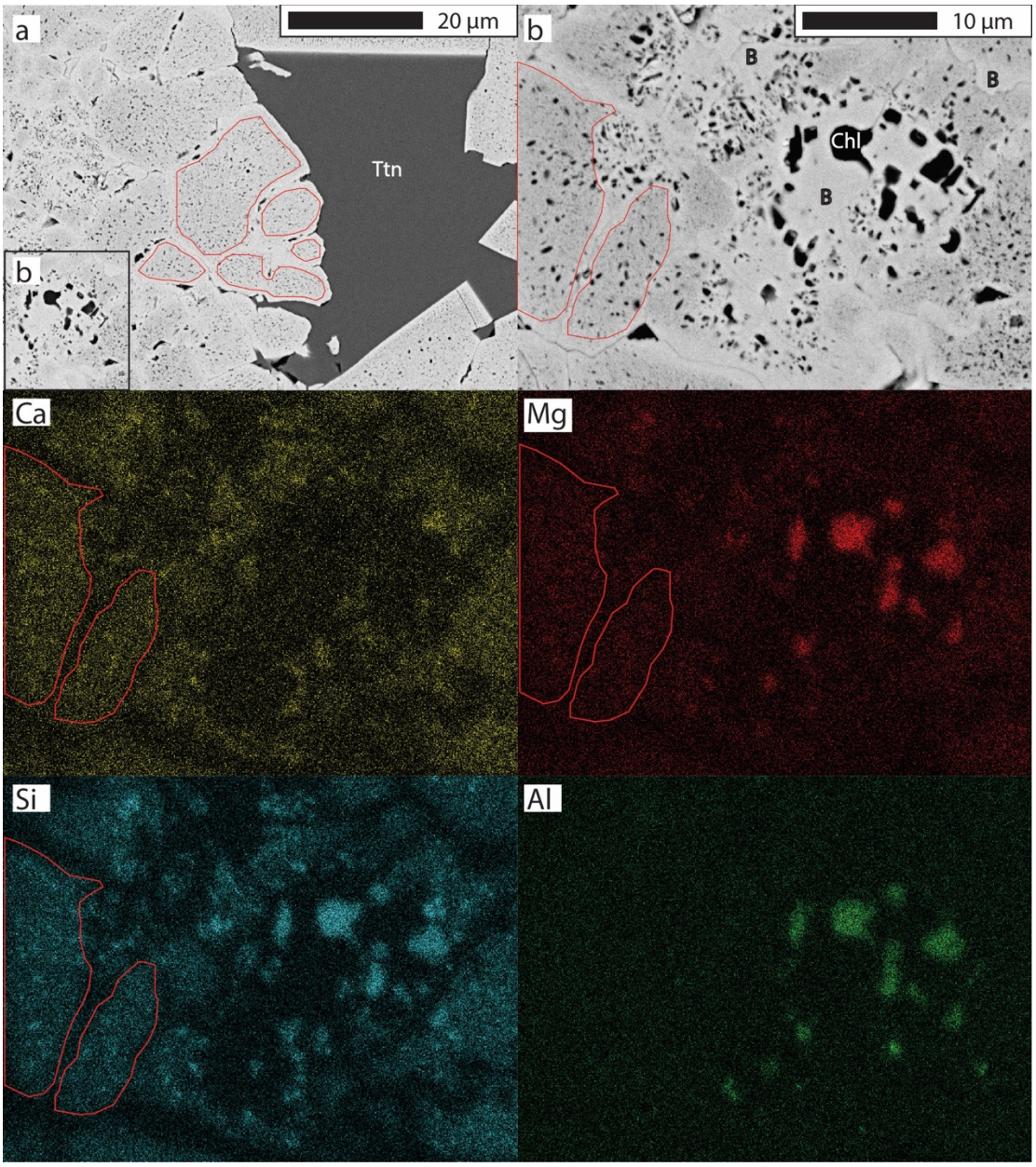

Figure 3-9: A. Magnetite type I cores outlined in red are surrounded by type B magnetite rims that are in contact with interstitial titanite (Ttn). B. Inset from a showing chloritized actinolite (Chl) intergrown with magnetite type B; note that the left side of b is outside and to the left of the lower left box in 8a. The elemental maps are from the same area as b and show that magnetite type I (outlined in red) is enriched in Si, Ca and Mg compared to magnetite type B.

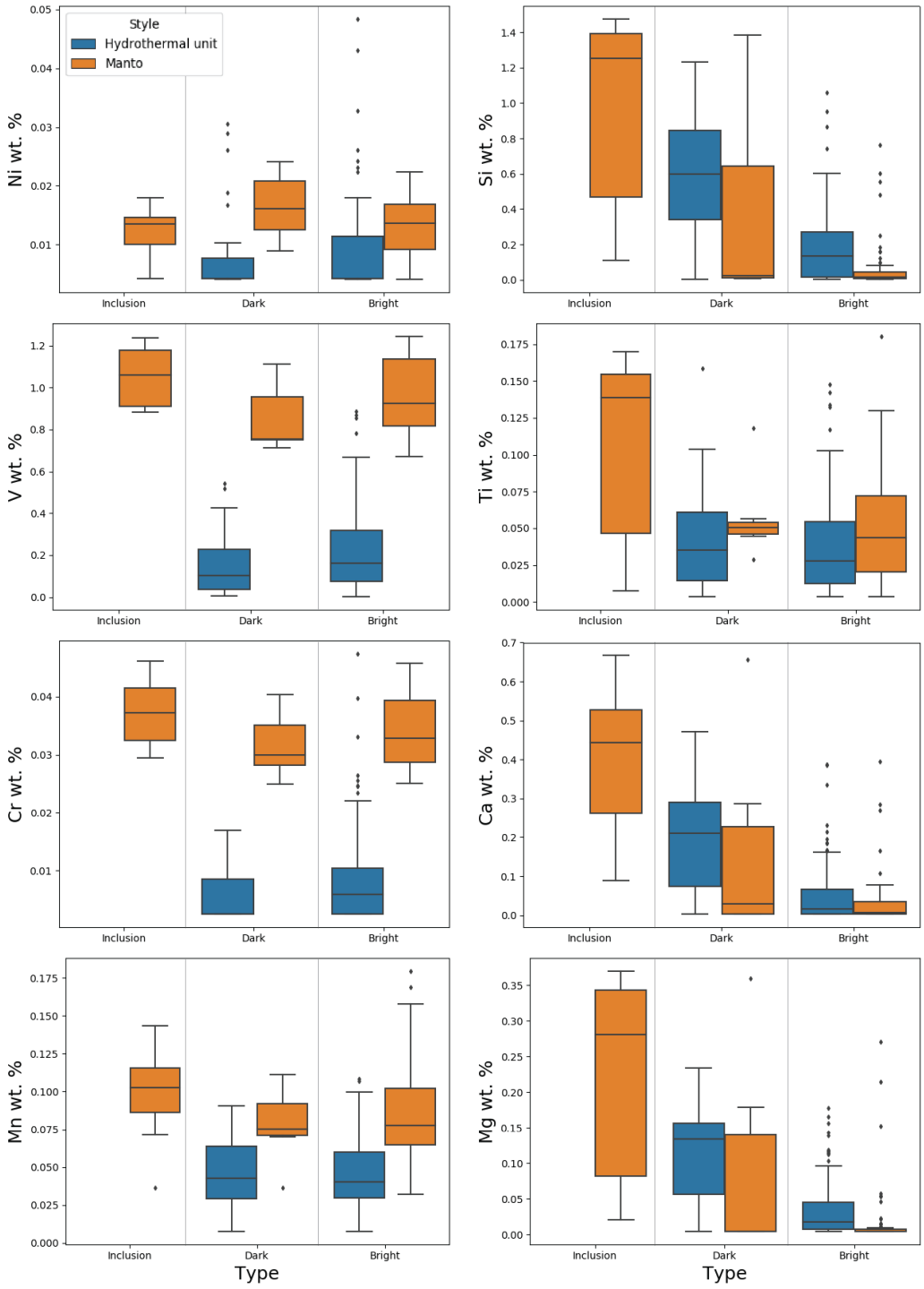

Figure 3-10: Box and whisker plots showing the trace element concentrations of the different magnetite types (Inclusion, Dark, Bright) at Mina Justa. The box comprises the interquartile range (IR), where the horizontal line corresponds to the median. The whiskers extend for 1.5 times the IR from the first and third quartiles. When a significant amount of the data is at the detection limit, the first quartile and the median are the same. The diamonds represent outliers. The color indicates if magnetite belongs to the hydrothermal unit (blue) or to the manto (orange). The manto magnetite is overall enriched in Ni, V, Cr and Mn when compared to the hydrothermal unit magnetite. Magnetite with inclusions (type I) has the highest concentrations of Si, Ti, Ca, and Mg, followed by magnetite type Dark (D), whereas magnetite type Bright (B) is depleted in the same elements.

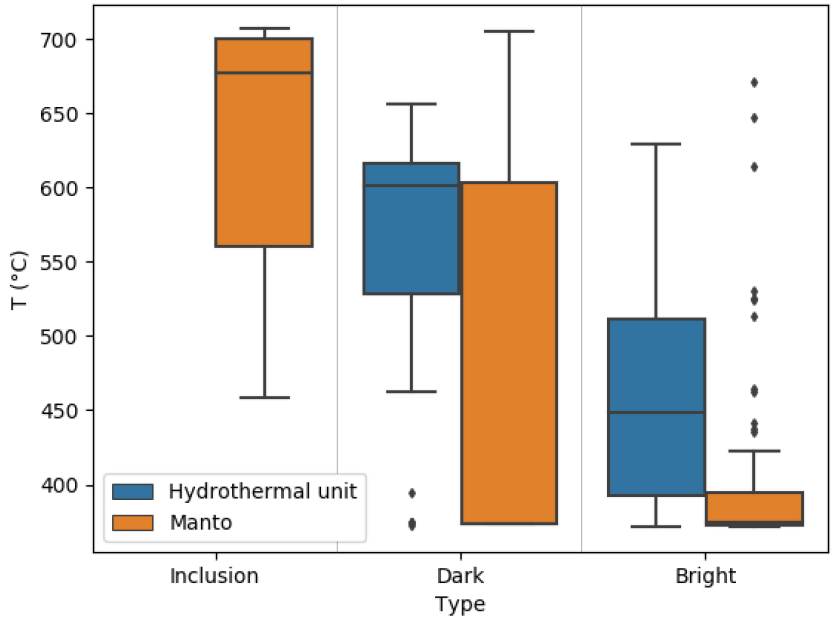

Figure 3-11: Box and whisker plots of the crystallization temperature estimations of the different magnetite types (Inclusion, Dark, Bright) for the manto (orange) and the hydrothermal unit (blue) at Mina Justa. The box comprises the interquartile range (IR), where the horizontal line corresponds to the median. The whiskers extend for 1.5 times the IR from the first and third quartiles. The diamonds represent outliers. Magnetite with inclusions (type I) found only in the manto has the highest median temperature, while type Bright (B) has the lowest in the manto and in the hydrothermal unit.

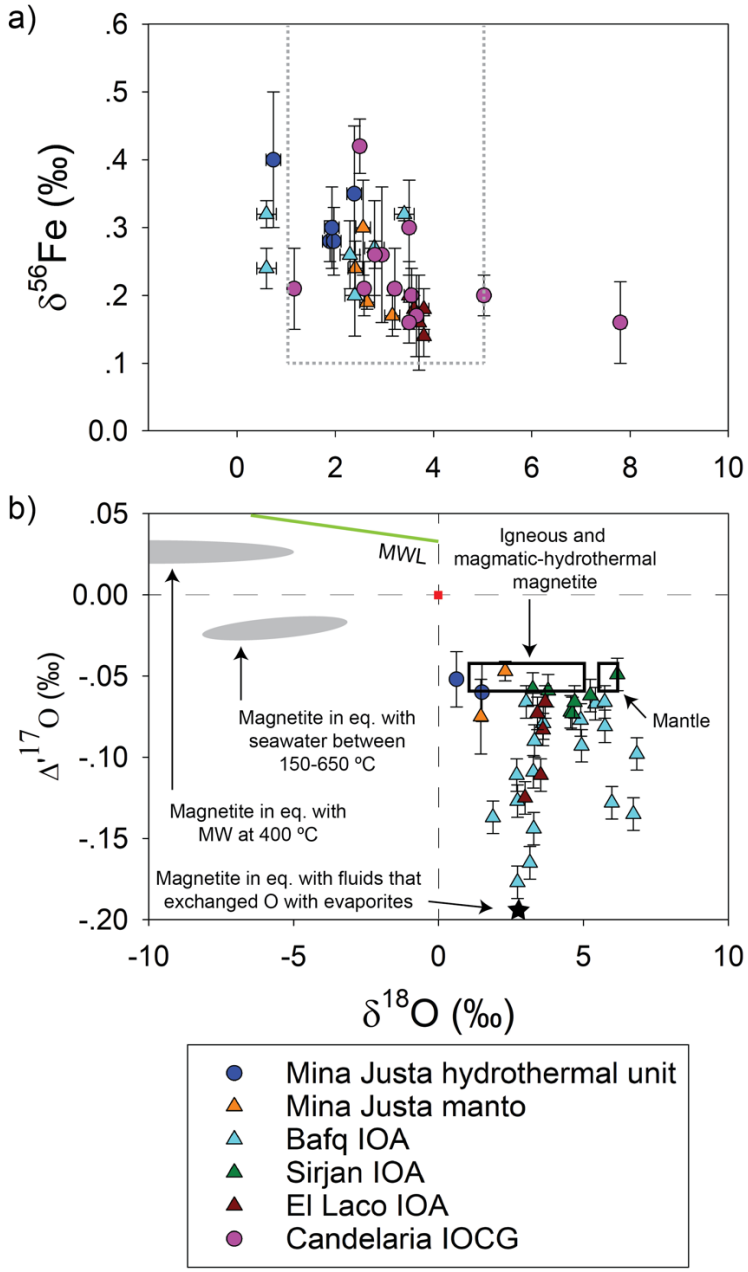

Figure 3-12: A. Scatter plot of $\delta^{18}O$ vs. $\delta^{56}Fe$ values for magnetite from Mina Justa and other IOCG (circles) and IOA (triangles) deposits. The dashed gray outline defines the field for magmatic and magmatic-hydrothermal magnetite (Taylor, 1968; Troll et al., 2019). Only one data point from Mina Justa is outside of the range for $\delta^{18}O$, but all values are within the range for $\delta^{56}Fe$. Some of the error bars for the $\delta^{18}O$ measurements are smaller than the symbol size. B. Plot of $\delta^{18}O$ vs. $\Delta'^{17}O$ values for magnetite from Mina Justa compared to data from the Bafq, Sirjan, and El Laco IOA deposits (Childress et al., 2020; Peters et al., 2020). The error bars for the $\delta^{18}O$ measurements are smaller than the symbol size. The red square marks the values for seawater and the green line shows the Meteoric Water Line (Luz and Barkan, 2010; Sharp et al., 2018). The magmatic and magmatic-hydrothermal magnetite and mantle fields are based on data from Taylor (1968), Pack et al. (2016), Sharp et al. (2018), Troll et al. (2019), Miller et al. (2020), and Peters et al. (2020). The gray ellipses and the black star are from Peters et al. (2020). The star indicates the end-member magnetite that equilibrated at high temperature (~800 °C) with fluids that had exchanged oxygen with sulfate from evaporites (Peters et al., 2020). The data from Mina Justa fall within error in the magmatic and magmatic-hydrothermal magnetite box and do not overlap the fields for magnetite in equilibrium with meteoric or seawater. eq.=equilibrium, MW=Meteoric water, MWL=Meteoric water line.

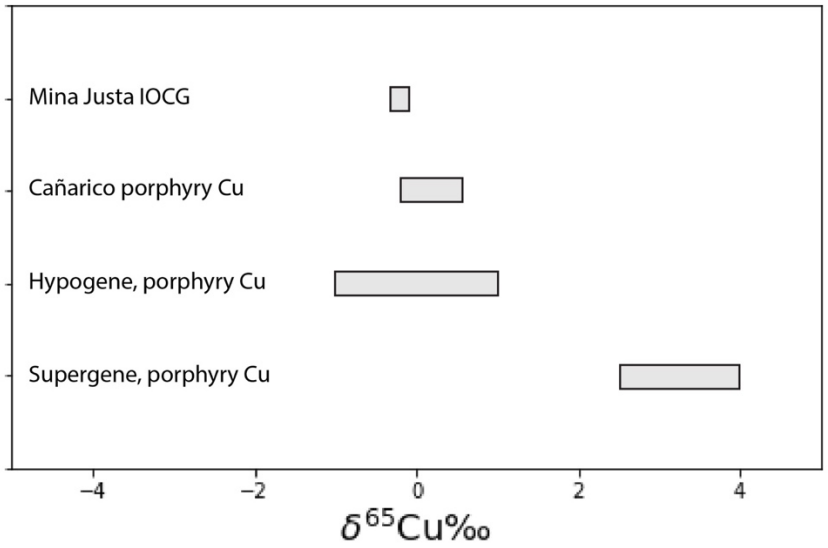

Figure 3-13: Ranges of δ^{65}Cu values from sulfides from porphyry copper deposits and the Mina Justa IOCG deposit. The data from Mina Justa is within the range for hypogene sulfides reported for several porphyry Cu deposits, and overlaps the range for sulfides from the Cañarico porphyry Cu deposit in northern Peru. Supergene data from the Morenci and El Salvador porphyry deposits from Mathur et al. (2012) and references therein. Hypogene data from the Silver Bell, Chuquicamata, El Salvador, and Morenci porphyry deposits from Mathur et al. (2009). Cañarico data from Mathur et al. (2012). Mina Justa data from this study.

Table 3-1: Sample details

Sample	Hole	*UTM (E) Zone 18L	*UTM (N) Zone 18L	Down-hole depth (m)	Geologic unit
NN01	MV-13-051	493352	8323759	159.5	Manto
NN03	MV-13-051	493352	8323759	183.1	Hydrothermal unit
NN02	MV-13-051	493352	8323759	288.5	Hydrothermal unit
NN50	MV-13-062	493550	8323758	87.3	Manto
NN51	MV-13-062	493550	8323758	93.1	Manto
NN52	MV-13-062	493550	8323758	103.5	Manto
NN53	MV-13-062	493550	8323758	344.9	Hydrothermal unit
NN54	MV-13-062	493550	8323758	362	Hydrothermal unit
NN04	MV-13-101	493209	8323849	178	Manto
NN56	MV-13-119	493482	8323776	129	Manto
NN57	MV-13-119	493482	8323776	395.5	Hydrothermal unit
NN58	MV-13-119	493482	8323776	396	Hydrothermal unit
NN59	MV-13-119	493482	8323776	403.8	Hydrothermal unit
NN06	MV-14-179	493759	8322822	282.63	Hydrothermal unit
GM07	MV-14-179	493759	8322822	290.5	Hydrothermal unit

GM13	MV-14-179	493759	8322822	461.68	Hydrothermal unit
GM14	MV-14-179	493759	8322822	463.1	Hydrothermal unit
NN15	MV-14-179	493759	8322822	467.4	Hydrothermal unit
NN16	MV-14-179	493759	8322822	472.8	Hydrothermal unit

*Coordinate system: WGS84

Table 3-2: Magnetite types and their estimated temperatures by using the Mg in magnetite geothermometer. sd: Standard deviation. n: Number of points analyzed

Type	Geologic unit	Visible inclusions	Equivalent type in Hu et al. 2020	Minimum temperature (°C)	Maximum temperature (°C)	Average temperature (°C ± 1sd)	n
Inclusion (I)	Manto	Yes	None	459	707	628 ± 95	8
Dark (D)	Manto and Hydrothermal unit	None	T_{M1}-2, T_{M2}-1	373	705	543 ± 106	37
Bright (B)	Manto and Hydrothermal unit	None	T_{M1}-3, T_{M2}-2	371*	671	443 ± 74	195

*Estimated as a function of half of the Mg detection limit. May impact the average temperature for this magnetite type.

Table 3-3:Summary statistics of EPMA magnetite data and temperature estimations from Mg content. All concentrations wt.%; oxygen content is stoichiometrically calculated. Hyd: Hydrothermal unit. Tav: Average temperature in °C estimated from Mg content in magnetite. n: Number of points analyzed. BDL: Below detection limit.

	Fe	Al	Ca	Si	Mg	Mn	Ti	V	Ni	Cr	O	Total	Tav
Manto n=78													
mean	70.71	0.05	0.08	0.19	0.05	0.09	0.06	0.96	0.01	0.03	21.12	93.35	438
std	1.10	0.04	0.16	0.38	0.10	0.03	0.04	0.17	0.01	0.01	0.51	1.29	104
min	68.09	BDL	BDL	BDL	BDL	0.03	BDL	0.67	BDL	0.02	20.01	89.17	372
median	70.82	0.04	0.01	0.02	0.01	0.08	0.05	0.92	0.01	0.03	21.10	93.73	393
max	72.13	0.23	0.67	1.47	0.37	0.18	0.18	1.24	0.02	0.05	22.56	95.58	707
Hyd. unit n=162													
mean	71.78	0.09	0.08	0.25	0.05	0.05	0.04	0.21	0.01	0.01	21.13	93.68	478
std	0.83	0.08	0.10	0.29	0.05	0.02	0.03	0.19	0.01	0.01	0.36	0.89	84
min	69.73	0.01	BDL	BDL	BDL	BDL	BDL	BDL	BDL	BDL	20.11	90.06	371
median	71.96	0.05	0.03	0.18	0.02	0.04	0.03	0.14	BDL	BDL	21.11	93.77	459
max	73.55	0.41	0.47	1.23	0.23	0.11	0.16	0.89	0.05	0.05	22.07	95.06	657
Type I n=8													
mean	69.10	0.11	0.41	0.97	0.22	0.10	0.11	1.05	0.01	0.04	21.93	94.06	628

std	1.22	0.06	0.19	0.55	0.15	0.03	0.06	0.15	0.00	0.01	0.65	1.06	95
min	68.09	0.03	0.09	0.11	0.02	0.04	BDL	0.88	BDL	0.03	20.95	92.16	459
median	68.61	0.11	0.44	1.25	0.28	0.10	0.14	1.06	0.01	0.04	22.21	94.35	677
max	71.06	0.23	0.67	1.47	0.37	0.14	0.17	1.24	0.02	0.05	22.56	95.58	707
Type D n=37													
mean	70.47	0.16	0.19	0.54	0.11	0.05	0.05	0.29	0.01	0.01	21.28	93.14	543
std	1.12	0.11	0.16	0.41	0.08	0.03	0.04	0.32	0.01	0.01	0.70	1.84	106
min	68.20	0.03	BDL	BDL	BDL	BDL	BDL	BDL	BDL	BDL	20.01	89.17	373
median	70.40	0.15	0.17	0.55	0.12	0.05	0.05	0.15	BDL	BDL	21.51	93.98	590
max	72.48	0.41	0.66	1.38	0.36	0.11	0.16	1.11	0.03	0.04	22.42	94.91	705
Type B n=195													
mean	71.71	0.06	0.04	0.14	0.03	0.06	0.04	0.46	0.01	0.02	21.07	93.64	443
std	0.78	0.05	0.07	0.20	0.04	0.03	0.03	0.39	0.01	0.01	0.26	0.79	74
min	69.52	BDL	BDL	BDL	BDL	BDL	BDL	BDL	BDL	BDL	20.15	90.34	371
median	71.83	0.04	0.01	0.04	0.01	0.05	0.03	0.31	0.01	0.01	21.08	93.74	422
max	73.55	0.36	0.39	1.06	0.27	0.18	0.18	1.24	0.05	0.05	22.02	95.06	671

Table 3-4: Stable isotope results for magnetite (Fe, O), actinolite (O, H) and sulfides (Cu). Isotope values in ‰ with respect to the standard IRMM-14 for Fe, VSMOW for O and H, and NIST 976 for Cu. Hyd: Hydrothermal unit. sd: Standard deviation. H_20 in wt.%.

Magnetite												**Sulfides**	
Sample	**Style**	**$\delta^{18}O$**	**2sd**	**$\delta^{56}Fe$**	**2sd**	**n56**	**$\delta^{17}O$**	**$\delta^{18}O$**	**$\Delta'^{17}O$**	**1sd**	**n**	**$\delta^{65}Cu$**	**2sd**
NN51	Manto											-0.25	0.08
NN50	Manto	2.65	0.15	0.19	0.01	3							
NN52	Manto	2.41	0.15	0.24	0.04	3	0.701	1.464	-0.076	0.023	4		
NN04	Manto	2.57	0.15	0.3	0.07	5	1.175	2.305	-0.048	0.006	5		
NN56	Manto	3.16	0.15	0.17	0.03	3							
NN02	Hyd. unit											-0.09	0.08
NN53	Hyd. unit											-0.26	0.08
NN03	Hyd. unit	2.39	0.15	0.35	0.1	5						-0.30	0.08
NN06	Hyd. unit	0.74	0.15	0.4	0.1	6	0.277	0.621	-0.052	0.017	5	-0.32	0.08
GM14	Hyd. unit	1.93	0.15	0.3	0.06	3						-0.11	0.08
GM13	Hyd. unit	1.97	0.15	0.28	0.05	6	0.738	1.505	-0.060	0.018	6		
NN57	Hyd. unit	1.89	0.15	0.28	0.03	3							

Actinolite						
Sample	**Style**	**$\delta^{18}O$**	**2sd**	**δD**	**2sd**	**H_2O**
NN15	Hyd. unit	8.16	0.15	-35.15	1.86	2.03
NN58	Hyd. unit	8.14	0.15	-43.14	1.86	2.24

3.8 References

Atkin, B.P., Injoque, J., and Harvey, P.K., 1985, Cu-Fe amphibole mineralization in the Arequipa segment, *in* Pitcher, W.S., Atherton, M.P., Cobbing, E.J., and Beckinsale, R.D., eds., Magmatism at the plate edge: The Peruvian Andes: Glasgow, UK, Blackie, p. 261–270.

Barra, F., Reich, M., Selby, D., Rojas, P., Simon, A., Salazar, E., and Palma, G., 2017, Unraveling the origin of the Andean IOCG clan: A Re–Os isotope approach: Ore Geology Reviews, v. 81, p. 62–78.

Barton, Jr., P. B., 1970, Sulfide Petrology: Mineralogical Society of America, v. 3, p. 187–198.

Barton, M. D., and Johnson, D. A., 1996, An evaporitic-source model for igneous-related Fe oxide(-REE – Cu-Au-U) mineralization: Geology, v. 24, p. 259–262.

Barton, M. D., 2014, Iron Oxide(–Cu–Au–REE–P–Ag–U–Co) Systems, in Holland, H. D. and Turekian, K. K. eds., Treatise on Geochemistry (Second Edition): Oxford, Elsevier, p. 515–541.

Bastrakov, E. N., Skirrow, R. G., and Davidson, G. J., 2007, Fluid Evolution and Origins of Iron Oxide Cu-Au Prospects in the Olympic Dam District, Gawler Craton, South Australia: Economic Geology, v. 102, p. 1415–1440.

Benavides, J., Kyser, T. K., Clark, A. H., Oates, C. J., Zamora, R., Tarnovschi, R., and Castillo, B., 2007, The Mantoverde Iron Oxide – copper – gold District, III Región, Chile: The Role of Regionally Derived, Nonmagmatic Fluids in Chalcopyrite Mineralization: Economic Geology, v. 102, p. 415–440.

Bilenker, L. D., Simon, A. C., Reich, M., Lundstrom, C. C., Gajos, N., Bindeman, I., Barra, F., and Munizaga, R., 2016, Fe–O stable isotope pairs elucidate a high-temperature origin of Chilean iron iron oxide – apatite deposits: Geochimica et Cosmochimica Acta, v. 177, p. 94–104.

Bindeman, I. N., Kamenetsky, V. S., Palandri, J., and Vennemann, T., 2012, Hydrogen and oxygen isotope behaviors during variable degrees of upper mantle melting: Example from the basaltic glasses from Macquarie Island: Chemical Geology, v. 310–311, p. 126–136.

Bindeman, I. N., Zakharov, D. O., Palandri, J., Greber, N. D., Dauphas, N., Retallack, G. J., Hofmann, A., Lackey, J. S., and Bekker, A., 2018, Rapid emergence of subaerial landmasses and onset of a modern hydrologic cycle 2.5 billion years ago: Nature, v. 557, p. 545–548.

Brett, R., 1964, Experimental data from the system Cu-Fe-S and their bearing on exsolution textures in ores: Economic Geology, v. 59, p. 1241–1269.

Caldas Vidal, J., 1978, Geología del cuadrángulo de San Juan, Acarí y Yauca 31-m, 31-n, 32-n - [Boletín A 30]: Instituto Geológico, Minero y Metalúrgico - INGEMMET.

Canil, D., and Lacourse, T., 2020, Geothermometry using minor and trace elements in igneous and hydrothermal magnetite: Chemical Geology, v. 541, p. 119576.

Chen, H., Clark, A. H., Kyser, T. K., Ullrich, T. D., Baxter, R., Chen, Y., and Moody, T. C., 2010, Evolution of the Giant Marcona-Mina Justa Iron Oxide – copper – gold District, South-Central Peru: Economic Geology, v. 105, p. 155–185.

Chen, H., Kyser, T. K., and Clark, A. H., 2011, Contrasting fluids and reservoirs in the contiguous Marcona and Mina Justa iron oxide–Cu (–Ag–Au) deposits, south-central Perú: Mineralium Deposita, v. 46, p. 677–706.

Chiaradia, M., Banks, D., Cliff, R., Marschik, R., and de Haller, A., 2006, Origin of fluids in iron oxide–copper–gold deposits: constraints from δ37Cl, 87Sr/86Sri and Cl/Br: Mineralium Deposita, v. 41, p. 565–573.

Childress, T. M., Simon, A. C., Reich, M., Barra, F., Bilenker, L. D., La Cruz, N. L., Bindeman, I. N., and Ovalle, J. T., 2020, Triple oxygen, hydrogen, and iron stable isotope signatures indicate a silicate magma source and magmatic-hydrothermal genesis for magnetite ore bodies at El Laco, Chile: Economic Geology.

Ciobanu, C. L., Cook, N. J., and Ehrig, K., 2017, Ore minerals down to the nanoscale: Cu-(Fe)-sulphides from the iron oxide copper gold deposit at Olympic Dam, South Australia: Ore Geology Reviews, v. 81, p. 1218–1235.

Clark, A. H., Farrar, E., Kontak, D. J., Langridge, R. J., F, M. J. A., France, L. J., McBride, S. L., Woodman, P. L., Wasteneys, H. A., Sandeman, H. A., and Archibald, D. A., 1990, Geologic and geochronologic constraints on the metallogenic evolution of the Andes of southeastern Peru: Economic Geology, v. 85, p. 1520–1583.

Cooke, D. R., Hollings, P., Wilkinson, J. J., and Tosdal, R. M., 2014, 13.14 - Geochemistry of Porphyry Deposits, in Holland, H. D. and Turekian, K. K. eds., Treatise on Geochemistry (Second Edition): Oxford, Elsevier, p. 357–381.

Craddock, P. R., and Dauphas, N., 2011, Iron Isotopic Compositions of Geological Reference Materials and Chondrites: Geostandards and Geoanalytical Research, v. 35, p. 101–123.

Craig, J. R., and Vaughan, D. J., 1994, Ore Mineral Textures, in Ore Microscopy and Ore Petrography: Wiley & Sons, p. 120–163.

de Melo, G. H. C., Monteiro, L. V. S., Xavier, R. P., Moreto, C. P. N., Santiago, E. S. B., Dufrane, S. A., Aires, B., and Santos, A. F. F., 2017, Temporal evolution of the giant Salobo IOCG deposit, Carajás Province (Brazil): constraints from paragenesis of hydrothermal alteration and U–Pb geochronology: Mineralium Deposita, v. 52, p. 709–732.

Einaudi, M.T., Hedenquist, J.W., and Inan, E.E., 2003, Sulfidation state of fluids in active and extinct hydrothermal systems: Transitions from porphyry to epithermal environments: Society of Economic Geologists Special Publication 10, p.285–313.

Espinoza, S., Veliz, H., Esquivel, J., Arias, J., and Moraga, A., 1996, The Cupriferous Province of the Coastal Range, Northern Chile, in Camus, F., Sillitoe, R. H., and Petersen, R. eds., Andean Copper Deposits: New discoveries, mineralization, styles and metallogeny: Society of Economic Geologists Special Publication, p. 19–32.

Fonseca, A., 2016, Mina Justa 3D Model Summary Report: SRK Consulting.

Fowler, A., and Stephenson, P. R., 2016, Mina Justa Estimation of Mineral Resource: AMC Mining Consultants Ltd. 716010.

Giggenbach, W. F., 1987, Redox processes governing the chemistry of fumarolic gas discharges from White Island, New Zealand: Applied Geochemistry, v. 2, p. 143–161.

Groves, D. I., Bierlein, F. P., Meinert, L. D., and Hitzman, M. W., 2010, Iron Oxide Copper-Gold (IOCG) Deposits through Earth History: Implications for Origin, Lithospheric Setting, and Distinction from Other Epigenetic Iron Oxide Deposits: Economic Geology, v. 105, p. 641–654.

de Haller, A., Corfu, F., Fontboté, L., Schaltegger, U., Barra, F., Chiaradia, M., Frank, M., and Zúñiga A., J., 2006, Geology, geochronology, and Hf and Pb isotopic data of the Raúl-Condestable iron oxide copper-gold deposit, central coast of Peru: ECONOMIC GEOLOGY, v. 101, p. 281–310.

de Haller, A., and Fontboté, L., 2009, The Raúl-Condestable Iron Oxide Copper-Gold Deposit, Central Coast of Peru: Ore and Related Hydrothermal Alteration, Sulfur Isotopes, and Thermodynamic Constraints: Economic Geology, v. 104, p. 365–384.

Hawkes, N., 2003, Model for the evolution of mineralisation at Mina Justa and the Marcona District: Rio Tinto, 2 p.

Hawkes, N., Clark, A. H., and Moody, T. C., 2002, Marcona and Pampa de Pongo: Giant Mesozoic Fe-(Cu, Au) deposits in the Peruvian Coastal Belt, in Hydrothermal Iron Oxide Copper-Gold & Related Deposits: A Global Perspective: Adelaide, PGC Publishing, p. 115–130.

Haynes, D. W., 2000, Iron Oxide Copper (-Gold) Deposits: Their Position In The Ore Spectrum And Modes of Origin, in Porter, T. M. ed., Hydrothermal Iron Oxide Copper-Gold & Related Deposits: A Global Perspective: Adelaide, PGC Publishing, p. 71–90.

Hemley, J. J., Cygan, G. L., Fein, J. B., Robinson, G. R., and d'Angelo, W. M., 1992, Hydrothermal ore-forming processes in the light of studies in rock-buffered systems; I, Iron-copper-zinc-lead sulfide solubility relations: Economic Geology, v. 87, p. 1–22.

Hitzman, M. W., 2000, Iron Oxide – cu-Au Deposits: What, Where, When, and Why, in Porter, T. M. ed., Hydrothermal Iron Oxide Copper-Gold & Related Deposits: A Global Perspective 1: Adelaide, PGC Publishing, p. 9–25.

Hitzman, M. W., Oreskes, N., and Einaudi, M. T., 1992, Geological characteristics and tectonic setting of proterozoic iron oxide (Cu – U – Au – REE) deposits: Precambrian Research, v. 58, p. 241–287.

Hu, X., Chen, H., Beaudoin, G., and Zhang, Y., 2020, Textural and compositional evolution of iron oxides at Mina Justa (Peru): Implications for mushketovite and formation of IOCG deposits: American Mineralogist, v. 105, p. 397–408.

Huang, F., Zhang, Z., Lundstrom, C. C., and Zhi, X., 2011, Iron and magnesium isotopic compositions of peridotite xenoliths from Eastern China: Geochimica et Cosmochimica Acta, v. 75, p. 3318–3334.

Injoque, J., 2002, Fe oxide – cu-Au deposits in Peru: An integrated view, *in* Porter, T.M., ed., Hydrothermal iron oxide copper-gold and related deposits: A global perspective: Adelaide, Australia, Porter GeoConsultancy Publishing, v. 2, p. 97–113.

Knipping, J. L., Bilenker, L. D., Simon, A. C., Reich, M., Barra, F., Deditius, A. P., Lundstrom, C., Bindeman, I., and Munizaga, R., 2015a, Giant Kiruna-type deposits form by efficient flotation of magmatic magnetite suspensions: Geology, v. 43, p. 591–594.

Knipping, J. L., Bilenker, L. D., Simon, A. C., Reich, M., Barra, F., Deditius, A. P., Wälle, M., Heinrich, C. A., Holtz, F., and Munizaga, R., 2015b, Trace elements in magnetite from massive iron iron oxide – apatite deposits indicate a combined formation by igneous and magmatic-hydrothermal processes: Geochimica et Cosmochimica Acta, v. 171, p. 15–38.

Li, R., Chen, H., Xia, X., Yang, Q., Danyushevsky, L. V., and Lai, C., 2018, Using integrated in-situ sulfide trace element geochemistry and sulfur isotopes to trace ore-forming fluids: Example from the Mina Justa IOCG deposit (southern Perú): Ore Geology Reviews, v. 101, p. 165–179.

Liu, S.-A., Huang, J., Liu, J., Wörner, G., Yang, W., Tang, Y.-J., Chen, Y., Tang, L., Zheng, J., and Li, S., 2015, Copper isotopic composition of the silicate Earth: Earth and Planetary Science Letters, v. 427, p. 95–103.

Loewen, M. W., and Bindeman, I. N., 2016, Oxygen isotope thermometry reveals high magmatic temperatures and short residence times in Yellowstone and other hot-dry rhyolites compared to cold-wet systems: American Mineralogist, v. 101, p. 1222–1227.

Luz, B., and Barkan, E., 2010, Variations of 17O/16O and 18O/16O in meteoric waters:

Geochimica et Cosmochimica Acta, v. 74, p. 6276–6286.

Marschik, R., and Fontboté, L., 2001, The Candelaria – Punta del Cobre Iron Oxide Cu-Au(-Zn-Ag) Deposits, Chile: Economic Geology, v. 96, p. 1799–1826.

Mathur, R., Titley, S., Barra, F., Brantley, S., Wilson, M., Phillips, A., Munizaga, F., Maksaev, V., Vervoort, J., and Hart, G., 2009, Exploration potential of Cu isotope fractionation in porphyry copper deposits: Journal of Geochemical Exploration, v. 102, p. 1–6.

Mathur, R., Ruiz, J., Casselman, M. J., Megaw, P., and van Egmond, R., 2012, Use of Cu isotopes to distinguish primary and secondary Cu mineralization in the Cañariaco Norte porphyry copper deposit, Northern Peru: Mineralium Deposita, v. 47, p. 755–762.

Miller, M. F., Pack, A., Bindeman, I. N., and Greenwood, R. C., 2020, Standardizing the reporting of Δ′17O data from high precision oxygen triple-isotope ratio measurements of silicate rocks and minerals: Chemical Geology, v. 532, p. 119332.

Naslund, H. R., Henriquez, F., Nyström, J. O., Vivallo, W., and Dobbs, F. M., 2002, Magmatic Iron Ires and Associated Mineralisation: Examples from the Chilean High Andes and Coastal Cordillera, in Porter, T. M. ed., Hydrothermal Iron Oxide Copper-Gold & Related Deposits: A Global Perspective 2: Adelaide, PGC Publishing, p. 207–226.

Pack, A., Tanaka, R., Hering, M., Sengupta, S., Peters, S., and Nakamura, E., 2016, The oxygen isotope composition of San Carlos olivine on the VSMOW2-SLAP2 scale: Rapid Communications in Mass Spectrometry, v. 30, p. 1495–1504.

Peters, S. T. M., Alibabaie, N., Pack, A., McKibbin, S. J., Raeisi, D., Nayebi, N., Torab, F., Ireland, T., and Lehmann, B., 2020, Triple oxygen isotope variations in magnetite from iron-oxide deposits, central Iran, record magmatic fluid interaction with evaporite and carbonate host rocks: Geology, v. 48, p. 211–215.

Pollard, P. J., 2006, An intrusion-related origin for Cu–Au mineralization in iron oxide–copper–gold (IOCG) provinces: Mineralium Deposita, v. 41, p. 179–187.

Qi, H., Coplen, T. B., Gehre, M., Vennemann, T. W., Brand, W. A., Geilmann, H., Olack, G., Bindeman, I. N., Palandri, J., Huang, L., and Longstaffe, F. J., 2017, New biotite and muscovite isotopic reference materials, USGS57 and USGS58, for δ2H measurements–A replacement for NBS 30: Chemical Geology, v. 467, p. 89–99.

del Real, I., Thompson, J. F. H., and Carriedo, J., 2018, Lithological and structural controls on the genesis of the Candelaria – Punta del Cobre Iron Oxide Copper Gold district, Northern Chile: Ore Geology Reviews, v. 102, p. 106–153.

del Real, I., Thompson, J. F. H., Simon, A. C., and Reich, M., 2020, Geochemical and Isotopic Signature of Pyrite as a Proxy for Fluid Source and Evolution in the Candelaria – Punta del Cobre Iron Oxide Copper-Gold District, Chile: Economic Geology, v. 115, p. 1493–1518.

Reich, M., Simon, A. C., Deditius, A. P., Barra, F., Chryssoulis, S., Lagas, G., Tardani, D., Knipping, J., Bilenker, L., Sánchez-Alfaro, P., Roberts, M., and Munizaga, R., 2016, Trace Element Signature of Pyrite from the Los Colorados Iron Iron oxide – apatite (IOA) Deposit, Chile: A Missing Link Between Andean IOA and IOCG Systems? Economic Geology, v. 111, p. 743–761.

Richards, J. P., 2015, The oxidation state, and sulfur and Cu contents of arc magmas: implications for metallogeny: Lithos, v. 233, p. 27–45.

Rieger, A. A., and Marschik, R., 2012, The evolution of the hydrothermal IOCG system in the Mantoverde district, northern Chile: new evidence from microthermometry and stable isotope geochemistry: Mineralium Deposita, v. 47, p. 359–369.

Roberts, D. E., and Hudson, G. R. T., 1983, The Olympic Dam copper-uranium-gold deposit, Roxby Downs, South Australia: Economic Geology, v. 78, p. 799–822.

Rodriguez-Mustafa, M. A., Simon, A. C., Real, I. del, Thompson, J. F. H., Bilenker, L. D., Barra, F., Bindeman, I., and Cadwell, D., 2020, A Continuum from Iron Oxide Copper-Gold to Iron Iron oxide – apatite Deposits: Evidence from Fe and O Stable Isotopes and Trace Element Chemistry of Magnetite: Economic Geology, v. 115, p. 1443–1459.

Rojas, P. A., Barra, F., Deditius, A., Reich, M., Simon, A., Roberts, M., and Rojo, M., 2018, New contributions to the understanding of Kiruna-type iron iron oxide – apatite deposits revealed by magnetite ore and gangue mineral geochemistry at the El Romeral deposit, Chile: Ore Geology Reviews, v. 93, p. 413–435.

Salazar, E., Barra, F., Reich, M., Simon, A., Leisen, M., Palma, G., Romero, R., and Rojo, M., 2019, Trace element geochemistry of magnetite from the Cerro Negro Norte iron oxide–apatite deposit, northern Chile: Mineralium Deposita.

Sharp, Z. D., Wostbrock, J. A. G., and Pack, A., 2018, Mass-dependent triple oxygen isotope variations in terrestrial materials: Geochemical Perspectives Letters, v. 7, p. 27–31.

Sillitoe, R. H., 2002, Implications of Sulphide Zoning Pattern, Mina Justa Copper Prospect, Marcona Project, Southern Peru: Rio Tinto, 9 p.

Sillitoe, R. H., 2003, Iron oxide – copper – gold deposits: an Andean view: Mineralium Deposita, v. 38, p. 787–812.

Simon, A., Knipping, J., Reich, M., Barra, F., Deditius, A., Bilenker, L., and Childress, T., 2018, A holistic model that combines igneous and magmatic-hydrothermal processes to explain Kiruna-type iron oxide - apatite deposits and iron oxide - copper - gold deposits as products of a single evolving ore system: Society of Economic Geologists Special Publication, v. 21, p. 89–114.

Sugaki, A., Shima, H., Kitakaze, A., and Harada, H., 1975, Isothermal phase relations in the system Cu-Fe-S under hydrothermal conditions at 350 degrees C and 300 degrees C: Economic Geology, v. 70, p. 806–823.

Taylor, H. P., 1968, The oxygen isotope geochemistry of igneous rocks: Contributions to Mineralogy and Petrology, v. 19, p. 1–71.

Troll, V. R., Weis, F. A., Jonsson, E., Andersson, U. B., Majidi, S. A., Högdahl, K., Harris, C., Millet, M.-A., Chinnasamy, S. S., Kooijman, E., and Nilsson, K. P., 2019, Global Fe–O isotope correlation reveals magmatic origin of Kiruna-type apatite-iron-oxide ores: Nature Communications, v. 10, p. 1712.

Vidal, C. E., Injoque-Espinoza, J., Sidder, G. B., and Mukasa, S. B., 1990, Amphibolitic Cu-Fe skarn deposits in the central coast of Peru: Economic Geology, v. 85, p. 1447–1461.

Wasteneys, H. A., Clark, A. H., Farrar, E., and Langridge, R. J., 1995, Grenvillian granulite-facies metamorphism in the Arequipa Massif, Peru: a Laurentia-Gondwana link: Earth and Planetary Science Letters, v. 132, p. 63–73.

Yund, R. A., and Kullerud, G., 1966, Thermal Stability of Assemblages in the Cu—Fe—S System: Journal of Petrology, v. 7, p. 454–488.

Zakharov, D. O., Bindeman, I. N., Tanaka, R., Friðleifsson, G. Ó., Reed, M. H., and Hampton, R. L., 2019, Triple oxygen isotope systematics as a tracer of fluids in the crust: A study from modern geothermal systems of Iceland: Chemical Geology, v. 530, p. 119312.

Chapter 4 : New Re–Os, Ar–Ar, and U–Pb Geochronology from the Mina Justa and Marcona Deposits Reveal Mid-Jurassic IOCG Mineralization in Peru

Co-authors: Maria A. Rodriguez-Mustafa, Adam C. Simon, Robert Holder, Holly Stein, Andrew Kylander-Clark, Daniel Blakemore, Brian Jicha, Edson L.B Machado

4.1 Abstract

Iron oxide – copper – gold (IOCG) and iron oxide – apatite (IOA) deposits are major sources of Cu and Fe, respectively. They contain abundant Fe-oxides and may contain Au, Ag, Co, rare earth elements (REE), U, Ni, and V as economically important byproducts. In Peru, the Mina Justa IOCG deposit is located next to the giant Marcona IOA deposit. Constraining the timing of Fe and Cu mineralization at Mina Justa is fundamental to understanding the duration and type of processes that generated this mineral deposit, and ultimately to test the genetic link with other deposits in the area. Previous authors used alteration minerals to indirectly date Cu mineralization at Mina Justa at around 100 Ma. We report Ar–Ar dates of actinolite, U–Pb dates of magnetite, apatite, and titanite grains collected by *in-situ* laser-ablation multi-collector inductively coupled plasma mass spectrometry, and Re–Os thermal ionization dates of sulfides. These results indicate that Cu mineralization at Mina Justa occurred at about 160 Ma and that Fe mineralization is older and coeval with the neighboring Marcona IOA deposit, consistent with Cu mineralization overprinting IOA-style mineralization at Mina Justa.

4.2 Introduction

Iron oxide – copper – gold (IOCG) and iron oxide – apatite (IOA) mineral deposits are distributed worldwide, from the Archean to the Pliocene. These deposits are enriched in Fe and Cu, and can contain economically important amounts of Au, Ag, Co, U, V, and rare earth elements (REE). They contain abundant magnetite and/or hematite, are structurally and/or stratigraphically controlled, and present extensive Na-Ca alteration (dominated by albite and

actinolite) (Hitzman et al., 1992; Hitzman, 2000; Williams et al., 2005; Groves et al., 2010; Barton, 2014; Corriveau et al., 2016).

The Mesozoic IOA-IOCG province in the Andes is the youngest province of this kind of deposits, providing an opportunity to understand their temporal evolution without the superposition of several metamorphic and/or deformation episodes as is common in Archean and Proterozoic provinces. Based on their spatial relationship in Chile, it has been suggested that IOA and IOCG deposits are genetically related (Espinoza et al., 1996; Naslund et al., 2002; Sillitoe, 2003; Knipping et al., 2015; Reich et al., 2016; Barra et al., 2017; Simon et al., 2018; Rodriguez-Mustafa et al., 2020). In Peru, several IOA and IOCG occurrences including economically important deposits such as Marcona and Mina Justa show a similar spatial distribution to the deposits found in Chile (Clark et al., 1990; Vidal et al., 1990; Hawkes et al., 2002; de Haller et al., 2006; Chen et al., 2010), but no genetic link between these IOA and IOCG deposits has been established yet.

In this study, we present the first geochronological data of ore minerals at Mina Justa and Marcona, including pioneering U–Pb dating of magnetite, that constrain the timing and duration of mineralization in the district, and provide new insights into its regional geologic setting and into the link between IOA and IOCG deposits.

4.3 Geologic Background

The Mina Justa IOCG deposit is located in central-coastal Peru, about 5 km NW from the Marcona IOA deposit described by Chen et al. (2010) (Figure 4-1). The Marcona Formation is at least Silurian in age and hosts most of the Fe mineralization at the Marcona IOA deposit (Hawkes et al., 2002; Injoque-Espinoza, 2002; Chen et al., 2010), although some of it is also hosted in the overlaying ~4000m thick Río Grande formation. The Marcona and Río Grande formations are separated by a disconformity over which the basal conglomerate of the Río Grande formation sits. This formation dips 40° to 60° to the NW and consists mainly of intercalations of porphyritic andesites, andesitic volcaniclastic rocks, fossiliferous limestones, arkoses, and mudstones (Caldas Vidal, 1978; Palacios Moncayo et al., 1995; Chen et al., 2010). The age of the Río Grande formation has been proposed to be Middle Jurassic based on an unreliable 164 ± 4 Ma K-Ar whole rock date of an altered andesitic flow near the top of the unit

(Aguirre and Offler, 1985; Aguirre, 1988) and a few indicator fossils in the lower part that have been assigned an Aalenian-Callovian range (Cox, 1956; Rüegg, 1957; Caldas Vidal, 1978; Romero et al., 1995). However, the base of the unit has not been dated.

The Mina Justa deposit has a combined measured, indicated, and inferred oxide resource of 219 Mt at 0.51% Cu and sulfide resource of 213 Mt at 1.00% Cu, 8.0 g/t Ag and 0.06 g/t Au (Fowler and Stephenson, 2016). The orebody consists of disseminated to locally massive magnetite, chalcopyrite, bornite, chalcocite, and pyrite accompanied by actinolite (± apatite, titanite, K-feldspar). Parts of the ore body referred as mantos extend outward probably replacing limestone-rich horizons but most of the deposit consists of pervasive alteration and mineralization that obscures original rock textures and is known locally as the hydrothermal unit. A porphyry with minor chloritization and albitization intrudes the Río Grande Formation in the pit and its relative timing with respect to mineralization is unclear. Several NE-trending, porphyritic andesitic dykes with glomerophyric plagioclase crystals from the Tunga Andesite unit cut the Río Grande Formation, the porphyritic rock, and the mineralization (Hawkes et al., 2002; Chen et al., 2010) (Supplementary cross-sections in Appendix C).

The paragenetic sequence at Marcona and Mina Justa system proposed by Chen et al. (2010) and modified by Hu et al., (2020) was constructed based on Ar–Ar dates from alteration minerals (cummingtonite, phlogopite, biotite, microcline, actinolite, and tremolite) and consists of:

1. Early Mg-silicate alteration at Marcona (cum 177.0 ± 1.5 Ma, 175.2 ± 2.3)
2. Magnetite – sulfides – actinolite±ap±cal±qz stage (bi 161.4 ± 0.9, phl 159.7 ± 0.8) interpreted as the main manto magnetite mineralization event at Marcona
3. Sulfide – actinolite – tremolite stage at Marcona (trm 158.5± 1.9, 157.3 ±3.2, 156.8 ±2.9, 156.2 ± 2.4, act 156.6 ± 4.2) contemporaneous with an early actinolite stage at Mina Justa (act 157.3 ±3.5, 154.3 ± 5.5)
4. Manto magnetite and K-feldspar alteration cross-cut by actinolite – apatite ± magnetite breccia (act 110.9 ± 0.7)
5. Magnetite – actinolite – K feldspar – albite ± apatite stage followed by magnetite + pyrite ± titanite ± quartz ± chlorite veins and aggregates (mc 103.7 ± 0.6 Ma, 101.5 ± 0.7 Ma) in the hydrothermal unit

6. Chalcopyrite replacement of pyrite and massive Ag-rich bornite – chalcocite mineralization (microcline envelopes 99.1 ± 0.9 Ma and 95.0 ± 0.6 Ma) in the hydrothermal unit at Mina Justa
7. Minor, later sphalerite – galena, calcite – quartz, and hematite veins

Chen et al. (2010) interpreted their data to indicate that the main Fe mineralization stage at Marcona occurred between 162 and 159 Ma and that Cu mineralization at Mina Justa occurred between 99 and 95 Ma. However, none of their results dates mineralization directly (Skirrow, 2022). In this study, we date for the first-time ore minerals from both deposits to test the absolute time relationship between the Fe mineralization at Marcona and Mina Justa as well as with the Cu mineralization at Mina Justa.

4.4 Methods

We selected 15 core samples from 7 drill holes and 3 samples from the Mina Justa pit, and 1 core sample from Marcona (Figure 4-1, Figure A-6 to Figure A-13; Table A-8). We characterized the samples at the University of Michigan by energy dispersive X-ray spectrometry (EDS) and back-scattered electron (BSE) imaging using a JEOL JSM-7800F field emission scanning electron microscope (SEM).

We collected in-situ U–Pb data from magnetite, apatite, and titanite grains in thin sections by using a Cetac/Teledyne Photon Machines 193 nm excimer Analyte laser with a HelExII cell connected to a Nu Instruments Plasma HR-ES MC-ICP-MS at the University of California, Santa Barbara following the procedure of Kylander-Clark et al. (2013). The spot size for magnetite was 65 micrometers and we varied between 5 (60 shots) and 10 Hz (120 shots), depending on Pb content. We used a 35-micrometer spot for apatite and titanite with 5 Hz and 60 total shots. Fluence was approximately 1 J/cm^2.The U–Pb data of titanite from the porphyry unit were collected using a ESI NWR193 excimer laser connected to an Agilent 7900s ICP-MS at the University of Michigan. All data were collected using sample-reference bracketing and processed using the commercially available software Iolite. Isotope ratios of individual analyses are reported as means with 2se uncertainties and calculated dates are the lower intercepts ± 2se of discordia in Tera-Wasserburg concordia diagrams. Individual measurements were not corrected for common Pb. Titanite measurements at the University of California, Santa Barbara

used the reference materials 91500 (Wiedenbeck et al., 1995), FC (Schmitz and Bowring, 2001), P5701G (Kylander-Clark et al., 2008), MKED1 (Spandler et al., 2016), and BLR (Aleinikoff et al., 2007). The latter two were used at the University of Michigan. Apatite measurements used the reference materials MAD (Thomson et al., 2012), 91500 (Wiedenbeck et al., 1995), McLure (Krestianinov et al., 2021), Durango (Paul et al., 2021), and Brazil (Apen et al., 2022). No matrix-matched U–Pb reference material is available for magnetite U–Pb dating; thus, magnetite dates were calculated by using the Mud Tank zircon standard (Black and Gulson, 1978) and a NIST614 glass as the secondary reference material. Trace elements from each spot analyzed were used to screen for mineral inclusions and contaminated points were excluded from the date calculations.

Actinolite grains were separated and incremental heating $^{40}Ar/^{39}Ar$ geochronology was performed at The University of Wisconsin using a Nu Instruments Noblesse mass spectrometer following the routine described in Jicha et al. (2016). All the $^{40}Ar/^{39}Ar$ ages are calculated using the decay constants of Min et al. (2000), and the plateau and isochron ages are reported with 2σ analytical uncertainty, which includes the J uncertainty. All data were reduced and plotted using the Pychron software (Ross, 2019).

Sulfides from high-grade ore samples were separated and Re–Os dated using a Carius tube digestion and simultaneous equilibration with a mixed Re-double Os spike. Re and Os were chemically isolated for each sample, and isotopic ratios were measured using negative thermal ionization mass spectrometry (NTIMS) on two Triton instruments held by the AIRIE Program at Colorado State University. The ages reported are inclusive of the decay constant uncertainty for lambda (λ) 187Re. Additional method details are reported in Appendix C.

4.5 Results

4.5.1 Mineral textures

Magnetite from Mina Justa is present as massive, fine-grained aggregates, disseminated in a matrix, or as veins (Figure 4-2a, b) while magnetite from Marcona is present as massive aggregates (Figure 4-2c). Magnetite crystals from both deposits commonly exhibit triple junctions (Figure 4-2c). Actinolite occurs as coarse, massive crystals intergrown with magnetite, apatite, and pyrite (Figure 4-2a, b). Apatite grains from Marcona are mostly interstitial to

magnetite grains (Figure 4-2) and apatite grains from both deposits are usually irregular and present porous and inclusion-rich rims and inclusion-free cores in BSE images (Figure 4-2d). Most titanite grains associated with mineralization at Mina Justa are subhedral to anhedral, sometimes present rounded borders, have irregular, patchy internal zonation in BSE, and occur either filling interstices or disseminated. The titanite grains from the porphyry unit show a strong zonation in BSE (Figure 4-2e, f). Sulfides at mina Justa occur as massive aggregates with calcite (Figure 4-2g) or as blades with magnetite (Figure 4-2h).

4.5.2 Geochronology

Table 4-1 and Figure 4-3 provide the compilation of all calculated dates and Table A-9 to Table A-11 present the data for each spot analyzed. Porphyry refers to the porphyritic rock found in the Mina Justa pit. Several individual samples record statistically distinguishable dates among the different studied minerals (Figure 4-4). For example, magnetite from sample NN50 yields a date of 198 ± 8 Ma whereas apatite from a vein in the same sample yields a date of 165 ±11 Ma (Figure 4-2a). Titanite that is interstitial to magnetite in the same sample yields a date of 159 ± 6 Ma. Similarly, magnetite from Marcona (sample EX17) yields a date of 201.2 ± 12.4 Ma whereas interstitial apatite in the same sample yields a date of 166.9 ± 8.5 Ma.

None of our data yield dates younger than 150 Ma. Sulfides, one actinolite, and many titanite dates (including the one from the porphyry unit) align around 160 Ma (Table 4-1, Table 4-2); the full range of titanite dates is c. 165–155 Ma. Two other actinolite dates are slightly older, 164.2 and 168.7 Ma (Table 4-1, Table 4-3). Apatites range from c. 200 – 150 Ma, but with larger uncertainties. The date from the Marcona apatite is c. 167 Ma and the average of the apatite dates from Mina Justa is 170 Ma, consistent with the oldest actinolite date and distinctly older than the sulfides or titanite dates. The date from the Marcona magnetite is c. 200 Ma. Magnetite dates from Mina Justa range from 215–155 Ma, similar to the apatite dates, and have an average of 190 Ma. They have relatively large uncertainties but are overall older than the titanite and the sulfides (Figure 4-3). Representative Tera-Wasserburg diagrams are presented in Figure A-14 in Appendix C.

4.6 Discussion

4.6.1 Timing of Cu mineralization

The Re–Os dates from the bornite – chalcocite and the pyrite – chalcopyrite samples at Mina Justa overlap within their uncertainties, indicating that Cu mineralization occurred at c. 160 Ma. The range from the Re–Os dates (161.3 – 156.8 Ma) falls within the range of dates obtained from the titanite from the Mina Justa ore bodies (c. 165 – 155 Ma) (Figure 4-3). Titanite from Mina Justa presents irregular chemical zoning (Figure 4-2f), which can be caused by hydrothermal alteration (Xiao et al., 2020). Even though the closure temperature of titanite is over 800 °C (Holder and Hacker, 2019), it has been demonstrated that it can precipitate from or be altered by hydrothermal fluids at lower temperatures (Holder and Hacker, 2019; Moser et al., 2022). Therefore, we interpret several of our U–Pb titanite dates to also record the hydrothermal event responsible for Cu mineralization at c. 160 Ma. As the titanite from the porphyritic unit also presents textural evidence of fluid alteration, its U–Pb date (162.9 ± 0.5 Ma) indicates the timing of hydrothermal alteration instead of the timing of igneous crystallization. This age is still slightly older than the range of the Re–Os dates but overlaps with the range from titanite from the ore bodies, indicating that the igneous activity associated with the porphyritic rock was pre or syn Cu mineralization.

Our youngest Ar–Ar date of actinolite at Mina Justa overlaps with our sulfide dates and most of our titanite data from Mina Justa. It also overlaps with the Ar–Ar dates of biotite, phlogopite, tremolite, and actinolite from Marcona and Mina Justa from Chen et al. (2010) (Figure 4-3) at c. 160 Ma, which they interpreted as the age of the main magnetite – sulfide mineralization stage at Marcona and an early actinolite stage at Mina Justa. This suggests that sulfide mineralization at Marcona and at Mina Justa was coeval.

Chen et al. (2010) also obtained Ar–Ar data of microcline from samples from the same pits from where the phlogopite and tremolite from Marcona where obtained. They interpreted those microcline dates of 105 and 112 Ma from the main magnetite – sulfide stage at Marcona to be reset ages. However, they interpreted their Ar–Ar microcline dates of 99.1 and 95 Ma on alteration envelopes at Mina Justa as the age of Cu mineralization. Our new Re–Os dates demonstrate that Cu mineralization at Mina Justa occurred at c. 160 Ma, coeval with the main magnetite – sulfide stage at Marcona. Therefore, we interpret the younger Mina Justa microcline

Ar–Ar dates reported by Chen et al. (2010) to also be reset ages (as their microcline from Marcona) that record younger hydrothermal activity, unrelated to the main Cu mineralization event in the district, and possibly associated with the emplacement of the Coastal Batholith in Peru (Shatwell, 2021).

4.6.2 Older hydrothermal episodes

The apatite and magnetite dates have lower precision than the titanite and the actinolite dates probably due to their very low U and Pb contents, but have an adequate spread in the discordia diagrams, yielding robust dates (Figure A-14). Magnetite and apatite dates also span a wider time range, from c. 200 to c. 160 Ma. This can be explained by the presence of multiple generations of these minerals in the deposits as supported by textural and cross-cutting relationships such as the apatite – actinolite vein (165 ±11 Ma) that cross-cuts the magnetite – actinolite matrix (198 ± 8 Ma) in sample NN50 (Figure 4-2).

Episodic hydrothermal activity where Fe-rich episodes precede Cu mineralization has been recorded at the giant Candelaria IOCG deposit in Chile (Del Real et al., 2021). At Mina Justa, our two older actinolite dates (164.2 ± 2.8 and 168.7 ± 3.4 Ma) do not show signs of Ar loss (Figure A-15 and Figure A-17 in Appendix C) and are consistent with hydrothermal activity that preceded the main Cu mineralization. When coupling those actinolite dates with the mode of apatite dates from Mina Justa and with the apatite date from Marcona, at least one hydrothermal actinolite – apatite (± magnetite) event at c. 170 Ma can be recognized, but additional events are also possible within the range of apatite data.

Some apatites from Mina Justa show clear fluid-mediated dissolution-reprecipitation textures and zonation in BSE, indicating that they have been altered and probably partially reset due to enhanced Pb loss (Figure 4-2d) (Corfu and Stone, 1998; Ruiz-Agudo et al., 2014; Zeng et al., 2016). We calculated the dates of altered vs. unaltered domains in two samples (Figure A-14). Sample Chen03 unaltered vs altered zones yielded dates of 162 ± 16 and 151 ± 12 Ma respectively. Sample NN16 unaltered apatite zones yielded 171 ± 15 Ma and altered apatite zones yielded 164 ± 14 Ma. Even though the average dates for the unaltered zones are older than the dates from the altered zones, the dates from altered vs unaltered domains from each sample overlap considerably within uncertainty. Thus, we cannot discern the timing of alteration from the timing of formation of a particular mineral in individual samples and can only say that the

average date of some of the samples may be indicating mixed ages between unaltered and altered apatite domains as a function of the degree of resetting caused by fluid alteration, a process that has been also documented in shear zones (Odlum and Stockli, 2020; Odlum et al., 2022). However, when the textural context is clear, we can interpret the timing of alteration, as with the apatite from Marcona (166.9 ± 8.5 Ma), which is interstitial to magnetite (201.2 ± 12.4 Ma) (Figure 4-2c), thus indicating that it would have been altered or precipitated later than magnetite.

Nevertheless, partial to total reset does not explain samples that do not overlap within uncertainty. For example, apatite from Mina Justa sample NN02 (195.9 ± 15.4 Ma) does not overlap with the range from three (younger) Mina Justa samples nor with the apatite from Marcona (166.9 ± 8.5 Ma), evidencing hydrothermal activity happening at least at c. 180 Ma (Figure 4-3). Similarly, magnetite from sample NN02 (205.1 ± 3.7 Ma) does not overlap with the range of three other Mina Justa magnetite samples. As the alteration process enhances Pb over U loss, even if the samples that yield statistically older dates were partially altered, their younger end would still be older than the oldest end of other samples, consistent with a magnetite – apatite episode older than 180 Ma.

4.6.3 Significance of magnetite dates

Despite that *in-situ* LA-ICP-MS U–Pb magnetite geochronology should be considered exploratory as accessible standards are still in development, a geologically meaningful age was obtained via that method for magnetite from the Olympic Dam IOCG deposit, Australia using in-house, synthetic standards (Courtney-Davies et al., 2020). Magnetite has also been dated using the (U–Th)/He method and authors have stressed the need to evaluate the potential contribution of the isotopes of interest from mineral inclusions (Blackburn et al., 2007; Cooperdock and Stockli, 2016; Cooperdock et al., 2020). Previous geochemical characterization of magnetite from Mina Justa (Hu et al., 2020; Rodriguez-Mustafa et al., 2022) combined with the characterization done in this study did not reveal U-rich mineral inclusions in the analyzed magnetite grains. Additionally, all the spots were screened for Ti, Ca, P, and Zr to avoid intervals that had intersected titanite, apatite and zircon inclusions not observable on the polished grain surfaces. Thus, all the U and Pb concentrations measured in our samples and used to calculate the magnetite dates are interpreted to have been structurally bounded in the magnetite.

Even though no experimental data are available on Pb diffusion in magnetite, its closure temperature has been estimated to be around 500 °C for grains with an 80-micron radius (Frei et al., 1999; Gelcich et al., 2005). Rodriguez-Mustafa et al. (2022) estimated that magnetite at Mina Justa formed from a hydrothermal fluid cooling from around 700 °C to around 400 °C and that the fluid from which Cu sulfides precipitated was 500 °C at most. Then, it is probable that some of the magnetite in the deposit was thermally reset and that some of the magnetite dates indicate the timing of alteration rather than of crystallization. It is also possible that dissolution-reprecipitation processes could have preferentially leached U from magnetite yielding apparent older ages. However, there is no evidence for such a fluid (above the magnetite-hematite buffer) that could have mobilized U in solution. Thus, similarly to the distribution of apatite and actinolite ages, we support the presence of multiple magnetite generations at Mina Justa as proposed by Rodriguez-Mustafa et al. (2022).

All our magnetite, all but one apatite sample, and two of our actinolite dates are older than 160 Ma. Additionally, the apatite and magnetite dates from Marcona are within the ranges of apatite and magnetite dates from Mina Justa. This is consistent with a hypothesis in which Cu mineralization is younger than Fe mineralization and Fe mineralization at Marcona occurred within the same timeframe as Fe mineralization at Mina Justa.

4.6.4 Implications for the evolution of the Andean margin and the geologic setting of IOA and IOCG deposits

Our new geochronological data suggest that Fe mineralization (±apatite±actinolite) at Marcona and Mina Justa is older than c. 160 Ma. Our magnetite and apatite data from mineralization at Marcona and Mina Justa also record dates older than 180 Ma (extending through c. 200 Ma). Therefore, the Río Grande formation, which hosts mineralization at Mina Justa and some mineralization at Marcona, should be older than its current accepted age. The age range of the Río Grande formation is problematic as it is in part constrained by a whole rock K–Ar date of an altered andesitic lava flow near the top of the unit (Aguirre and Offler, 1985; Aguirre, 1988). The andesites dated by Aguirre (1988) range between 164 ± 4 and 95 ± 3 Ma. As the K–Ar system has a very low closure temperature, it is very probable that andesite dates represent reset ages rather than a crystallization age.

The other age constraints of the Río Grande formation consist of marine fossils that indicate an Aalenian-Callovian age (175 – 162 Ma according to the current chronostratigraphic chart). In the ~4000m thick Río Grande formation, the first limestone horizons appear intercalated with lava flows halfway through the volcano-sedimentary sequence, above hundreds of meters of basal conglomerate rocks (Caldas Vidal, 1978). Therefore, it is possible for the sedimentation of the sequence to have started long before the Aelenian fauna was swimming in the Jurassic basin. Given that the base of the Río Grande formation has not been dated and that there is a disconformity between it and the underlying Marcona formation (which is at least Ordovician) (Caldas Vidal, 1978), our new geochronological data indicates that the volcano-sedimentary sequence that composes the Río Grande Formation could have started to be deposited as far back as c. 200 Ma.

An extensional regime within the subduction setting is thought to have dominated this part of the Andean margin until the Middle Jurassic, when oblique subduction generated the volcanic rocks from the Río Grande formation in a back-arc or pull-apart basin (Jaillard et al., 1990; Romeuf et al., 1995; Sempere et al., 2002; Mohammadzaheri et al., 2021). Our data suggest that the onset of such subduction would have happened in the Lower Jurassic instead, as the breakup of Gondwana began (Blakey, 2008; Scotese, 2021). Our data also suggest that Cu mineralization overprinted IOA-style mineralization at around 160 Ma within an extensional (possibly transtensional) setting (Richards et al., 2017), and not at around 100 Ma associated with the inversion of the basin as previously suggested by Chen et al. (2010). This suggests that even though IOA and IOCG mineralization in the Andes can be associated in space, laterally or vertically (Espinoza et al., 1996; Sillitoe, 2003; Barra et al., 2017; Rodriguez-Mustafa et al., 2020), Cu mineralization can occur significantly later than Fe mineralization (Skirrow, 2022), though using the same fluid pathways.

4.7 Conclusion

The mineralization and alteration history of the Marcona-Mina Justa IOA-IOCG district in Peru was investigated by detailed geochronological studies. We made emphasis on dating the ore minerals and highlighted the potential for magnetite to be used as a geochronometer. The results of our study indicate that this is a long-lived system with evidence of multiple

hydrothermal events spanning at least 10 Ma, from c. 170 to c. 160 Ma, and possibly extending back to 180 Ma. Copper mineralization at Mina Justa occurred at c. 160 Ma while Fe mineralization at Mina Justa and Marcona were coeval and older, verifying the hypothesis of overprinting IOCG style mineralization over IOA style mineralization at Mina Justa proposed by Rodriguez-Mustafa et al., (2022). We also suggest that other IOA-IOCG provinces might record extensive alteration-mineralization histories that have remained unveiled due to biased sampling that restricts our understanding of these long-lived systems.

Exploration efforts for IOCG deposits in coastal-central Peru should focus on the extensional setting of the sequence at around 160 Ma rather than on the compressional events related to the inversion of the basin at around 95 Ma. This conceptual shift will allow for the generation of new targets, accelerating the discovery of critical resources.

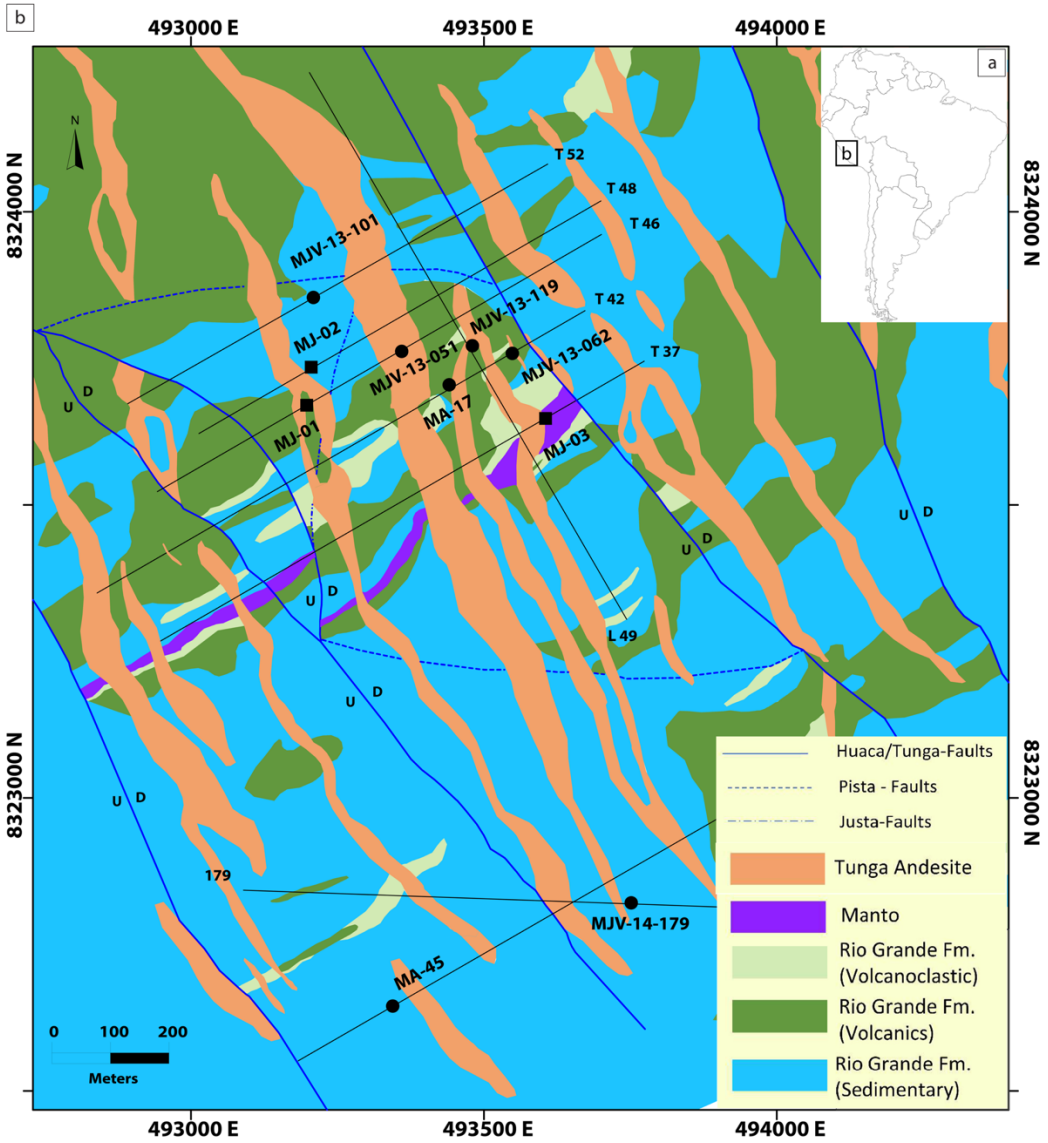

Figure 4-1: a (inset): Map of South America with the area of interest marked by the black rectangle and shown in b. b: Geological map of Mina Justa showing the location of the samples (circles for drill holes and squares for main pit samples) and the cross-sections associated with them. Coordinate system: WGS84, UTM Zone 18L. Map provided by Marcobre.

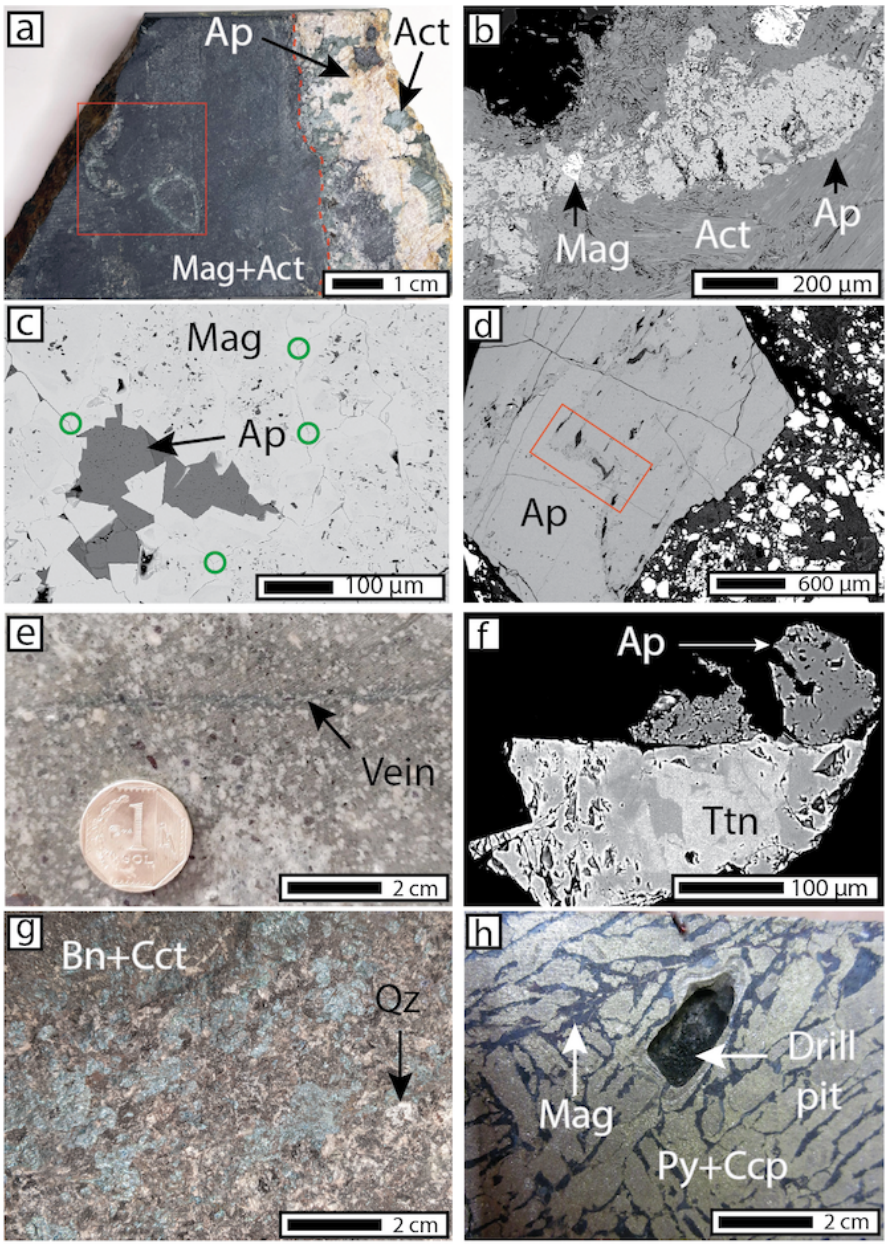

Figure 4-2: Photographs of hand samples (a, e, g, h) and BSE images (b, c, d, f) from Marcona and Mina Justa. a. Mina Justa sample NN50: massive, fine-grained magnetite – actinolite manto sample with fossil remains replaced by actinolite (red square) and a later apatite – actinolite vein. b. Mina Justa sample NN58 from the hydrothermal unit showing detail of coexisting actinolite, magnetite, and apatite. c. Sample EX17 from Marcona showing massive magnetite aggregates with triple junctions (green squares) and interstitial apatite. d. Mina Justa sample NN16 showing a grain of apatite with altered, darker areas and deformed pores/inclusions (some in the red rectangle). The bright, smaller minerals are magnetite grains. e. Mina Justa sample MJ03 (porphyry unit) showing weak chlorite – albite alteration and a thin sulfide-barren veinlet. f. BSE image of representative titanite dated from the porphyry unit. Note metasomatic reaction textures. g. Mina Justa sample MJ02 from the hydrothermal unit showing massive bornite – chalcocite mineralization with interstitial quartz. h. Mina Justa sample MJ01 from the hydrothermal showing bladed pyrite replaced by chalcopyrite and location where the sample was drilled to obtain the material for Re–Os geochronology. Ap: apatite, Act: actinolite, Bn: bornite, Cct: chalcocite, Ccp: chalcopyrite, Mag: magnetite, Py: pyrite, Qz: quartz, Ttn: titanite.

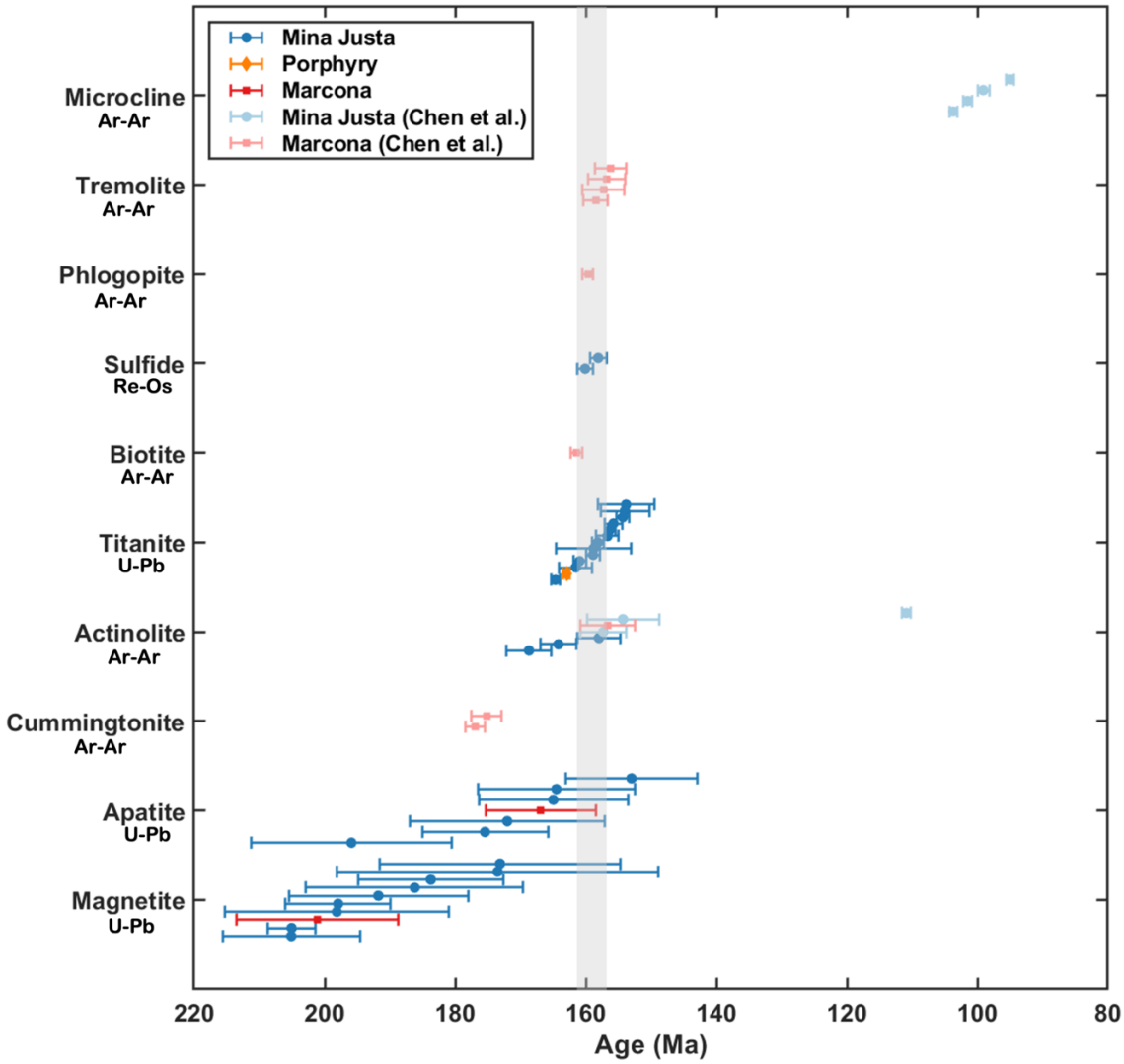

Figure 4-3: Summary of geochronology results from the Mina Justa and Marcona deposits grouped by mineral phase. Samples from this study are shown in bold colors while samples from Chen et al., (2010) are shown in faded colors. No sample from our study yielded an average date younger than 150 Ma. Copper mineralization occurred at c. 160 Ma (gray bar), as dated directly in the sulfides. The uncertainty for each datum is two times the standard error.

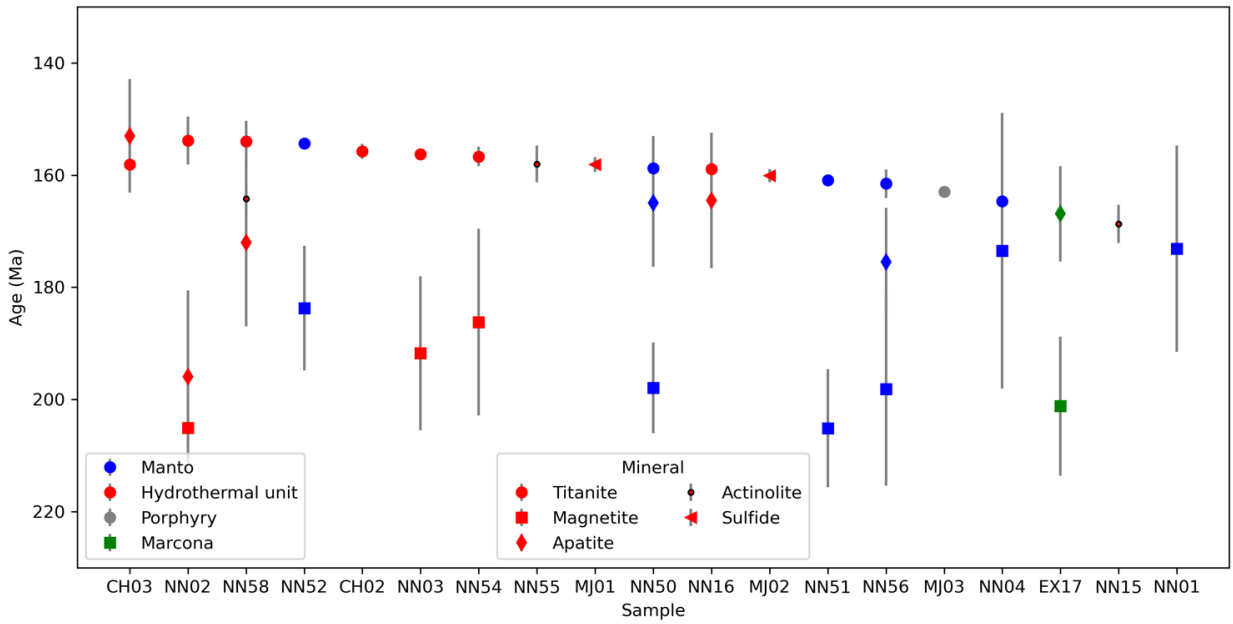

Figure 4-4: Summary of dates by sample. Note how different minerals within a sample yield distinct dates.

Table 4-1: Summary of U–Pb dates of titanite, apatite, and magnetite from Marcona and Mina Justa

Source	Sample	Hole/Pit	Deposit	Phase	Age (Ma)	2se	n	MSWD
This work	EX17	13-562	Marcona	Apatite	166.89	8.48	29	2
This work	EX17	13-562	Marcona	Magnetite	201.16	12.4	27	1.2
This work	CH02	MA45	Mina Justa	Titanite	155.76	1.34	20	2.3
This work	CH03	MA17	Mina Justa	Apatite	153	10.1	30	1
This work	CH03	MA17	Mina Justa	Titanite	158.12	0.84	31	3
This work	MJ01	Main Pit	Mina Justa	Sulfide	158.1	1.3		
This work	MJ02	Main Pit	Mina Justa	Sulfide	160.1	1.2		
This work	MJ03	Main Pit	Mina Justa	Titanite	162.94	0.54	70	5.4
This work	NN01	MJV-13-051	Mina Justa	Magnetite	173.13	18.4	16	1.2
This work	NN02	MJV-13-051	Mina Justa	Apatite	195.9	15.36	26	1.4
This work	NN02	MJV-13-051	Mina Justa	Magnetite	205.07	3.7	8	1.1
This work	NN02	MJV-13-051	Mina Justa	Titanite	153.82	4.28	9	1
This work	NN03	MJV-13-051	Mina Justa	Magnetite	191.77	13.74	21	2.8
This work	NN03	MJV-13-051	Mina Justa	Titanite	156.29	0.8	41	1.8
This work	NN04	MJV-13-101	Mina Justa	Magnetite	173.5	24.6	14	1.5

This work	NN04	MJV-13-101	Mina Justa	Titanite	164.64	0.62	69	1.9
This work	NN15	MJV-14-179	Mina Justa	Actinolite	168.7	3.4	12	0.7
This work	NN16	MJV-14-179	Mina Justa	Apatite	164.51	12.04	29	0.92
This work	NN16	MJV-14-179	Mina Justa	Titanite	158.89	1.04	29	0.82
This work	NN50	MJV-13-062	Mina Justa	Apatite	164.98	11.4	32	1.5
This work	NN50	MJV-13-062	Mina Justa	Magnetite	197.94	8.08	29	3.9
This work	NN50	MJV-13-062	Mina Justa	Titanite	158.8	5.74	5	3.7
This work	NN51	MJV-13-062	Mina Justa	Magnetite	205.12	10.5	29	2.4
This work	NN51	MJV-13-062	Mina Justa	Titanite	160.93	1	29	4.1
This work	NN52	MJV-13-062	Mina Justa	Magnetite	183.74	11.1	29	2.3
This work	NN52	MJV-13-062	Mina Justa	Titanite	154.34	1	39	1.4
This work	NN54	MJV-13-062	Mina Justa	Magnetite	186.2	16.64	30	1
This work	NN54	MJV-13-062	Mina Justa	Titanite	156.68	1.72	12	1.4
This work	NN55	MJV-13-119	Mina Justa	Actinolite	158	3.3	12	0.6
This work	NN56	MJV-13-119	Mina Justa	Apatite	175.44	9.62	30	1.6
This work	NN56	MJV-13-119	Mina Justa	Magnetite	198.15	17.2	20	1
This work	NN56	MJV-13-119	Mina Justa	Titanite	161.52	2.54	11	1.8
This work	NN58	MJV-13-119	Mina Justa	Actinolite	164.2	2.8	11	0.77
This work	NN58	MJV-13-119	Mina Justa	Apatite	172.03	14.92	23	1.2
This work	NN58	MJV-13-119	Mina Justa	Titanite	154.01	3.72	7	0.62
Chen et al. (2010)	DDM3-3-8	M3-3	Marcona	Tremolite	158.5	1.9		
Chen et al. (2010)	DDM5-4-2	M5-4	Marcona	Actinolite	156.6	4.2		
Chen et al. (2010)	MA3-19	Mina 3	Marcona	Phlogopite	159.7	0.8		
Chen et al. (2010)	MA5-9A	Mina 5	Marcona	Cummingtonite	177	1.5		
Chen et al. (2010)	MA5-9A	Mina 5	Marcona	Cummingtonite	175.2	2.3		

Chen et al. (2010)	MA5-9B	Mina 5	Marcona	Biotite	161.4	0.9
Chen et al. (2010)	MA91-2	MA91	Marcona	Tremolite	157.3	3.2
Chen et al. (2010)	MA91-2	MA91	Marcona	Tremolite	156.8	2.9
Chen et al. (2010)	MA91-2	MA91	Marcona	Tremolite	156.2	2.4
Chen et al. (2010)	MA14-3	MA14	Mina Justa	Microcline	101.5	0.7
Chen et al. (2010)	MA17-7	MA17	Mina Justa	Microcline	103.7	0.6
Chen et al. (2010)	MA17-9	MA17	Mina Justa	Microcline	95	0.6
Chen et al. (2010)	MA45-2	MA45	Mina Justa	Actinolite	157.3	3.5
Chen et al. (2010)	MA45-2	MA45	Mina Justa	Actinolite	154.3	5.5
Chen et al. (2010)	MA45-6	MA45	Mina Justa	Microcline	99.1	0.9
Chen et al. (2010)	MA64-3	MA64	Mina Justa	Actinolite	110.9	0.7

Table 4-2: Re–Os dating of two sulfide samples from Mina Justa, Peru

AIRIE Run #	Mineral and Sample Number	Re, ppb	Re error, abs (ppb)	187Os, ppb	187Os error, abs (ppb)	OsC, ppb	OsC error, abs (ppb)	**Age, Ma**	**Full error with lambda abs (Ma)**	Analytical error only, abs (Ma)	Sample Weight (g)
MD-2168	MJ01 chalcopyrite – pyrite	11.1624	0.0094	0.01850	0.00014	0.001060	0.000053	**158.1**	**1.3**	1.2	0.42299
MD-2169	MJ02 chalcocite – bornite	124.65	0.40	0.2092	0.0012	0.000281	0.000046	**160.1**	**1.2**	1.1	0.42124

Re–Os data acquired by Carius tube digestion equilibrated with a mixed Re-double Os spike
Isotopic ratios measured by NTIMS on Triton machines held by the AIRIE Program, CSU.
Re blank = 1.686 ± 0.019 pg, Os blank = 0.052 ± 0.016 pg with a 187Os/188Os = 0.193 ± 0.053

Table 4-3: Summary of $^{40}Ar/^{39}Ar$ data of actinolite

			Isochron					Plateau	
Sample	40Ar/36Ari	± 2σ	Age (Ma)	± 2σ	N	39Ar %	MSWD	Age (Ma)	± 2σ
NN55	303.0	± 5.5	155.6	± 4.4	12/12	100.0	0.60	158.0	± 3.3
NN58	297.9	± 6.5	164.3	± 3.2	11/11	100.0	0.77	164.2	± 2.8
NN15	297.7	± 8.6	169.1	± 5.0	12/12	100.0	0.70	168.7	± 3.4

Ages calculated relative to 28.201 Ma Fish Canyon sanidine (Kuiper et al., 2008) using decay constants of Min et al. (2000)
Atmospheric 40Ar/36Ar = 298.56 ± 0.31 (Lee et al., 2006).
N = number of plateau steps/number of total incremental heating steps; plateau steps used to calculate isochron

4.8 References

Aguirre, L., 1988, Chemical mobility during low-grade metamorphism of a Jurassic lava flow: Río Grande Formation, Peru: Journal of South American Earth Sciences, v. 1, p. 343–361, doi:10.1016/0895-9811(88)90022-3.

Aguirre, L., and Offler, R., 1985, Burial metamorphism in the Western Peruvian Trough: its relation to Andean magmatism and tectonics, in Magmatism at a Plate Edge, Boston, MA, Springer US, p. 59–71, doi:10.1007/978-1-4899-5820-4_7.

Aleinikoff, J.N., Wintsch, R.P., Tollo, R.P., Unruh, D.M., Fanning, C.M., and Schmitz, M.D., 2007, Ages and origins of rocks of the Killingworth dome, south-central Connecticut: Implications for the tectonic evolution of southern New England: American Journal of Science, v. 307, p. 63–118, doi:10.2475/01.2007.04.

Apen, F.E., Wall, C.J., Cottle, J.M., Schmitz, M.D., Kylander-Clark, A.R.C., and Seward, G.G.E., 2022, Apatites for destruction: Reference apatites from Morocco and Brazil for U–Pb petrochronology and Nd and Sr isotope geochemistry: Chemical Geology, v. 590, p. 120689, doi:10.1016/j.chemgeo.2021.120689.

Barra, F., Reich, M., Selby, D., Rojas, P., Simon, A., Salazar, E., and Palma, G., 2017, Unraveling the origin of the Andean IOCG clan: A Re–Os isotope approach: Ore Geology Reviews, v. 81, p. 62–78, doi:10.1016/j.oregeorev.2016.10.016.

Barton, M.D., 2014, Iron Oxide(–Cu–Au–REE–P–Ag–U–Co) Systems, in Holland, H.D. and Turekian, K.K. eds., Treatise on Geochemistry (Second Edition), Oxford, Elsevier, p. 515–541, doi:10.1016/B978-0-08-095975-7.01123-2.

Black, L.P., and Gulson, B.L., 1978, The age of the Mud Tank Carbonatite, Strangways Range, Northern Territory: Journal of Australian Geology and Geophysics, v. 3, p. 227–232.

Blackburn, T.J., Stockli, D.F., and Walker, J.D., 2007, Magnetite (U–Th)/He dating and its application to the geochronology of intermediate to mafic volcanic rocks: Earth and Planetary Science Letters, v. 259, p. 360–371, doi:10.1016/j.epsl.2007.04.044.

Blakey, R.C., 2008, Gondwana paleogeography from assembly to breakup—A 500 m.y. odyssey, in Special Paper 441: Resolving the Late Paleozoic Ice Age in Time and Space, Geological Society of America, v. 441, p. 1–28, doi:10.1130/2008.2441(01).

Caldas Vidal, J., 1978, Geología del cuadrángulo de San Juan, Acarí y Yauca 31-m, 31-n, 32-n - [Boletín A 30]: Instituto Geológico, Minero y Metalúrgico - INGEMMET, https://repositorio.ingemmet.gob.pe/handle/20.500.12544/149 (accessed May 2020).

Chen, H., Clark, A.H., Kyser, T.K., Ullrich, T.D., Baxter, R., Chen, Y., and Moody, T.C., 2010, Evolution of the Giant Marcona-Mina Justa Iron Oxide – copper – gold District, South-Central Peru: Economic Geology, v. 105, p. 155–185, doi:10.2113/gsecongeo.105.1.155.

Chew, D.M., Sylvester, P.J., and Tubrett, M.N., 2011, U–Pb and Th–Pb dating of apatite by LA-ICPMS: Chemical Geology, v. 280, p. 200–216, doi:10.1016/j.chemgeo.2010.11.010.

Clark, A.H. et al., 1990, Geologic and geochronologic constraints on the metallogenic evolution of the Andes of southeastern Peru: Economic Geology, v. 85, p. 1520–1583, doi:10.2113/gsecongeo.85.7.1520.

Cooperdock, E.H.G., and Stockli, D.F., 2016, Unraveling alteration histories in serpentinites and associated ultramafic rocks with magnetite (U-Th)/He geochronology: Geology, v. 44, p. 967–970, doi:10.1130/G38587.1.

Cooperdock, E.H.G., Stockli, D.F., Kelemen, P.B., and de Obeso, J.C., 2020, Timing of Magnetite Growth Associated With Peridotite-Hosted Carbonate Veins in the SE Samail Ophiolite, Wadi Fins, Oman: Journal of Geophysical Research: Solid Earth, v. 125, p. e2019JB018632, doi:10.1029/2019JB018632.

Corfu, F., and Stone, D., 1998, The significance of titanite and apatite U–Pb ages: constraints for the post-magmatic thermal-hydrothermal evolution of a batholithic complex, Berens River area, northwestern Superior Province, Canada: Geochimica et Cosmochimica Acta, v. 62, p. 2979–2995, doi:10.1016/S0016-7037(98)00225-7.

Corriveau, L., Montreuil, J.-F., and Potter, E.G., 2016, Alteration Facies Linkages Among Iron Oxide Copper-Gold, Iron Iron oxide – apatite, and Affiliated Deposits in the Great Bear Magmatic Zone, Northwest Territories, Canada: Economic Geology, v. 111, p. 2045–2072, doi:10.2113/econgeo.111.8.2045.

Courtney-Davies, L., Ciobanu, C.L., Verdugo-Ihl, M.R., Cook, N.J., Ehrig, K.J., Wade, B.P., Zhu, Z.-Y., and Kamenetsky, V.S., 2020, ~1760 Ma magnetite-bearing protoliths in the Olympic

Dam deposit, South Australia: Implications for ore genesis and regional metallogeny: Ore Geology Reviews, v. 118, p. 103337, doi:10.1016/j.oregeorev.2020.103337.

Cox, L.R., 1956, Jurassic Mollusca from Peru: Journal of Paleontology, v. 30, p. 1179–1186.

Del Real, I., Reich, M., Simon, A.C., Deditius, A., Barra, F., Rodríguez-Mustafa, M.A., Thompson, J.F.H., and Roberts, M.P., 2021, Formation of giant iron oxide – copper – gold deposits by superimposed, episodic hydrothermal pulses: Communications Earth & Environment, v. 2, p. 1–9, doi:10.1038/s43247-021-00265-w.

Espinoza, S., Veliz, H., Esquivel, J., Arias, J., and Moraga, A., 1996, The Cupriferous Province of the Coastal Range, Northern Chile, in Camus, F., Sillitoe, R.H., and Petersen, R. eds., Andean Copper Deposits: New discoveries, mineralization, styles and metallogeny, Society of Economic Geologists Special Publication, Special Publication, v. 5, p. 19–32.

Fowler, A., and Stephenson, P.R., 2016, Mina Justa Estimation of Mineral Resource: AMC Mining Consultants Ltd. 716010.

Frei, R., Bridgwater, D., Rosing, M., and Stecher, O., 1999, Controversial Pb-Pb and Sm-Nd isotope results in the early Archean Isua (West Greenland) oxide iron formation: preservation of primary signatures versus secondary disturbances: Geochimica et Cosmochimica Acta, v. 63, p. 473–488, doi:10.1016/S0016-7037(98)00290-7.

Gelcich, S., Davis, D.W., and Spooner, E.T.C., 2005, Testing the apatite – magnetite geochronometer: U–Pb and 40Ar/39Ar geochronology of plutonic rocks, massive magnetite – apatite tabular bodies, and IOCG mineralization in Northern Chile: Geochimica et Cosmochimica Acta, v. 69, p. 3367–3384, doi:10.1016/j.gca.2004.12.020.

Groves, D.I., Bierlein, F.P., Meinert, L.D., and Hitzman, M.W., 2010, Iron Oxide Copper-Gold (IOCG) Deposits through Earth History: Implications for Origin, Lithospheric Setting, and Distinction from Other Epigenetic Iron Oxide Deposits: Economic Geology, v. 105, p. 641–654.

de Haller, A., Corfu, F., Fontboté, L., Schaltegger, U., Barra, F., Chiaradia, M., Frank, M., and Alvarado, J.Z., 2006, Geology, Geochronology, and Hf and Pb Isotope Data of the Raúl-Condestable Iron Oxide – copper – gold Deposit, Central Coast of Peru: Economic Geology, v. 101, p. 281–310, doi:10.2113/gsecongeo.101.2.281.

Hawkes, N., Clark, A.H., and Moody, T.C., 2002, Marcona and Pampa de Pongo: Giant Mesozoic Fe-(Cu, Au) deposits in the Peruvian Coastal Belt, in Hydrothermal Iron Oxide Copper-Gold & Related Deposits: A Global Perspective, Adelaide, PGC Publishing, v. 2, p. 115–130.

Hitzman, M.W., 2000, Iron Oxide – cu-Au Deposits: What, Where, When, and Why, in Porter, T.M. ed., Hydrothermal Iron Oxide Copper-Gold & Related Deposits: A Global Perspective, Adelaide, PGC Publishing, v. 1, p. 9–25.

Hitzman, M.W., Oreskes, N., and Einaudi, M.T., 1992, Geological characteristics and tectonic setting of proterozoic iron oxide (Cu – U – Au – REE) deposits: Precambrian Research, v. 58, p. 241–287, doi:10.1016/0301-9268(92)90121-4.

Holder, R.M., and Hacker, B.R., 2019, Fluid-driven resetting of titanite following ultrahigh-temperature metamorphism in southern Madagascar: Chemical Geology, v. 504, p. 38–52, doi:10.1016/j.chemgeo.2018.11.017.

Hu, X., Chen, H., Beaudoin, G., and Zhang, Y., 2020, Textural and compositional evolution of iron oxides at Mina Justa (Peru): Implications for mushketovite and formation of IOCG deposits: American Mineralogist, v. 105, p. 397–408, doi:10.2138/am-2020-7024.

Injoque-Espinoza, J., 2002, Fe oxide – cu-Au deposits in Peru: An integrated view, in Porter, T.M. ed., Hydrothermal Iron Oxide Copper-Gold and Related Deposits., Adelaide, PGC Publishing, v. 2, p. 97–113.

Jaillard, E., Soler, P., Carlier, G., and Mourier, T., 1990, Geodynamic evolution of the northern and central Andes during early to middle Mesozoic times: a Tethyan model: Journal of the Geological Society, v. 147, p. 1009–1022, doi:10.1144/gsjgs.147.6.1009.

Jicha, B.R., Singer, B.S., and Sobol, P., 2016, Re-evaluation of the ages of 40Ar/39Ar sanidine standards and supereruptions in the western U.S. using a Noblesse multi-collector mass spectrometer: Chemical Geology, v. 431, p. 54–66, doi:10.1016/j.chemgeo.2016.03.024.

Knipping, J.L., Bilenker, L.D., Simon, A.C., Reich, M., Barra, F., Deditius, A.P., Lundstrom, C., Bindeman, I., and Munizaga, R., 2015, Giant Kiruna-type deposits form by efficient flotation of magmatic magnetite suspensions: Geology, v. 43, p. 591–594, doi:10.1130/G36650.1.

Krestianinov, E., Amelin, Y., Neymark, L.A., and Aleinikoff, J.N., 2021, U–Pb systematics of uranium-rich apatite from Adirondacks: Inferences about regional geological and geochemical evolution, and evaluation of apatite reference materials for in situ dating: Chemical Geology, v. 581, p. 120417, doi:10.1016/j.chemgeo.2021.120417.

Kylander-Clark, A.R.C., Hacker, B.R., and Mattinson, J.M., 2008, Slow exhumation of UHP terranes: Titanite and rutile ages of the Western Gneiss Region, Norway: Earth and Planetary Science Letters, v. 272, no. 3, p. 531–540.

Kylander-Clark, A.R.C., Hacker, B.R., and Cottle, J.M., 2013, Laser-ablation split-stream ICP petrochronology: Chemical Geology, v. 345, p. 99–112, doi:10.1016/j.chemgeo.2013.02.019.

Min, K., Mundil, R., Renne, P.R., and Ludwig, K.R., 2000, A test for systematic errors in 40Ar/39Ar geochronology through comparison with U/Pb analysis of a 1.1-Ga rhyolite: Geochimica et Cosmochimica Acta, v. 64, p. 73–98, doi:10.1016/S0016-7037(99)00204-5.

Mohammadzaheri, A., Sigloch, K., Hosseini, K., and Mihalynuk, M.G., 2021, Subducted Lithosphere Under South America From Multifrequency P Wave Tomography: Journal of Geophysical Research: Solid Earth, v. 126, p. e2020JB020704, doi:10.1029/2020JB020704.

Moser, A.C., Hacker, B.R., Gehrels, G.E., Seward, G.G.E., Kylander-Clark, A.R.C., and Garber, J.M., 2022, Linking titanite U–Pb dates to coupled deformation and dissolution–reprecipitation: Contributions to Mineralogy and Petrology, v. 177, p. 42, doi:10.1007/s00410-022-01906-9.

Naslund, H.R., Henriquez, F., Nyström, J.O., Vivallo, W., and Dobbs, F.M., 2002, Magmatic Iron Ires and Associated Mineralisation: Examples from the Chilean High Andes and Coastal Cordillera, in Porter, T.M. ed., Hydrothermal Iron Oxide Copper-Gold & Related Deposits: A Global Perspective 2, Adelaide, PGC Publishing, v. 2, p. 207–226, https://ci.nii.ac.jp/naid/10027158267/ (accessed January 2019).

Odlum, M.L., Levy, D.A., Stockli, D.F., Stockli, L.D., and DesOrmeau, J.W., 2022, Deformation and metasomatism recorded by single-grain apatite petrochronology: Geology, v. 50, p. 697–703, doi:10.1130/G49809.1.

Odlum, M.L., and Stockli, D.F., 2020, Geochronologic constraints on deformation and metasomatism along an exhumed mylonitic shear zone using apatite U–Pb, geochemistry, and microtextural analysis: Earth and Planetary Science Letters, v. 538, p. 116177, doi:10.1016/j.epsl.2020.116177.

Palacios Moncayo, O., Sánchez Fernández, A.W., and Herrera Romero, F., 1995, Geología del Perú – [Boletín A 55]: Instituto Geológico, Minero y Metalúrgico - INGEMMET, https://repositorio.ingemmet.gob.pe/handle/20.500.12544/176 (accessed October 2022).

Paul, A.N., Spikings, R.A., and Gaynor, S.P., 2021, U–Pb ID-TIMS reference ages and initial Pb isotope compositions for Durango and Wilberforce apatites: Chemical Geology, v. 586, p. 120604, doi:10.1016/j.chemgeo.2021.120604.

Reich, M. et al., 2016, Trace Element Signature Of Pyrite From The Los Colorados Iron Iron oxide – apatite (IOA) Deposit, Chile: A Missing Link Between Andean IOA And Iron Oxide Copper-Gold Systems? Economic Geology, v. 111, p. 743–761.

Richards, J.P., López, G.P., Zhu, J., Creaser, R.A., Locock, A.J., and Mumin, A.H., 2017, Contrasting Tectonic Settings and Sulfur Contents of Magmas Associated with: Economic Geology, v. 112, p. 295–318.

Rodriguez-Mustafa, M.A., Simon, A.C., Bilenker, L.D., Bindeman, I., Mathur, R., and Machado, E.L.B., 2022, The Mina Justa Iron Oxide Copper-Gold (IOCG) Deposit, Peru: Constraints on Metal and Ore Fluid Sources: Economic Geology, v. 117, p. 645–666, doi:10.5382/econgeo.4875.

Rodriguez-Mustafa, M.A., Simon, A.C., Real, I. del, Thompson, J.F.H., Bilenker, L.D., Barra, F., Bindeman, I., and Cadwell, D., 2020, A Continuum from Iron Oxide Copper-Gold to Iron

Iron oxide – apatite Deposits: Evidence from Fe and O Stable Isotopes and Trace Element Chemistry of Magnetite: Economic Geology, v. 115, p. 1443–1459, doi:10.5382/econgeo.4752.

Romero, L., Aldana, M., Rangel, C., Villavicencio, E., and Ramírez, J., 1995, Fauna y Flora del Peru: Lima, INGEMMET, https://repositorio.ingemmet.gob.pe/bitstream/20.500.12544/334/2/D017-Boletin-Fauna_flora_del_Peru.pdf (accessed May 2022).

Romeuf, N., Aguirre, L., Soler, P., Feraud, G., Jaillard, E., and Ruffet, G., 1995, Middle Jurassic volcanism in the Northern and Central Andes: Andean Geology, v. 22, p. 245–259, doi:10.5027/andgeoV22n2-a08.

Ross, J., 2019, NMGRL/pychron v18.2:, doi:10.5281/zenodo.3237834.

Rüegg, W., 1957, Geologie zwischen Cañete-San Juan 13°00′-15°24′ Südperu: Geologische Rundschau, v. 45, p. 775–858, doi:10.1007/BF02296863.

Ruiz-Agudo, E., Putnis, C.V., and Putnis, A., 2014, Coupled dissolution and precipitation at mineral–fluid interfaces: Chemical Geology, v. 383, p. 132–146, doi:10.1016/j.chemgeo.2014.06.007.

Schmitz, M.D., and Bowring, S.A., 2001, U–Pb zircon and titanite systematics of the Fish Canyon Tuff: an assessment of high-precision U–Pb geochronology and its application to young volcanic rocks: Geochimica et Cosmochimica Acta, v. 65, p. 2571–2587, doi:10.1016/S0016-7037(01)00616-0.

Scotese, C.R., 2021, An Atlas of Phanerozoic Paleogeographic Maps: The Seas Come In and the Seas Go Out: Annual Review of Earth and Planetary Sciences, v. 49, p. 679–728, doi:10.1146/annurev-earth-081320-064052.

Sempere, T. et al., 2002, Late Permian–Middle Jurassic lithospheric thinning in Peru and Bolivia, and its bearing on Andean-age tectonics: Tectonophysics, v. 345, p. 153–181, doi:10.1016/S0040-1951(01)00211-6.

Shatwell, D., 2021, Mesozoic Metallogenesis of Peru: A Reality Check on Geodynamic Models: SEG Discovery, no. 124, p. 15–24.

Sillitoe, R.H., 2003, Iron oxide – copper – gold deposits: an Andean view: Mineralium Deposita, v. 38, p. 787–812, doi:10.1007/s00126-003-0379-7.

Simon, A.C., Knipping, J., Reich, M., Barra, F., Deditius, A.P., Bilenker, L., and Childress, T., 2018, Kiruna-Type Iron Iron oxide – apatite (IOA) and Iron Oxide Copper-Gold (IOCG) Deposits Form by a Combination of Igneous and Magmatic-Hydrothermal Processes: Evidence from the Chilean Iron Belt: SEG Special Publications, v. 21, p. 26, doi:10.5382/SP.21.06.

Skirrow, R.G., 2022, Iron oxide copper-gold (IOCG) deposits – A review (part 1): Settings, mineralogy, ore geochemistry and classification: Ore Geology Reviews, v. 140, p. 104569, doi:10.1016/j.oregeorev.2021.104569.

Spandler, C., Hammerli, J., Sha, P., Hilbert-Wolf, H., Hu, Y., Roberts, E., and Schmitz, M., 2016, MKED1: A new titanite standard for in situ analysis of Sm–Nd isotopes and U–Pb geochronology: Chemical Geology, v. 425, p. 110–126, doi:10.1016/j.chemgeo.2016.01.002.

Thomson, S.N., Gehrels, G.E., Ruiz, J., and Buchwaldt, R., 2012, Routine low-damage apatite U–Pb dating using laser ablation–multicollector–ICPMS: Geochemistry, Geophysics, Geosystems, v. 13, doi:10.1029/2011GC003928.

Vidal, C.E., Injoque-Espinoza, J., Sidder, G.B., and Mukasa, S.B., 1990, Amphibolitic Cu-Fe skarn deposits in the central coast of Peru: Economic Geology, v. 85, p. 1447–1461, doi:10.2113/gsecongeo.85.7.1447.

Wiedenbeck, M., Allé, P., Corfu, F., Griffin, W. l., Meier, M., Oberli, F., Quadt, A.V., Roddick, J. c., and Spiegel, W., 1995, Three Natural Zircon Standards for U-Th-Pb, Lu-Hf, Trace Element and Ree Analyses: Geostandards Newsletter, v. 19, p. 1–23, doi:10.1111/j.1751-908X.1995.tb00147.x.

Williams, P., Barton, M.D., Johnson, D.A., Fontboté, L., De Haller, A., Mark, G., Oliver, N.H.S., and Marschik, R., 2005, Iron Oxide Copper-Gold Deposits: Geology, Space-Time Distribution, and Possible Modes of Origin: Economic Geology, v. 100, p. 371–405.

Xiao, X., Zhou, T., White, N.C., Zhang, L., Fan, Y., and Chen, X., 2020, Multiple generations of titanites and their geochemical characteristics record the magmatic-hydrothermal processes and timing of the Dongguashan porphyry-skarn Cu-Au system, Tongling district, Eastern China: Mineralium Deposita.

Zeng, L.-P., Zhao, X.-F., Li, X.-C., Hu, H., and McFarlane, C., 2016, In situ elemental and isotopic analysis of fluorapatite from the Taocun magnetite – apatite deposit, Eastern China: Constraints on fluid metasomatism: American Mineralogist, v. 101, p. 2468–2483, doi:10.2138/am-2016-5743.

Chapter 5 : Conclusions

As the demand for energy-critical metals such as iron and copper increases, the need to understand how and where such elements concentrate in Earth's crust is vital to effectively find such resources. Iron oxide deposits in the Andes are important sources of iron and copper, but the processes by which they form are still not completely understood. The geochemistry of ore minerals present in these deposits can be used to evaluate the source of the fluids and the metals as well as to constrain the timing of mineralization. This dissertation integrated the elemental composition and isotopic abundances of ore and alteration minerals to investigate the formation and spatiotemporal links between iron oxide – apatite (IOA) and iron oxide – copper – gold (IOCG) deposits in the Andes.

After a brief introduction on mineral chemistry and the geology of iron oxide deposits in chapter 1, chapter 2 presented a comparative study of magnetite and actinolite from an IOA prospect and an IOCG deposit in Chile. I characterized the textures and variation in the major, minor, and trace element concentrations in the mineral magnetite and measured its iron, hydrogen, and oxygen isotopic abundances. The isotopes fingerprinted an igneous/magmatic-hydrothermal source for the fluids and metals and the textures indicated the presence of original titanomagnetite that had gone through dissolution-reprecipitation processes at both deposits. The increase in minor and trace elements with depth indicated an increase in the temperature of formation of magnetite from shallower to deeper levels in the IOCG deposit and even higher temperatures in the IOA deposit, which is consistent with temperature estimations from oxygen isotope abundances and actinolite composition from the same samples. Overall, this chapter identified the source of metals and fluids as igneous to magmatic-hydrothermal and discovered a vertical transition from IOCG to IOA style mineralization, demonstrating the link in both deposit types in Chile.

Chapters 3 and 4 further explored the connection between IOA and IOCG systems in the Andes by investigating the evolution of the Mina Justa IOCG deposit and the neighboring Marcona IOA deposit in Peru. In chapter 3, I used copper and iron isotope abundances to fingerprint the source of the metals at Mina Justa and triple oxygen isotopes to examine the

source of the fluids that carried the metals. The combined isotopic data support an igneous to magmatic-hydrothermal source for the metals and preclude a substantial input of meteoric water or basinal brines as ore fluids. I also estimated the temperature of formation and characterized the textures and composition of ore minerals (magnetite and copper sulfides) from the tabular (manto-style) and the pervasive, disseminated to massive mineralization styles at Mina Justa. The higher content of trace elements in some of the magnetite from the mantos that is not associated with copper mineralization indicates that it formed at a higher temperature than magnetite associated with copper mineralization. This suggests that two magnetite events occurred at Mina Justa, with the second one being related with the copper mineralization.

In chapter 4, I tested the hypothesis from chapter 3 of two mineralizing events at Mina Justa and explored their relationship with iron mineralization at the neighboring Marcona IOA deposit. I used traditional geochronological methods (Ar–Ar in actinolite, *in-situ* U–Pb in apatite and titanite, and Re–Os in sulfides) and developed the new *in-situ* U–Pb in magnetite geochronometer to directly date the timing of mineralization at Marcona and Mina Justa. Our data indicate that copper mineralization at Mina Justa occurred at c. 160 Ma, about 70 Ma older than previously published, and that iron mineralization is older and coeval at both deposits.

Magnetite geochronology has the potential to become a tool that can be applied to solve questions in other areas of the geosciences such as tectonics, igneous and metamorphic petrology, and planetary sciences. However, further workers should focus on developing a matrix-matched standard and in performing experiments to constrain the Pb diffusion in magnetite to refine its closure temperature. In the meantime, magnetite geochronology should be paired with other dating techniques to verify the validity of the results.

This dissertation showcased the usefulness of integrated, detailed mineral chemistry (elemental composition, isotopic abundances, and geochronology) to understand the source of metals and fluids that result in IOA and IOCG deposits in the Andes as well as the spatiotemporal relationship between both deposit types. This increased understanding on the formation of these deposits is critical to develop more efficient strategies to find the critical mineral resources for future generations.

Appendices

Appendix A

Table A-1: EPMA conditions

Magnetite and ilmenite

Element/Line	Crystal	Standard	Counting time (s)	MDL (wt%)
Mg Kα	TAP	Geikielite	100	0.01 – 0.04
Al Kα	TAP	Jadeite	100	0.01
Si Kα	LTAP	Wollastonite	100	0.01
P Kα	LTAP	BaCl	100	0.01
Ca Kα	LPET	Wollastonite	100	0.01
Ti Kα	LPET	Ilmenite (USNM)	120	0.01
V Kα	LLIF	V2O5	120	0.01
Cr Kα	LLIF	Cr2O3	100	0.01
Mn Kα	LIF	Rhodonite	100	0.02 – 0.03
Fe Kα	LIF	Magnetite (USNM)	20	0.01 – 0.02

Actinolite

Element	Crystal	Standard	Peak counting time (s)	MDL (wt%)
Si	TAP	Adularia	10	0.03
Ti	LPET	Rutile (Synthetic)	30	0.01
Al	TAP	Silliminite	40	0.02
Fe	LIF	FeSiO3 (Synthetic)	20	0.07
Mn	LIF	Rhodonite	40	0.04
Mg	LTAP	Pyroxene PX69	40	0.01
Ca	LPET	Wollastonite	30	0.01
Na	LTAP	Jadeite	20	0.02
K	LPET	Adularia	30	0.01
P	LPET	Alforsite (Synthetic)	30	0.02

MDL: Mean Detection Limit

Table A-2: EPMA magnetite results. All values in wt.% unless stated differently. Oxygen content is stoichiometrically calculated. Concentrations below detection limit appear as zero. AQ: Quince. LD: Candelaria mine.

Drill core	Sample	Mg	Al	Si	Ti	Ca	P	V	Cr	Fe	Mn	O	Total
AQ-19	2	0.00	0.06	0.01	0.03	0.00	0.00	0.21	0.01	72.76	0.00	28.38	101.46
AQ-19	2	0.05	0.07	0.01	0.03	0.00	0.00	0.22	0.01	72.55	0.00	28.38	101.31

AQ-19	2	0.23	0.15	0.01	0.14	0.00	0.00	0.21	0.02	71.85	0.07	28.56	101.24
AQ-19	2	0.13	0.07	0.01	0.06	0.00	0.00	0.21	0.01	72.57	0.03	28.47	101.57
AQ-19	2	0.10	0.08	0.01	0.07	0.00	0.00	0.21	0.01	72.47	0.03	28.44	101.43
AQ-19	2	0.16	0.08	0.07	0.06	0.00	0.00	0.21	0.01	72.40	0.03	28.51	101.53
AQ-19	2	0.07	0.05	0.01	0.04	0.00	0.00	0.21	0.01	72.81	0.00	28.44	101.64
AQ-19	2	0.05	0.09	0.01	0.04	0.00	0.00	0.21	0.01	72.70	0.00	28.49	101.61
AQ-19	2	0.07	0.07	0.03	0.05	0.02	0.00	0.21	0.01	72.37	0.00	28.34	101.16
AQ-19	2	0.10	0.07	0.01	0.06	0.00	0.00	0.21	0.01	72.61	0.03	28.47	101.58
AQ-19	2	0.05	0.05	0.01	0.09	0.00	0.00	0.21	0.02	71.94	0.00	28.13	100.50
AQ-19	2	0.04	0.07	0.01	0.07	0.00	0.00	0.21	0.02	71.85	0.00	28.10	100.36
AQ-19	2	0.04	0.06	0.01	0.06	0.00	0.00	0.21	0.02	71.94	0.00	28.13	100.47
AQ-19	2	0.08	0.07	0.01	0.05	0.00	0.00	0.21	0.01	71.75	0.00	28.11	100.30
AQ-19	2	0.05	0.07	0.01	0.05	0.00	0.00	0.21	0.02	71.82	0.00	28.12	100.35
AQ-19	2	0.07	0.07	0.01	0.06	0.00	0.00	0.21	0.02	71.93	0.00	28.18	100.55
AQ-19	2	0.05	0.07	0.01	0.07	0.00	0.00	0.21	0.02	71.92	0.00	28.15	100.50
AQ-19	2	0.00	0.07	0.01	0.08	0.00	0.00	0.22	0.02	71.84	0.00	28.08	100.31
AQ-19	2	0.12	0.08	0.01	0.09	0.00	0.00	0.21	0.02	71.70	0.00	28.15	100.38
AQ-19	2	0.14	0.07	0.01	0.05	0.00	0.00	0.21	0.02	71.64	0.00	28.12	100.26
AQ-19	2	0.10	0.06	0.01	0.09	0.00	0.00	0.21	0.02	71.94	0.00	28.19	100.62
AQ-19	2	0.11	0.05	0.01	0.04	0.00	0.00	0.21	0.02	71.90	0.00	28.14	100.48
AQ-19	2	0.08	0.05	0.01	0.08	0.00	0.00	0.21	0.02	71.82	0.00	28.10	100.37
AQ-19	2	0.07	0.05	0.01	0.07	0.00	0.00	0.21	0.01	72.05	0.00	28.17	100.65
AQ-19	2	0.06	0.05	0.02	0.05	0.00	0.00	0.21	0.02	71.89	0.00	28.10	100.39
AQ-19	2	0.10	0.07	0.00	0.06	0.00	0.00	0.21	0.02	71.89	0.00	28.16	100.50
AQ-19	2	0.10	0.06	0.01	0.08	0.00	0.00	0.21	0.01	71.75	0.04	28.11	100.37
AQ-19	3	0.20	0.03	0.01	0.07	0.00	0.00	0.21	0.01	72.44	0.00	28.37	101.34
AQ-19	3	0.18	0.04	0.01	0.07	0.00	0.00	0.21	0.01	72.65	0.00	28.45	101.62
AQ-19	3	0.22	0.04	0.01	0.03	0.00	0.00	0.21	0.01	72.49	0.00	28.41	101.42
AQ-19	3	0.18	0.04	0.01	0.06	0.00	0.00	0.21	0.01	72.91	0.00	28.55	101.97
AQ-19	3	0.21	0.03	0.01	0.01	0.01	0.00	0.21	0.01	72.56	0.04	28.41	101.51
AQ-19	3	0.11	0.01	0.01	0.02	0.05	0.00	0.22	0.01	72.52	0.00	28.27	101.21
AQ-19	3	0.18	0.03	0.01	0.06	0.00	0.00	0.21	0.01	72.68	0.03	28.46	101.68
AQ-19	3	0.12	0.01	0.01	0.09	0.00	0.00	0.21	0.01	72.57	0.00	28.31	101.34
AQ-19	3	0.13	0.04	0.00	0.05	0.00	0.00	0.21	0.01	72.43	0.00	28.30	101.17
AQ-19	3	0.17	0.05	0.01	0.04	0.00	0.00	0.22	0.01	72.29	0.00	28.33	101.12
AQ-19	3	0.16	0.06	0.01	0.05	0.00	0.00	0.22	0.01	71.84	0.00	28.19	100.53
AQ-19	3	0.16	0.04	0.01	0.02	0.00	0.00	0.22	0.01	72.11	0.00	28.22	100.79
AQ-19	3	0.21	0.07	0.01	0.02	0.00	0.00	0.22	0.01	71.96	0.00	28.28	100.77
AQ-19	3	0.11	0.06	0.01	0.10	0.00	0.00	0.22	0.01	71.90	0.03	28.19	100.62
AQ-19	3	0.16	0.06	0.01	0.04	0.00	0.00	0.22	0.01	72.10	0.00	28.28	100.88
AQ-19	3	0.05	0.04	0.00	0.02	0.00	0.00	0.21	0.01	72.69	0.00	28.31	101.32

AQ-19	3	0.11	0.09	0.01	0.02	0.00	0.00	0.21	0.01	72.93	0.00	28.61	101.99
AQ-19	3	0.12	0.08	0.01	0.03	0.00	0.00	0.21	0.01	72.75	0.03	28.54	101.78
AQ-19	3	0.07	0.04	0.01	0.04	0.00	0.00	0.21	0.01	72.76	0.00	28.40	101.54
AQ-19	3	0.11	0.06	0.01	0.04	0.00	0.00	0.21	0.01	72.79	0.00	28.47	101.69
AQ-19	3	0.12	0.03	0.00	0.28	0.00	0.00	0.20	0.01	72.81	0.00	28.50	101.94
AQ-19	3	0.12	0.04	0.00	0.02	0.01	0.00	0.21	0.01	72.31	0.00	28.24	100.96
AQ-19	3	0.13	0.06	0.00	0.05	0.00	0.00	0.21	0.01	72.50	0.00	28.37	101.32
AQ-19	3	0.10	0.06	0.01	0.07	0.00	0.00	0.21	0.01	72.64	0.00	28.43	101.52
AQ-19	3	0.06	0.01	0.00	0.02	0.00	0.00	0.22	0.01	73.23	0.00	28.49	102.04
AQ-19	3	0.00	0.06	0.00	0.03	0.00	0.00	0.21	0.01	72.97	0.00	28.45	101.74
AQ-19	3	0.00	0.03	0.00	0.00	0.00	0.00	0.22	0.01	73.06	0.00	28.40	101.72
AQ-19	3	0.00	0.07	0.01	0.02	0.00	0.00	0.21	0.01	72.36	0.00	28.24	100.92
AQ-19	3	0.00	0.04	0.01	0.02	0.00	0.00	0.21	0.01	72.72	0.00	28.30	101.31
AQ-19	3	0.17	0.05	0.01	0.32	0.00	0.00	0.20	0.01	72.52	0.03	28.51	101.82
AQ-19	3	0.20	0.04	0.01	0.09	0.04	0.00	0.21	0.01	72.17	0.04	28.33	101.14
AQ-19	3	0.11	0.04	0.01	0.07	0.00	0.00	0.22	0.01	71.04	0.00	27.79	99.28
AQ-19	3	0.14	0.04	0.01	0.07	0.00	0.00	0.22	0.01	70.96	0.00	27.79	99.24
AQ-19	3	0.16	0.04	0.01	0.06	0.00	0.00	0.21	0.01	71.07	0.00	27.83	99.39
AQ-19	3	0.13	0.05	0.01	0.07	0.00	0.00	0.22	0.01	71.31	0.00	27.92	99.71
AQ-19	3	0.13	0.18	0.01	0.07	0.00	0.00	0.22	0.01	71.05	0.00	28.19	99.87
AQ-19	3	0.14	0.13	0.01	0.08	0.00	0.00	0.22	0.01	70.98	0.00	28.03	99.59
AQ-19	3	0.16	0.04	0.01	0.09	0.00	0.00	0.22	0.01	71.02	0.00	27.85	99.40
AQ-19	3	0.15	0.06	0.01	0.10	0.00	0.00	0.22	0.01	70.93	0.00	27.83	99.29
AQ-19	3	0.11	0.09	0.00	0.10	0.00	0.00	0.21	0.01	71.08	0.00	27.94	99.55
AQ-19	3	0.14	0.04	0.01	0.10	0.00	0.00	0.21	0.01	71.30	0.00	27.91	99.72
AQ-19	3	0.12	0.06	0.01	0.10	0.00	0.00	0.21	0.01	70.90	0.00	27.80	99.21
AQ-19	3	0.07	0.05	0.01	0.10	0.00	0.00	0.21	0.01	71.18	0.00	27.83	99.46
AQ-19	3	0.07	0.03	0.01	0.15	0.00	0.00	0.19	0.01	72.40	0.00	28.24	101.11
AQ-19	3	0.07	0.05	0.01	0.16	0.00	0.00	0.20	0.01	72.51	0.00	28.34	101.36
AQ-19	3	0.11	0.05	0.01	0.19	0.00	0.00	0.20	0.01	72.40	0.00	28.37	101.34
AQ-19	3	0.09	0.09	0.01	0.20	0.00	0.00	0.21	0.01	72.63	0.00	28.54	101.78
AQ-19	3	0.09	0.05	0.00	0.19	0.00	0.00	0.21	0.01	72.45	0.00	28.37	101.37
AQ-19	3	0.10	0.06	0.01	0.16	0.00	0.00	0.21	0.01	72.47	0.00	28.40	101.41
AQ-19	3	0.51	0.21	0.04	0.14	0.00	0.00	0.20	0.01	71.58	0.00	28.81	101.51
AQ-19	3	0.10	0.06	0.02	0.13	0.00	0.00	0.21	0.01	72.46	0.00	28.39	101.38
AQ-19	3	0.07	0.07	0.01	0.12	0.00	0.00	0.21	0.01	72.57	0.00	28.42	101.48
AQ-19	3	0.12	0.06	0.01	0.12	0.00	0.00	0.21	0.01	72.52	0.00	28.42	101.46
AQ-19	3	0.09	0.07	0.01	0.15	0.00	0.00	0.21	0.01	72.54	0.00	28.45	101.53
AQ-19	3	0.07	0.05	0.00	0.18	0.00	0.00	0.21	0.01	72.56	0.00	28.38	101.46
AQ-19	3	0.12	0.05	0.01	0.02	0.00	0.00	0.21	0.01	72.54	0.00	28.36	101.33
AQ-19	3	0.10	0.05	0.01	0.04	0.00	0.00	0.21	0.01	72.48	0.00	28.33	101.23
AQ-19	3	0.13	0.04	0.01	0.05	0.00	0.00	0.21	0.01	72.41	0.00	28.30	101.16
AQ-19	3	0.12	0.05	0.01	0.03	0.00	0.00	0.21	0.01	72.27	0.00	28.25	100.95
AQ-19	3	0.12	0.10	0.01	0.03	0.00	0.00	0.21	0.01	72.48	0.00	28.47	101.43
AQ-19	3	0.13	0.12	0.01	0.06	0.00	0.00	0.21	0.01	72.32	0.00	28.49	101.36
AQ-19	3	0.10	0.15	0.01	0.03	0.00	0.00	0.21	0.01	72.57	0.00	28.62	101.70
AQ-19	3	0.12	0.06	0.01	0.05	0.00	0.00	0.21	0.01	72.56	0.00	28.40	101.41
AQ-19	3	0.00	0.04	0.01	0.03	0.00	0.00	0.21	0.01	72.36	0.00	28.16	100.82

AQ-19	3	0.11	0.06	0.01	0.03	0.00	0.00	0.21	0.01	72.38	0.00	28.31	101.12
AQ-19	3	0.08	0.03	0.01	0.22	0.00	0.00	0.20	0.01	72.41	0.00	28.30	101.27
AQ-19	3	0.07	0.05	0.01	0.02	0.00	0.00	0.21	0.01	72.85	0.00	28.45	101.67
AQ-19	3	0.05	0.04	0.01	0.02	0.00	0.00	0.22	0.01	72.57	0.00	28.29	101.21
AQ-19	3	0.07	0.03	0.00	0.04	0.00	0.00	0.22	0.01	72.52	0.00	28.28	101.18
AQ-19	3	0.07	0.02	0.01	0.05	0.00	0.00	0.21	0.01	72.57	0.00	28.27	101.21
AQ-19	3	0.16	0.04	0.01	0.05	0.00	0.00	0.21	0.01	70.79	0.00	27.72	99.00
AQ-19	3	0.19	0.05	0.01	0.03	0.00	0.00	0.21	0.01	70.93	0.00	27.80	99.22
AQ-19	3	0.19	0.05	0.01	0.03	0.00	0.00	0.21	0.01	71.08	0.00	27.87	99.45
AQ-19	3	0.16	0.11	0.01	0.03	0.00	0.00	0.21	0.01	70.92	0.00	27.93	99.38
AQ-19	3	0.15	0.05	0.01	0.04	0.00	0.00	0.21	0.01	70.89	0.00	27.76	99.12
AQ-19	3	0.15	0.05	0.01	0.08	0.00	0.00	0.21	0.01	70.76	0.00	27.72	98.99
AQ-19	3	0.16	0.05	0.01	0.14	0.00	0.00	0.21	0.01	70.97	0.00	27.84	99.39
AQ-19	3	0.16	0.05	0.01	0.27	0.00	0.00	0.21	0.01	70.73	0.00	27.83	99.27
AQ-19	3	0.16	0.05	0.01	0.29	0.00	0.00	0.21	0.01	70.35	0.00	27.67	98.75
AQ-19	3	0.21	0.05	0.01	0.06	0.00	0.00	0.21	0.01	70.30	0.00	27.60	98.44
AQ-19	3	0.20	0.05	0.01	0.05	0.00	0.00	0.21	0.01	70.41	0.00	27.64	98.59
AQ-19	3	0.21	0.04	0.01	0.13	0.00	0.00	0.21	0.01	70.19	0.00	27.56	98.35
AQ-19	3	0.19	0.04	0.01	0.06	0.00	0.00	0.21	0.01	70.34	0.00	27.56	98.41
AQ-19	3	0.19	0.05	0.01	0.05	0.00	0.00	0.21	0.01	70.71	0.00	27.74	98.96
AQ-19	3	0.19	0.04	0.01	0.04	0.00	0.00	0.21	0.01	70.89	0.00	27.76	99.14
AQ-19	3	0.22	0.07	0.01	0.11	0.00	0.00	0.21	0.01	70.80	0.00	27.89	99.32
AQ-19	3	0.17	0.06	0.01	0.32	0.00	0.00	0.19	0.01	71.10	0.00	27.97	99.83
AQ-19	3	0.12	0.06	0.01	0.49	0.00	0.00	0.19	0.01	70.82	0.04	27.93	99.68
AQ-19	3	0.09	0.21	0.02	0.94	0.02	0.00	0.18	0.01	70.25	0.06	28.27	100.05
AQ-19	3	0.15	0.04	0.01	0.25	0.00	0.00	0.21	0.01	71.02	0.00	27.87	99.56
AQ-19	4	0.05	0.06	0.01	0.04	0.00	0.00	0.21	0.01	71.62	0.00	27.97	99.97
AQ-19	4	0.07	0.05	0.01	0.02	0.00	0.00	0.21	0.01	71.49	0.00	27.90	99.76
AQ-19	4	0.06	0.06	0.01	0.02	0.00	0.00	0.21	0.01	71.93	0.00	28.09	100.40
AQ-19	4	0.07	0.07	0.01	0.02	0.00	0.00	0.21	0.01	71.73	0.00	28.05	100.17
AQ-19	4	0.07	0.09	0.01	0.03	0.00	0.00	0.20	0.01	71.66	0.00	28.08	100.16
AQ-19	4	0.07	0.11	0.01	0.08	0.00	0.00	0.20	0.01	71.74	0.00	28.19	100.42
AQ-19	4	0.18	0.22	0.01	0.23	0.00	0.00	0.20	0.01	70.89	0.04	28.31	100.09
AQ-19	4	0.10	0.10	0.01	0.02	0.00	0.00	0.21	0.01	71.26	0.00	27.98	99.69
AQ-19	4	0.19	0.14	0.01	0.07	0.00	0.00	0.20	0.01	71.54	0.00	28.27	100.43
AQ-19	4	0.17	0.09	0.01	0.09	0.00	0.00	0.21	0.01	71.16	0.00	28.01	99.75
AQ-19	4	0.13	0.07	0.01	0.02	0.00	0.00	0.21	0.01	71.44	0.00	27.99	99.87
AQ-19	4	0.55	0.65	0.01	0.41	0.00	0.00	0.20	0.01	68.69	0.08	29.00	99.61
AQ-19	4	0.12	0.07	0.01	0.13	0.00	0.00	0.21	0.01	71.68	0.00	28.14	100.37
AQ-19	4	0.10	0.06	0.01	0.04	0.00	0.00	0.21	0.01	72.00	0.00	28.17	100.60
AQ-19	4	0.08	0.07	0.01	0.05	0.00	0.00	0.21	0.01	71.40	0.00	27.96	99.79
AQ-19	4	0.05	0.06	0.01	0.05	0.00	0.00	0.21	0.01	70.33	0.00	27.49	98.21
AQ-19	4	0.07	0.07	0.00	0.09	0.00	0.00	0.20	0.01	70.34	0.00	27.54	98.32
AQ-19	4	0.00	0.06	0.01	0.36	0.00	0.00	0.19	0.01	70.50	0.05	27.63	98.82
AQ-19	4	0.10	0.07	0.01	0.03	0.00	0.00	0.20	0.01	71.15	0.00	27.84	99.40
AQ-19	4	0.28	0.35	0.01	0.06	0.00	0.00	0.20	0.01	70.10	0.00	28.35	99.37
AQ-19	4	0.11	0.05	0.01	0.05	0.00	0.00	0.20	0.01	71.01	0.00	27.75	99.19
AQ-19	4	0.10	0.06	0.01	0.13	0.00	0.00	0.20	0.01	71.11	0.00	27.85	99.46
AQ-19	4	0.07	0.06	0.01	0.53	0.00	0.00	0.20	0.01	70.91	0.00	27.92	99.71

AQ-19	4	0.09	0.06	0.01	0.11	0.00	0.00	0.20	0.01	71.07	0.00	27.82	99.36
AQ-19	4	0.12	0.05	0.01	0.04	0.00	0.00	0.20	0.01	71.36	0.00	27.90	99.68
AQ-19	4	0.09	0.05	0.00	0.03	0.00	0.00	0.21	0.01	70.75	0.00	27.64	98.77
AQ-19	4	0.10	0.05	0.01	0.02	0.00	0.00	0.20	0.01	71.25	0.00	27.82	99.46
AQ-19	4	0.12	0.08	0.01	0.03	0.00	0.00	0.20	0.01	71.47	0.00	28.02	99.94
AQ-19	4	0.05	0.06	0.01	0.05	0.00	0.00	0.20	0.01	71.09	0.00	27.77	99.24
DH703	4	0.06	0.18	0.68	0.05	0.29	0.00	0.03	0.00	69.64	0.07	27.88	98.87
DH703	4	0.07	0.24	0.94	0.08	0.35	0.00	0.03	0.00	68.79	0.06	27.96	98.53
DH703	4	0.07	0.22	0.87	0.08	0.29	0.00	0.03	0.00	69.19	0.07	27.99	98.81
DH703	4	0.04	0.15	0.55	0.06	0.19	0.00	0.03	0.00	69.86	0.07	27.72	98.66
DH703	4	0.00	0.04	0.07	0.01	0.00	0.00	0.03	0.00	70.72	0.03	27.24	98.14
DH703	4	0.00	0.02	0.04	0.01	0.02	0.00	0.02	0.00	71.61	0.03	27.51	99.27
DH703	4	0.00	0.05	0.22	0.01	0.04	0.00	0.03	0.00	71.51	0.02	27.70	99.59
DH703	4	0.04	0.20	0.82	0.05	0.20	0.00	0.03	0.00	69.39	0.04	27.87	98.63
DH703	4	0.00	0.01	0.04	0.00	0.00	0.00	0.03	0.00	71.81	0.03	27.56	99.48
DH703	4	0.00	0.01	0.04	0.00	0.00	0.00	0.03	0.00	71.74	0.03	27.52	99.38
DH703	4	0.00	0.67	0.12	0.01	0.01	0.00	0.03	0.00	69.36	0.02	28.38	98.59
DH703	4	0.03	0.08	0.72	0.03	0.16	0.00	0.02	0.00	70.06	0.06	27.70	98.87
DH703	4	0.00	0.06	0.18	0.03	0.06	0.00	0.02	0.00	71.46	0.05	27.69	99.54
DH703	4	0.00	0.04	0.35	0.02	0.02	0.00	0.02	0.00	71.12	0.05	27.60	99.22
DH703	4	0.00	0.02	0.25	0.01	0.01	0.00	0.02	0.00	71.34	0.05	27.55	99.25
DH703	4	0.00	0.08	0.38	0.03	0.09	0.00	0.02	0.00	71.02	0.05	27.74	99.41
DH703	4	0.00	0.07	0.37	0.04	0.05	0.00	0.02	0.00	70.99	0.07	27.68	99.29
DH703	4	0.00	0.01	0.07	0.01	0.01	0.00	0.03	0.00	71.60	0.04	27.51	99.29
DH703	4	0.00	0.01	0.04	0.01	0.01	0.00	0.03	0.00	71.68	0.03	27.51	99.32
DH703	4	0.00	0.02	0.02	0.01	0.03	0.00	0.02	0.00	71.52	0.06	27.46	99.14
DH703	4	0.00	0.02	0.06	0.01	0.01	0.00	0.02	0.00	71.76	0.04	27.57	99.49
DH703	4	0.00	0.03	0.27	0.01	0.03	0.00	0.02	0.00	71.43	0.04	27.64	99.48
DH703	4	0.04	0.16	0.66	0.06	0.17	0.00	0.03	0.00	70.02	0.06	27.89	99.07
DH703	4	0.02	0.08	0.48	0.04	0.15	0.00	0.03	0.00	70.54	0.05	27.69	99.08
DH703	4	0.00	0.02	0.22	0.01	0.02	0.00	0.03	0.00	71.45	0.03	27.60	99.38
DH703	4	0.00	0.02	0.09	0.01	0.01	0.00	0.03	0.00	71.46	0.02	27.49	99.14
DH703	4	0.00	0.05	0.09	0.01	0.01	0.00	0.03	0.00	71.33	0.03	27.52	99.08
DH703	4	0.02	0.03	0.23	0.02	0.03	0.00	0.03	0.00	71.33	0.04	27.61	99.33
DH703	4	0.01	0.04	0.27	0.01	0.04	0.00	0.03	0.00	71.27	0.02	27.61	99.29
DH703	4	0.00	0.05	0.01	0.04	0.01	0.00	0.03	0.00	71.58	0.05	27.57	99.34
DH703	4	0.03	0.10	0.37	0.05	0.14	0.00	0.04	0.00	70.83	0.06	27.82	99.44
DH703	4	0.00	0.01	0.00	0.01	0.00	0.00	0.03	0.00	71.79	0.05	27.53	99.42
DH703	4	0.03	0.14	0.50	0.07	0.13	0.00	0.02	0.00	70.30	0.05	27.77	99.00
DH703	4	0.00	0.01	0.15	0.00	0.00	0.00	0.03	0.01	70.63	0.03	27.21	98.08
DH703	4	0.02	0.03	0.25	0.03	0.05	0.00	0.04	0.00	71.23	0.04	27.61	99.29
DH703	4	0.00	0.02	0.01	0.02	0.00	0.00	0.07	0.01	71.27	0.02	27.42	98.83
DH703	4	0.00	0.06	0.02	0.00	0.08	0.00	0.05	0.01	71.35	0.00	27.56	99.12
DH703	4	0.00	0.02	0.03	0.01	0.03	0.00	0.05	0.01	71.24	0.00	27.41	98.79
DH703	4	0.00	0.00	0.02	0.01	0.01	0.00	0.04	0.00	71.47	0.00	27.42	98.98
DH703	4	0.00	0.01	0.02	0.01	0.01	0.00	0.05	0.01	71.46	0.00	27.44	99.01
DH703	4	0.00	0.01	0.03	0.01	0.01	0.00	0.05	0.01	71.50	0.00	27.47	99.08
DH703	4	0.00	0.06	0.03	0.01	0.02	0.00	0.05	0.01	71.39	0.02	27.58	99.17
DH703	4	0.00	0.01	0.02	0.00	0.02	0.00	0.05	0.00	71.39	0.02	27.43	98.94

DH703	4	0.00	0.01	0.02	0.02	0.02	0.00	0.05	0.01	71.49	0.00	27.46	99.08
DH703	4	0.00	0.01	0.03	0.01	0.03	0.00	0.05	0.01	71.68	0.00	27.54	99.35
DH703	4	0.00	0.01	0.04	0.01	0.05	0.00	0.05	0.00	71.30	0.00	27.41	98.86
DH703	4	0.00	0.03	0.15	0.01	0.03	0.00	0.03	0.00	71.13	0.04	27.44	98.85
DH703	4	0.00	0.01	0.08	0.00	0.01	0.00	0.02	0.00	71.76	0.02	27.56	99.47
DH703	4	0.00	0.01	0.01	0.00	0.01	0.00	0.02	0.00	71.91	0.00	27.54	99.50
DH703	4	0.00	0.02	0.06	0.01	0.01	0.00	0.03	0.00	71.49	0.03	27.46	99.10
DH703	4	0.00	0.05	0.30	0.02	0.05	0.00	0.03	0.00	70.64	0.03	27.43	98.55
DH703	4	0.00	0.01	0.05	0.00	0.00	0.00	0.03	0.00	71.47	0.00	27.42	98.98
DH703	4	0.00	0.01	0.01	0.00	0.01	0.00	0.03	0.00	71.41	0.03	27.37	98.87
DH703	4	0.00	0.02	0.10	0.02	0.01	0.00	0.02	0.00	71.47	0.05	27.50	99.18
DH703	4	0.06	0.22	0.81	0.13	0.26	0.00	0.03	0.00	68.91	0.08	27.84	98.33
DH703	4	0.00	0.02	0.01	0.02	0.00	0.00	0.04	0.00	71.79	0.06	27.59	99.53
DH703	4	0.00	0.02	0.00	0.01	0.00	0.00	0.03	0.00	71.92	0.05	27.61	99.65
DH703	4	0.00	0.02	0.00	0.02	0.00	0.00	0.03	0.00	71.91	0.06	27.61	99.66
DH703	4	0.00	0.03	0.01	0.01	0.00	0.00	0.03	0.00	71.93	0.07	27.64	99.71
DH703	4	0.07	0.19	0.79	0.08	0.27	0.00	0.03	0.00	69.51	0.08	27.97	98.99
DH703	4	0.07	0.19	0.80	0.08	0.28	0.00	0.03	0.00	69.53	0.07	28.00	99.05
DH703	4	0.08	0.20	0.84	0.08	0.29	0.00	0.03	0.00	69.36	0.08	28.00	98.97
DH703	4	0.08	0.21	0.92	0.09	0.31	0.00	0.03	0.00	69.09	0.07	27.99	98.80
DH703	4	0.07	0.20	0.87	0.10	0.29	0.00	0.02	0.00	69.26	0.08	27.96	98.84
DH703	4	0.03	0.10	0.43	0.04	0.11	0.00	0.02	0.00	70.77	0.05	27.79	99.35
DH703	4	0.00	0.02	0.10	0.01	0.04	0.00	0.02	0.00	71.62	0.04	27.56	99.42
DH703	4	0.00	0.04	0.06	0.00	0.01	0.00	0.02	0.00	72.03	0.00	27.71	99.87
ES032	12	0.00	0.05	0.01	0.05	0.01	0.00	0.02	0.00	71.36	0.02	27.46	98.97
ES032	12	0.00	0.03	0.01	0.03	0.00	0.00	0.02	0.00	71.60	0.00	27.49	99.20
ES032	12	0.00	0.04	0.02	0.04	0.00	0.00	0.02	0.00	71.47	0.00	27.48	99.07
ES032	12	0.00	0.07	0.03	0.06	0.01	0.00	0.02	0.00	71.23	0.03	27.49	98.94
ES032	12	0.00	0.04	0.03	0.04	0.00	0.00	0.02	0.00	71.13	0.00	27.36	98.62
ES032	12	0.00	0.06	0.01	0.05	0.00	0.00	0.02	0.00	71.31	0.03	27.46	98.94
ES032	12	0.00	0.05	0.02	0.06	0.01	0.00	0.02	0.00	71.59	0.02	27.57	99.34
ES032	12	0.04	0.06	0.09	0.06	0.03	0.00	0.02	0.00	71.25	0.02	27.56	99.14
ES032	12	0.00	0.05	0.01	0.05	0.01	0.00	0.02	0.00	71.27	0.02	27.42	98.85
ES032	12	0.00	0.05	0.01	0.05	0.01	0.00	0.02	0.00	71.31	0.02	27.45	98.91
ES032	12	0.00	0.04	0.01	0.05	0.01	0.00	0.02	0.00	71.46	0.02	27.48	99.09
ES032	12	0.02	0.11	0.20	0.07	0.07	0.00	0.02	0.00	70.66	0.02	27.56	98.73
ES032	12	0.48	0.09	0.76	0.06	0.27	0.00	0.02	0.00	69.58	0.04	28.03	99.32
ES032	12	0.10	0.07	0.24	0.06	0.10	0.00	0.02	0.00	70.82	0.03	27.63	99.06
ES032	12	0.03	0.06	0.07	0.06	0.03	0.00	0.02	0.00	71.28	0.04	27.54	99.12
ES032	12	0.00	0.05	0.01	0.04	0.01	0.00	0.02	0.00	71.42	0.00	27.47	99.01
ES032	12	0.14	0.06	0.34	0.05	0.13	0.00	0.02	0.00	70.61	0.03	27.65	99.02
ES032	12	0.02	0.05	0.06	0.05	0.03	0.00	0.02	0.00	71.23	0.00	27.47	98.93
ES032	12	0.30	0.13	0.70	0.08	0.25	0.00	0.02	0.00	69.38	0.04	27.85	98.75
ES032	12	0.06	0.07	0.18	0.06	0.07	0.00	0.02	0.00	71.02	0.00	27.61	99.08
ES032	12	0.00	0.05	0.01	0.05	0.01	0.00	0.02	0.00	71.19	0.02	27.39	98.74
ES032	12	0.00	0.05	0.01	0.05	0.02	0.00	0.02	0.00	71.13	0.02	27.38	98.68
ES032	12	0.00	0.06	0.02	0.05	0.01	0.00	0.02	0.00	71.09	0.02	27.39	98.65
ES032	12	0.03	0.07	0.12	0.06	0.01	0.00	0.02	0.00	70.27	0.02	27.23	97.83
ES032	12	0.00	0.05	0.01	0.05	0.00	0.00	0.02	0.00	71.25	0.03	27.42	98.83

ES032	12	0.02	0.06	0.06	0.05	0.02	0.00	0.02	0.00	70.92	0.03	27.38	98.55
ES032	12	0.05	0.05	0.07	0.05	0.02	0.00	0.02	0.00	71.18	0.02	27.50	98.97
ES032	12	0.03	0.05	0.02	0.04	0.01	0.00	0.02	0.00	71.18	0.02	27.43	98.80
ES032	12	0.05	0.11	0.06	0.06	0.03	0.00	0.02	0.00	70.69	0.02	27.47	98.52
ES032	12	0.00	0.05	0.01	0.05	0.00	0.00	0.02	0.00	71.14	0.02	27.39	98.70
ES032	12	0.00	0.05	0.01	0.04	0.01	0.00	0.02	0.00	71.30	0.02	27.44	98.90
ES032	12	0.00	0.05	0.01	0.05	0.01	0.00	0.02	0.00	71.38	0.02	27.46	99.00
ES032	12	0.00	0.05	0.01	0.05	0.00	0.00	0.02	0.00	71.53	0.00	27.52	99.17
ES032	12	0.00	0.05	0.01	0.05	0.03	0.00	0.02	0.00	71.29	0.00	27.43	98.87
ES032	12	0.00	0.05	0.01	0.05	0.01	0.00	0.02	0.00	71.35	0.02	27.45	98.95
ES032	12	0.00	0.08	0.02	0.07	0.01	0.00	0.02	0.00	71.18	0.00	27.49	98.87
ES032	12	0.08	0.05	0.19	0.05	0.08	0.00	0.02	0.00	70.88	0.02	27.52	98.89
ES032	12	0.00	0.04	0.03	0.04	0.03	0.00	0.02	0.00	71.18	0.00	27.38	98.71
ES032	12	0.01	0.04	0.03	0.04	0.02	0.00	0.02	0.00	71.28	0.00	27.44	98.90
ES032	12	0.12	0.07	0.24	0.05	0.08	0.00	0.02	0.00	70.91	0.02	27.65	99.15
ES032	12	0.00	0.04	0.01	0.04	0.02	0.00	0.02	0.00	71.42	0.00	27.47	99.03
ES032	12	0.00	0.05	0.04	0.05	0.03	0.00	0.02	0.00	71.14	0.02	27.41	98.76
ES032	12	0.01	0.05	0.11	0.04	0.08	0.00	0.02	0.00	70.67	0.00	27.32	98.31
ES032	12	0.01	0.06	0.05	0.05	0.03	0.00	0.02	0.00	71.01	0.00	27.40	98.63
ES032	12	0.00	0.05	0.01	0.04	0.01	0.00	0.02	0.00	71.10	0.00	27.36	98.59
ES032	12	0.00	0.05	0.01	0.05	0.01	0.00	0.02	0.00	70.99	0.02	27.33	98.48
ES032	12	0.00	0.07	0.01	0.06	0.01	0.00	0.02	0.00	70.76	0.03	27.29	98.25
ES032	12	0.00	0.05	0.02	0.05	0.01	0.00	0.02	0.00	70.71	0.02	27.23	98.11
ES032	12	0.00	0.05	0.01	0.05	0.00	0.00	0.02	0.00	70.64	0.02	27.19	97.98
ES032	12	0.04	0.06	0.11	0.05	0.03	0.00	0.02	0.00	70.53	0.02	27.30	98.15
ES032	12	0.00	0.05	0.02	0.05	0.01	0.00	0.02	0.00	70.99	0.02	27.33	98.49
ES032	12	0.00	0.05	0.01	0.05	0.01	0.00	0.02	0.00	70.95	0.02	27.31	98.42
ES032	12	0.00	0.05	0.02	0.03	0.02	0.00	0.02	0.00	71.29	0.03	27.43	98.88
ES032	12	0.00	0.05	0.01	0.03	0.01	0.00	0.02	0.00	71.31	0.03	27.44	98.90
ES032	12	0.26	0.07	0.43	0.03	0.11	0.00	0.02	0.00	70.44	0.03	27.76	99.16
ES032	12	0.14	0.10	0.38	0.06	0.13	0.00	0.02	0.00	69.97	0.09	27.56	98.45
ES032	12	0.05	0.08	0.11	0.04	0.03	0.00	0.02	0.00	71.03	0.03	27.55	98.95
ES032	12	0.00	0.04	0.01	0.03	0.01	0.00	0.02	0.00	71.48	0.03	27.47	99.09
ES032	12	0.00	0.06	0.01	0.04	0.01	0.00	0.02	0.00	71.27	0.03	27.44	98.86
ES032	12	0.00	0.03	0.02	0.03	0.01	0.00	0.02	0.00	71.48	0.00	27.45	99.05
ES032	12	0.02	0.07	0.01	0.05	0.00	0.00	0.02	0.00	71.16	0.08	27.46	98.86
LD0987	9	0.00	0.02	0.03	0.01	0.31	0.00	0.04	0.00	71.13	0.02	27.50	99.07
LD0987	9	0.00	0.01	0.04	0.01	0.19	0.00	0.03	0.01	70.85	0.00	27.30	98.44
LD0987	9	0.00	0.01	0.01	0.02	0.12	0.00	0.05	0.00	71.31	0.02	27.46	99.02
LD0987	9	0.00	0.02	0.02	0.01	0.21	0.00	0.03	0.00	71.04	0.02	27.37	98.71
LD0987	9	0.00	0.02	0.02	0.02	0.31	0.00	0.06	0.00	70.95	0.00	27.45	98.83
LD0987	9	0.00	0.02	0.02	0.01	0.19	0.00	0.07	0.00	70.82	0.04	27.36	98.52
LD0987	9	0.00	0.02	0.03	0.00	0.11	0.00	0.07	0.01	70.90	0.03	27.35	98.50
LD0987	9	0.00	0.02	0.01	0.05	0.00	0.00	0.07	0.01	71.51	0.03	27.55	99.25
LD0987	9	0.00	0.02	0.01	0.02	0.00	0.00	0.07	0.00	71.62	0.03	27.56	99.33
LD0987	9	0.00	0.01	0.02	0.01	0.00	0.00	0.06	0.00	71.58	0.02	27.53	99.24
LD0987	9	0.00	0.01	0.01	0.01	0.00	0.00	0.05	0.00	71.58	0.03	27.50	99.20
LD0987	9	0.00	0.01	0.02	0.01	0.01	0.00	0.04	0.00	71.52	0.02	27.44	99.06
LD0987	9	0.02	0.02	0.05	0.04	0.00	0.00	0.08	0.00	71.15	0.03	27.47	98.87

LD0987	9	0.00	0.02	0.01	0.05	0.00	0.00	0.07	0.01	71.22	0.03	27.45	98.85
LD1111	3	0.00	0.04	0.02	0.03	0.01	0.00	0.01	0.00	71.56	0.04	27.50	99.19
LD1111	3	0.00	0.03	0.18	0.02	0.02	0.00	0.01	0.00	71.35	0.04	27.52	99.17
LD1111	3	0.00	0.05	0.04	0.04	0.03	0.00	0.01	0.00	71.48	0.09	27.54	99.29
LD1111	3	0.00	0.02	0.02	0.20	0.02	0.00	0.01	0.00	70.24	0.07	27.06	97.64
LD1111	3	0.00	0.04	0.02	0.08	0.00	0.00	0.01	0.00	70.93	0.05	27.28	98.40
LD1111	3	0.00	0.03	0.02	0.07	0.00	0.00	0.01	0.00	71.64	0.04	27.51	99.30
LD1111	3	0.00	0.03	0.02	0.08	0.01	0.00	0.01	0.00	71.37	0.04	27.42	98.97
LD1111	3	0.00	0.01	0.04	0.06	0.05	0.00	0.01	0.00	71.33	0.03	27.38	98.90
LD1111	3	0.00	0.01	0.06	0.06	0.06	0.00	0.01	0.00	71.34	0.04	27.42	98.99
LD1111	3	0.00	0.01	0.04	0.06	0.07	0.00	0.01	0.00	71.26	0.03	27.37	98.85
LD1111	3	0.00	0.03	0.03	0.22	0.04	0.00	0.01	0.00	71.10	0.11	27.44	98.98
LD1111	3	0.00	0.03	0.02	0.17	0.01	0.00	0.01	0.00	70.01	0.07	26.97	97.29
LD1111	3	0.00	0.04	0.03	0.22	0.02	0.00	0.01	0.00	70.53	0.08	27.22	98.17
LD1111	3	0.00	0.03	0.02	0.26	0.03	0.00	0.01	0.00	70.41	0.12	27.20	98.09
LD1111	3	0.00	0.03	0.03	0.20	0.03	0.00	0.01	0.00	70.83	0.06	27.31	98.51
LD1111	3	0.00	0.03	0.03	0.19	0.04	0.00	0.01	0.00	70.74	0.08	27.28	98.40
LD1111	3	0.00	0.04	0.33	0.37	0.44	0.00	0.01	0.00	69.40	0.09	27.31	97.99
LD1111	3	0.00	0.03	0.13	0.07	0.01	0.00	0.01	0.00	71.24	0.06	27.48	99.04
LD1111	3	0.00	0.04	0.02	0.16	0.02	0.00	0.01	0.00	71.39	0.11	27.54	99.28
LD1111	3	0.00	0.03	0.02	0.10	0.00	0.00	0.01	0.00	70.96	0.05	27.28	98.46
LD1111	3	0.00	0.02	0.02	0.07	0.00	0.00	0.01	0.00	71.25	0.03	27.34	98.74
LD1111	3	0.00	0.03	0.02	0.08	0.00	0.00	0.01	0.00	70.65	0.06	27.14	97.99
LD1111	3	0.03	0.08	0.27	0.08	0.02	0.00	0.01	0.00	70.39	0.04	27.39	98.32
LD1111	3	0.00	0.03	0.02	0.07	0.00	0.00	0.01	0.00	71.85	0.05	27.59	99.61
LD1111	3	0.00	0.02	0.04	0.07	0.00	0.00	0.01	0.00	70.78	0.04	27.19	98.16
LD1111	3	0.00	0.03	0.02	0.09	0.01	0.00	0.02	0.00	71.72	0.04	27.58	99.50
LD1111	3	0.00	0.03	0.30	0.08	0.06	0.00	0.02	0.00	70.50	0.08	27.36	98.43
LD1111	3	0.00	0.03	0.02	0.09	0.00	0.00	0.02	0.00	71.26	0.07	27.42	98.91
LD1111	3	0.00	0.04	0.07	0.10	0.01	0.01	0.02	0.00	71.62	0.08	27.65	99.60
LD1111	3	0.00	0.02	0.12	0.07	0.06	0.00	0.02	0.00	71.47	0.04	27.55	99.35
LD1111	3	0.00	0.03	0.36	0.09	0.03	0.00	0.02	0.00	70.91	0.09	27.57	99.11
LD1111	3	0.00	0.03	0.05	0.09	0.03	0.01	0.02	0.00	71.39	0.17	27.59	99.39
LD1111	3	0.00	0.02	0.03	0.09	0.00	0.00	0.02	0.00	71.11	0.04	27.33	98.65
LD1111	3	0.00	0.03	0.03	0.10	0.01	0.00	0.02	0.00	71.42	0.05	27.46	99.11
LD1111	3	0.01	0.03	0.10	0.19	0.02	0.00	0.02	0.00	71.02	0.16	27.47	99.02
LD1111	3	0.00	0.03	0.10	0.18	0.02	0.00	0.02	0.00	70.61	0.15	27.30	98.39
LD1111	3	0.02	0.05	0.31	0.23	0.02	0.00	0.02	0.00	70.33	0.16	27.45	98.58
LD1111	3	0.00	0.04	0.45	0.19	0.02	0.00	0.02	0.00	70.11	0.17	27.41	98.39
LD1111	3	0.00	0.02	0.15	0.06	0.00	0.00	0.02	0.00	71.04	0.03	27.37	98.69
LD1111	3	0.00	0.03	0.11	0.20	0.04	0.01	0.04	0.00	71.19	0.09	27.60	99.30
LD1111	3	0.00	0.04	0.05	0.08	0.01	0.00	0.02	0.00	71.80	0.05	27.65	99.69
LD1111	3	0.00	0.03	0.06	0.20	0.04	0.00	0.04	0.00	71.10	0.05	27.47	98.99
LD1111	3	0.00	0.03	0.64	0.04	0.01	0.00	0.01	0.00	70.22	0.04	27.45	98.44
LD1111	3	0.00	0.03	0.69	0.04	0.01	0.00	0.01	0.00	70.39	0.05	27.55	98.77
LD1111	3	0.00	0.02	0.33	0.04	0.03	0.00	0.01	0.00	70.72	0.05	27.39	98.59
LD1111	3	0.00	0.02	0.04	0.04	0.04	0.00	0.01	0.00	71.04	0.05	27.29	98.52
LD1111	18	0.00	0.08	0.01	0.08	0.00	0.00	0.01	0.00	71.08	0.04	27.43	98.73
LD1111	18	0.00	0.03	0.00	0.03	0.00	0.00	0.00	0.00	71.72	0.04	27.50	99.32

LD1111	18	0.00	0.06	0.01	0.11	0.00	0.00	0.00	0.00	71.43	0.08	27.52	99.20
LD1111	18	0.00	0.06	0.01	0.09	0.00	0.00	0.01	0.00	71.18	0.04	27.41	98.79
LD1111	18	0.00	0.13	0.07	0.11	0.01	0.00	0.01	0.00	70.74	0.04	27.48	98.58
LD1111	18	0.00	0.13	0.01	0.15	0.00	0.00	0.00	0.00	70.82	0.09	27.51	98.72
LD1111	18	0.00	0.13	0.00	0.12	0.00	0.00	0.01	0.00	70.73	0.07	27.43	98.49
LD1111	18	0.00	0.11	0.01	0.14	0.00	0.00	0.00	0.00	70.89	0.07	27.45	98.66
LD1111	18	0.00	0.08	0.01	0.14	0.00	0.00	0.00	0.00	70.74	0.08	27.33	98.39
LD1111	18	0.00	0.06	0.02	0.08	0.00	0.00	0.00	0.00	71.17	0.05	27.41	98.79
LD1111	18	0.00	0.08	0.01	0.12	0.00	0.00	0.00	0.00	71.09	0.07	27.47	98.85
LD1111	18	0.00	0.09	0.02	0.14	0.00	0.00	0.01	0.00	70.98	0.08	27.45	98.75
LD1111	18	0.00	0.11	0.16	0.11	0.02	0.00	0.01	0.00	70.74	0.07	27.52	98.74
LD1111	18	0.02	0.13	0.17	0.13	0.02	0.00	0.00	0.00	70.46	0.05	27.47	98.45
LD1111	18	0.00	0.11	0.01	0.13	0.00	0.00	0.00	0.00	71.19	0.04	27.56	99.04
LD1111	18	0.00	0.07	0.01	0.09	0.00	0.00	0.01	0.00	71.30	0.04	27.49	99.00
LD1111	18	0.00	0.09	0.01	0.12	0.00	0.00	0.00	0.00	71.19	0.05	27.50	98.97
LD1111	18	0.00	0.06	0.09	0.07	0.01	0.00	0.00	0.00	71.09	0.03	27.43	98.78
LD1111	18	0.00	0.14	0.01	0.12	0.00	0.00	0.00	0.00	70.64	0.06	27.43	98.39
LD1111	18	0.00	0.13	0.01	0.14	0.00	0.00	0.01	0.00	70.87	0.06	27.51	98.72
LD1111	18	0.00	0.02	0.01	0.03	0.00	0.00	0.00	0.00	71.42	0.03	27.39	98.91
LD1111	18	0.00	0.12	0.01	0.18	0.00	0.00	0.00	0.00	70.75	0.11	27.47	98.64
LD1111	18	0.00	0.10	0.01	0.12	0.00	0.00	0.01	0.00	70.77	0.05	27.38	98.44
LD1111	18	0.00	0.11	0.12	0.09	0.01	0.00	0.00	0.00	70.67	0.04	27.45	98.50
LD1111	18	0.02	0.17	0.05	0.13	0.01	0.00	0.00	0.00	70.41	0.07	27.49	98.36
LD1111	18	0.00	0.07	0.01	0.16	0.00	0.00	0.00	0.00	70.83	0.04	27.34	98.45
LD1111	18	0.00	0.06	0.01	0.14	0.00	0.00	0.01	0.00	71.04	0.07	27.41	98.74
LD1111	18	0.00	0.19	0.01	0.16	0.00	0.00	0.00	0.00	70.85	0.08	27.67	98.97
LD1111	18	0.00	0.07	0.01	0.15	0.00	0.00	0.00	0.00	71.16	0.05	27.46	98.90
LD1111	18	0.00	0.06	0.01	0.11	0.00	0.00	0.01	0.00	71.45	0.06	27.53	99.21
LD1111	18	0.00	0.03	0.01	0.08	0.00	0.00	0.01	0.00	71.56	0.04	27.47	99.20
LD1687B	6	0.00	0.04	0.35	0.30	0.01	0.00	0.01	0.00	71.26	0.10	27.77	99.83
LD1687B	6	0.00	0.03	0.40	0.16	0.02	0.00	0.00	0.00	71.65	0.06	27.85	100.17
LD1687B	6	0.00	0.01	0.52	0.11	0.06	0.00	0.00	0.00	71.87	0.04	27.98	100.60
LD1687B	6	0.00	0.03	0.04	0.16	0.02	0.00	0.01	0.00	71.89	0.08	27.67	99.89
LD1687B	6	0.00	0.03	0.17	0.16	0.01	0.00	0.01	0.00	72.05	0.04	27.83	100.30
LD1687B	6	0.00	0.04	0.45	0.18	0.01	0.00	0.00	0.00	71.79	0.09	27.99	100.55
LD1687B	6	0.00	0.04	0.49	0.18	0.01	0.00	0.00	0.00	71.43	0.09	27.88	100.13
LD1687B	6	0.00	0.03	0.73	0.16	0.02	0.00	0.01	0.00	71.20	0.07	27.96	100.18
LD1687B	6	0.00	0.03	0.88	0.18	0.04	0.00	0.01	0.00	70.56	0.10	27.85	99.65
LD1687B	6	0.00	0.06	1.07	0.20	0.03	0.00	0.01	0.00	70.31	0.10	27.97	99.73
LD1687B	6	0.00	0.02	0.07	0.09	0.01	0.00	0.01	0.00	72.51	0.05	27.88	100.64
LD1687B	6	0.00	0.03	0.30	0.15	0.01	0.00	0.01	0.00	72.13	0.07	27.96	100.65
LD1687B	6	0.00	0.04	0.78	0.17	0.02	0.00	0.00	0.00	71.34	0.08	28.06	100.49
LD1687B	6	0.00	0.03	0.13	0.29	0.03	0.00	0.01	0.00	72.09	0.10	27.90	100.58
LD1687B	6	0.04	0.10	0.58	0.67	0.01	0.00	0.00	0.00	68.01	0.27	27.12	96.80
LD1687B	6	0.00	0.04	0.42	0.21	0.00	0.00	0.00	0.00	71.90	0.08	28.01	100.66
LD1687B	6	0.00	0.04	0.21	0.21	0.00	0.00	0.00	0.00	72.26	0.10	27.99	100.81
LD1687B	6	0.00	0.04	0.38	0.21	0.01	0.00	0.00	0.00	71.53	0.10	27.84	100.10
LD1687B	6	0.00	0.04	0.38	0.22	0.00	0.00	0.00	0.00	72.14	0.09	28.08	100.95
LD1687B	6	0.00	0.04	0.36	0.19	0.01	0.00	0.00	0.00	72.07	0.07	28.02	100.77

LD1687B	6	0.00	0.03	0.21	0.19	0.01	0.00	0.01	0.00	72.28	0.07	27.97	100.76
LD1687B	6	0.00	0.03	0.02	0.16	0.00	0.00	0.01	0.00	72.26	0.08	27.80	100.35
LD1687B	6	0.00	0.04	1.00	0.19	0.01	0.00	0.00	0.00	70.51	0.09	27.92	99.76
LD1687B	6	0.00	0.02	0.12	0.82	0.02	0.00	0.00	0.00	70.45	0.66	27.70	99.80
LD1687B	6	0.00	0.03	0.11	0.05	0.00	0.00	0.01	0.00	72.43	0.06	27.88	100.58
LD1687B	6	0.00	0.03	0.51	0.05	0.00	0.00	0.01	0.00	71.64	0.07	27.88	100.19
LD1687B	6	0.00	0.02	0.03	0.05	0.00	0.00	0.01	0.00	72.74	0.07	27.93	100.85
LD1687B	6	0.00	0.02	0.02	0.05	0.01	0.00	0.00	0.00	72.34	0.05	27.76	100.25
LD1687B	6	0.00	0.03	0.59	0.06	0.01	0.00	0.00	0.00	71.61	0.06	27.93	100.28
LD1687B	6	0.00	0.06	1.09	0.13	0.02	0.00	0.01	0.00	70.53	0.07	28.03	99.94
LD1687B	6	0.00	0.03	0.36	0.09	0.00	0.00	0.00	0.00	72.12	0.08	27.98	100.66
LD1687B	6	0.00	0.03	0.13	0.04	0.01	0.00	0.00	0.00	72.18	0.07	27.81	100.27
LD1687B	6	0.00	0.03	0.15	0.05	0.01	0.00	0.00	0.00	72.53	0.06	27.94	100.77
LD1687B	6	0.00	0.02	0.17	0.05	0.01	0.00	0.00	0.00	72.11	0.06	27.78	100.19
LD1687B	6	0.00	0.02	0.35	0.05	0.02	0.00	0.00	0.00	71.96	0.07	27.88	100.36
LD1687B	6	0.00	0.03	1.08	0.05	0.03	0.00	0.00	0.00	70.80	0.06	28.00	100.05
LD1687B	6	0.00	0.03	0.65	0.05	0.05	0.00	0.00	0.00	71.27	0.06	27.86	99.96
LD1687B	6	0.00	0.03	0.47	0.05	0.01	0.00	0.01	0.00	71.71	0.07	27.89	100.24
LD1687B	6	0.00	0.03	0.59	0.06	0.00	0.00	0.01	0.00	71.45	0.07	27.89	100.11
LD1687B	6	0.00	0.03	0.66	0.06	0.00	0.00	0.01	0.00	71.20	0.07	27.85	99.88
LD1687B	6	0.00	0.03	0.57	0.06	0.01	0.00	0.01	0.00	71.76	0.06	27.99	100.49
LD1687B	6	0.00	0.03	0.28	0.06	0.01	0.00	0.00	0.00	71.89	0.06	27.80	100.13
LD1687B	6	0.00	0.03	0.05	0.05	0.01	0.00	0.00	0.00	72.66	0.05	27.92	100.77
LD1687B	6	0.00	0.03	0.03	0.05	0.01	0.00	0.01	0.00	72.38	0.05	27.80	100.35
LD1687B	6	0.00	0.03	0.03	0.05	0.01	0.00	0.00	0.00	72.52	0.04	27.85	100.54
LD1687B	6	0.00	0.03	0.03	0.05	0.02	0.00	0.01	0.00	72.45	0.05	27.84	100.48
LD1687B	6	0.00	0.03	0.52	0.06	0.00	0.00	0.01	0.00	71.40	0.06	27.81	99.90
LD1687B	6	0.00	0.03	0.72	0.05	0.01	0.00	0.01	0.00	71.04	0.10	27.85	99.82
LD1687B	6	0.00	0.02	0.16	0.05	0.01	0.00	0.00	0.00	72.07	0.07	27.77	100.16
LD1687B	6	0.00	0.03	0.04	0.07	0.01	0.00	0.01	0.00	72.06	0.03	27.68	99.91
LD1687B	6	0.00	0.03	0.65	0.07	0.01	0.00	0.01	0.00	71.20	0.07	27.85	99.89
LD1687B	6	0.00	0.03	0.85	0.06	0.01	0.00	0.01	0.00	71.07	0.06	27.94	100.04
LD1687B	6	0.00	0.02	0.63	0.06	0.02	0.00	0.01	0.00	71.34	0.06	27.86	99.99
LD1687B	6	0.00	0.03	0.64	0.06	0.02	0.00	0.01	0.00	70.99	0.07	27.75	99.56
LD1687B	6	0.00	0.02	0.02	0.06	0.02	0.00	0.01	0.00	72.40	0.04	27.80	100.37
LD1687B	6	0.00	0.02	0.02	0.06	0.04	0.00	0.01	0.00	72.10	0.05	27.68	99.96
LD1687B	6	0.00	0.02	0.03	0.06	0.06	0.00	0.01	0.00	72.15	0.05	27.73	100.11
LD1687B	6	0.00	0.03	0.46	0.07	0.01	0.00	0.01	0.00	71.45	0.06	27.80	99.89
LD1687B	6	0.00	0.02	0.18	0.07	0.01	0.00	0.01	0.00	71.85	0.02	27.69	99.85
LD1687B	6	0.00	0.03	0.74	0.07	0.01	0.00	0.01	0.00	70.89	0.12	27.81	99.68
LD1687B	6	0.00	0.03	0.49	0.09	0.01	0.00	0.01	0.00	71.43	0.09	27.84	100.00
LD1687B	6	0.00	0.02	0.05	0.07	0.01	0.00	0.01	0.00	72.11	0.07	27.71	100.06
LD1687B	6	0.00	0.02	0.26	0.09	0.01	0.00	0.01	0.00	72.05	0.04	27.85	100.33
LD1687B	6	0.00	0.02	0.33	0.08	0.01	0.00	0.01	0.00	71.94	0.05	27.86	100.30
LD1687B	6	0.00	0.03	0.25	0.06	0.02	0.00	0.01	0.00	72.01	0.07	27.85	100.30
LD1687B	6	0.00	0.03	0.30	0.09	0.04	0.00	0.01	0.00	71.81	0.06	27.84	100.18
LD1687B	6	0.00	0.07	1.04	0.09	0.02	0.00	0.01	0.00	70.84	0.03	28.11	100.21
LD1687B	6	0.00	0.08	0.96	0.09	0.03	0.00	0.01	0.00	70.93	0.05	28.11	100.25
LD1687B	6	0.00	0.04	0.14	0.06	0.01	0.00	0.01	0.00	72.41	0.04	27.93	100.64

LD1687B	6	0.00	0.04	0.26	0.08	0.03	0.00	0.01	0.00	72.23	0.04	27.98	100.68
LD1687B	6	0.00	0.04	0.05	0.07	0.01	0.01	0.01	0.00	72.51	0.05	27.91	100.65
LD1687B	6	0.00	0.03	0.06	0.09	0.01	0.00	0.01	0.00	72.23	0.07	27.83	100.33
LD1687B	6	0.00	0.04	0.31	0.11	0.00	0.00	0.01	0.00	71.90	0.07	27.89	100.32
LD1687B	12	0.17	0.21	0.83	0.11	0.05	0.00	0.02	0.01	69.60	0.02	28.05	99.08
LD1687B	12	0.07	0.12	0.37	1.01	0.03	0.00	0.02	0.01	70.05	0.14	27.99	99.81
LD1687B	12	0.00	0.03	0.01	0.11	0.02	0.00	0.03	0.00	71.77	0.05	27.64	99.66
LD1687B	12	0.10	0.13	0.29	0.15	0.01	0.00	0.03	0.00	70.80	0.03	27.82	99.37
LD1687B	12	0.12	0.19	0.56	1.17	0.05	0.00	0.02	0.01	69.11	0.09	28.05	99.36
LD1687B	12	0.00	0.05	0.01	0.12	0.00	0.00	0.03	0.01	71.80	0.03	27.68	99.72
LD1687B	12	0.00	0.04	0.02	0.09	0.00	0.00	0.03	0.01	71.85	0.03	27.68	99.74
LD1687B	12	0.00	0.03	0.02	0.08	0.00	0.00	0.03	0.01	71.75	0.02	27.62	99.56
LD1687B	12	0.00	0.03	0.02	0.07	0.00	0.00	0.03	0.01	71.86	0.00	27.65	99.67
LD1687B	12	0.00	0.05	0.01	0.11	0.00	0.00	0.03	0.02	71.76	0.05	27.70	99.73
LD1687B	12	0.00	0.05	0.02	0.08	0.00	0.00	0.02	0.02	71.59	0.02	27.61	99.41
LD1687B	12	0.00	0.05	0.03	0.09	0.01	0.00	0.02	0.00	71.73	0.05	27.65	99.63
LD1687B	12	0.00	0.05	0.04	0.07	0.01	0.00	0.02	0.00	71.70	0.06	27.64	99.60
LD1687B	12	0.02	0.04	0.13	0.08	0.00	0.00	0.03	0.01	71.46	0.03	27.65	99.45
LD1687B	12	0.00	0.00	0.09	0.00	0.02	0.00	0.00	0.00	71.62	0.00	27.43	99.16
LD1687B	12	0.00	0.03	0.02	0.07	0.00	0.00	0.02	0.03	71.35	0.02	27.46	99.00
LD1687B	12	0.06	0.16	0.50	0.17	0.10	0.00	0.02	0.00	70.33	0.08	27.90	99.31
LD1687B	12	0.09	0.12	0.26	0.25	0.01	0.00	0.02	0.00	70.48	0.03	27.65	98.89
LD1687B	12	0.00	0.07	0.01	0.13	0.01	0.00	0.02	0.01	71.36	0.05	27.58	99.24
LD1687B	12	0.04	0.11	0.60	0.15	0.10	0.00	0.02	0.00	69.84	0.05	27.64	98.55
LD1687B	12	0.02	0.13	0.54	0.18	0.10	0.00	0.02	0.00	69.41	0.06	27.47	97.92
LD1687B	12	0.00	0.05	0.24	0.15	0.03	0.00	0.02	0.00	70.58	0.04	27.40	98.49
LD1687B	12	0.00	0.03	0.06	0.11	0.00	0.00	0.02	0.00	71.15	0.03	27.42	98.83
LD1687B	12	0.02	0.04	0.45	0.22	0.00	0.00	0.02	0.00	70.31	0.02	27.47	98.56
LD1687B	12	0.02	0.05	0.31	0.12	0.00	0.00	0.02	0.01	71.00	0.04	27.61	99.16
LD1687B	12	0.00	0.04	0.14	0.10	0.00	0.00	0.02	0.01	71.34	0.03	27.56	99.25
LD1687B	12	0.02	0.15	0.92	0.14	0.12	0.00	0.03	0.01	69.81	0.04	27.97	99.21
LD1687B	34	0.00	0.04	0.01	0.12	0.00	0.00	0.04	0.00	71.24	0.08	27.48	99.01
LD1687B	34	0.07	0.07	0.44	0.10	0.11	0.00	0.03	0.00	70.46	0.09	27.68	99.05
LD1687B	34	0.40	0.15	0.88	0.16	0.26	0.00	0.03	0.00	69.07	0.12	28.10	99.18
LD1687B	34	0.16	0.11	0.45	0.13	0.14	0.00	0.03	0.00	70.10	0.10	27.76	98.99
LD1687B	34	0.14	0.10	0.37	0.11	0.10	0.00	0.03	0.00	70.42	0.09	27.75	99.10
LD1687B	34	0.07	0.06	0.14	0.09	0.03	0.00	0.03	0.00	71.13	0.08	27.63	99.26
LD1687B	34	0.21	0.21	0.49	0.07	0.01	0.00	0.03	0.00	68.64	0.15	27.45	97.25
LD1687B	34	0.15	0.07	0.33	0.13	0.10	0.00	0.03	0.00	70.91	0.08	27.83	99.62
LD1687B	34	0.18	0.08	0.44	0.16	0.16	0.00	0.03	0.00	70.16	0.10	27.75	99.06
LD1687B	34	0.37	0.06	0.44	0.10	0.10	0.00	0.03	0.00	70.47	0.04	27.90	99.51
LD1687B	34	0.00	0.05	0.01	0.09	0.00	0.00	0.03	0.00	71.25	0.04	27.46	98.94
LD1687B	34	0.36	0.18	0.83	0.19	0.24	0.00	0.03	0.00	68.08	0.07	27.71	97.69
LD1687B	34	0.18	0.12	0.53	0.16	0.13	0.00	0.03	0.00	68.72	0.05	27.35	97.28
LD1687B	34	0.16	0.09	0.48	0.18	0.12	0.00	0.03	0.00	69.99	0.14	27.73	98.93
LD1687B	34	0.00	0.06	0.01	0.16	0.00	0.00	0.03	0.00	71.27	0.10	27.54	99.17
LD1687B	34	0.47	0.16	0.99	0.11	0.28	0.00	0.03	0.00	68.63	0.13	28.09	98.89
LD1687B	34	0.17	0.07	0.46	0.07	0.05	0.00	0.03	0.00	70.45	0.09	27.73	99.13
LD1687B	34	0.35	0.10	0.73	0.07	0.22	0.00	0.03	0.00	69.68	0.10	27.97	99.24

LD1687B	34	0.37	0.22	0.86	0.13	0.22	0.00	0.03	0.00	67.93	0.13	27.77	97.67
LD1687B	34	0.29	0.19	0.77	0.11	0.21	0.00	0.03	0.00	68.29	0.12	27.67	97.67
LD1687B	34	0.37	0.49	0.61	0.18	0.16	0.00	0.03	0.00	66.78	0.11	27.81	96.52
LD1687B	34	0.00	0.05	0.01	0.07	0.00	0.00	0.03	0.00	71.45	0.04	27.52	99.17
LD1687B	34	0.01	0.07	0.01	0.09	0.00	0.00	0.03	0.00	71.25	0.08	27.55	99.09
LD1687B	34	0.00	0.04	0.01	0.07	0.00	0.00	0.04	0.00	71.72	0.00	27.61	99.48
LD1687B	34	0.08	0.06	0.18	0.10	0.06	0.00	0.04	0.00	71.10	0.08	27.70	99.40
LD1687B	34	0.19	0.09	0.37	0.31	0.11	0.00	0.04	0.00	70.31	0.16	27.88	99.47
LD1687B	34	0.22	0.07	0.47	0.10	0.17	0.00	0.04	0.00	70.46	0.07	27.87	99.46
LD1687B	34	0.26	0.11	0.57	0.23	0.19	0.00	0.04	0.00	69.84	0.10	27.95	99.29
LD1687B	34	0.00	0.04	0.01	0.10	0.00	0.00	0.04	0.00	71.70	0.06	27.65	99.60
LD1687B	34	0.00	0.04	0.01	0.04	0.01	0.00	0.04	0.00	68.78	0.03	28.16	99.09
LD1687B	34	0.00	0.05	0.03	0.12	0.01	0.00	0.04	0.00	71.44	0.05	27.60	99.34
LD1687B	34	0.21	0.11	0.47	0.17	0.15	0.00	0.04	0.00	70.04	0.10	27.85	99.14
LD1687B	43	0.00	0.02	0.02	0.07	0.02	0.00	0.03	0.02	70.12	0.03	26.98	97.31
LD1687B	43	0.00	0.03	0.08	0.07	0.06	0.00	0.03	0.01	72.21	0.06	27.87	100.43
LD1687B	43	0.00	0.03	0.02	0.10	0.04	0.00	0.03	0.01	72.50	0.05	27.92	100.70
LD1687B	43	0.00	0.03	0.03	0.07	0.03	0.00	0.03	0.01	72.59	0.03	27.94	100.76
LD1687B	43	0.00	0.01	0.03	0.05	0.02	0.00	0.03	0.01	70.03	0.03	26.91	97.12
LD1687B	43	0.00	0.02	0.03	0.07	0.05	0.00	0.02	0.00	71.16	0.04	27.39	98.79
LD1687B	43	0.00	0.07	0.16	0.10	0.05	0.00	0.03	0.01	72.09	0.04	27.99	100.52
LD1687B	43	0.00	0.01	0.02	0.05	0.01	0.00	0.03	0.01	72.67	0.03	27.91	100.73
LD1687B	43	0.00	0.02	0.02	0.02	0.00	0.00	0.03	0.02	72.72	0.03	27.95	100.82
LD1687B	43	0.00	0.03	0.06	0.06	0.04	0.00	0.02	0.01	72.16	0.04	27.80	100.22
LD1687B	43	0.00	0.02	0.05	0.09	0.03	0.00	0.03	0.01	72.54	0.05	27.95	100.78
LD1687B	43	0.00	0.05	0.01	0.13	0.00	0.00	0.03	0.07	72.15	0.04	27.94	100.41
LD1687B	43	0.00	0.03	0.01	0.08	0.00	0.00	0.03	0.01	72.52	0.04	27.91	100.62
LD1687B	43	0.00	0.01	0.01	0.05	0.00	0.00	0.02	0.02	72.70	0.03	27.92	100.78
LD1687B	43	0.00	0.05	0.01	0.12	0.00	0.00	0.03	0.19	72.24	0.04	28.18	100.85
LD1687B	43	0.37	0.11	0.96	0.13	0.32	0.00	0.03	0.04	70.03	0.05	28.47	100.52
LD1687B	43	0.38	0.11	1.02	0.13	0.36	0.00	0.03	0.04	69.69	0.04	28.39	100.18
LD1687B	43	0.13	0.04	0.26	0.08	0.09	0.00	0.03	0.04	71.88	0.03	28.08	100.64
LD1687B	43	0.00	0.03	0.01	0.07	0.00	0.00	0.03	0.03	72.60	0.04	27.97	100.78
LD1687B	43	0.00	0.03	0.02	0.08	0.00	0.00	0.03	0.03	72.57	0.04	27.95	100.73
LD1687B	43	0.00	0.02	0.01	0.04	0.00	0.00	0.03	0.02	72.73	0.02	27.96	100.83
LD1687B	43	0.00	0.02	0.01	0.05	0.01	0.00	0.03	0.01	72.51	0.03	27.86	100.53
LD1687B	43	0.00	0.03	0.02	0.10	0.04	0.00	0.02	0.14	71.89	0.03	27.93	100.21
LD1687B	43	0.00	0.03	0.00	0.10	0.01	0.00	0.03	0.06	72.34	0.05	27.92	100.53
LD1687B	43	0.17	0.07	0.45	0.10	0.15	0.00	0.03	0.39	70.51	0.04	28.51	100.43
LD1687B	43	0.00	0.02	0.02	0.10	0.01	0.00	0.03	0.04	72.34	0.06	27.89	100.51
LD1687B	43	0.00	0.01	0.02	0.01	0.03	0.00	0.03	0.00	70.78	0.03	27.16	98.06
LD1687B	43	0.01	0.01	0.05	0.01	0.06	0.00	0.03	0.00	70.14	0.02	26.96	97.28
LD1687B	43	0.00	0.02	0.04	0.01	0.02	0.00	0.03	0.00	70.25	0.00	26.98	97.35
LD1687B	43	0.00	0.01	0.03	0.01	0.01	0.00	0.03	0.00	70.56	0.04	27.07	97.75
LD1687B	43	0.00	0.02	0.03	0.07	0.00	0.00	0.03	0.00	72.10	0.03	27.71	99.97
LD1687B	43	0.00	0.04	0.01	0.11	0.00	0.00	0.03	0.00	72.44	0.05	27.90	100.59
LD1687B	43	0.19	0.12	0.49	0.10	0.15	0.00	0.02	0.00	71.17	0.08	28.23	100.55
LD1687B	43	0.03	0.04	0.07	0.05	0.03	0.00	0.02	0.00	72.34	0.04	27.92	100.54
LD1687B	43	0.15	0.12	0.62	0.06	0.10	0.00	0.03	0.00	71.41	0.05	28.35	100.90

LD1687B	43	0.43	0.26	1.03	0.09	0.22	0.00	0.03	0.00	68.89	0.06	28.38	99.39
LD1687B	43	0.02	0.08	0.16	0.09	0.02	0.00	0.02	0.00	72.00	0.09	27.98	100.47
LD1687B	43	0.38	0.17	1.00	0.15	0.32	0.00	0.02	0.00	70.19	0.07	28.66	100.96
LD1687B	43	0.20	0.15	0.63	0.11	0.20	0.00	0.02	0.00	70.95	0.05	28.35	100.66
LD1687B	43	0.14	0.06	0.27	0.11	0.10	0.00	0.03	0.00	72.23	0.03	28.23	101.19
LD1687B	43	0.25	0.16	0.72	0.13	0.23	0.00	0.03	0.00	70.93	0.05	28.52	101.02
LD1687B	43	0.28	0.16	0.78	0.13	0.25	0.00	0.03	0.00	70.51	0.05	28.45	100.64
LD1687B	43	0.21	0.14	0.53	0.13	0.16	0.00	0.03	0.00	71.48	0.03	28.44	101.15
LD1687B	43	0.02	0.06	0.04	0.10	0.01	0.00	0.03	0.00	72.91	0.02	28.15	101.33
LD1687B	43	0.05	0.08	0.17	0.11	0.05	0.00	0.03	0.00	72.48	0.05	28.21	101.23
LD1687B	43	0.10	0.09	0.42	0.06	0.09	0.00	0.02	0.00	71.62	0.06	28.15	100.62
LD1687B	43	0.14	0.08	0.36	0.06	0.03	0.00	0.02	0.00	71.94	0.06	28.18	100.86
LD1687B	43	0.15	0.13	0.29	0.10	0.13	0.00	0.03	0.00	71.32	0.05	28.12	100.32
LD1687B	43	0.20	0.12	0.73	0.07	0.15	0.00	0.03	0.00	71.00	0.07	28.35	100.72
LD1687B	43	0.44	0.21	1.10	0.09	0.38	0.00	0.03	0.00	69.28	0.09	28.56	100.19
LD1687B	43	0.32	0.22	1.19	0.11	0.27	0.00	0.03	0.00	69.49	0.09	28.57	100.28
LD1687B	43	0.26	0.19	0.71	0.09	0.20	0.00	0.03	0.00	70.44	0.07	28.39	100.39
LD1687B	43	0.07	0.10	0.24	0.06	0.07	0.00	0.02	0.00	71.84	0.05	28.07	100.52
LD1687B	43	0.29	0.15	0.68	0.09	0.23	0.00	0.02	0.00	70.52	0.07	28.34	100.40
LD1687B	43	0.00	0.06	0.02	0.05	0.01	0.00	0.03	0.00	72.68	0.04	28.03	100.92
LD1687B	43	0.10	0.04	0.20	0.14	0.06	0.00	0.03	0.01	72.27	0.03	28.12	100.99
LD1687B	43	0.00	0.05	0.01	0.09	0.00	0.00	0.03	0.01	72.53	0.02	27.95	100.68
LD1687B	43	0.22	0.09	0.39	0.15	0.11	0.00	0.03	0.01	71.62	0.05	28.29	100.95
LD1687B	43	0.32	0.13	0.82	0.17	0.28	0.00	0.03	0.01	70.31	0.03	28.39	100.48
LD1687B	43	0.29	0.10	0.65	0.16	0.21	0.00	0.03	0.01	70.93	0.05	28.36	100.78
LD1687B	43	0.18	0.07	0.35	0.13	0.11	0.00	0.03	0.01	71.85	0.03	28.23	100.98
LD1687B	43	0.04	0.05	0.08	0.12	0.02	0.00	0.03	0.01	72.54	0.04	28.07	100.99
LD1687B	43	0.10	0.06	0.23	0.10	0.07	0.00	0.03	0.00	71.98	0.03	28.08	100.69
LD1687B	43	0.18	0.07	0.37	0.15	0.09	0.00	0.03	0.00	71.87	0.07	28.26	101.08
LD1687B	43	0.00	0.05	0.04	0.10	0.02	0.00	0.03	0.01	72.51	0.03	27.98	100.75
LD1687B	43	0.00	0.05	0.06	0.10	0.02	0.00	0.03	0.01	72.61	0.03	28.04	100.95
LD1687B	43	0.00	0.04	0.04	0.12	0.02	0.00	0.03	0.00	72.42	0.03	27.91	100.60
LD1687B	43	0.00	0.05	0.04	0.12	0.01	0.00	0.03	0.00	72.52	0.04	27.98	100.80
LD1687B	43	0.11	0.06	0.17	0.12	0.05	0.00	0.03	0.00	72.13	0.05	28.07	100.77
LD1687B	43	0.19	0.09	0.40	0.17	0.12	0.00	0.03	0.00	71.37	0.04	28.19	100.61
LD1687B	43	0.12	0.09	0.35	0.17	0.11	0.00	0.03	0.00	71.51	0.05	28.12	100.53
LD1687B	43	0.05	0.05	0.19	0.14	0.06	0.00	0.03	0.00	71.95	0.05	27.97	100.50
LD1687B	43	0.21	0.07	0.64	0.16	0.18	0.00	0.03	0.00	70.91	0.05	28.17	100.42
LD1687B	43	0.03	0.05	0.14	0.14	0.02	0.00	0.03	0.00	72.10	0.02	27.94	100.48
LD1687B	43	0.34	0.06	0.67	0.17	0.20	0.00	0.03	0.00	70.75	0.06	28.24	100.52
LD1687B	43	0.06	0.05	0.18	0.13	0.06	0.00	0.03	0.00	71.67	0.03	27.86	100.08
LD1687B	43	0.12	0.06	0.35	0.11	0.14	0.00	0.03	0.00	71.70	0.04	28.10	100.65
LD1687B	43	0.00	0.04	0.02	0.16	0.06	0.00	0.03	0.00	72.74	0.08	28.10	101.22
LD1687B	43	0.00	0.05	0.02	0.10	0.00	0.00	0.03	0.00	72.65	0.02	28.02	100.90
LD1687B	43	0.00	0.05	0.01	0.14	0.00	0.00	0.03	0.00	72.73	0.00	28.03	100.98
LD1687B	43	0.00	0.08	0.01	0.11	0.00	0.00	0.03	0.01	72.60	0.06	28.08	100.98
LD1687B	43	0.00	0.06	0.01	0.08	0.00	0.00	0.03	0.00	73.27	0.03	28.26	101.74
LD1687B	43	0.07	0.07	0.18	0.10	0.07	0.00	0.03	0.00	72.17	0.02	28.08	100.80
LD1687B	43	0.00	0.05	0.05	0.08	0.02	0.00	0.02	0.00	72.77	0.04	28.08	101.12

LD1687B	43	0.16	0.06	0.37	0.10	0.13	0.00	0.02	0.00	71.55	0.03	28.09	100.52
LD1687B	43	0.19	0.07	0.42	0.11	0.14	0.00	0.02	0.00	72.22	0.05	28.43	101.66
LD1687B	43	0.19	0.10	0.49	0.10	0.14	0.00	0.03	0.00	71.69	0.03	28.37	101.15
LD1687B	43	0.25	0.15	0.77	0.13	0.25	0.00	0.03	0.00	70.72	0.04	28.45	100.78
LD1687B	52	0.00	0.04	0.01	0.08	0.01	0.00	0.07	0.00	70.43	0.02	27.19	97.85
LD1687B	52	0.00	0.08	0.02	0.07	0.03	0.00	0.06	0.00	69.24	0.02	26.84	96.37
LD1687B	52	0.35	0.07	0.75	0.63	0.33	0.00	0.06	0.00	69.19	0.03	28.08	99.51
LD1687B	52	0.04	0.03	0.04	1.19	0.02	0.00	0.06	0.01	70.78	0.08	27.86	100.11
LD1687B	52	0.00	0.02	0.01	0.09	0.01	0.00	0.06	0.02	71.38	0.02	27.51	99.12
LD1687B	52	0.00	0.01	0.02	0.04	0.04	0.00	0.06	0.02	71.48	0.02	27.53	99.21
LD1687B	52	0.00	0.02	0.02	0.11	0.03	0.00	0.06	0.02	69.41	0.00	26.80	96.48
LD1687B	52	0.00	0.04	0.01	0.10	0.01	0.00	0.07	0.03	71.27	0.02	27.57	99.11
LD1687B	52	0.28	0.04	0.57	0.07	0.17	0.00	0.05	0.02	70.26	0.02	27.90	99.39
LD1687B	52	0.00	0.02	0.03	0.02	0.04	0.00	0.06	0.02	70.44	0.00	27.14	97.76
LD1687B	52	0.00	0.05	0.01	0.30	0.00	0.00	0.07	0.01	71.24	0.02	27.63	99.33
LD1687B	52	0.00	0.08	0.01	0.14	0.00	0.00	0.07	0.00	71.59	0.00	27.75	99.64
LD1687B	52	0.07	0.08	0.18	0.22	0.05	0.00	0.07	0.02	71.26	0.03	27.91	99.88
LD1687B	52	0.00	0.01	0.02	0.45	0.02	0.00	0.07	0.01	70.55	0.04	27.36	98.53
LD1687B	52	0.00	0.06	0.05	0.91	0.00	0.00	0.06	0.00	70.81	0.04	27.78	99.72
LD1687B	52	0.00	0.03	0.01	0.08	0.03	0.00	0.06	0.03	71.46	0.02	27.61	99.34
LD1687B	52	0.00	0.07	0.03	0.19	0.01	0.00	0.07	0.00	69.10	0.03	26.82	96.33
LD1687B	52	0.12	0.05	0.25	0.13	0.07	0.00	0.07	0.00	71.37	0.00	27.90	99.95
LD1687B	58	0.00	0.01	0.02	0.43	0.26	0.00	0.03	0.00	71.37	0.03	27.69	99.83
LD1687B	58	0.01	0.12	0.09	0.28	0.11	0.00	0.04	0.00	70.80	0.02	27.70	99.18
LD1687B	58	0.00	0.07	0.01	0.26	0.09	0.00	0.04	0.00	71.36	0.02	27.69	99.55
LD1687B	58	0.02	0.09	0.04	0.11	0.01	0.00	0.04	0.01	71.29	0.02	27.65	99.29
LD1687B	58	0.00	0.06	0.01	0.10	0.03	0.00	0.05	0.00	71.31	0.04	27.55	99.14
LD1687B	58	0.00	0.05	0.01	0.10	0.01	0.00	0.05	0.00	71.49	0.03	27.61	99.36
LD1687B	58	0.00	0.04	0.01	0.08	0.01	0.00	0.05	0.00	71.49	0.00	27.55	99.24
LD1687B	58	0.00	0.06	0.03	0.09	0.02	0.00	0.05	0.00	68.75	0.03	26.58	95.60
LD1687B	58	0.24	0.10	0.57	0.14	0.23	0.00	0.05	0.00	70.15	0.05	27.99	99.53
LD1687B	58	0.00	0.07	0.01	0.12	0.00	0.00	0.05	0.00	71.61	0.03	27.68	99.56
LD1687B	58	0.36	0.29	0.56	0.05	0.04	0.00	0.04	0.00	67.36	0.06	27.37	96.13
LD1687B	58	0.01	0.05	0.02	0.07	0.00	0.00	0.04	0.00	71.53	0.02	27.59	99.34
LD1687B	58	0.02	0.07	0.01	0.09	0.01	0.00	0.05	0.00	71.20	0.08	27.55	99.07
LD1687B	58	0.03	0.10	0.02	0.10	0.01	0.00	0.04	0.00	71.29	0.09	27.69	99.37
LD1687B	58	0.32	0.18	0.76	0.11	0.16	0.00	0.04	0.00	69.45	0.12	28.11	99.25
LD1687B	58	0.00	0.11	0.02	0.09	0.25	0.00	0.04	0.00	70.13	0.03	27.34	98.01
LD1687B	58	0.00	0.15	0.33	0.04	0.12	0.00	0.03	0.00	69.64	0.00	27.39	97.71
LD1687B	58	0.04	0.07	0.10	0.09	0.04	0.00	0.03	0.00	71.15	0.02	27.60	99.15
LD1687B	58	0.31	0.07	0.42	0.09	0.13	0.00	0.03	0.00	70.47	0.02	27.88	99.43
LD1687B	58	0.88	0.35	0.69	0.05	0.08	0.00	0.04	0.00	68.06	0.03	28.33	98.51
LD1687B	58	0.23	0.05	0.40	0.09	0.14	0.00	0.04	0.00	70.37	0.03	27.72	99.08
LD1687B	58	0.47	0.10	0.79	0.10	0.26	0.00	0.04	0.00	69.39	0.04	28.03	99.22
LD1687B	58	0.56	0.17	0.76	0.10	0.27	0.00	0.04	0.00	68.98	0.04	28.13	99.04
LD1687B	58	0.35	0.12	0.40	0.11	0.11	0.00	0.04	0.00	70.19	0.02	27.92	99.26
LD1687B	58	0.14	0.08	0.28	0.08	0.07	0.00	0.04	0.00	70.61	0.02	27.67	99.00
LD1687B	58	0.06	0.06	0.14	0.09	0.05	0.00	0.04	0.00	71.13	0.03	27.64	99.24
LD1687B	58	0.11	0.07	0.18	0.10	0.06	0.00	0.04	0.00	70.79	0.02	27.60	98.96

LD1687B	58	0.32	0.08	0.57	0.10	0.18	0.00	0.04	0.00	70.25	0.06	28.00	99.61
LD1687B	58	0.21	0.09	0.39	0.09	0.15	0.00	0.04	0.00	70.52	0.04	27.86	99.40
LD1687B	58	0.25	0.17	0.52	0.13	0.10	0.00	0.04	0.00	69.71	0.03	27.89	98.84
LD1687B	58	0.03	0.06	0.08	0.10	0.02	0.00	0.04	0.00	71.55	0.04	27.70	99.61
LD1687B	58	0.00	0.08	0.01	0.10	0.00	0.00	0.04	0.00	71.60	0.02	27.68	99.54
LD1687B	58	0.00	0.09	0.01	0.11	0.00	0.00	0.04	0.00	71.08	0.03	27.52	98.87
LD1687B	58	0.00	0.04	0.01	0.04	0.01	0.00	0.04	0.00	68.78	0.03	26.50	95.45
LD1687B	58	0.31	0.22	0.86	0.15	0.32	0.00	0.04	0.00	68.61	0.04	28.03	98.58
LD1687B	58	0.14	0.13	0.37	0.10	0.12	0.00	0.04	0.00	70.27	0.04	27.79	99.01
LD1687B	58	0.00	0.09	0.01	0.08	0.00	0.00	0.05	0.00	71.22	0.02	27.57	99.04
LD1687B	58	0.01	0.10	0.05	0.10	0.02	0.00	0.05	0.00	70.80	0.00	27.49	98.63
LD1687B	58	0.34	0.22	0.93	0.17	0.32	0.00	0.04	0.00	68.80	0.07	28.18	99.05
LD1687B	61	0.00	0.01	0.01	0.04	0.01	0.00	0.07	0.00	72.86	0.07	28.07	101.15
LD1687B	61	0.00	0.05	0.01	0.02	0.00	0.00	0.07	0.01	72.88	0.03	28.13	101.20
LD1687B	61	0.00	0.02	0.01	0.00	0.09	0.00	0.06	0.01	72.71	0.02	28.02	100.94
LD1687B	61	0.00	0.02	0.00	0.01	0.01	0.00	0.08	0.01	72.84	0.02	28.04	101.03
LD1687B	61	0.00	0.02	0.02	0.01	0.02	0.00	0.07	0.01	72.96	0.00	28.08	101.18
LD1687B	61	0.00	0.05	0.01	0.03	0.00	0.00	0.07	0.02	72.98	0.04	28.20	101.39
LD1687B	61	0.00	0.04	0.01	0.02	0.01	0.00	0.07	0.00	72.75	0.05	28.05	100.99
LD1687B	61	0.00	0.06	0.04	0.00	0.01	0.00	0.07	0.01	69.74	0.00	26.97	96.90
LD1687B	61	0.00	0.01	0.03	0.00	0.01	0.00	0.07	0.01	72.79	0.02	28.01	100.94
LD1687B	61	0.00	0.01	0.05	0.00	0.00	0.00	0.07	0.01	70.22	0.00	27.03	97.38
LD1687B	61	0.00	0.02	0.01	0.02	0.07	0.00	0.07	0.01	72.54	0.03	27.97	100.74
LD1687B	61	0.00	0.03	0.01	0.02	0.07	0.00	0.07	0.01	72.36	0.00	27.94	100.51
LD1687B	61	0.00	0.04	0.01	0.02	0.06	0.00	0.07	0.01	72.25	0.00	27.90	100.36
LD1687B	61	0.00	0.03	0.02	0.03	0.06	0.00	0.07	0.01	72.61	0.00	28.03	100.86
LD1687B	61	0.00	0.03	0.02	0.03	0.06	0.00	0.07	0.01	72.68	0.00	28.06	100.97
LD1687B	61	0.00	0.03	0.02	0.05	0.07	0.00	0.07	0.01	72.56	0.02	28.03	100.87
LD1687B	61	0.00	0.04	0.01	0.02	0.00	0.00	0.07	0.02	72.75	0.00	28.07	100.99
LD1687B	61	0.00	0.04	0.02	0.02	0.01	0.00	0.07	0.01	72.73	0.02	28.06	100.97
LD1687B	61	0.00	0.02	0.05	0.01	0.02	0.00	0.07	0.01	73.06	0.02	28.16	101.41
LD1687B	61	0.00	0.03	0.01	0.02	0.00	0.00	0.07	0.01	72.84	0.00	28.06	101.04
LD1687B	61	0.00	0.06	0.07	0.03	0.04	0.00	0.07	0.01	72.28	0.02	27.99	100.56
LD1687B	61	0.00	0.04	0.01	0.04	0.04	0.00	0.07	0.01	72.75	0.02	28.10	101.09
LD1687B	61	0.00	0.01	0.01	0.07	0.06	0.00	0.07	0.01	71.04	0.02	27.38	98.68
LD1687B	61	0.00	0.01	0.02	0.06	0.03	0.00	0.06	0.00	70.52	0.03	27.14	97.87
LD1687B	61	0.00	0.06	0.01	0.04	0.00	0.00	0.07	0.01	72.69	0.03	28.11	101.03
LD1687B	61	0.00	0.06	0.01	0.04	0.01	0.00	0.07	0.00	72.43	0.02	28.01	100.67
LD1687B	61	0.00	0.04	0.01	0.03	0.03	0.00	0.07	0.01	73.33	0.04	28.30	101.87
LD1687B	61	0.00	0.02	0.01	0.01	0.02	0.00	0.06	0.02	73.04	0.03	28.12	101.33
LD1687B	61	0.00	0.02	0.01	0.03	0.12	0.00	0.06	0.02	72.68	0.00	28.03	100.96
LD1687B	61	0.00	0.03	0.01	0.02	0.00	0.00	0.07	0.01	73.01	0.02	28.15	101.33
LD1687B	61	0.00	0.05	0.10	0.13	0.01	0.00	0.09	0.03	72.05	0.03	28.01	100.49
LD1687B	61	0.00	0.01	0.04	0.63	0.00	0.00	0.08	0.03	72.36	0.08	28.21	101.44
LD1687B	61	0.00	0.02	0.04	0.02	0.01	0.00	0.09	0.02	72.73	0.00	28.08	101.01
LD1687B	61	0.00	0.10	0.22	0.03	0.03	0.00	0.09	0.03	72.17	0.03	28.24	100.95
LD1687B	61	0.00	0.05	0.11	0.02	0.02	0.00	0.09	0.03	72.53	0.02	28.14	100.99
LD1687B	61	0.00	0.02	0.03	0.18	0.01	0.00	0.09	0.03	72.50	0.04	28.07	100.96
LD1687B	61	0.00	0.02	0.01	0.24	0.01	0.00	0.09	0.03	72.60	0.03	28.12	101.13

LD1687B	61	0.00	0.01	0.01	0.24	0.01	0.00	0.08	0.03	72.70	0.03	28.14	101.25
LD1687B	61	0.00	0.02	0.04	0.01	0.01	0.00	0.08	0.03	73.20	0.00	28.25	101.64
LD1687B	61	0.00	0.03	0.01	0.05	0.00	0.00	0.09	0.03	73.17	0.00	28.26	101.64
LD1687B	61	0.00	0.01	0.01	0.07	0.03	0.00	0.08	0.04	72.73	0.02	28.08	101.07
LD1687B	61	0.00	0.01	0.02	0.02	0.01	0.00	0.07	0.00	73.03	0.04	28.10	101.31
LD1687B	61	0.00	0.01	0.03	0.01	0.04	0.00	0.06	0.01	69.77	0.02	26.85	96.80
LD1687B	61	0.00	0.02	0.00	0.02	0.01	0.00	0.07	0.01	72.65	0.03	27.98	100.79
LD1687B	61	0.00	0.01	0.02	0.01	0.05	0.00	0.07	0.01	70.73	0.00	27.24	98.14
LD1687B	61	0.00	0.03	0.01	0.01	0.02	0.00	0.07	0.01	73.01	0.02	28.14	101.32
LD1687B	61	0.00	0.03	0.01	0.02	0.02	0.00	0.07	0.01	73.16	0.03	28.21	101.56
LD1687B	61	0.00	0.01	0.03	0.01	0.12	0.00	0.03	0.00	72.81	0.03	28.00	101.05
LD1687B	61	0.00	0.02	0.01	0.01	0.06	0.00	0.03	0.00	72.87	0.03	27.99	101.03
LD1687B	61	0.00	0.02	0.01	0.02	0.03	0.00	0.04	0.00	72.54	0.02	27.87	100.55
LD1687B	61	0.00	0.02	0.00	0.03	0.02	0.00	0.04	0.01	72.77	0.04	27.99	100.92
LD1687B	61	0.00	0.02	0.01	0.01	0.01	0.00	0.05	0.01	73.09	0.03	28.10	101.33
LD1687B	61	0.00	0.03	0.02	0.02	0.02	0.00	0.05	0.01	72.63	0.03	27.97	100.77
LD1687B	61	0.00	0.02	0.01	0.02	0.01	0.00	0.06	0.02	72.75	0.03	28.01	100.91
LD1687B	61	0.00	0.03	0.01	0.01	0.00	0.00	0.06	0.01	72.86	0.04	28.07	101.10
LD1687B	61	0.00	0.03	0.01	0.02	0.00	0.00	0.07	0.01	73.10	0.03	28.17	101.44
LD1687B	61	0.03	0.03	0.10	0.03	0.04	0.00	0.07	0.01	72.61	0.03	28.11	101.06
LD1687B	61	0.00	0.01	0.02	0.01	0.01	0.00	0.07	0.00	73.04	0.03	28.09	101.28
LD1687B	61	0.07	0.05	0.15	0.02	0.04	0.00	0.07	0.01	72.22	0.04	28.08	100.75
LD1687B	61	0.00	0.02	0.02	0.01	0.04	0.00	0.07	0.01	72.92	0.02	28.09	101.20
LD1687B	61	0.00	0.01	0.01	0.02	0.01	0.00	0.07	0.01	70.67	0.02	27.21	98.04
LD1687B	61	0.02	0.03	0.07	0.01	0.02	0.00	0.08	0.01	72.59	0.03	28.06	100.92
LD1687B	61	0.03	0.02	0.08	0.02	0.03	0.00	0.08	0.01	73.05	0.03	28.25	101.60
LD1687B	61	0.00	0.01	0.03	0.02	0.14	0.00	0.07	0.01	70.22	0.02	27.11	97.63
LD1687B	61	0.00	0.01	0.09	0.24	0.26	0.00	0.07	0.01	69.61	0.03	27.09	97.41
LD1687B	61	0.00	0.01	0.00	0.03	0.04	0.00	0.07	0.01	70.47	0.00	27.13	97.76
LD1687B	61	0.00	0.02	0.02	0.01	0.03	0.00	0.07	0.01	72.91	0.03	28.09	101.21
LD1687B	61	0.08	0.04	0.15	0.01	0.04	0.00	0.07	0.01	72.37	0.00	28.10	100.87
LD1687B	61	0.00	0.03	0.03	0.01	0.01	0.00	0.07	0.01	72.92	0.03	28.12	101.23
LD1687B	61	0.00	0.01	0.01	0.11	0.01	0.00	0.07	0.01	72.75	0.03	28.04	101.05
LD1687B	62	0.00	0.01	0.02	0.19	0.01	0.00	0.05	0.01	72.89	0.02	28.08	101.26
LD1687B	62	0.00	0.02	0.01	0.05	0.01	0.00	0.06	0.01	72.88	0.00	28.04	101.07
LD1687B	62	0.00	0.02	0.01	0.07	0.00	0.00	0.05	0.01	73.14	0.02	28.16	101.50
LD1687B	62	0.00	0.01	0.01	0.70	0.04	0.00	0.04	0.01	72.16	0.11	28.04	101.11
LD1687B	62	0.00	0.03	0.02	0.14	0.01	0.00	0.08	0.01	73.10	0.04	28.25	101.66
LD1687B	62	0.00	0.02	0.01	1.22	0.00	0.00	0.07	0.01	72.37	0.06	28.41	102.17
LD1687B	62	0.00	0.02	0.01	0.91	0.00	0.00	0.07	0.01	72.87	0.06	28.48	102.44
LD1687B	62	0.00	0.08	0.03	0.06	0.00	0.00	0.06	0.00	72.97	0.00	28.23	101.42
LD1687B	62	0.02	0.13	0.04	0.07	0.01	0.00	0.06	0.00	72.50	0.02	28.23	101.09
LD1687B	62	0.04	0.11	0.18	0.07	0.05	0.00	0.06	0.00	72.49	0.00	28.30	101.29
LD1687B	62	0.01	0.11	0.07	0.06	0.01	0.00	0.06	0.00	72.68	0.02	28.27	101.30
LD1687B	62	0.00	0.02	0.01	0.05	0.00	0.00	0.07	0.00	73.01	0.00	28.10	101.26
LD1687B	62	0.00	0.02	0.02	0.03	0.01	0.00	0.06	0.00	73.23	0.00	28.18	101.56
LD1687B	62	0.00	0.01	0.01	0.30	0.01	0.00	0.05	0.01	72.89	0.02	28.14	101.44
LD1687B	62	0.00	0.03	0.04	0.06	0.01	0.00	0.07	0.01	73.57	0.00	28.38	102.15

Table A-3: EPMA ilmenite results. All values in wt.% unless stated differently. Oxygen content is stoichiometrically calculated. Concentrations below detection limit appear as zero. AQ: Quince. LD: Candelaria mine.

Drill core	Sample	Si	Ti	Al	V	Cr	Fe	Mn	Mg	Ca	P	O	Total
AQ-19	2	0.03	29.34	0.02	0.12	0.00	29.65	7.54	0.04	0.00	0.00	30.59	97.34
AQ-19	2	0.00	29.70	0.01	0.11	0.00	32.70	5.70	0.00	0.00	0.00	30.92	99.14
AQ-19	2	0.07	30.07	0.01	0.11	0.00	30.31	6.82	0.00	0.27	0.00	30.88	98.54
AQ-19	3	0.00	29.55	0.03	0.12	0.00	34.35	3.59	0.47	0.00	0.00	31.07	99.18
AQ-19	3	0.00	28.89	0.01	0.12	0.00	32.85	3.93	0.62	0.02	0.00	30.62	97.06
AQ-19	3	0.00	29.32	0.01	0.12	0.00	32.36	2.64	1.68	0.01	0.00	30.93	97.06
AQ-19	3	0.00	29.35	0.01	0.11	0.00	33.48	3.54	0.00	0.00	0.00	30.45	96.94
AQ-19	3	0.00	29.97	0.01	0.11	0.00	34.29	3.44	0.42	0.00	0.00	31.08	99.33
AQ-19	3	0.01	30.16	0.01	0.10	0.00	34.20	4.00	0.00	0.00	0.00	31.01	99.48
AQ-19	3	0.00	30.09	0.01	0.11	0.00	33.56	3.26	0.96	0.00	0.00	31.21	99.20
AQ-19	3	0.00	30.00	0.01	0.12	0.00	33.29	3.13	1.45	0.00	0.00	31.37	99.36
AQ-19	3	0.00	29.46	0.01	0.12	0.00	34.86	3.66	0.14	0.00	0.00	30.96	99.20
AQ-19	3	0.00	29.05	0.01	0.12	0.00	34.76	2.85	0.70	0.00	0.00	30.92	98.42
AQ-19	3	0.00	29.75	0.01	0.12	0.00	33.51	4.41	0.00	0.02	0.00	30.84	98.64
AQ-19	3	0.00	29.32	0.01	0.12	0.00	34.53	2.66	1.18	0.00	0.00	31.17	98.98
AQ-19	3	0.00	29.70	0.01	0.13	0.00	34.21	2.23	1.78	0.00	0.00	31.46	99.52
AQ-19	3	0.00	29.32	0.01	0.12	0.00	34.45	2.66	1.29	0.00	0.00	31.23	99.08
AQ-19	3	0.00	29.05	0.01	0.13	0.00	34.89	2.70	1.21	0.00	0.00	31.22	99.20
AQ-19	4	0.00	28.09	0.01	0.12	0.00	31.39	6.65	0.25	0.00	0.00	30.48	97.00
AQ-19	4	0.00	28.53	0.01	0.12	0.00	28.77	8.88	0.16	0.00	0.00	30.47	96.95
AQ-19	4	0.05	27.64	0.01	0.12	0.00	29.75	8.58	0.14	0.00	0.00	30.37	96.66
AQ-19	4	0.00	27.96	0.00	0.12	0.00	29.65	8.58	0.16	0.00	0.00	30.42	96.89
AQ-19	4	0.09	27.86	0.18	0.12	0.00	29.00	8.65	0.15	0.01	0.00	30.56	96.62
AQ-19	4	0.01	27.17	0.03	0.12	0.00	30.18	8.41	0.00	0.17	0.00	30.26	96.34
AQ-19	4	0.00	28.98	0.00	0.11	0.00	27.43	9.67	0.00	0.00	0.00	30.37	96.57
AQ-19	4	0.01	28.95	0.01	0.12	0.00	30.40	5.70	0.76	0.00	0.00	30.55	96.48
AQ-19	4	0.00	29.45	0.01	0.11	0.00	30.82	3.72	1.73	0.00	0.00	30.86	96.69
LD1687B	12	0.06	27.79	0.01	0.00	0.00	35.46	3.33	0.00	0.12	0.00	30.33	97.12
LD1687B	52	0.29	20.82	0.05	0.01	0.00	43.20	2.63	0.24	0.09	0.00	30.19	97.51
LD1687B	52	0.01	34.30	0.00	0.01	0.00	29.00	0.28	0.02	0.02	0.00	29.78	93.41
LD1687B	52	0.00	28.66	0.00	0.00	0.00	34.11	4.48	0.09	0.00	0.00	30.51	97.85
LD1687B	52	0.01	28.41	0.00	0.00	0.00	35.06	3.85	0.06	0.00	0.00	30.50	97.89
LD1687B	52	0.02	40.25	0.01	0.00	0.00	21.68	0.18	0.00	0.04	0.00	29.64	91.82
LD1687B	52	0.02	29.15	0.00	0.00	0.01	34.04	4.22	0.05	0.05	0.00	30.61	98.15
LD1687B	52	0.01	30.84	0.00	0.00	0.01	33.15	0.29	0.00	0.01	0.00	29.79	94.10
LD1687B	52	0.00	28.70	0.00	0.00	0.00	35.96	2.59	0.12	0.00	0.00	30.54	97.91
LD1687B	52	0.01	33.15	0.00	0.00	0.00	30.13	0.37	0.00	0.02	0.00	29.71	93.39

LD1687B	52	0.03	28.55	0.04	0.00	0.00	34.81	3.84	0.04	0.03	0.00	30.55	97.88
LD1687B	52	0.01	28.14	0.01	0.00	0.00	36.36	3.38	0.10	0.01	0.00	30.65	98.65
LD1687B	52	0.02	17.99	0.03	0.02	0.00	46.89	4.35	0.08	0.01	0.00	30.28	99.66
LD1687B	52	0.08	29.11	0.00	0.00	0.00	30.32	5.84	0.14	0.06	0.00	30.13	95.68
LD1687B	61	0.28	28.83	0.01	0.00	0.00	26.83	####	0.02	0.30	0.00	30.62	97.79
LD1687B	61	0.00	32.85	0.00	0.01	0.01	28.56	2.11	0.01	0.01	0.00	29.71	93.28
LD1687B	61	0.01	30.35	0.01	0.02	0.01	28.80	4.10	0.02	0.01	0.00	29.56	92.89
LD1687B	61	0.03	29.40	0.00	0.01	0.01	29.51	4.22	0.01	0.02	0.00	29.47	92.70
LD1687B	61	0.01	28.73	0.01	0.01	0.01	28.57	9.25	0.02	0.01	0.00	30.39	97.01
LD1687B	61	0.01	27.91	0.01	0.01	0.01	31.69	7.52	0.03	0.02	0.00	30.47	97.66
LD1687B	61	0.01	27.90	0.00	0.01	0.01	31.36	7.80	0.02	0.02	0.00	30.44	97.56
LD1687B	61	0.17	27.67	0.04	0.01	0.01	30.38	8.52	0.06	0.21	0.00	30.53	97.59
LD1687B	61	0.09	35.05	0.01	0.01	0.01	26.44	1.19	0.00	0.15	0.00	29.70	92.66
LD1687B	61	0.03	28.22	0.00	0.01	0.01	32.88	6.37	0.02	0.01	0.00	30.56	98.11
LD1687B	61	0.21	30.47	0.01	0.00	0.00	25.83	6.01	0.01	0.28	0.00	29.46	92.30
LD1687B	62	0.12	31.79	0.01	0.00	0.00	30.49	1.40	0.06	0.02	0.00	29.81	93.71
LD1687B	62	0.02	29.93	0.01	0.00	0.00	31.76	3.33	0.02	0.01	0.00	30.00	95.09
LD1687B	62	0.01	28.72	0.01	0.01	0.00	31.89	3.88	0.02	0.01	0.00	29.78	94.31
LD1687B	62	0.01	28.69	0.00	0.00	0.00	34.94	4.01	0.03	0.00	0.00	30.59	98.27
LD1687B	62	0.02	28.58	0.01	0.01	0.00	34.32	4.76	0.03	0.00	0.00	30.62	98.36
LD1687B	62	0.08	28.48	0.02	0.01	0.00	31.90	5.44	0.04	0.01	0.00	30.20	96.17
LD1687B	62	0.05	28.45	0.01	0.01	0.00	34.18	1.22	0.02	0.04	0.00	29.62	93.59
LD1687B	62	0.03	28.18	0.01	0.01	0.00	35.35	3.66	0.02	0.00	0.00	30.47	97.72
LD1687B	62	0.05	28.37	0.00	0.00	0.00	35.65	3.06	0.02	0.01	0.00	30.45	97.62
LD1687B	62	0.02	33.26	0.00	0.00	0.00	28.88	0.71	0.02	0.10	0.00	29.52	92.50
LD1687B	62	0.14	30.08	0.01	0.00	0.00	30.02	1.91	0.10	0.11	0.00	29.28	91.65
LD1687B	62	0.15	28.31	0.02	0.00	0.00	34.47	3.63	0.04	0.12	0.00	30.40	97.13
LD1687B	62	0.03	27.65	0.00	0.00	0.00	36.50	3.12	0.03	0.01	0.00	30.43	97.77
LD1687B	62	0.10	28.73	0.04	0.00	0.00	34.41	3.93	0.07	0.01	0.00	30.59	97.88
LD1687B	62	0.01	27.98	0.01	0.00	0.00	36.41	3.03	0.03	0.08	0.00	30.51	98.05
LD1687B	62	0.08	27.71	0.02	0.00	0.00	35.77	2.91	0.04	0.15	0.00	30.33	97.02
LD1687B	62	0.02	27.96	0.01	0.00	0.00	36.03	3.04	0.03	0.04	0.00	30.40	97.53
LD1687B	62	0.02	31.47	0.01	0.00	0.00	30.81	0.85	0.00	0.02	0.00	29.49	92.67
LD1687B	62	0.02	28.16	0.01	0.00	0.00	35.93	3.17	0.03	0.02	0.00	30.48	97.82
LD1687B	62	0.02	28.48	0.00	0.00	0.00	35.74	3.40	0.00	0.02	0.00	30.56	98.23
LD1687B	62	0.01	28.62	0.00	0.00	0.00	35.96	3.16	0.01	0.02	0.00	30.60	98.37

Table A-4: EPMA actinolite results. All values in wt.% unless stated differently. Oxygen content is stoichiometrically calculated. Concentrations below detection limit appear as zero. AQ: Quince. LD: Candelaria mine.

Drill core	Sam-ple	SiO_2	TiO_2	Al_2O_3	FeO	MnO	MgO	CaO	Na_2O	K_2O	P_2O_5	Total	Si a.p.f.u	Al a.p.f.u	Fe a.p.f.u	Mg a.p.f.u	Ca a.p.f.u
LD1687		52.	0.1		10.3	0.1	17.	12.	0.2	0.1				0.2	1.3		
B	43	8	1	3.2	8	4	5	5	6	3	0	97	8.0	9	2	4.0	2.0
LD1687		51.	0.1	4.1			16.	12.	0.3	0.1		96.		0.3	1.5		
B	43	1	4	9	11.7	0.2	2	4	9	6	0	4	7.9	8	2	3.7	2.1
LD1687		51.	0.1	4.1	11.1	0.2	16.	12.	0.3	0.2		96.		0.3	1.4		
B	43	2	5	1	6	3	2	5	6	6	0	2	8.0	8	5	3.8	2.1

LD1687		51.	0.1	4.0	11.8	0.1	16.	12.	0.3	0.2				0.3	1.5			
B	43	3	5	4	1	3	5	5	6	4	0	97	7.9	7	3	3.8	2.1	
LD1687		52.	0.1	3.2	10.3	0.1	17.	12.	0.2	0.1		96.		0.3	1.3			
B	43	5	2	7	3	4	2	5	8	7	0	5	8.1	0	2	3.9	2.0	
LD1687		52.	0.1		11.3	0.2	16.	12.	0.3	0.1		97.		0.3	1.4			
B	43	5	5	3.7	5	1	6	6	6	4	0	7	8.0	3	5	3.8	2.1	
LD1687		54.	0.1	2.9			17.	12.	0.2			98.		0.2	1.3			
B	43	4	1	9	10.5	0.2	6	5	4	0.1	0	6	8.1	6	1	3.9	2.0	
LD1687		51.			11.3	0.3	15.	12.		0.0		95.		0.3	1.4			
B	43	6	0.2	3.7	9	1	9	5	0.3	7	0	9	8.0	4	8	3.7	2.1	
LD1687		51.	0.2	3.9	11.4	0.2		12.	0.3	0.1		96.		0.3	1.4			
B	43	8	1	2	5	6	16	4	7	2	0	5	8.0	6	8	3.7	2.1	
LD1687			0.1	3.0	10.1	0.2	17.	12.	0.2	0.1		97.		0.2	1.2			
B	43	54	1	2	8	5	5	5	6	2	0	8	8.1	7	8	3.9	2.0	
LD1687		51.		3.3	11.4	0.2	16.	12.	0.3			96.		0.3	1.4			
B	43	7	0	6	6	2	6	5	1	0.1	0	2	8.0	1	8	3.8	2.1	
LD1687		49.	0.2	6.6	12.2	0.1	14.	12.	0.6	0.1		96.		0.6	1.6			
B	43	1	1	3	9	9	7	3	1	7	0	2	7.8	2	3	3.5	2.1	
LD1687			0.0	6.5	15.2	0.2	15.	10.	0.3	0.2		96.		0.6	2.0			
B	43	48	9	3	5	4	4	5	6	6	0	7	7.7	1	3	3.6	1.8	
LD1687		52.	0.0	4.0	10.6	0.1	16.	12.	0.3	0.0		97.		0.3	1.3			
B	43	3	6	2	9	7	9	5	4	8	0	2	8.0	6	7	3.9	2.1	
LD1687		52.	0.0	3.6		0.2	17.	12.	0.3	0.1		95.		0.3	1.1			
B	43	2	9	3	9.23	6	2	6	2	5	0	7	8.1	3	9	4.0	2.1	
LD1687		52.	0.1	3.7	10.4	0.1	16.	12.	0.3	0.1		96.		0.3	1.3			
B	43	1	4	2	4	8	7	5	5	2	0	2	8.0	4	5	3.8	2.1	
LD1687		52.	0.1	3.9	10.4	0.1	16.	12.	0.3	0.1		97.		0.3	1.3			
B	43	7	5	1	5	8	9	4	5	3	0	2	8.0	5	3	3.8	2.0	
LD1687		51.	0.1	3.7	11.5	0.2		12.	0.3	0.1		96.		0.3	1.5			
B	43	8	4	8	7	5	16	4	6	9	0	5	8.0	5	0	3.7	2.1	
LD1687			0.1	3.7	11.9	0.2		12.	0.3	0.1	0.0	96.		0.3	1.5			
B	43	51	4	5	8	6	16	5	5	1	2	2	8.0	5	6	3.7	2.1	
LD1687		52.	0.0	3.5	11.8	0.2	16.	12.	0.2			97.		0.3	1.5			
B	43	6	2	2	2	5	3	4	8	0.1	0	3	8.0	2	1	3.7	2.0	
LD1687		48.	0.0	6.2		0.3	13.	12.	0.5	0.1		96.		0.5	1.8			
B	43	9	8	9	13.8	6	6	4	1	5	0	1	7.8	9	4	3.2	2.1	
LD1687		48.	0.2	7.1	13.6	0.1	13.	12.	0.7	0.1		97.		0.6	1.8			
B	43	8	8	9	5	9	8	3	1	8	0	1	7.7	7	1	3.3	2.1	
LD1687		43.	0.2	2.7	25.1	0.1	14.		0.3			96.		0.2	3.5			
B	43	8	5	7	5	8	7	9.2	3	0.1	0	5	7.3	7	1	3.7	1.6	
LD1687		52.	0.1	2.5	10.9	0.2	17.	12.	0.4	0.1		96.		0.2	1.4			
B	52	6	9	8	5	4	1	2	4	3	0	5	8.1	3	1	3.9	2.0	
LD1687		52.	0.2	2.7		0.2	17.	12.	0.3	0.1		95.		0.2	1.2			
B	52	3	9	1	10	5	5	4	2	7	0	9	8.1	5	9	4.0	2.0	
LD1687		51.	0.2	3.3	10.9		16.	12.				96.		0.3	1.4			
B	52	8	7	8	5	0.2	8	3	0.5	0.2	0	4	8.0	1	2	3.9	2.0	
LD1687		52.	0.3	3.1	10.6	0.1	16.	12.	0.4	0.1	0.0	96.		0.2	1.3			
B	52	2	1	7	5	9	9	2	2	8	2	2	8.1	9	8	3.9	2.0	
LD1687		50.	0.2	3.9	13.2		15.		0.6	0.2	0.0			0.3	1.7			
B	52	9	9	2	3	0.2	6	12	1	1	2	97	8.0	6	3	3.6	2.0	
LD1687			0.2	3.4	12.0	0.2	15.	12.	0.6	0.1		96.		0.3	1.5			
B	52	52	8	9	1	7	8	1	4	9	0	8	8.1	2	6	3.7	2.0	
LD1687		51.	0.3	3.8	12.4	0.2	15.	12.	0.6	0.2		96.		0.3	1.6			
B	52	1	7	4	3	5	3	2	2	4	0	3	8.0	5	3	3.6	2.0	
LD1687		51.	0.2	2.9	11.6	0.2	16.	12.	0.4	0.1		96.		0.2	1.5			
B	52	9	6	3	1	1	9	3	5	5	0	7	8.0	7	0	3.9	2.0	
LD1687		51.	0.2		11.3	0.2	16.	12.	0.5	0.1		95.		0.2	1.4			
B	52	3	6	3	3	7	3	1	6	6	0	3	8.1	8	9	3.8	2.0	
LD1687		52.	0.1	3.0	10.2	0.1	17.	12.	0.4	0.1		96.		0.2	1.3			
B	52	4	8	6	6	8	2	3	4	6	0	1	8.1	8	2	3.9	2.0	
LD1687		51.	0.1	3.1	13.3	0.2	15.	12.	0.3	0.2				0.2	1.7			
B	58	8	2	6	3	2	4	3	6	3	0	97	8.0	9	3	3.6	2.0	
LD1687		53.	0.0		13.0	0.2	16.	12.	0.2	0.1		98.		0.1	1.6			
B	58	6	6	2.1	4	2	4	4	7	2	0	2	8.1	9	5	3.7	2.0	
LD1687		50.	0.1	4.8	13.5	0.2	15.	12.	0.5	0.3		98.		0.4	1.7			
B	58	7	6	6	6	8	7	2	2	6	0	4	7.9	4	6	3.6	2.0	
LD1687		49.	0.1	4.8	14.0	0.2			0.7	0.3		96.		0.4	1.8			
B	58	8	9	7	6	6	14	12	1	3	0	2	7.9	6	7	3.3	2.1	
LD1687		50.	0.0	3.7	12.1	0.2	16.	11.	0.3	0.1		95.		0.3	1.6			
B	58	8	5	2	8	5	1	9	1	7	0	5	8.0	4	0	3.8	2.0	

AQ-19	2	51.6	0.32	3.64	8.63	0.27	19.4	11.5	0.62	0.14	0	96.2	7.9	0.33	1.11	4.4	1.9
AQ-19	2	51.1	0.38	4.86	9.85	0.18	18.6	11.5	0.72	0.22	0	97.4	7.9	0.44	1.27	4.3	1.9
AQ-19	2	50.1	0.53	5.43	9.71	0.25	17.9	11.6	0.93	0.28	0	96.7	7.8	0.50	1.27	4.2	1.9
AQ-19	2	55.1	0.17	2.14	7.57	0.25	20.3	11.7	0.31	0.07	0	97.6	8.2	0.19	0.94	4.5	1.9
AQ-19	2	50.7	0.44	4.77	8.66	0.23	18.4	11.6	0.86	0.24	0	95.9	7.9	0.44	1.13	4.3	1.9
AQ-19	2	54.4	0.14	2.24	7.72	0.23	20.3	11.5	0.39	0.06	0	97.1	8.1	0.20	0.96	4.5	1.8
AQ-19	2	52	0.39	4.21	8.88	0.27	18.8	11.5	0.71	0.21	0	97	8.0	0.38	1.14	4.3	1.9
AQ-19	2	50	0.59	6.39	9.58	0.25	17.7	11.6	1.05	0.33	0	97.3	7.8	0.58	1.25	4.1	1.9
AQ-19	2	50.8	0.52	5.52	9.86	0.23	18.3	11.5	0.94	0.28	0	98	7.8	0.50	1.27	4.2	1.9

Table A-5: Ilmenite reintegration

mag: Magnetite ilm: Ilmenite			Mineral fraction (% of pixels in image)			EPMA concentrations (wt.%)				Element content in image (wt.%)				Element content per sample (wt.%)			
Area	Sample	Image	Ilm	Mag	Phase	Ti	V	Al	Mn	Ti	V	Al	Mn	Ti	V	Al	Mn
Candelaria	LD1687B 12	1	1.53	11.61	mag	0.05	0.01	0.02	0.07	2.92	0.00	0.00	0.35	2.92	0.00	0.00	0.35
		2	1.39	10.49	ilm	27.79	0.00	0.02	3.33								
	LD1687B 52	3	1.24	39.34	ilm	28.70	0.01	0.00	2.59	0.41	0.03	0.03	0.03	0.53	0.03	0.03	0.05
		3			mag	0.15	0.07	0.08	0.00								
		4	1.16	40.97	ilm	28.55	0.00	0.04	3.84	0.42	0.03	0.03	0.06				
		4			mag	0.22	0.07	0.08	0.03								
		5	1.26	44.93	ilm	28.14	0.00	0.01	3.38	0.76	0.03	0.03	0.06				
		5			mag	0.91	0.06	0.06	0.04								
	LD1687B 62	6	5.82	9.99	ilm	28.11	0.00	0.01	3.27	1.67	0.00	0.00	0.20	2.35	0.01	0.00	0.26
		6			mag	0.39	0.05	0.01	0.07								
		7	10.89	11.79	ilm	27.71	0.00	0.02	2.91	3.02	0.01	0.01	0.32				
		7			mag	0.06	0.07	0.03	0.00								
Quince	AQ-19 2	8	1.81	74.00	ilm	29.70	0.13	0.01	5.70	0.56	0.16	0.05	0.10	0.56	0.16	0.05	0.10
		8			mag	0.03	0.21	0.07	0.00								
	AQ-19 3	9	3.55	73.40	ilm	30.09	0.13	0.01	3.26	1.09	0.16	0.03	0.13	1.19	0.15	0.03	0.15
		9			mag	0.04	0.21	0.03	0.02								
		10	4.32	72.42	ilm	29.46	0.14	0.01	3.66	1.32	0.16	0.02	0.16				
		10			mag	0.07	0.21	0.02	0.00								
		11	3.74	51.91	ilm	29.75	0.14	0.01	4.41	1.15	0.12	0.03	0.17				
		11			mag	0.07	0.22	0.06	0.02								
	AQ-19 4	12	10.96	76.96	ilm	28.69	0.13	0.02	6.77	3.25	0.17	0.05	0.75	3.03	0.17	0.05	0.70
		12			mag	0.13	0.20	0.06	0.01								

		13	5.57	80.27	ilm	28.69	0.13	0.04	6.49	1.68	0.17	0.07	0.36	
		13			mag	0.10	0.20	0.09	0.00					

Appendix B

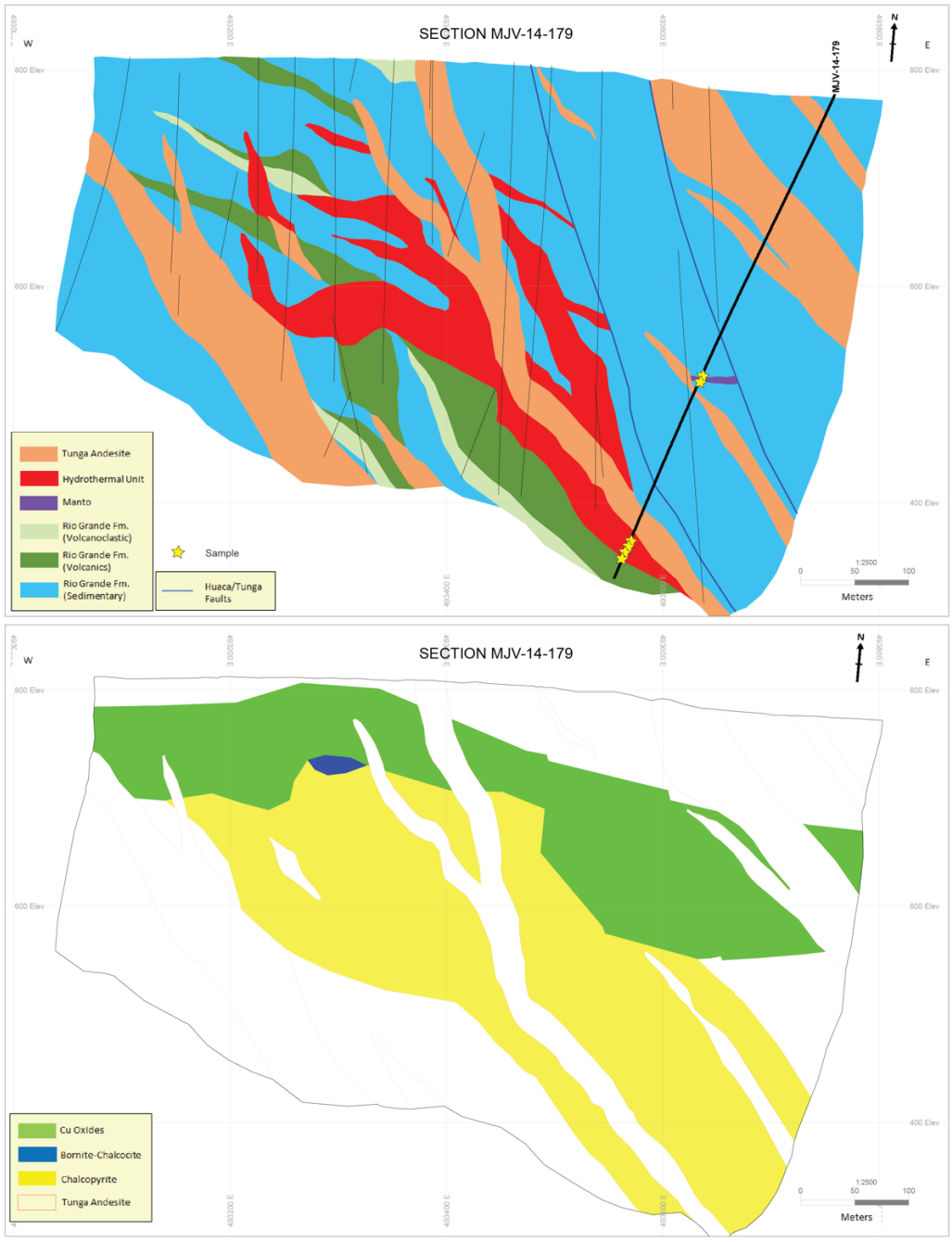

Figure A-1: Cross-section MJV-14-179. The top panel shows lithology while the bottom one shows Cu mineralization. The black lines represent the drill holes used to construct the section, including the bold, labelled line, which corresponds to a sampled drill hole. The stars indicate the location of samples. (Diagrams provided by Marcobre).

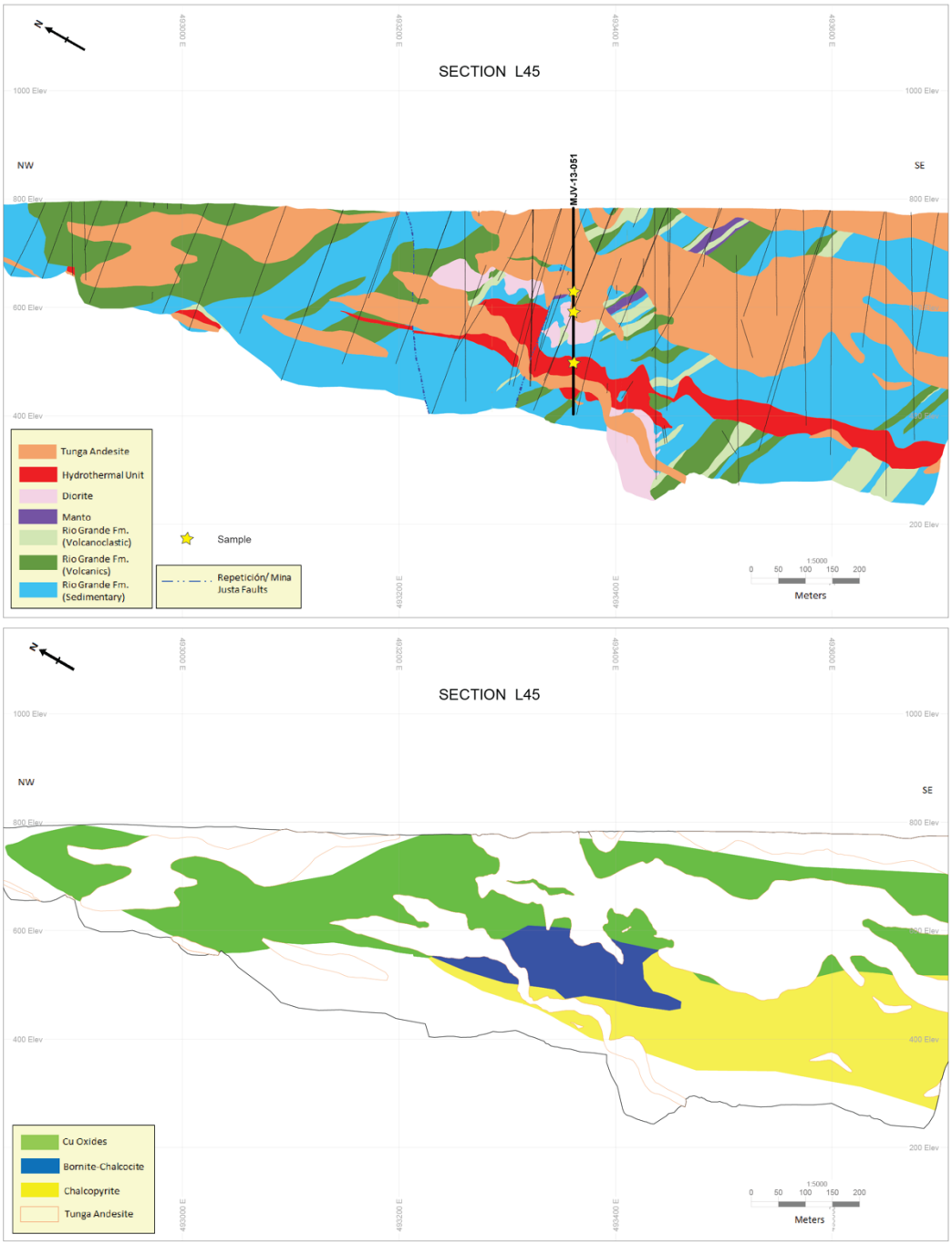

Figure A-2: Cross-section L45. The top panel shows lithology while the bottom one shows Cu mineralization. The black lines represent the drill holes used to construct the section, including the bold, labelled line, which corresponds to a sampled drill hole. The stars indicate the location of samples. (Diagrams provided by Marcobre).

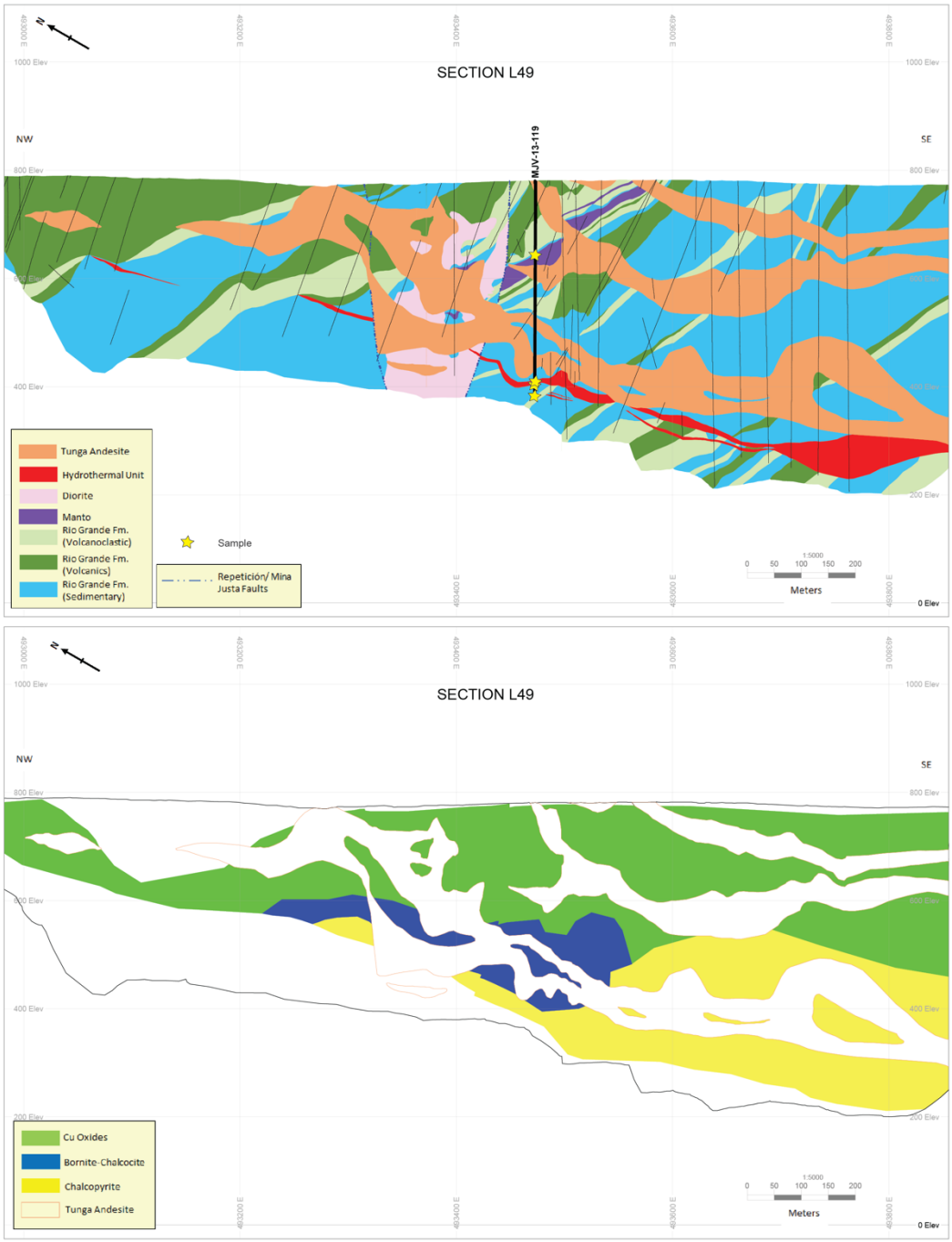

Figure A-3: Cross-section L49. The top panel shows lithology while the bottom one shows Cu mineralization. The black lines represent the drill holes used to construct the section, including the bold, labelled line, which corresponds to a sampled drill hole. The stars indicate the location of samples. (Diagrams provided by Marcobre).

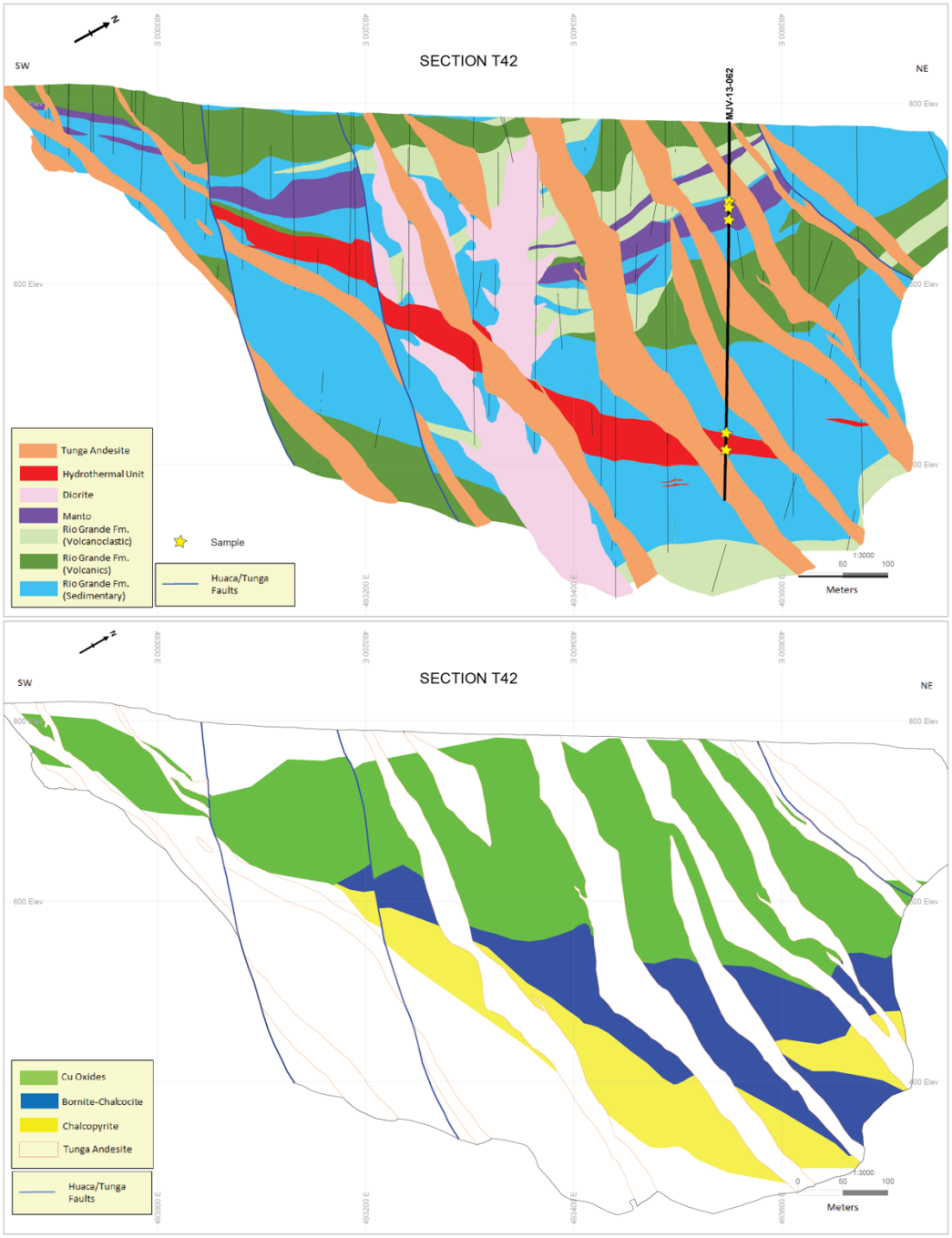

Figure A-4: Cross-section T42. The top panel shows lithology while the bottom one shows Cu mineralization. The black lines represent the drill holes used to construct the section, including the bold, labelled line, which corresponds to a sampled drill hole. The stars indicate the location of samples. (Diagrams provided by Marcobre).

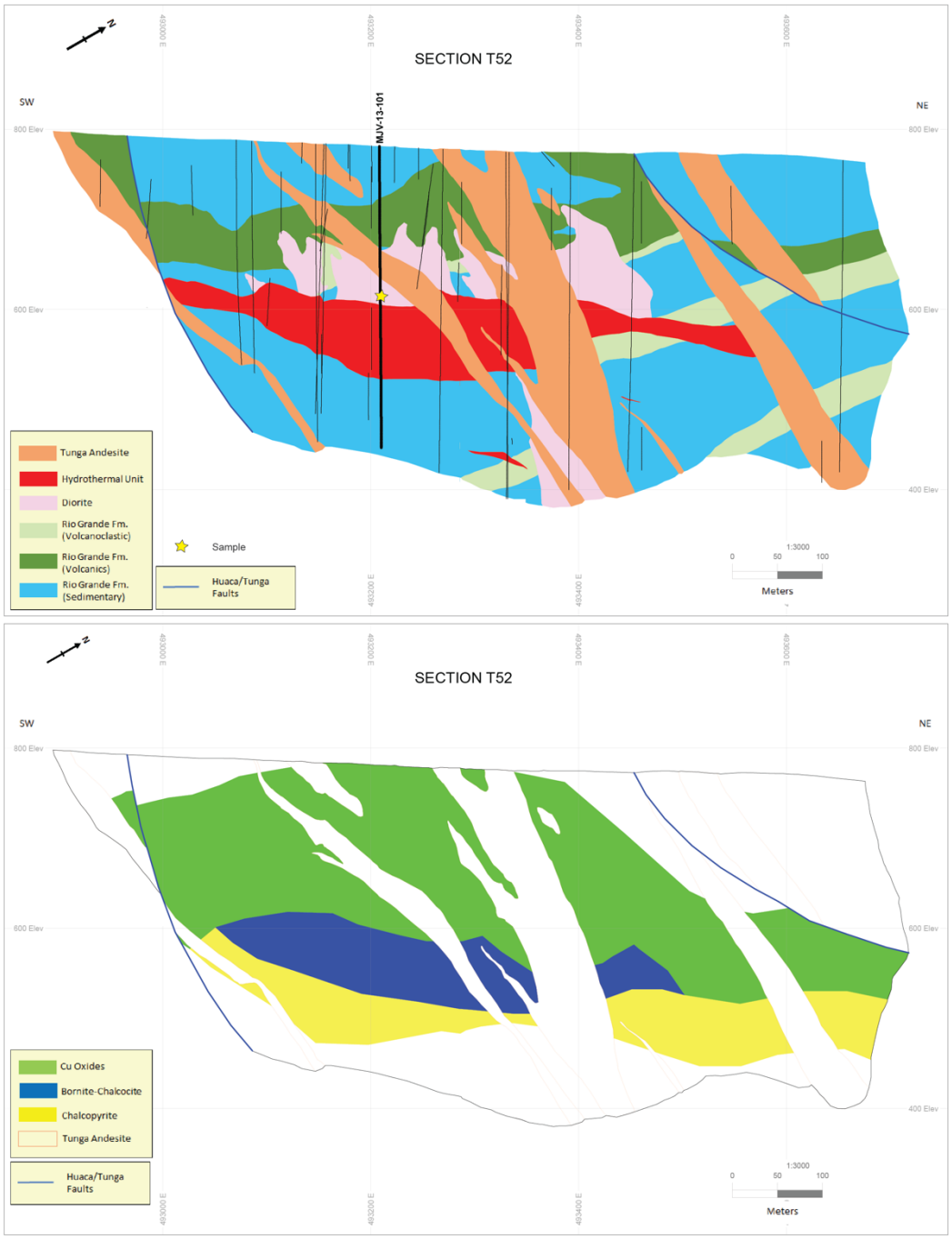

Figure A-5: Cross-section T52. The top panel shows lithology while the bottom one shows Cu mineralization. The black lines represent the drill holes used to construct the section, including the bold, labelled line, which corresponds to a sampled drill hole. The star indicates the location of the sample. (Diagrams provided by Marcobre).

Table A-6: EPMA conditions.

Element/Line	Crystal	Standard	Counting time (s)	MDL (wt.%)
Mg Kα	LTAP	Geikielite	80	0.01
Al Kα	LTAP	Jadeite	80	0.01

Si Kα	LTAP	Wollastonite	80	0.01
Ca Kα	PET	Wollastonite	120	0.01
Ti Kα	PET	Ilmenite (USNM)	120	0.01
V Kα	LLIF	V2O5	120	0.01
Cr Kα	LLIF	Cr2O3	120	0.01
Mn Kα	LIF	BHRH	120	0.02
Fe Kα	LIF	Magnetite (USNM)	120	0.02
Co Kα	LLIF	Co (Tryon)	120	0.00 – 0.01
Ni Kα	LLIF	NiAl	120	0.01

MDL: Mean detection limit

Table A-7: EPMA results (All values in wt.% unless stated differently). Oxygen content is stoichiometrically calculated. Concentrations below detection limit appear as zero.

Sample	Al	Ca	Co	Cr	Fe	Mg	Mn	Ni	Si	V	Ti	O	Total
NN01	0.05	0.00	0.02	0.04	71.38	0.00	0.10	0.00	0.01	1.05	0.10	21.12	93.88
NN01	0.08	0.00	0.02	0.04	71.21	0.00	0.13	0.00	0.00	1.17	0.06	21.14	93.88
NN01	0.09	0.00	0.02	0.04	71.11	0.00	0.17	0.00	0.00	1.17	0.09	21.14	93.84
NN01	0.10	0.01	0.02	0.04	71.24	0.00	0.14	0.00	0.01	1.17	0.07	21.18	93.97
NN01	0.10	0.00	0.02	0.04	70.93	0.00	0.14	0.00	0.01	1.17	0.08	21.10	93.61
NN01	0.03	0.00	0.02	0.04	71.36	0.00	0.07	0.01	0.04	0.98	0.03	21.05	93.62
NN01	0.24	0.15	0.00	0.01	68.63	0.00	0.01	0.00	0.33	0.38	0.24	20.67	90.68
NN01	0.10	0.01	0.01	0.04	71.27	0.01	0.11	0.00	0.06	1.14	0.05	21.22	94.04
NN01	0.10	0.02	0.01	0.04	69.75	0.00	0.07	0.00	0.07	1.14	0.05	20.78	92.05
NN01	0.10	0.00	0.02	0.04	71.32	0.01	0.16	0.01	0.01	1.15	0.08	21.21	94.10
NN01	0.46	0.01	0.00	0.03	68.40	0.00	0.02	0.00	0.38	0.73	0.16	20.92	91.10
NN01	0.04	0.00	0.02	0.04	71.58	0.00	0.13	0.01	0.01	1.07	0.07	21.17	94.13
NN01	0.07	0.00	0.01	0.04	71.55	0.00	0.15	0.00	0.01	1.16	0.11	21.26	94.37
NN01	0.23	0.43	0.01	0.04	68.15	0.23	0.14	0.00	1.16	1.17	0.17	22.10	93.83
NN01	0.06	0.00	0.02	0.05	71.27	0.00	0.10	0.00	0.01	1.14	0.07	21.13	93.87
NN01	0.03	0.09	0.02	0.03	70.77	0.02	0.04	0.01	0.11	0.91	0.01	20.95	92.99
NN01	0.02	0.00	0.01	0.04	70.36	0.00	0.06	0.01	0.04	1.04	0.01	20.76	92.37
NN01	0.01	0.02	0.01	0.04	70.60	0.00	0.04	0.01	0.02	0.97	0.00	20.76	92.49
NN01	0.04	0.16	0.02	0.04	68.75	0.08	0.08	0.01	1.18	0.97	0.02	21.72	93.08
NN01	0.03	0.00	0.01	0.04	71.64	0.00	0.07	0.01	0.03	1.01	0.03	21.12	93.98
NN01	0.05	0.07	0.01	0.04	70.09	0.02	0.06	0.01	0.27	1.04	0.02	21.02	92.71
NN01	0.03	0.05	0.01	0.04	68.83	0.07	0.08	0.01	0.26	0.98	0.02	20.64	91.04
NN02	0.24	0.22	0.00	0.01	70.85	0.15	0.06	0.00	0.54	0.30	0.05	21.51	93.93
NN02	0.05	0.00	0.00	0.01	72.70	0.02	0.02	0.01	0.02	0.15	0.03	21.01	94.01
NN02	0.18	0.12	0.00	0.03	70.90	0.10	0.05	0.01	0.37	0.87	0.13	21.54	94.32
NN02	0.11	0.05	0.00	0.02	71.48	0.07	0.05	0.01	0.16	0.86	0.09	21.32	94.23

NN02	0.02	0.00	0.00	0.00	70.54	0.00	0.01	0.00	0.01	0.03	0.01	20.25	90.84
NN02	0.02	0.00	0.00	0.00	70.76	0.00	0.01	0.00	0.01	0.01	0.00	20.30	91.08
NN02	0.01	0.00	0.00	0.00	70.63	0.00	0.01	0.00	0.00	0.00	0.00	20.25	90.88
NN02	0.03	0.00	0.00	0.00	70.56	0.00	0.01	0.00	0.00	0.02	0.00	20.26	90.86
NN02	0.04	0.00	0.00	0.00	72.30	0.00	0.06	0.00	0.13	0.16	0.04	21.02	93.75
NN02	0.05	0.00	0.00	0.01	72.45	0.00	0.07	0.00	0.03	0.23	0.06	21.00	93.89
NN02	0.03	0.00	0.00	0.00	70.38	0.00	0.01	0.00	0.01	0.01	0.00	20.20	90.62
NN02	0.05	0.00	0.00	0.00	70.23	0.00	0.01	0.00	0.00	0.01	0.00	20.17	90.45
NN02	0.10	0.08	0.00	0.01	71.98	0.07	0.04	0.00	0.37	0.30	0.05	21.40	94.40
NN02	0.11	0.02	0.00	0.00	70.08	0.00	0.01	0.00	0.01	0.03	0.00	20.21	90.46
NN02	0.15	0.15	0.00	0.02	71.14	0.10	0.04	0.00	0.38	0.52	0.10	21.40	94.00
NN03	0.07	0.00	0.00	0.02	71.79	0.03	0.01	0.00	0.02	0.46	0.09	20.96	93.45
NN03	0.05	0.00	0.00	0.01	71.89	0.01	0.07	0.00	0.01	0.45	0.06	20.94	93.49
NN03	0.05	0.00	0.00	0.01	71.92	0.02	0.05	0.00	0.03	0.37	0.06	20.93	93.44
NN03	0.07	0.03	0.00	0.01	71.32	0.01	0.09	0.01	0.13	0.28	0.05	20.85	92.84
NN03	0.03	0.00	0.00	0.01	71.47	0.00	0.10	0.00	0.01	0.27	0.03	20.70	92.62
NN03	0.04	0.00	0.00	0.01	71.61	0.01	0.07	0.00	0.01	0.33	0.04	20.77	92.88
NN03	0.04	0.01	0.00	0.01	71.92	0.00	0.09	0.00	0.08	0.30	0.04	20.94	93.44
NN03	0.04	0.00	0.00	0.01	71.86	0.02	0.04	0.01	0.02	0.28	0.04	20.83	93.14
NN03	0.05	0.00	0.00	0.02	71.52	0.02	0.03	0.00	0.02	0.49	0.05	20.86	93.06
NN03	0.05	0.00	0.00	0.02	71.37	0.01	0.08	0.00	0.01	0.64	0.07	20.90	93.16
NN03	0.15	0.00	0.00	0.01	69.26	0.00	0.02	0.00	0.05	0.23	0.03	20.17	89.91
NN03	0.03	0.00	0.00	0.01	71.27	0.00	0.10	0.00	0.01	0.32	0.03	20.66	92.43
NN03	0.04	0.00	0.00	0.01	71.50	0.00	0.06	0.00	0.04	0.32	0.05	20.76	92.78
NN03	0.03	0.00	0.00	0.01	72.08	0.00	0.07	0.00	0.02	0.31	0.02	20.89	93.43
NN03	0.09	0.10	0.00	0.00	71.27	0.04	0.11	0.00	0.27	0.16	0.08	21.04	93.17
NN03	0.06	0.00	0.00	0.01	71.86	0.00	0.07	0.00	0.04	0.33	0.06	20.90	93.33
NN50	0.02	0.04	0.00	0.03	70.39	0.00	0.06	0.02	0.02	0.70	0.02	20.61	91.91
NN50	0.03	0.01	0.00	0.03	70.25	0.00	0.06	0.02	0.02	0.70	0.01	20.55	91.67
NN50	0.03	0.00	0.00	0.03	68.20	0.00	0.08	0.02	0.01	0.75	0.04	20.01	89.17
NN50	0.04	0.00	0.00	0.03	70.68	0.00	0.09	0.02	0.01	0.78	0.04	20.73	92.41
NN50	0.03	0.00	0.00	0.03	68.52	0.00	0.07	0.02	0.01	0.75	0.05	20.09	89.55
NN50	0.03	0.00	0.00	0.03	70.75	0.00	0.09	0.02	0.01	0.79	0.05	20.75	92.49
NN50	0.03	0.01	0.00	0.03	70.47	0.00	0.06	0.02	0.03	0.72	0.01	20.63	92.00
NN50	0.02	0.00	0.00	0.03	70.44	0.02	0.05	0.02	0.03	0.74	0.01	20.64	91.99
NN50	0.03	0.00	0.00	0.03	70.34	0.00	0.11	0.01	0.01	0.78	0.08	20.66	92.03
NN50	0.03	0.00	0.00	0.03	68.28	0.00	0.09	0.02	0.01	0.76	0.06	20.04	89.32
NN50	0.03	0.03	0.00	0.02	68.60	0.00	0.07	0.02	0.02	0.71	0.03	20.11	89.64
NN50	0.03	0.07	0.00	0.03	70.37	0.00	0.07	0.02	0.01	0.75	0.04	20.64	92.02
NN51	0.05	0.04	0.00	0.04	70.76	0.01	0.10	0.02	0.10	1.20	0.07	21.12	93.50
NN51	0.05	0.01	0.00	0.04	70.81	0.02	0.07	0.01	0.04	1.18	0.06	21.04	93.33
NN51	0.10	0.46	0.00	0.04	68.09	0.35	0.11	0.01	1.37	1.24	0.15	22.31	94.23
NN51	0.01	0.00	0.00	0.04	71.40	0.01	0.07	0.02	0.01	1.05	0.02	21.03	93.64
NN51	0.02	0.01	0.00	0.03	71.70	0.01	0.08	0.01	0.03	1.09	0.02	21.17	94.18

NN51	0.06	0.29	0.00	0.04	69.85	0.18	0.09	0.01	0.72	1.11	0.05	21.73	94.13
NN51	0.02	0.00	0.00	0.04	71.36	0.01	0.09	0.02	0.01	1.17	0.04	21.10	93.84
NN51	0.02	0.02	0.00	0.03	71.60	0.01	0.06	0.01	0.06	0.95	0.01	21.11	93.88
NN51	0.01	0.00	0.00	0.03	71.26	0.01	0.06	0.02	0.01	1.00	0.02	20.95	93.36
NN51	0.08	0.26	0.00	0.03	69.01	0.09	0.09	0.02	0.49	0.96	0.04	21.09	92.16
NN51	0.03	0.06	0.00	0.03	72.28	0.01	0.06	0.01	0.13	0.77	0.01	21.31	94.67
NN51	0.07	0.11	0.00	0.03	71.56	0.05	0.07	0.02	0.25	0.87	0.02	21.38	94.42
NN51	0.09	0.39	0.00	0.03	70.40	0.21	0.09	0.01	0.76	0.95	0.03	21.93	94.91
NN51	0.02	0.05	0.00	0.03	71.99	0.01	0.07	0.02	0.04	0.95	0.01	21.21	94.39
NN51	0.01	0.08	0.00	0.03	72.01	0.01	0.06	0.02	0.03	0.95	0.18	21.30	94.64
NN51	0.05	0.26	0.00	0.03	71.06	0.06	0.07	0.01	0.39	0.88	0.13	21.53	94.47
NN51	0.13	0.57	0.00	0.04	68.13	0.34	0.11	0.01	1.47	1.20	0.15	22.48	94.63
NN51	0.02	0.00	0.00	0.04	71.98	0.01	0.08	0.02	0.01	1.12	0.03	21.25	94.55
NN51	0.14	0.67	0.00	0.03	69.41	0.37	0.10	0.01	1.35	0.90	0.05	22.56	95.58
NN51	0.03	0.02	0.00	0.04	71.87	0.01	0.09	0.01	0.01	1.21	0.06	21.30	94.64
NN51	0.04	0.04	0.00	0.03	72.00	0.01	0.07	0.02	0.12	0.81	0.01	21.24	94.37
NN51	0.03	0.01	0.00	0.04	72.11	0.01	0.09	0.01	0.01	1.14	0.02	21.30	94.77
NN51	0.02	0.07	0.00	0.03	72.13	0.01	0.05	0.01	0.08	0.82	0.01	21.23	94.46
NN51	0.05	0.28	0.00	0.03	70.71	0.27	0.08	0.01	0.60	0.91	0.02	21.77	94.74
NN51	0.04	0.00	0.00	0.04	72.01	0.01	0.04	0.01	0.01	1.22	0.06	21.33	94.76
NN51	0.13	0.66	0.00	0.04	68.56	0.36	0.11	0.01	1.38	1.06	0.05	22.42	94.79
NN51	0.02	0.02	0.00	0.04	72.07	0.01	0.08	0.02	0.02	1.02	0.01	21.23	94.53
NN51	0.05	0.00	0.02	0.04	71.59	0.00	0.08	0.02	0.01	1.24	0.06	21.25	94.36
NN51	0.01	0.01	0.02	0.04	71.19	0.00	0.08	0.02	0.02	1.13	0.05	21.05	93.63
NN51	0.04	0.00	0.02	0.04	71.29	0.01	0.08	0.01	0.16	1.12	0.02	21.24	94.04
NN51	0.07	0.44	0.01	0.03	69.49	0.15	0.08	0.02	0.63	0.98	0.05	21.50	93.45
NN51	0.13	0.51	0.01	0.05	68.21	0.34	0.13	0.02	1.45	1.16	0.16	22.45	94.61
NN51	0.09	0.05	0.01	0.04	69.52	0.01	0.10	0.01	0.16	1.17	0.08	20.86	92.09
NN51	0.02	0.00	0.02	0.04	71.81	0.00	0.05	0.02	0.00	1.04	0.02	21.14	94.17
NN52	0.02	0.01	0.00	0.03	70.70	0.00	0.04	0.02	0.01	0.87	0.02	20.75	92.48
NN52	0.04	0.00	0.00	0.03	70.80	0.00	0.06	0.02	0.01	0.92	0.04	20.83	92.76
NN52	0.03	0.00	0.00	0.03	70.70	0.00	0.07	0.01	0.01	0.91	0.04	20.78	92.58
NN52	0.03	0.00	0.00	0.03	71.31	0.00	0.08	0.00	0.01	0.91	0.04	20.96	93.37
NN52	0.03	0.00	0.00	0.03	70.84	0.00	0.08	0.01	0.01	0.92	0.05	20.85	92.83
NN52	0.02	0.01	0.00	0.04	70.69	0.00	0.06	0.01	0.02	0.90	0.02	20.77	92.53
NN52	0.03	0.00	0.00	0.03	70.40	0.00	0.07	0.01	0.01	0.91	0.03	20.69	92.17
NN52	0.03	0.00	0.00	0.04	70.62	0.00	0.07	0.00	0.01	0.91	0.03	20.76	92.48
NN53	0.04	0.00	0.02	0.01	72.20	0.00	0.08	0.03	0.02	0.37	0.03	20.98	93.77
NN53	0.06	0.00	0.01	0.01	72.15	0.00	0.08	0.00	0.07	0.34	0.05	21.03	93.82
NN53	0.24	0.14	0.02	0.01	70.87	0.12	0.04	0.00	0.50	0.35	0.14	21.51	93.96
NN53	0.07	0.03	0.02	0.01	72.26	0.00	0.08	0.02	0.15	0.26	0.05	21.14	94.09
NN53	0.10	0.08	0.02	0.01	71.99	0.02	0.07	0.00	0.22	0.28	0.05	21.20	94.02
NN53	0.02	0.00	0.00	0.00	70.08	0.00	0.01	0.00	0.00	0.02	0.07	20.15	90.34
NN53	0.03	0.00	0.02	0.01	72.32	0.00	0.06	0.00	0.01	0.26	0.01	20.91	93.63
NN53	0.16	0.01	0.00	0.00	69.16	0.02	0.02	0.00	0.29	0.03	0.01	20.33	90.04
NN53	0.13	0.10	0.01	0.01	71.37	0.07	0.03	0.00	0.30	0.43	0.06	21.26	93.79
NN53	0.11	0.07	0.01	0.01	71.58	0.05	0.02	0.00	0.27	0.38	0.05	21.19	93.74
NN53	0.05	0.02	0.02	0.01	71.97	0.04	0.06	0.00	0.22	0.33	0.03	21.15	93.90
NN53	0.12	0.09	0.02	0.02	71.30	0.09	0.01	0.00	0.38	0.43	0.06	21.33	93.85

NN53	0.28	0.27	0.02	0.01	70.40	0.17	0.02	0.00	0.73	0.30	0.10	21.69	93.98
NN53	0.23	0.29	0.02	0.00	70.35	0.14	0.08	0.00	0.87	0.01	0.00	21.61	93.62
NN53	0.05	0.18	0.02	0.00	71.38	0.07	0.08	0.03	0.53	0.02	0.00	21.26	93.63
NN54	0.47	0.03	0.00	0.01	69.28	0.06	0.21	0.02	0.16	0.27	1.44	21.65	93.57
NN54	0.30	0.12	0.00	0.00	71.56	0.02	0.14	0.02	0.38	0.13	0.33	21.59	94.59
NN54	0.01	0.02	0.00	0.00	73.50	0.01	0.08	0.00	0.02	0.00	0.01	21.12	94.75
NN54	0.09	0.02	0.00	0.02	72.40	0.01	0.10	0.00	0.16	0.53	0.04	21.32	94.68
NN54	0.01	0.01	0.00	0.00	71.19	0.01	0.01	0.00	0.01	0.01	0.12	20.50	91.83
NN54	0.03	0.00	0.00	0.00	70.11	0.01	0.01	0.00	0.01	0.01	0.89	20.71	91.72
NN54	0.11	0.00	0.00	0.01	72.57	0.01	0.10	0.00	0.07	0.40	0.06	21.23	94.55
NN54	0.11	0.00	0.00	0.01	72.96	0.01	0.11	0.00	0.06	0.41	0.06	21.34	95.06
NN54	0.06	0.00	0.00	0.00	70.39	0.01	0.01	0.00	0.02	0.02	0.19	20.38	91.05
NN54	0.09	0.00	0.00	0.01	72.84	0.01	0.08	0.01	0.02	0.29	0.07	21.19	94.61
NN54	0.53	0.37	0.00	0.00	68.36	0.20	0.15	0.00	1.06	0.03	0.83	22.16	93.70
NN54	0.05	0.01	0.00	0.00	73.55	0.03	0.05	0.00	0.02	0.00	0.00	21.17	94.87
NN54	0.18	0.16	0.00	0.00	71.39	0.06	0.07	0.00	0.67	0.01	0.01	21.51	94.05
NN54	0.09	0.00	0.00	0.00	73.23	0.01	0.07	0.00	0.01	0.01	0.02	21.12	94.56
NN54	0.34	0.27	0.00	0.00	70.94	0.14	0.09	0.00	0.85	0.01	0.03	21.84	94.51
NN54	0.09	0.00	0.00	0.00	73.20	0.02	0.05	0.00	0.01	0.00	0.00	21.08	94.44
NN54	0.35	0.31	0.00	0.00	70.50	0.16	0.08	0.00	1.00	0.01	0.01	21.90	94.30
NN54	0.11	0.01	0.00	0.01	72.84	0.01	0.07	0.01	0.18	0.25	0.04	21.36	94.88
NN54	0.03	0.00	0.00	0.00	70.78	0.01	0.01	0.00	0.01	0.01	0.08	20.37	91.26
NN54	0.07	0.00	0.00	0.00	73.46	0.01	0.08	0.00	0.01	0.00	0.01	21.15	94.78
NN54	0.09	0.00	0.00	0.00	70.86	0.01	0.01	0.00	0.03	0.02	0.05	20.45	91.49
NN04	0.04	0.01	0.00	0.02	69.09	0.01	0.08	0.02	0.21	0.49	0.05	20.37	90.36
NN04	0.06	0.04	0.00	0.03	70.66	0.05	0.03	0.01	0.10	0.85	0.08	20.94	92.85
NN04	0.08	0.17	0.00	0.03	69.68	0.10	0.04	0.01	0.56	0.85	0.12	21.31	92.92
NN04	0.07	0.09	0.00	0.03	69.36	0.00	0.07	0.01	0.01	0.79	0.12	20.47	90.99
NN04	0.06	0.01	0.00	0.03	71.70	0.01	0.03	0.00	0.01	0.79	0.10	21.08	93.81
NN04	0.07	0.01	0.00	0.03	69.19	0.00	0.10	0.00	0.01	0.79	0.13	20.40	90.71
NN04	0.12	0.27	0.00	0.03	70.16	0.15	0.18	0.01	0.56	0.79	0.13	21.57	93.95
NN04	0.07	0.03	0.00	0.03	70.84	0.00	0.10	0.00	0.01	0.79	0.06	20.84	92.76
NN04	0.05	0.00	0.00	0.03	69.34	0.00	0.12	0.01	0.00	0.71	0.10	20.36	90.71
NN04	0.07	0.16	0.00	0.03	70.03	0.06	0.14	0.01	0.48	0.82	0.10	21.28	93.15
NN04	0.07	0.04	0.00	0.03	70.38	0.00	0.12	0.01	0.08	0.82	0.07	20.82	92.44
NN04	0.02	0.00	0.00	0.03	71.61	0.00	0.10	0.01	0.02	0.74	0.02	20.98	93.54
NN04	0.06	0.00	0.00	0.03	70.69	0.00	0.13	0.00	0.01	0.78	0.10	20.81	92.61
NN04	0.09	0.06	0.00	0.03	71.26	0.05	0.12	0.00	0.18	0.83	0.10	21.27	93.99
NN04	0.03	0.00	0.00	0.03	72.07	0.00	0.08	0.02	0.00	0.67	0.04	21.06	93.98
NN04	0.07	0.00	0.00	0.03	71.64	0.02	0.09	0.01	0.01	0.83	0.12	21.12	93.93
NN04	0.07	0.00	0.00	0.03	71.39	0.00	0.10	0.01	0.04	0.82	0.09	21.06	93.62
NN04	0.06	0.02	0.00	0.03	69.79	0.00	0.08	0.01	0.08	0.81	0.06	20.60	91.52
NN56	0.02	0.01	0.02	0.01	72.17	0.00	0.04	0.01	0.01	0.26	0.02	20.87	93.43
NN56	0.01	0.01	0.00	0.01	70.13	0.00	0.02	0.02	0.03	0.25	0.01	20.27	90.76
NN56	0.06	0.00	0.00	0.01	72.12	0.02	0.03	0.02	0.01	0.27	0.10	20.95	93.59
NN56	0.04	0.00	0.01	0.01	72.54	0.00	0.03	0.01	0.01	0.27	0.06	21.02	94.01
NN56	0.04	0.00	0.00	0.01	72.63	0.00	0.04	0.02	0.01	0.26	0.05	21.03	94.10
NN56	0.26	0.02	0.00	0.01	68.82	0.11	0.02	0.00	0.43	0.23	0.07	20.68	90.65
NN56	0.09	0.00	0.00	0.01	72.67	0.04	0.02	0.02	0.01	0.28	0.13	21.17	94.44

NN56	0.06	0.00	0.01	0.01	72.13	0.02	0.02	0.02	0.01	0.27	0.09	20.95	93.59
NN56	0.16	0.00	0.01	0.01	72.00	0.04	0.02	0.01	0.04	0.27	0.15	21.08	93.77
NN56	0.11	0.00	0.02	0.01	71.98	0.03	0.02	0.02	0.01	0.28	0.12	20.98	93.57
NN56	0.01	0.03	0.02	0.01	71.93	0.00	0.02	0.01	0.02	0.26	0.01	20.81	93.15
NN56	0.02	0.01	0.00	0.01	72.29	0.00	0.02	0.02	0.01	0.26	0.03	20.91	93.58
NN57	0.02	0.01	0.00	0.00	73.27	0.01	0.05	0.01	0.01	0.05	0.00	21.07	94.49
NN57	0.04	0.01	0.01	0.00	73.28	0.02	0.05	0.00	0.01	0.03	0.03	21.10	94.56
NN57	0.41	0.39	0.00	0.00	69.92	0.23	0.06	0.02	1.12	0.06	0.01	22.05	94.28
NN57	0.17	0.15	0.00	0.00	71.95	0.05	0.07	0.00	0.45	0.04	0.06	21.46	94.40
NN57	0.39	0.41	0.00	0.00	69.83	0.17	0.07	0.00	1.18	0.08	0.06	22.07	94.26
NN57	0.28	0.34	0.00	0.00	70.02	0.10	0.06	0.02	0.96	0.12	0.06	21.72	93.65
NN57	0.02	0.01	0.00	0.00	73.17	0.01	0.03	0.01	0.01	0.09	0.03	21.07	94.45
NN57	0.19	0.20	0.00	0.00	71.54	0.19	0.06	0.01	0.77	0.10	0.02	21.83	94.91
NN57	0.10	0.19	0.00	0.00	70.80	0.05	0.06	0.02	0.60	0.09	0.02	21.25	93.17
NN57	0.36	0.39	0.00	0.00	70.16	0.18	0.08	0.01	1.06	0.12	0.06	22.02	94.45
NN57	0.34	0.33	0.00	0.00	70.47	0.14	0.08	0.01	0.95	0.11	0.05	21.92	94.41
NN57	0.12	0.17	0.00	0.00	71.79	0.12	0.06	0.01	0.66	0.09	0.03	21.65	94.70
NN57	0.11	0.07	0.00	0.00	71.70	0.13	0.05	0.02	0.37	0.08	0.01	21.24	93.77
NN57	0.03	0.08	0.00	0.00	72.66	0.03	0.06	0.01	0.36	0.06	0.01	21.36	94.65
NN57	0.04	0.09	0.00	0.00	72.58	0.04	0.05	0.01	0.39	0.05	0.01	21.38	94.63
NN57	0.28	0.32	0.00	0.00	70.28	0.19	0.07	0.01	0.99	0.07	0.04	21.86	94.13
NN57	0.03	0.17	0.00	0.00	72.04	0.03	0.05	0.01	0.28	0.05	0.01	21.13	93.81
NN57	0.07	0.04	0.00	0.01	72.64	0.02	0.05	0.01	0.14	0.41	0.04	21.30	94.72
NN57	0.20	0.22	0.00	0.02	71.22	0.10	0.03	0.01	0.50	0.54	0.16	21.69	94.70
NN57	0.05	0.00	0.00	0.02	72.46	0.02	0.02	0.01	0.05	0.66	0.06	21.24	94.60
NN57	0.10	0.04	0.00	0.01	72.45	0.03	0.03	0.01	0.30	0.17	0.03	21.34	94.51
NN57	0.08	0.13	0.00	0.01	72.22	0.06	0.04	0.00	0.33	0.31	0.05	21.43	94.67
NN57	0.09	0.08	0.00	0.01	72.49	0.01	0.05	0.01	0.24	0.36	0.05	21.38	94.76
NN57	0.25	0.38	0.00	0.00	70.24	0.19	0.07	0.03	1.02	0.09	0.02	21.87	94.16
NN57	0.12	0.12	0.00	0.01	72.21	0.04	0.04	0.00	0.31	0.39	0.07	21.48	94.80
NN57	0.22	0.28	0.00	0.00	71.30	0.12	0.06	0.03	0.78	0.06	0.04	21.79	94.69
NN57	0.02	0.03	0.00	0.00	72.38	0.02	0.04	0.02	0.27	0.08	0.00	21.14	94.00
NN57	0.04	0.00	0.00	0.01	72.88	0.01	0.04	0.01	0.01	0.30	0.03	21.11	94.44
NN57	0.04	0.00	0.01	0.00	72.80	0.01	0.03	0.01	0.03	0.13	0.01	21.00	94.06
NN57	0.05	0.05	0.00	0.00	72.70	0.04	0.05	0.01	0.36	0.08	0.01	21.39	94.75
NN57	0.30	0.47	0.00	0.00	69.73	0.20	0.08	0.03	1.23	0.06	0.03	22.04	94.17
NN57	0.09	0.08	0.00	0.01	72.12	0.03	0.06	0.02	0.23	0.26	0.04	21.22	94.15
NN58	0.13	0.17	0.00	0.01	70.67	0.12	0.04	0.00	0.55	0.02	0.03	21.18	92.90
NN58	0.02	0.06	0.00	0.00	71.53	0.01	0.06	0.01	0.18	0.03	0.00	20.78	92.68
NN58	0.01	0.02	0.01	0.00	71.58	0.01	0.03	0.00	0.06	0.00	0.00	20.62	92.35
NN58	0.02	0.01	0.00	0.02	71.43	0.01	0.02	0.00	0.00	0.41	0.03	20.74	92.71
NN58	0.02	0.11	0.00	0.00	71.31	0.00	0.05	0.01	0.20	0.02	0.01	20.76	92.49
NN58	0.03	0.01	0.00	0.00	71.80	0.00	0.04	0.00	0.01	0.12	0.03	20.70	92.73
NN58	0.03	0.01	0.00	0.00	69.73	0.00	0.02	0.00	0.02	0.12	0.03	20.11	90.06
NN58	0.05	0.07	0.00	0.00	71.31	0.02	0.05	0.00	0.31	0.05	0.16	21.01	93.03
NN58	0.01	0.00	0.00	0.00	72.11	0.02	0.01	0.00	0.01	0.02	0.00	20.71	92.88
NN59	0.05	0.00	0.03	0.03	72.41	0.01	0.02	0.01	0.01	0.67	0.06	21.19	94.48
NN59	0.03	0.00	0.02	0.02	72.31	0.00	0.07	0.02	0.01	0.47	0.05	21.05	94.04
NN59	0.05	0.01	0.02	0.01	72.37	0.02	0.04	0.02	0.04	0.41	0.04	21.08	94.11

NN59	0.10	0.00	0.02	0.04	71.61	0.02	0.05	0.00	0.01	0.95	0.11	21.19	94.11
NN59	0.06	0.00	0.02	0.05	71.97	0.01	0.04	0.01	0.01	0.89	0.08	21.21	94.35
NN59	0.05	0.00	0.02	0.04	71.97	0.02	0.03	0.01	0.02	0.78	0.07	21.15	94.16
NN59	0.05	0.01	0.02	0.01	72.53	0.02	0.04	0.01	0.04	0.54	0.05	21.20	94.51
NN59	0.05	0.00	0.02	0.03	72.17	0.00	0.03	0.00	0.00	0.64	0.06	21.10	94.11
NN59	0.05	0.01	0.01	0.02	72.17	0.02	0.02	0.00	0.09	0.50	0.05	21.14	94.10
NN59	0.02	0.00	0.02	0.01	72.59	0.00	0.05	0.04	0.01	0.20	0.01	20.97	93.92
NN59	0.03	0.01	0.00	0.00	70.45	0.00	0.01	0.00	0.10	0.01	0.08	20.38	91.06
NN59	0.05	0.00	0.00	0.00	70.32	0.00	0.01	0.00	0.20	0.02	0.02	20.45	91.08
GM07	0.21	0.32	0.03	0.00	68.33	0.18	0.05	0.00	1.14	0.03	0.00	21.35	91.66
GM07	0.05	0.09	0.01	0.00	69.46	0.03	0.05	0.00	0.37	0.02	0.00	20.45	90.55
GM07	0.03	0.06	0.00	0.00	69.94	0.01	0.05	0.00	0.19	0.02	0.00	20.35	90.66
GM07	0.06	0.11	0.01	0.00	69.26	0.03	0.06	0.00	0.48	0.02	0.00	20.53	90.55
GM07	0.20	0.29	0.03	0.00	69.25	0.16	0.05	0.00	0.88	0.03	0.00	21.28	92.17
GM07	0.15	0.19	0.04	0.00	70.02	0.10	0.05	0.00	0.71	0.03	0.00	21.20	92.51
GM07	0.16	0.20	0.04	0.00	69.97	0.11	0.04	0.00	0.72	0.03	0.00	21.20	92.47
GM07	0.16	0.20	0.04	0.00	70.16	0.10	0.04	0.00	0.71	0.03	0.01	21.24	92.71
GM07	0.16	0.20	0.05	0.00	70.11	0.10	0.04	0.00	0.72	0.03	0.00	21.23	92.63
GM07	0.16	0.20	0.04	0.00	70.15	0.10	0.05	0.00	0.71	0.03	0.00	21.24	92.69
GM07	0.19	0.23	0.01	0.00	69.88	0.10	0.05	0.00	0.89	0.03	0.00	21.39	92.78
GM07	0.02	0.02	0.01	0.00	71.76	0.03	0.03	0.00	0.04	0.04	0.00	20.68	92.63
GM07	0.02	0.05	0.00	0.00	70.55	0.02	0.06	0.00	0.03	0.05	0.00	20.34	91.13
GM07	0.06	0.15	0.00	0.00	68.80	0.02	0.05	0.00	0.57	0.02	0.00	20.51	90.19
GM07	0.06	0.11	0.01	0.00	71.34	0.05	0.03	0.00	0.36	0.02	0.00	20.99	92.96
GM07	0.09	0.11	0.03	0.00	68.89	0.05	0.05	0.00	0.44	0.01	0.00	20.42	90.09
GM07	0.14	0.36	0.02	0.00	69.76	0.14	0.06	0.00	0.75	0.03	0.00	21.24	92.50
GM07	0.03	0.02	0.01	0.00	69.50	0.01	0.03	0.00	0.22	0.03	0.00	20.23	90.07
GM13	0.04	0.06	0.00	0.00	71.52	0.09	0.04	0.00	0.49	0.01	0.00	21.17	93.40
GM13	0.03	0.07	0.00	0.00	71.65	0.00	0.06	0.01	0.03	0.03	0.00	20.65	92.51
GM13	0.05	0.01	0.00	0.00	71.71	0.07	0.03	0.00	0.21	0.17	0.04	20.98	93.25
GM13	0.04	0.01	0.00	0.00	72.29	0.07	0.02	0.00	0.14	0.11	0.03	21.03	93.74
GM13	0.04	0.01	0.00	0.00	71.71	0.07	0.02	0.00	0.23	0.11	0.03	20.97	93.18
GM13	0.02	0.00	0.00	0.00	72.12	0.02	0.03	0.00	0.01	0.02	0.00	20.72	92.92
GM13	0.03	0.00	0.00	0.00	72.24	0.02	0.01	0.00	0.00	0.03	0.00	20.76	93.09
GM13	0.03	0.14	0.00	0.00	70.15	0.02	0.06	0.00	0.04	0.01	0.00	20.25	90.69
GM13	0.04	0.04	0.00	0.01	71.51	0.02	0.03	0.00	0.25	0.13	0.01	20.92	92.95
GM13	0.04	0.04	0.00	0.01	71.99	0.05	0.04	0.00	0.30	0.14	0.01	21.13	93.73
GM13	0.05	0.03	0.00	0.00	71.87	0.04	0.03	0.00	0.29	0.04	0.01	21.03	93.37
GM13	0.07	0.10	0.00	0.00	71.48	0.16	0.03	0.00	0.44	0.09	0.02	21.25	93.61
GM13	0.07	0.14	0.00	0.00	71.11	0.12	0.03	0.00	0.50	0.08	0.02	21.19	93.25
GM13	0.03	0.11	0.00	0.00	72.13	0.00	0.03	0.00	0.15	0.12	0.01	20.97	93.54
GM13	0.03	0.07	0.00	0.01	71.92	0.01	0.03	0.01	0.19	0.27	0.01	21.02	93.55
GM13	0.05	0.03	0.00	0.01	72.17	0.05	0.04	0.00	0.32	0.15	0.02	21.24	94.08
GM13	0.02	0.03	0.00	0.00	72.69	0.00	0.02	0.00	0.01	0.00	0.00	20.88	93.64
GM13	0.04	0.04	0.00	0.00	72.04	0.01	0.03	0.00	0.11	0.08	0.00	20.87	93.22
GM13	0.03	0.04	0.00	0.00	72.05	0.02	0.03	0.00	0.07	0.03	0.00	20.79	93.04
GM13	0.02	0.00	0.00	0.00	72.82	0.00	0.03	0.01	0.00	0.01	0.00	20.89	93.77
GM13	0.02	0.03	0.00	0.00	72.33	0.00	0.02	0.00	0.01	0.01	0.00	20.77	93.19
GM13	0.05	0.03	0.00	0.00	72.01	0.03	0.06	0.00	0.08	0.04	0.00	20.84	93.13

GM13	0.13	0.12	0.00	0.00	71.36	0.06	0.04	0.00	0.27	0.01	0.00	20.98	92.96
GM13	0.13	0.39	0.00	0.00	70.41	0.12	0.04	0.00	0.87	0.01	0.00	21.52	93.46
GM13	0.07	0.16	0.00	0.00	71.37	0.06	0.04	0.00	0.51	0.05	0.00	21.22	93.46
GM14	0.03	0.01	0.00	0.00	72.39	0.01	0.03	0.00	0.19	0.13	0.01	21.08	93.90
GM14	0.04	0.02	0.01	0.00	72.25	0.02	0.03	0.00	0.27	0.06	0.02	21.12	93.85
GM14	0.03	0.00	0.01	0.00	72.23	0.01	0.03	0.00	0.24	0.12	0.01	21.08	93.77
GM14	0.16	0.19	0.01	0.00	70.89	0.12	0.04	0.00	0.52	0.14	0.05	21.31	93.44
GM14	0.03	0.01	0.02	0.00	72.23	0.02	0.04	0.01	0.24	0.11	0.01	21.09	93.82
GM14	0.10	0.17	0.01	0.01	71.12	0.07	0.03	0.00	0.39	0.31	0.05	21.21	93.47
GM14	0.03	0.09	0.01	0.00	72.39	0.03	0.03	0.00	0.16	0.08	0.01	21.06	93.89
GM14	0.06	0.06	0.02	0.01	71.83	0.04	0.03	0.00	0.35	0.18	0.01	21.20	93.79
GM14	0.03	0.03	0.00	0.00	72.42	0.01	0.03	0.00	0.17	0.10	0.02	21.07	93.89
GM14	0.25	0.32	0.01	0.00	69.91	0.23	0.04	0.00	0.84	0.10	0.06	21.59	93.36
GM14	0.03	0.03	0.01	0.00	72.21	0.02	0.03	0.00	0.20	0.08	0.02	21.04	93.67
GM14	0.03	0.03	0.00	0.00	72.06	0.01	0.03	0.00	0.27	0.09	0.02	21.07	93.64
GM14	0.04	0.04	0.01	0.00	72.22	0.05	0.03	0.00	0.29	0.09	0.02	21.18	93.98
GM14	0.02	0.02	0.01	0.00	71.92	0.03	0.02	0.05	0.18	0.10	0.00	20.93	93.29
GM14	0.05	0.06	0.00	0.00	71.78	0.10	0.03	0.00	0.28	0.14	0.02	21.10	93.57
GM14	0.03	0.02	0.01	0.00	72.09	0.03	0.03	0.00	0.23	0.08	0.02	21.03	93.57
GM14	0.03	0.04	0.01	0.00	72.22	0.03	0.03	0.00	0.18	0.11	0.01	21.04	93.72
GM14	0.04	0.01	0.00	0.00	72.11	0.01	0.03	0.00	0.23	0.09	0.01	21.03	93.57
NN06	0.04	0.04	0.04	0.00	71.54	0.04	0.03	0.00	0.48	0.01	0.00	21.15	93.39
NN06	0.02	0.00	0.03	0.00	72.29	0.01	0.04	0.00	0.00	0.03	0.00	20.78	93.22
NN06	0.16	0.17	0.04	0.00	70.81	0.09	0.03	0.00	0.54	0.01	0.01	21.20	93.06
NN06	0.02	0.01	0.03	0.00	70.12	0.00	0.04	0.00	0.00	0.00	0.01	20.14	90.37
NN06	0.03	0.02	0.03	0.00	70.18	0.00	0.06	0.00	0.01	0.01	0.00	20.19	90.54
NN06	0.11	0.09	0.03	0.00	71.68	0.05	0.05	0.00	0.24	0.01	0.00	21.00	93.25
NN06	0.01	0.00	0.04	0.00	70.41	0.00	0.03	0.00	0.00	0.00	0.01	20.22	90.73
NN06	0.02	0.00	0.04	0.00	72.68	0.01	0.03	0.00	0.00	0.00	0.00	20.88	93.67
NN06	0.16	0.19	0.03	0.00	70.76	0.10	0.05	0.01	0.58	0.00	0.00	21.24	93.13
NN06	0.02	0.00	0.04	0.00	72.51	0.00	0.04	0.00	0.02	0.01	0.00	20.85	93.51
NN06	0.18	0.25	0.03	0.00	69.73	0.10	0.07	0.00	0.84	0.00	0.00	21.29	92.50
NN06	0.10	0.00	0.03	0.00	69.79	0.00	0.05	0.00	0.00	0.02	0.39	20.39	90.78
NN06	0.01	0.00	0.04	0.00	72.31	0.00	0.05	0.00	0.00	0.00	0.01	20.77	93.21
NN06	0.03	0.02	0.03	0.00	70.83	0.01	0.06	0.00	0.06	0.01	0.00	20.43	91.48
NN06	0.02	0.00	0.03	0.00	70.36	0.00	0.05	0.00	0.00	0.00	0.00	20.21	90.68
NN06	0.03	0.03	0.05	0.00	71.70	0.00	0.02	0.00	0.42	0.00	0.00	21.08	93.33
NN06	0.02	0.04	0.04	0.00	71.01	0.00	0.03	0.00	0.29	0.00	0.00	20.73	92.17
NN06	0.03	0.04	0.03	0.00	72.56	0.00	0.03	0.01	0.05	0.00	0.00	20.91	93.67
NN06	0.05	0.03	0.05	0.00	69.97	0.02	0.03	0.00	0.11	0.01	0.00	20.27	90.55
NN16	0.23	0.22	0.00	0.00	70.69	0.14	0.05	0.00	0.68	0.15	0.05	21.53	93.74
NN16	0.03	0.00	0.00	0.01	72.48	0.02	0.03	0.00	0.13	0.24	0.03	21.09	94.04
NN16	0.15	0.17	0.00	0.01	71.55	0.15	0.04	0.00	0.55	0.18	0.06	21.57	94.42
NN16	0.27	0.33	0.00	0.00	70.03	0.15	0.05	0.00	0.87	0.11	0.09	21.66	93.57
NN16	0.06	0.04	0.00	0.01	72.37	0.05	0.03	0.00	0.17	0.22	0.07	21.19	94.19
NN16	0.18	0.23	0.00	0.00	70.88	0.17	0.05	0.00	0.74	0.13	0.04	21.62	94.05
NN16	0.11	0.13	0.00	0.01	71.44	0.07	0.05	0.00	0.39	0.21	0.05	21.25	93.68
NN16	0.15	0.21	0.00	0.00	71.09	0.14	0.05	0.00	0.60	0.16	0.08	21.50	93.99
NN16	0.05	0.01	0.00	0.01	71.73	0.06	0.05	0.00	0.25	0.30	0.04	21.11	93.61

NN16	0.15	0.15	0.00	0.01	71.22	0.11	0.04	0.01	0.43	0.39	0.10	21.42	94.02
NN16	0.07	0.03	0.00	0.01	71.85	0.09	0.02	0.00	0.21	0.29	0.04	21.12	93.71
NN16	0.20	0.24	0.00	0.01	70.67	0.14	0.03	0.00	0.65	0.20	0.09	21.52	93.74
NN16	0.04	0.01	0.00	0.01	72.21	0.03	0.04	0.00	0.10	0.28	0.05	21.04	93.81

Appendix C

Sample preparation, irradiation, and incremental heating for Ar–Ar geochronology:

Actinolite (250 – 500 μm) was isolated from the crushed/sieved separates, washed ultrasonically in deionized water for 10 – 15 minutes, and then handpicked under a binocular microscope to remove any crystals that had visible inclusions or adhering material. Purified separates were placed in a 2.5 cm Al disk and irradiated in the cadmium-lined in-core tube at the Oregon State University reactor for 50 hours. The 28.201 Ma Fish Canyon sanidine (FCs) (Kuiper et al., 2008) was used as a neutron fluence monitor. J values were interpolated geometrically across each 2.5 cm diameter irradiation disk based on numerous measurements of FCs, which was distributed in eight to ten positions within each disk.

A small amount (~4-5 crystals) of actinolite was loaded into 2mm diameter wells within a copper tray and incrementally heated with a 55W CO2 laser in the WiscAr Laboratory at the University of Wisconsin-Madison. The extracted gas was purified via exposure to two SAES GP50 getters in series (both at 50 W/400 °C) for 90 seconds each and to an ARS cryotrap (at -125 °C) for another 60 seconds. Argon isotope analyses were done using a Nu Instruments Noblesse mass spectrometer. Sample analyses consisted of a continuous measurement for ~1200 seconds, whereas blank and gas cocktail measurements were made with a peak hop routine described in Jicha et al. (2016). All of the $^{40}Ar/^{39}Ar$ ages are calculated using the decay constants of Min et al. (2000), and the plateau and isochron ages are reported with 2σ analytical uncertainty, which includes the J uncertainty. All data were reduced and plotted using Pychron software (Ross, 2019).

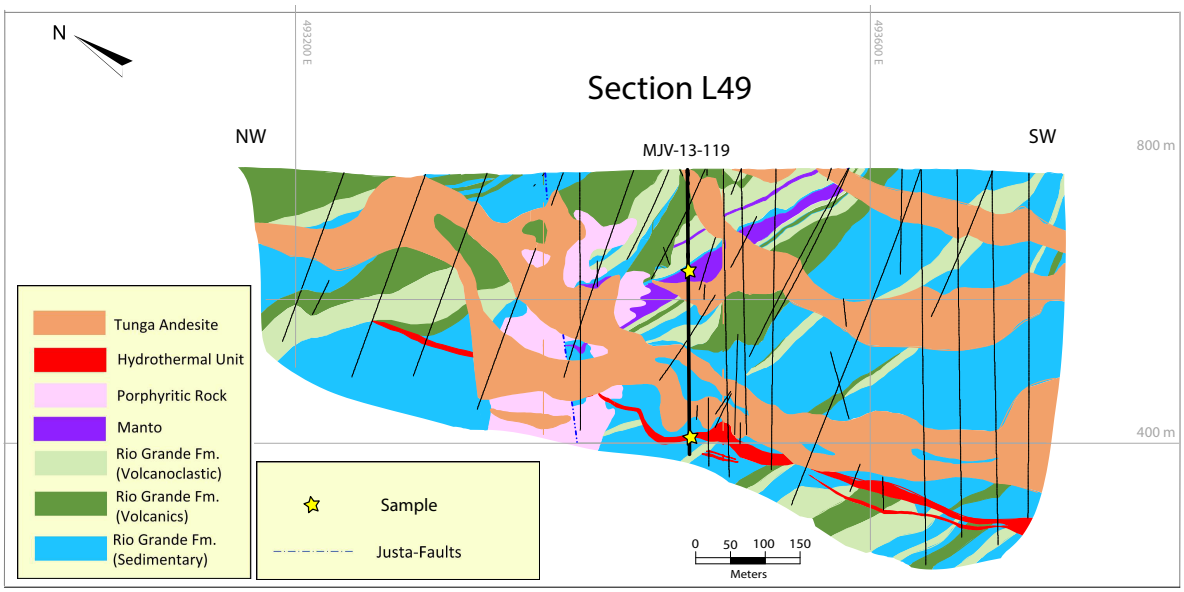

Figure A-6: Cross-section L49. The black lines represent the drill holes used to construct the section, including the bold, labelled line, which corresponds to a sampled drill hole. The stars indicate the location of samples. (Diagram provided by Marcobre).

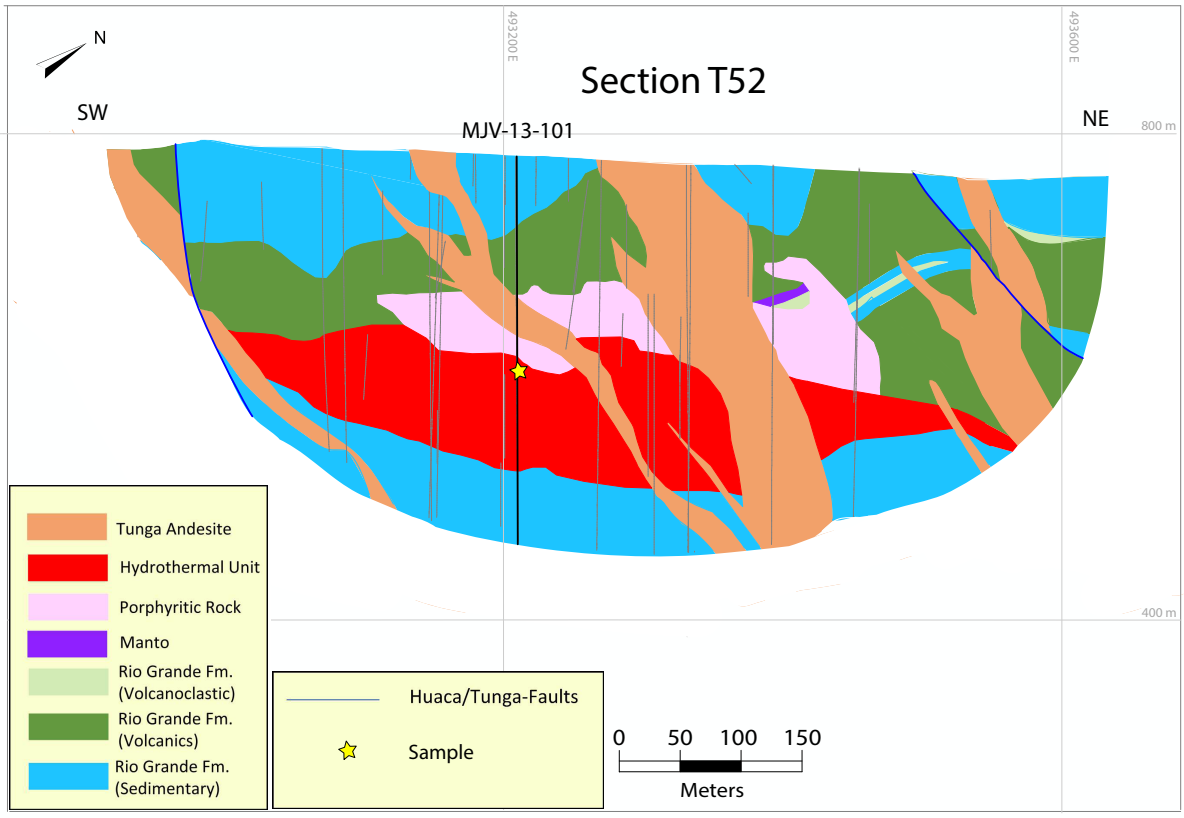

Figure A-7: Cross-section T52. The black lines represent the drill holes used to construct the section, including the bold, labelled line, which corresponds to a sampled drill hole. The star indicates the location of a sample. (Diagram provided by Marcobre).

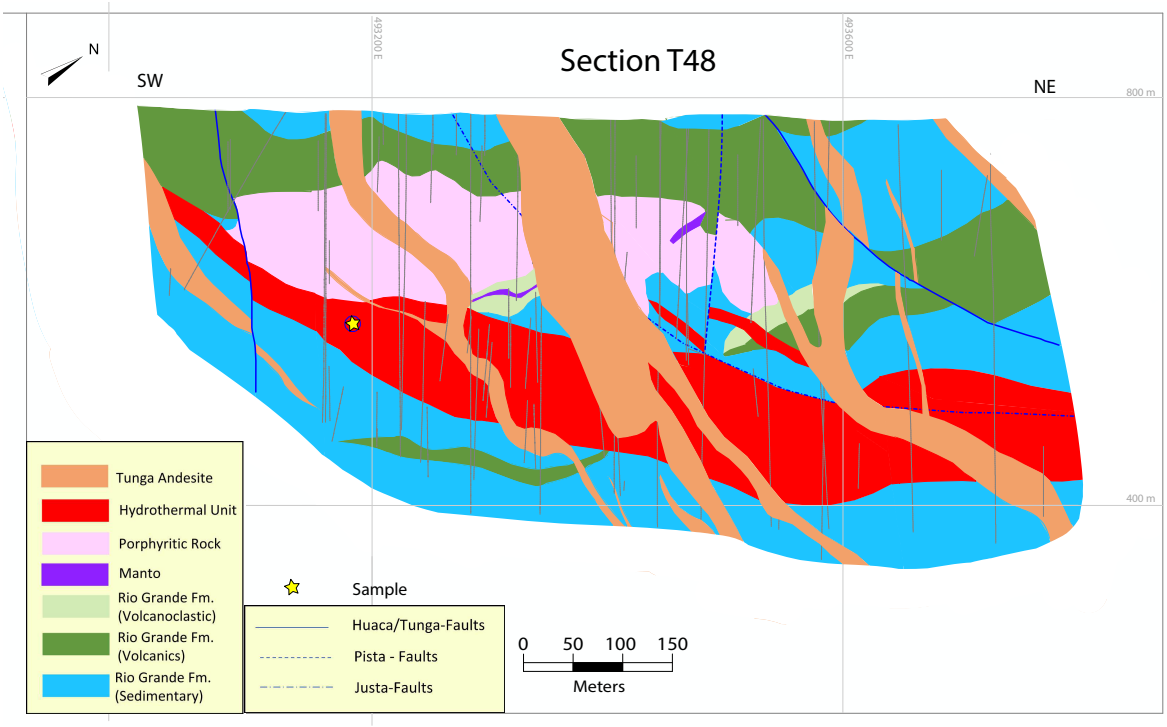

Figure A-8: Cross-section T48. The black lines represent the drill holes used to construct the section. The star indicates the location of a sample from the pit. (Diagram provided by Marcobre).

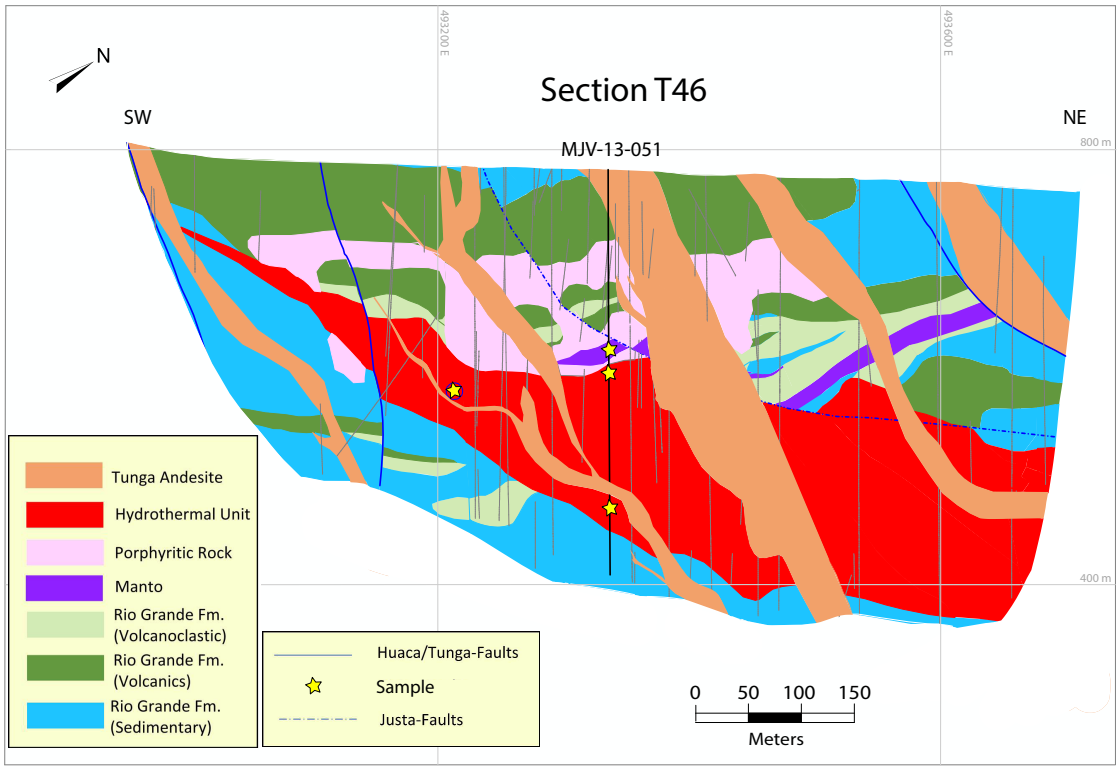

Figure A-9: Cross-section T46. The black lines represent the drill holes used to construct the section, including the bold, labelled line, which corresponds to a sampled drill hole. The stars indicate the location of samples. The sample that does not come from a drill hole was taken from the pit. (Diagram provided by Marcobre).

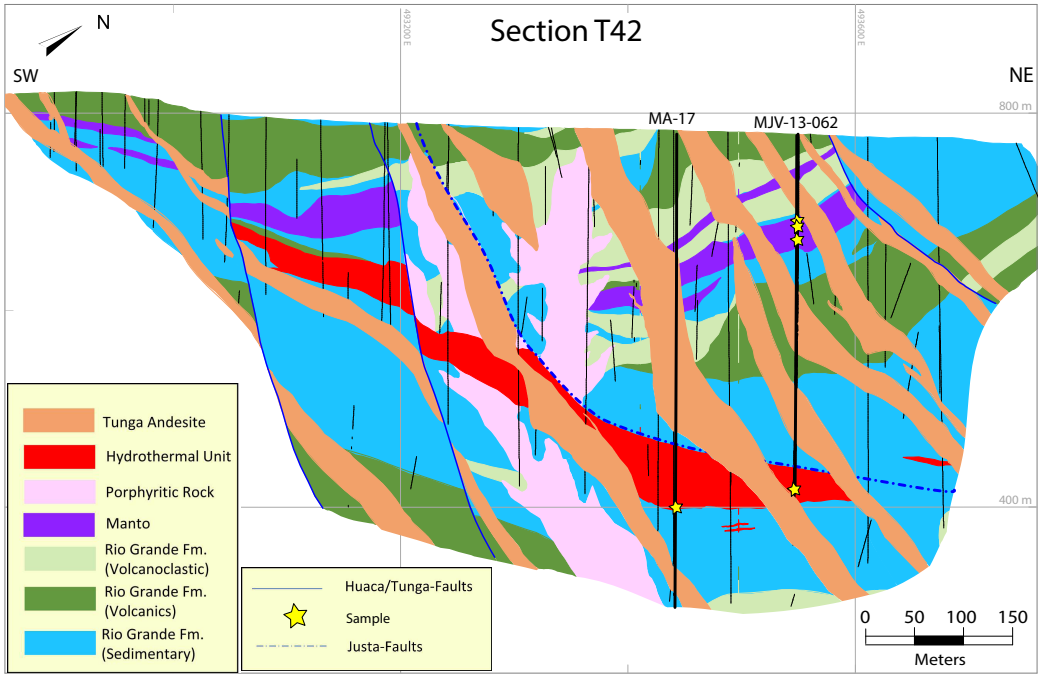

Figure A-10: Cross-section T42. The black lines represent the drill holes used to construct the section, including the bold, labelled line, which corresponds to a sampled drill hole. The stars indicate the location of samples. (Diagram provided by Marcobre).

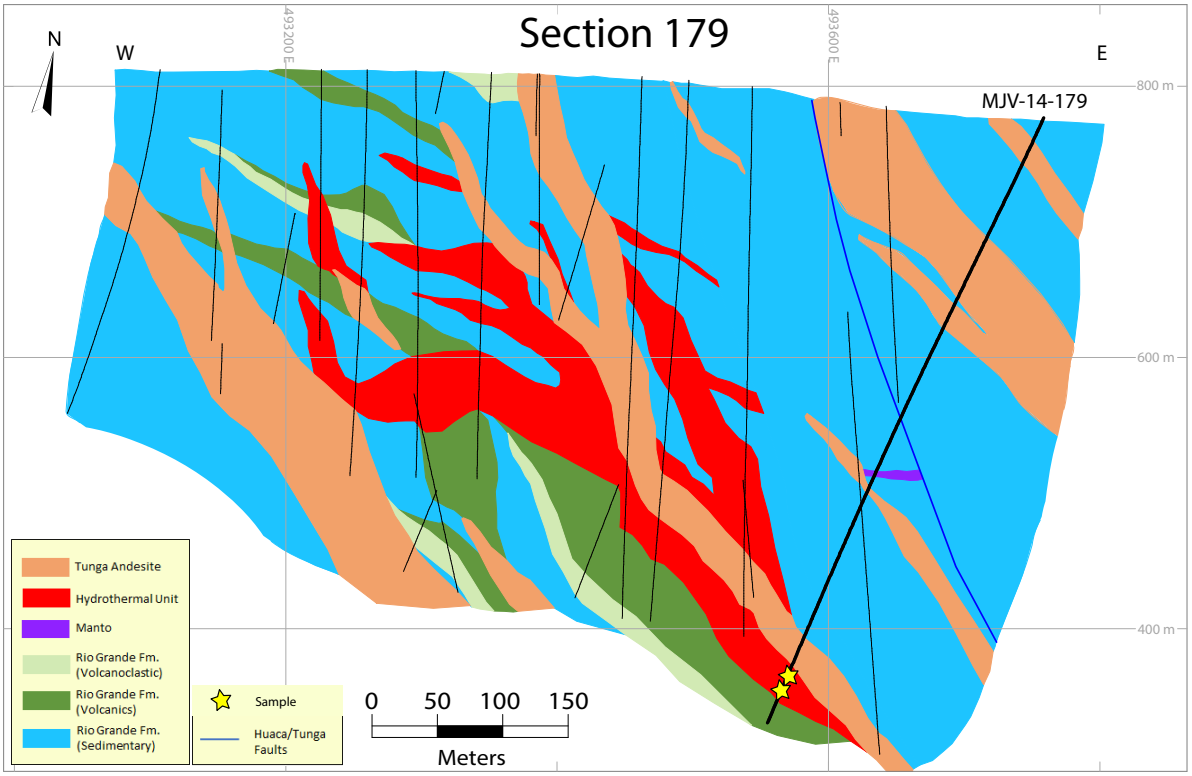

Figure A-11: Cross-section 179. The black lines represent the drill holes used to construct the section, including the bold, labelled line, which corresponds to a sampled drill hole. The stars indicate the location of samples. (Diagram provided by Marcobre).

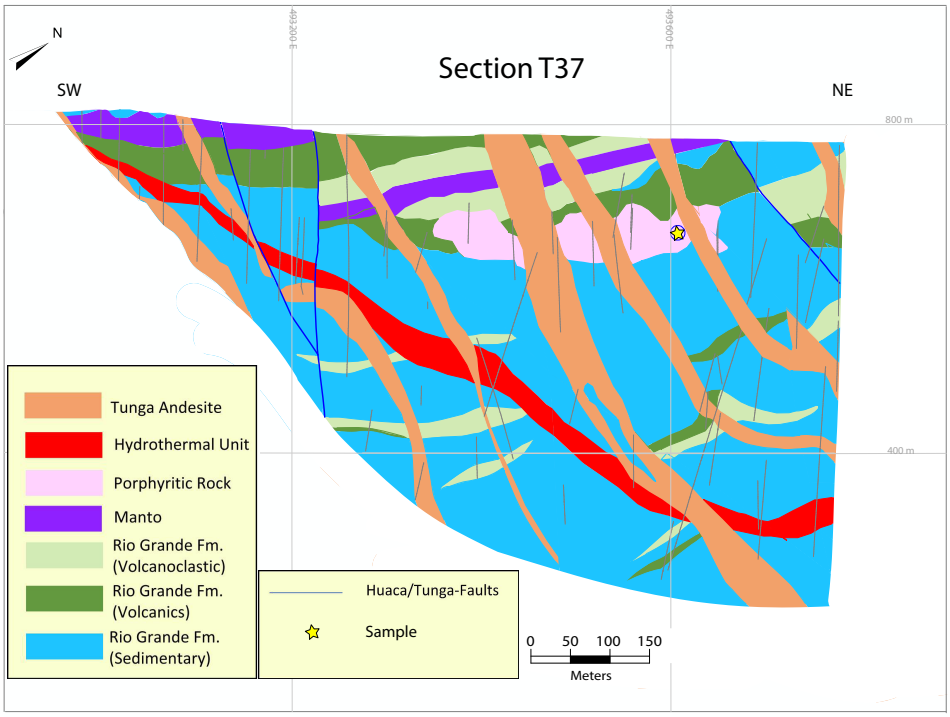

Figure A-12: Cross-section T37. The black lines represent the drill holes used to construct the section. The star indicates the location of a sample from the pit. (Diagram provided by Marcobre).

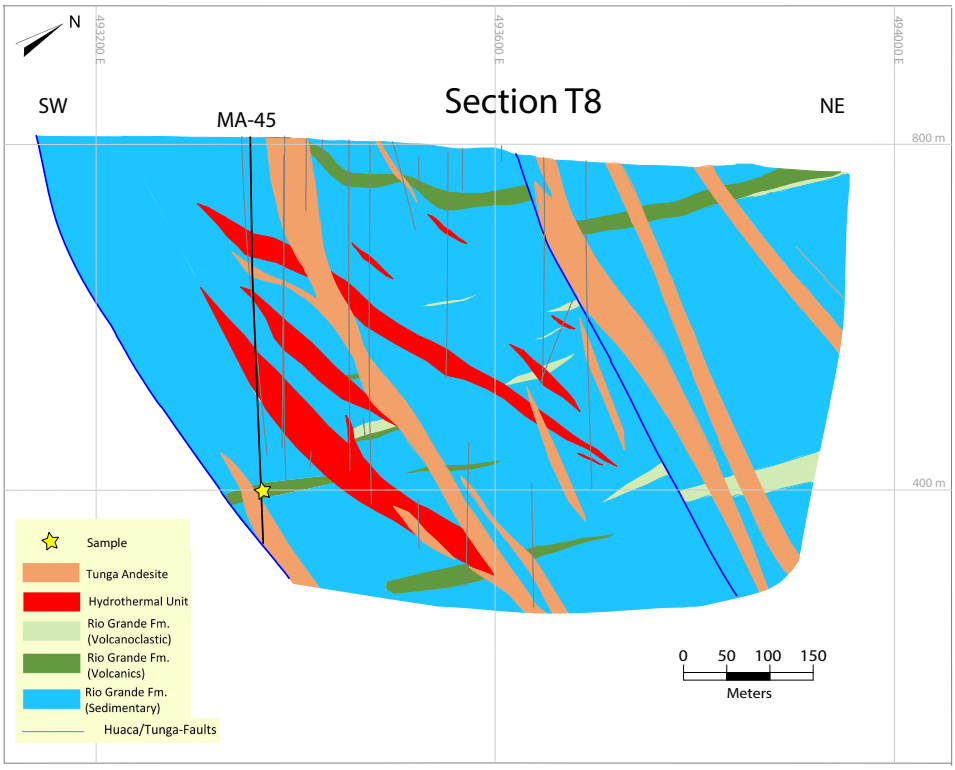

Figure A-13: Cross-section T8. The black lines represent the drill holes used to construct the section, including the bold, labelled line, which corresponds to a sampled drill hole. The star indicates the location of a sample. (Diagram provided by Marcobre).

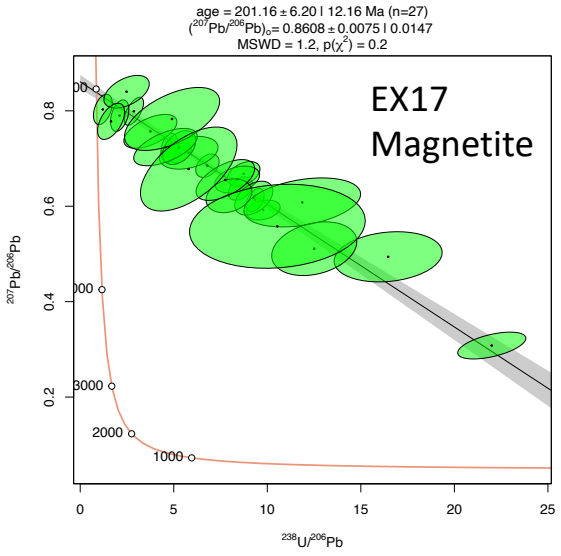
age = 201.16 ± 6.20 I 12.16 Ma (n=27)
(207Pb/206Pb)o= 0.8608 ± 0.0075 I 0.0147
MSWD = 1.2, p(χ2) = 0.2
EX17
Magnetite
207Pb/206Pb
238U/206Pb

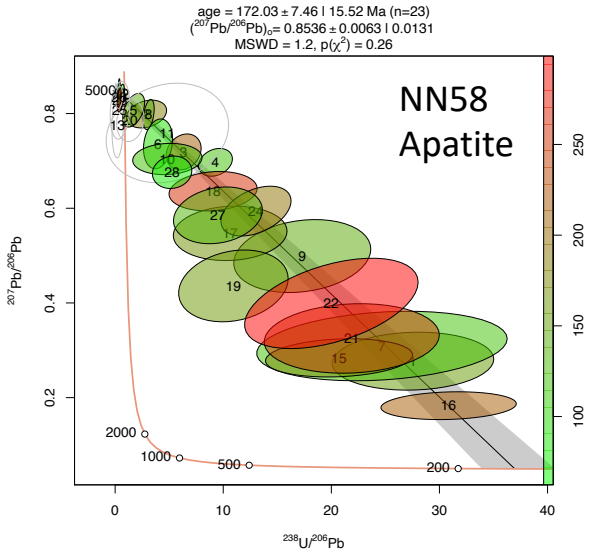
age = 172.03 ± 7.46 I 15.52 Ma (n=23)
(207Pb/206Pb)o= 0.8536 ± 0.0063 I 0.0131
MSWD = 1.2, p(χ2) = 0.26
NN58
Apatite
207Pb/206Pb
238U/206Pb

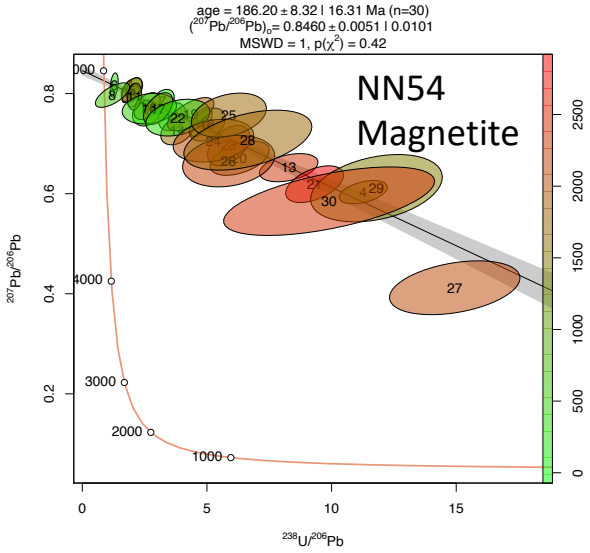
age = 186.20 ± 8.32 I 16.31 Ma (n=30)
(207Pb/206Pb)o= 0.8460 ± 0.0051 I 0.0101
MSWD = 1, p(χ2) = 0.42
NN54
Magnetite
207Pb/206Pb
238U/206Pb

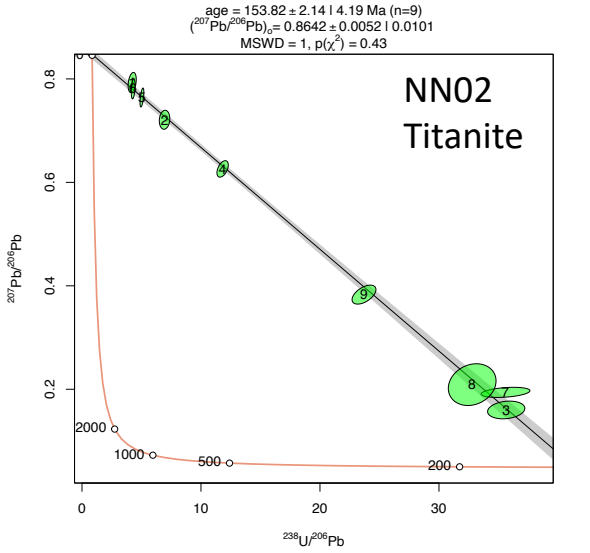
age = 153.82 ± 2.14 I 4.19 Ma (n=9)
(207Pb/206Pb)o= 0.8642 ± 0.0052 I 0.0101
MSWD = 1, p(χ2) = 0.43
NN02
Titanite
207Pb/206Pb
238U/206Pb

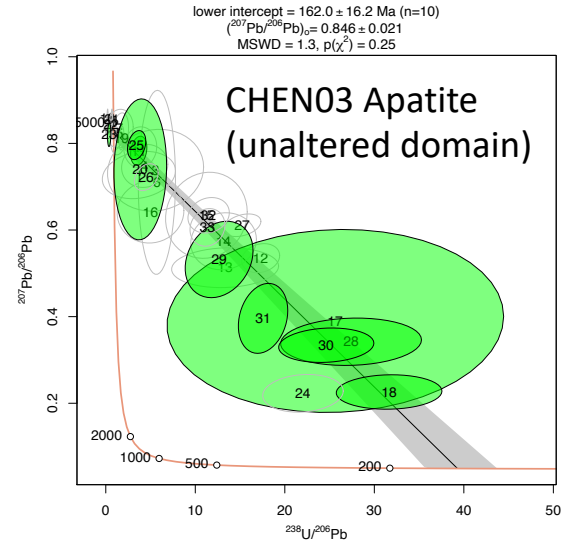
lower intercept = 162.0 ± 16.2 Ma (n=10)
(207Pb/206Pb)o= 0.846 ± 0.021
MSWD = 1.3, p(χ2) = 0.25
CHEN03 Apatite
(unaltered domain)
207Pb/206Pb
238U/206Pb

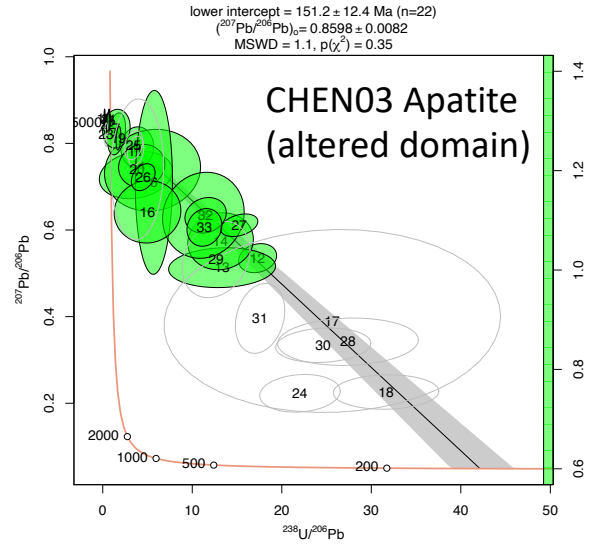
lower intercept = 151.2 ± 12.4 Ma (n=22)
(207Pb/206Pb)o= 0.8598 ± 0.0082
MSWD = 1.1, p(χ2) = 0.35
CHEN03 Apatite
(altered domain)
207Pb/206Pb
238U/206Pb

Figure A-14: Representative Tera-Wasserburg plots of samples from Marcona (sample EX17) and Mina Justa (other samples). The lower two panels show the dates of altered and unaltered domains in sample Chen03.

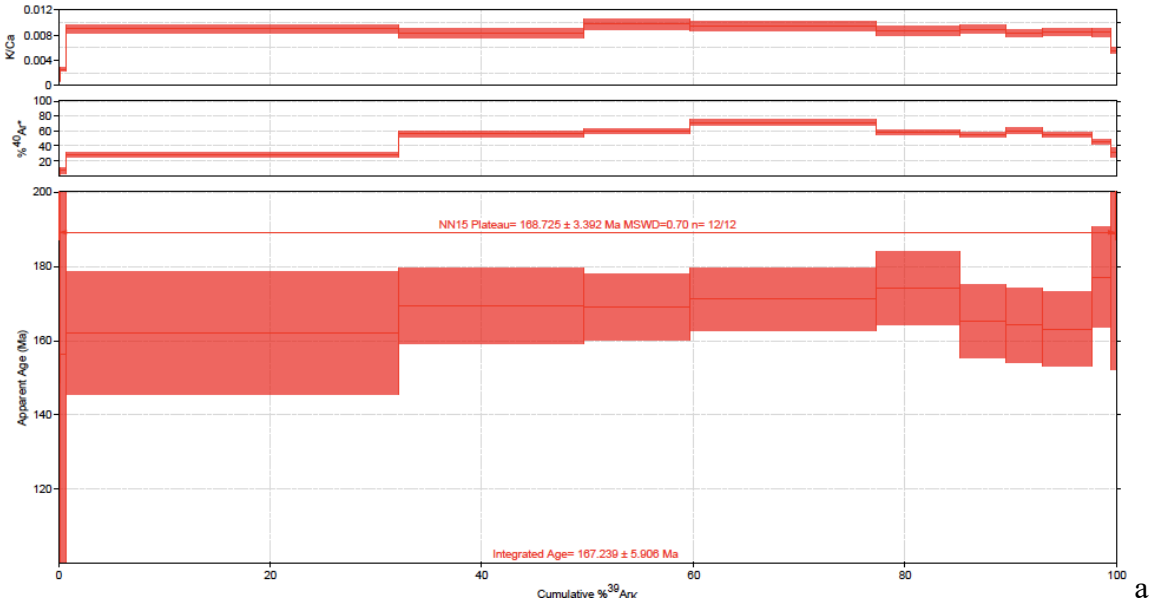

a

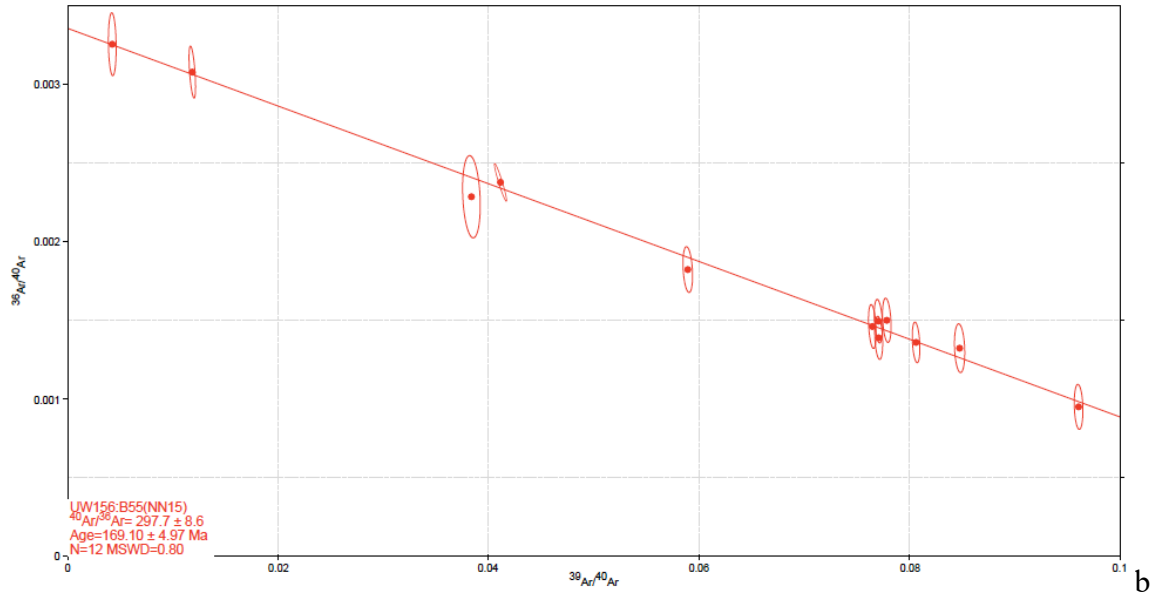

b

Figure A-15: a. Age spectrum plot and b. isochron diagram for sample NN15.

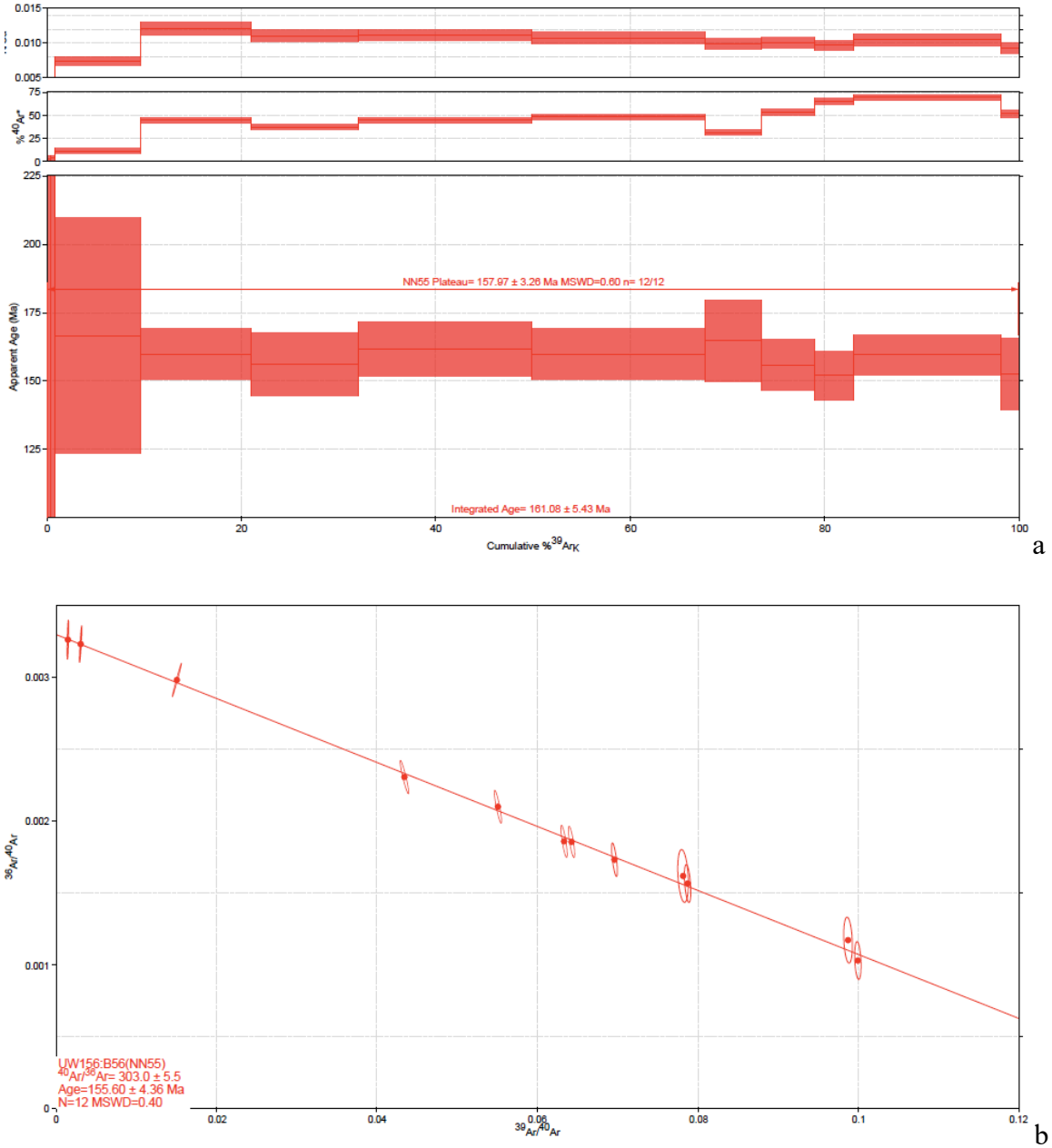

Figure A-16: a. Age spectrum plot and b. isochron diagram for sample NN55.

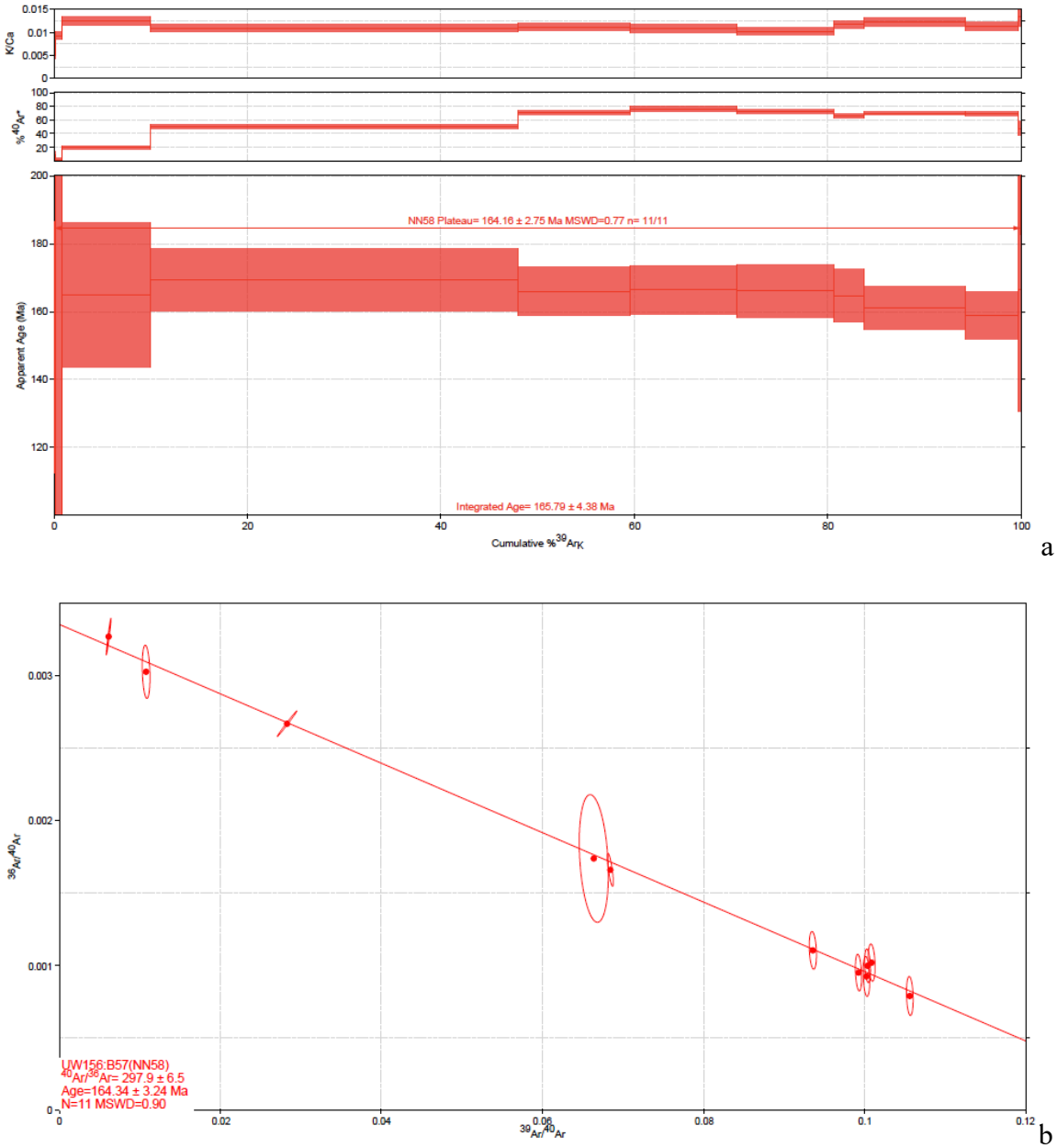

Figure A-17: a. Age spectrum plot and b. isochron diagram for sample NN58.

Table A-8: Location details of samples from this study

Sample	Hole	*UTM (E) Zone 18L	*UTM (N) Zone 18L	Depth (m)	Geologic unit
NN01	MV-13-051	493352	8323759	159.5	Mina Justa manto
NN03	MV-13-051	493352	8323759	183.1	Mina Justa hydrothermal unit
NN02	MV-13-051	493352	8323759	288.5	Mina Justa hydrothermal unit
NN50	MV-13-062	493550	8323758	87.3	Mina Justa manto
NN51	MV-13-062	493550	8323758	93.1	Mina Justa manto
NN52	MV-13-062	493550	8323758	103.5	Mina Justa manto

NN54	MV-13-062	493550	8323758	362	Mina Justa hydrothermal unit
NN04	MV-13-101	493209	8323849	178	Mina Justa manto
NN55	MV-13-119	493482	8323776	125	Mina Justa manto
NN56	MV-13-119	493482	8323776	129	Mina Justa manto
NN58	MV-13-119	493482	8323776	396	Mina Justa hydrothermal unit
NN15	MV-14-179	493759	8322822	467.4	Mina Justa hydrothermal unit
NN16	MV-14-179	493759	8322822	472.8	Mina Justa hydrothermal unit
CH02	MA-45	493358.191	8322643.219	404	Mina Justa hydrothermal unit
CH03	MA-17	493434.98	8323703.807	400	Mina Justa hydrothermal unit
EX17	13-562			280	Marcona manto
MJ01	Main Pit	493216	8323674	578	Mina Justa hydrothermal unit
MJ02	Main Pit	493181	8323724	578	Mina Justa hydrothermal unit
MJ03	Main Pit	493606	8323649	668	Mina Justa porphyritic rock

Table A-9: Concentrations of U and Th, and isotopic ratios of each spot in apatite grains used to calculate U–Pb dates.

Spot	U (ppm)	Th (ppm)	$^{238}U/^{206}Pb$	2s	$^{207}Pb/^{206}Pb$	2s	rho
NN04_01	2	13	14.94	1.50	0.667	0.031	0.34
NN04_02	1	5	7.19	1.47	0.361	0.022	0.11
NN01_a04_1	2	6	17.37	1.05	0.603	0.027	0.42
NN01_a04_4	2	5	26.24	3.31	0.682	0.041	0.47
NN01_a06_1	1	2	8.23	1.76	0.626	0.033	0.05
NN01_a06_2	1	2	9.91	2.21	0.655	0.022	0.21
NN01_a06_3	1	2	4.55	1.02	0.713	0.021	0.39
NN01_a05_1	0	2	20.71	12.58	0.550	0.111	0.07
NN01_a05_2	0	1	16.57	10.42	0.430	0.280	0.11
NN01_a07_2	0	9	15.26	5.03	0.532	0.062	0.12
NN01_a07_4	0	21	14.68	12.27	0.650	0.151	0.03
NN01_a07_5	0	30	25.22	12.07	0.299	0.079	0.09
NN01_a07_9	0	12	21.09	8.83	0.690	0.121	0.04
NN01_a07_11	0	14	11.15	6.55	0.632	0.074	0.04
NN01_a07_13	0	14	5.52	3.42	0.731	0.075	0.06
NN01_a09_5	0	10	9.59	5.00	0.590	0.121	0.08
NN58_a08_1	0	3	27.55	6.11	0.277	0.050	0.07
NN58_a08_2	0	4	2.90	1.52	0.799	0.024	0.26
NN58_a08_3	1	4	6.34	1.32	0.719	0.031	0.20
NN58_a08_4	1	3	9.28	1.28	0.697	0.024	0.25
NN58_a08_5	0	2	1.71	0.83	0.807	0.029	0.45
NN58_a08_6	0	1	3.97	1.10	0.736	0.043	0.19
NN58_a08_7	1	2	24.68	9.47	0.309	0.060	0.21

NN58_a08_8	1	3	3.11	0.41	0.798	0.026	0.38
NN58_a08_9	1	3	17.31	5.18	0.499	0.063	0.19
NN58_a08_10	1	3	4.83	2.62	0.704	0.027	0.09
NN58_a08_11	0	1	4.83	4.63	0.759	0.086	0.16
NN58_a08_12	1	1	0.65	0.18	0.840	0.018	0.20
NN58_a05_2	0	3	0.37	0.09	0.843	0.025	0.19
NN58_a05_3	0	4	20.71	5.56	0.284	0.033	0.15
NN58_a05_4	1	4	30.85	5.12	0.183	0.024	0.14
NN58_a05_5	0	3	10.64	4.30	0.547	0.047	0.08
NN58_a05_6	1	6	9.06	3.33	0.636	0.034	0.14
NN58_a06_1	0	7	10.94	4.14	0.436	0.062	0.20
NN58_a06_2	0	4	1.40	1.03	0.785	0.036	0.13
NN58_a06_3	1	5	21.89	6.62	0.325	0.060	0.10
NN58_a06_4	1	9	20.00	6.56	0.399	0.078	0.47
NN58_a06_5	0	6	0.45	0.22	0.829	0.021	0.34
NN58_a07_1	1	2	13.03	2.65	0.594	0.043	0.41
NN58_a07_3	0	1	0.37	0.27	0.834	0.019	0.20
NN58_a08_14	0	2	9.51	3.36	0.585	0.049	0.19
NN58_a08_15	0	2	5.27	1.49	0.676	0.028	0.09
NN50_a01_1	1	23	17.58	3.48	0.401	0.031	0.20
NN50_a01_2	1	25	26.42	4.19	0.334	0.031	0.10
NN50_a01_3	1	30	25.49	2.41	0.331	0.026	0.11
NN50_a01_4	1	23	22.75	3.95	0.332	0.029	0.08
NN50_a01_5	1	22	33.43	5.63	0.224	0.037	0.08
NN50_a01_6	1	22	28.50	4.52	0.328	0.028	0.20
NN50_a01_7	1	10	34.73	4.63	0.211	0.021	0.35
NN50_a01_8	1	27	24.63	3.02	0.341	0.018	0.23
NN50_a01_9	1	17	26.01	3.02	0.200	0.027	0.19
NN50_a01_10	1	19	31.35	3.20	0.213	0.026	0.18
NN50_a01_11	1	8	27.95	5.69	0.384	0.054	0.08
NN50_a01_12	1	11	30.53	9.66	0.147	0.032	0.09
NN50_a01_13	1	24	28.78	5.39	0.250	0.025	0.11
NN50_a01_14	1	27	25.78	6.32	0.197	0.019	0.06
NN50_a01_15	1	16	36.36	4.28	0.196	0.028	0.14
NN50_a01_16	1	27	30.53	8.86	0.173	0.019	0.07
NN50_a01_17	1	25	31.10	4.88	0.223	0.038	0.08
NN50_a02_1	1	19	30.21	5.46	0.141	0.032	0.11
NN50_a02_2	1	21	32.77	4.67	0.136	0.016	0.12
NN50_a02_3	1	16	30.61	5.53	0.156	0.023	0.09
NN50_a02_4	1	23	35.26	4.24	0.178	0.019	0.06

NN50_a02_5	1	28	31.61	5.63	0.191	0.024	0.06
NN50_a02_6	1	22	30.37	5.60	0.196	0.021	0.09
NN50_a02_7	1	22	24.68	9.47	0.221	0.038	0.03
NN50_a02_8	0	21	28.29	6.92	0.153	0.032	0.05
NN50_a02_9	1	23	32.22	5.76	0.169	0.027	0.02
NN50_a02_10	1	17	36.25	6.05	0.175	0.020	0.15
NN50_a03_1	0	10	32.13	8.13	0.144	0.030	0.09
NN50_a03_2	1	27	27.95	4.28	0.240	0.031	0.05
NN50_a03_3	1	19	26.36	6.01	0.206	0.019	0.05
NN50_a03_4	0	17	13.33	7.97	0.117	0.050	0.03
NN50_a03_5	0	22	11.72	9.59	0.109	0.034	0.02
NN50_a03_6	1	4	24.68	7.89	0.172	0.041	0.02
NN50_a03_7	1	15	25.22	7.14	0.283	0.031	0.20
NN51a-Ap1-1	2	4	34.97	7.86	0.118	0.048	0.16
NN51a-Ap1-3	1	5	60.24	20.36	0.130	0.120	0.10
NN51a-Ap1-4	1	11	32.26	10.43	0.195	0.039	0.18
NN51a-Ap1-5	1	17	32.26	11.46	0.120	0.071	0.09
NN51a-Ap1-6	1	4	5.88	3.46	0.890	0.151	0.38
NN51a-Ap1-8	1	3	30.30	10.12	0.277	0.094	0.03
NN51a-Ap2-1	5	8	8.26	0.84	0.628	0.022	0.09
NN51a-Ap3-1	5	6	7.29	0.39	0.649	0.020	0.32
NN51a-Ap3-2	3	6	18.59	2.69	0.395	0.035	0.12
NN51a-Ap3-3	2	5	14.29	2.06	0.384	0.030	0.17
NN51a-Ap3-4	3	4	18.80	2.57	0.370	0.025	0.06
NN51a-Ap4-1	4	5	20.53	1.45	0.368	0.021	0.15
NN51a-Ap6-1	3	12	16.31	1.58	0.424	0.024	0.11
NN51a-Ap7-1	1	3	28.33	7.16	0.176	0.039	0.08
NN51a-Ap7-2	1	9	22.73	11.37	0.178	0.073	0.03
NN51a-Ap7-3	1	41	25.00	12.51	0.193	0.096	0.07
NN51a-Ap7-4	1	26	27.03	11.70	0.174	0.049	0.06
NN51a-Ap7-5	1	19	25.00	13.13	0.236	0.052	0.06
NN51a-Ap7-6	1	24	41.84	16.48	0.196	0.071	0.12
NN51a-Ap8-1	3	19	10.81	1.03	0.492	0.022	0.09
NN51a-Ap8-2	3	17	8.06	1.18	0.571	0.026	0.41
NN51a-Ap9-1	3	6	19.01	3.20	0.338	0.030	0.10
NN51a-Ap10-1	3	8	13.68	1.54	0.470	0.030	0.13
NN51a-Ap10-2	2	6	15.63	2.70	0.441	0.042	0.08
NN51a-Ap11-1	1	7	6.67	5.78	0.596	0.081	0.57
NN51a-Ap13-1	2	6	14.08	6.16	0.516	0.037	0.13
NN51a-Ap14-1	2	6	15.15	5.29	0.503	0.044	0.04

NN51a-Ap16-1	2	4	11.24	1.66	0.623	0.027	0.14
EX19-Ap5-2	3	7	0.65	0.08	0.870	0.019	0.29
EX19-Ap4-1	1	2	0.09	0.03	0.919	0.020	0.19
EX19-Ap4-2	1	1	0.46	0.18	0.879	0.021	0.28
EX19-Ap4-3	2	3	0.43	0.07	0.882	0.019	0.28
EX19-Ap3-2	2	3	0.30	0.07	0.876	0.019	0.16
EX19-Ap2-1	1	5	0.11	0.02	0.884	0.018	0.13
EX19-Ap1-1	1	2	0.06	0.02	0.887	0.018	0.24
EX19-Ap1-2	2	1	4.65	0.74	0.773	0.023	0.20
EX19-Ap1-3	2	2	0.25	0.03	0.866	0.018	0.36
EX19-Ap1-4	3	2	1.06	0.18	0.850	0.018	0.56
EX19-Ap1-5	2	3	0.14	0.03	0.858	0.017	0.20
EX19-Ap1-6	2	5	0.07	0.01	0.867	0.017	0.25
EX19-Ap1-7	2	4	0.14	0.03	0.858	0.018	0.24
EX17-Ap1-1	2	2	23.26	6.51	0.331	0.053	0.10
EX17-Apt9-1	2	2	7.94	2.15	0.661	0.043	0.39
EX17-Apt-10-1	1	1	1.72	1.43	0.845	0.082	0.38
EX17-Apt-10-2	1	2	9.52	2.00	0.718	0.040	0.15
EX17-Apt-10-3	2	3	14.77	1.71	0.535	0.026	0.09
EX17-Apt-10-4	2	1	13.70	2.64	0.551	0.030	0.17
EX17-Ap8-1	3	1	33.00	3.44	0.235	0.028	0.27
EX17-Ap8-2	3	1	30.77	3.18	0.183	0.024	0.11
EX17-Ap8-3	3	1	24.45	3.62	0.301	0.051	0.27
EX17-Ap8-4	3	1	3.51	0.60	0.770	0.025	0.49
EX17-Ap8-5	3	2	9.62	1.40	0.596	0.030	0.40
EX17-Ap8-6	2	1	28.74	3.60	0.174	0.025	0.05
EX17-Ap4-1	2	1	3.48	0.68	0.758	0.030	0.21
EX17-Ap4-2	9	8	9.71	3.12	0.529	0.083	0.37
EX17-Ap3-1	7	4	9.43	0.73	0.634	0.026	0.43
EX17-Ap3-2	10	5	7.69	1.72	0.656	0.045	0.28
EX17-Ap11-1	1	3	9.17	3.04	0.711	0.057	0.23
EX17-Ap12-1	1	3	0.05	0.04	0.813	0.025	0.32
EX17-Ap13-1	0	1	5.56	5.25	0.776	0.021	0.00
EX17-Ap13-2	1	3	9.09	2.24	0.756	0.055	0.20
EX17-Ap13-5	1	3	9.26	4.98	0.588	0.059	0.05
EX17-Ap21-1	18	10	26.88	2.87	0.311	0.031	0.47
EX17-Ap21-2	18	12	31.55	3.15	0.227	0.031	0.29
EX17-Ap22-1	8	4	23.92	2.45	0.376	0.053	0.32
EX17-Ap23-1	2	4	9.26	1.38	0.686	0.027	0.20
EX17-Ap23-2	2	5	10.99	2.18	0.657	0.033	0.21

EX17-Ap23-3	1	6	7.09	2.02	0.726	0.035	0.08
EX17-Ap23-4	1	0	5.49	1.60	0.796	0.031	0.10
EX17-Ap23-5	2	5	8.85	2.59	0.729	0.045	0.07
NN56-Ap1-1	1	30	30.96	4.74	0.308	0.032	0.18
NN56-Ap1-2	1	36	23.53	4.29	0.259	0.040	0.07
NN56-Ap1-3	2	27	25.64	7.25	0.312	0.050	0.05
NN56-Ap1-4	2	34	24.39	5.97	0.423	0.044	0.14
NN56-Ap1-5	1	35	21.01	3.25	0.311	0.038	0.15
NN56-Ap1-6	2	36	15.63	4.65	0.488	0.043	0.14
NN56-Ap1-7	2	36	31.95	8.80	0.258	0.054	0.08
NN56-Ap1-8	1	38	21.28	5.45	0.275	0.043	0.03
NN56-Ap1-9	2	39	21.74	5.22	0.360	0.030	0.05
NN56-Ap1-10	2	50	26.81	7.06	0.229	0.032	0.10
NN56-Ap2-1	2	44	22.22	7.91	0.245	0.039	0.03
NN56-Ap2-2	1	44	24.15	4.40	0.251	0.036	0.06
NN56-Ap2-3	2	28	33.44	6.52	0.210	0.052	0.03
NN56-Ap2-4	1	24	18.87	4.29	0.350	0.038	0.10
NN56-Ap1-11	2	48	25.32	5.60	0.232	0.031	0.07
NN56-Ap1-12	1	0	3.94	1.35	0.796	0.027	0.07
NN56-Ap3-1	1	19	4.31	1.51	0.770	0.048	0.13
NN56-Ap3-2	1	24	17.54	5.24	0.310	0.047	0.11
NN56-Ap3-3	2	18	25.58	6.10	0.431	0.042	0.09
NN56-Ap3-4	1	14	28.33	5.41	0.261	0.051	0.11
NN56-Ap3-5	1	7	16.67	5.01	0.598	0.081	0.14
NN56-Ap3-6	2	25	22.99	4.52	0.351	0.045	0.09
NN56-Ap2-5	2	41	27.86	6.15	0.231	0.035	0.05
NN56-Ap2-6	2	38	26.11	4.80	0.285	0.026	0.11
NN56-Ap2-7	2	40	25.64	8.56	0.198	0.025	0.09
NN56-Ap2-8	1	41	10.20	4.07	0.527	0.041	0.14
NN56-Ap1-13	1	0	2.38	1.47	0.823	0.040	0.06
NN56-Ap1-14	0	0	3.03	1.01	0.867	0.059	0.02
NN56-Ap1-16	2	41	20.04	4.00	0.423	0.049	0.04
NN56-Ap1-17	2	37	26.39	6.08	0.288	0.040	0.13
NN02-Ap1-1	1	29	20.83	7.39	0.281	0.047	0.08
NN02-Ap1-3	1	28	4.00	3.20	0.723	0.040	0.03
NN02-Ap1-5	2	30	12.36	1.49	0.538	0.039	0.11
NN02-Ap1-7	1	23	18.87	6.06	0.462	0.074	0.07
NN02-Ap2-2	1	21	3.26	1.04	0.793	0.023	0.08
NN02-Ap2-3	1	9	2.39	0.56	0.820	0.030	0.02
NN02-Ap2-4	1	24	17.54	4.63	0.296	0.047	0.07

NN02-Ap3-2	1	9	2.33	0.76	0.766	0.026	0.04
NN02-Ap3-3	1	5	1.41	0.69	0.849	0.044	0.02
NN02-Ap3-4	1	10	4.35	1.27	0.772	0.027	0.05
NN02-Ap3-5	1	6	1.69	0.98	0.817	0.032	0.05
NN02-Ap5-1	1	7	35.71	8.83	0.086	0.043	0.03
NN02-Ap5-2	1	10	14.08	2.40	0.522	0.042	0.16
NN02-Ap5-3	1	19	3.45	2.02	0.691	0.030	0.19
NN02-Ap13-1	1	18	1.79	0.45	0.763	0.052	0.04
NN02-Ap13-2	1	16	3.76	0.98	0.785	0.026	0.23
NN02-Ap16-2	1	7	1.15	0.82	0.883	0.031	0.03
NN02-Ap16-3	1	11	1.08	0.80	0.856	0.048	0.03
NN02-Ap11-1	1	7	1.19	0.38	0.851	0.038	0.06
NN02-Ap11-2	1	7	0.99	0.64	0.859	0.057	0.02
NN02-Ap15-1	1	12	0.12	0.04	0.894	0.019	0.06
NN02-Ap15-2	2	15	0.23	0.09	0.881	0.019	0.02
NN02-Ap15-3	1	13	0.07	0.05	0.881	0.020	0.04
NN02-Ap18-1	1	30	15.63	3.92	0.481	0.041	0.11
NN02-Ap18-2	1	34	30.12	5.66	0.113	0.031	0.04
NN02-Ap18-3	2	31	9.62	1.58	0.697	0.033	0.13
Chen3-Ap2-1	1	2	3.70	3.29	0.727	0.044	0.18
Chen3-Ap3-1	1	0	3.85	1.48	0.791	0.038	0.04
Chen3-Ap3-2	1	2	5.56	4.32	0.738	0.076	0.08
Chen3-Ap4-1	1	0	4.35	2.08	0.748	0.040	0.08
Chen3-Ap4-2	1	2	1.54	0.81	0.822	0.039	0.30
Chen3-Ap4-3	1	0	5.71	1.67	0.710	0.171	0.03
Chen3-Ap5-2	1	1	1.52	1.24	0.834	0.036	0.09
Chen3-Ap10-1	2	4	0.54	0.09	0.849	0.018	0.61
Chen3-Ap10-2	2	4	0.66	0.11	0.852	0.019	0.43
Chen3-Ap11-1	1	9	0.20	0.05	0.857	0.018	0.15
Chen3-Ap11-2	2	11	3.68	0.73	0.783	0.027	0.22
Chen3-Ap8-1	3	1	17.30	1.71	0.535	0.027	0.18
Chen3-Ap7-1	1	1	13.33	4.81	0.513	0.037	0.08
Chen3-Ap7-2	1	1	13.16	2.95	0.574	0.053	0.07
Chen3-Ap7-3	1	0	11.24	3.67	0.634	0.080	0.08
Chen3-Ap7-4	1	1	5.00	3.00	0.642	0.058	0.04
Chen3-Ap22-1	1	6	25.64	15.13	0.390	0.170	0.05
Chen3-Ap22-2	2	13	31.65	4.75	0.226	0.032	0.05
Chen3-Ap20-1	3	4	1.76	0.21	0.812	0.022	0.27
Chen3-Ap15-1	1	9	3.85	2.37	0.740	0.131	0.05
Chen3-Ap15-2	3	3	0.67	0.08	0.857	0.018	0.36

Chen3-Ap1-1	2	3	0.60	0.15	0.845	0.020	0.22
Chen3-Ap1-2	1	12	0.38	0.15	0.820	0.022	0.11
Chen3-Ap1-3	2	18	22.03	3.62	0.223	0.035	0.12
Chen3-Ap1-4	2	13	3.45	0.82	0.796	0.027	0.27
Chen3-Ap19-1	2	2	4.52	1.07	0.722	0.025	0.32
Chen3-Ap19-2	3	1	15.24	1.68	0.611	0.021	0.34
Chen3-Ap23-1	2	17	27.40	6.33	0.342	0.044	0.08
Chen3-Ap23-2	3	21	12.66	3.05	0.532	0.071	0.23
Chen3-Ap23-3	2	19	24.63	4.28	0.334	0.032	0.12
Chen3-Ap23-4	4	23	17.57	2.22	0.396	0.065	0.22
Chen3-Ap23-5	2	17	11.49	1.86	0.634	0.033	0.15
Chen3-Ap23-6	2	8	11.36	1.57	0.606	0.035	0.12
NN54-Ap2-1	5	8	20.12	2.98	0.419	0.064	0.56
NN54-Ap2-2	1	3	1.67	1.36	0.779	0.059	0.12
Chen2-Ap10-1	1	10	1.52	0.41	0.809	0.021	0.16
Chen2-Ap10-2	2	9	1.64	0.30	0.828	0.022	0.09
Chen2-Ap10-3	2	9	1.79	0.45	0.821	0.024	0.11
Chen2-Ap11-1	6	12	3.33	0.25	0.803	0.019	0.13
Chen2-Ap11-2	4	15	3.75	0.40	0.808	0.022	0.27
Chen2-Ap12-1	3	13	5.43	1.10	0.747	0.025	0.14
Chen2-Ap12-2	2	8	2.36	0.51	0.823	0.032	0.18
Chen2-Ap12-3	10	25	8.43	0.57	0.711	0.021	0.47
Chen2-Ap9-1	2	14	3.23	0.43	0.810	0.022	0.08
Chen2-Ap9-2	2	20	3.04	0.56	0.800	0.023	0.09
Chen2-Ap9-3	3	11	3.69	0.37	0.788	0.022	0.20
Chen2-Ap8-1	2	13	4.15	0.59	0.794	0.022	0.13
Chen2-Ap8-2	2	10	4.03	0.48	0.779	0.018	0.21
Chen2-Ap8-3	3	11	1.92	0.41	0.834	0.022	0.60
Chen2-Ap7-1	1	7	1.69	0.35	0.825	0.019	0.13
Chen2-Ap7-2	2	9	1.49	0.29	0.825	0.022	0.09
Chen2-Ap6-1	5	9	7.41	0.57	0.735	0.022	0.21
Chen2-Ap6-2	4	7	5.65	0.62	0.751	0.025	0.06
Chen2-Ap6-3	2	9	2.95	0.41	0.788	0.024	0.18
Chen2-Ap6-4	2	8	3.28	0.68	0.802	0.029	0.21
Chen2-Ap5-1	7	17	5.71	0.63	0.748	0.023	0.23
Chen2-Ap5-2	3	11	4.33	0.40	0.775	0.021	0.14
Chen2-Ap5-3	5	9	2.51	0.17	0.826	0.019	0.51
Chen2-Ap5-4	4	12	6.10	0.64	0.760	0.022	0.18
Chen2-Ap4-1	3	11	4.74	0.35	0.764	0.025	0.12
Chen2-Ap4-2	2	11	4.83	0.48	0.769	0.020	0.27

Chen2-Ap2-1	4	11	2.87	0.25	0.799	0.018	0.11
Chen2-Ap2-2	4	8	3.14	0.25	0.794	0.022	0.29
Chen2-Ap1-1	3	38	2.22	0.31	0.815	0.019	0.30
Chen2-Ap1-2	3	12	5.65	0.46	0.746	0.022	0.32
Chen2-Ap1-3	4	31	1.19	0.08	0.850	0.018	0.44
Chen2-Ap1-4	4	17	3.69	0.23	0.789	0.019	0.36
NN16-Ap1-1	2	25	29.76	5.35	0.198	0.056	0.05
NN16-Ap1-2	1	15	3.57	1.28	0.766	0.035	0.03
NN16-Ap1-3	1	23	17.24	9.82	0.360	0.160	0.32
NN16-Ap1-4	1	20	4.76	1.12	0.756	0.033	0.21
NN16-Ap2	2	21	27.62	4.84	0.319	0.040	0.24
NN16-Ap5-1	2	17	11.90	1.86	0.634	0.041	0.26
NN16-Ap5-2	3	21	10.10	2.76	0.601	0.055	0.44
NN16-Ap5-3	2	21	16.16	1.93	0.532	0.033	0.28
NN16-Ap6-2	2	44	2.76	0.46	0.800	0.025	0.25
NN16-Ap6-3	2	34	24.39	5.97	0.263	0.061	0.15
NN16-Ap6-4	2	33	4.46	0.82	0.761	0.037	0.55
NN16-Ap8-1	0	23	28.57	13.07	0.450	0.120	0.07
NN16-Ap9-1	1	19	0.25	0.19	0.816	0.036	0.68
NN16-Ap9-2	2	31	3.10	0.69	0.756	0.028	0.42
NN16-Ap10-1	1	12	0.41	0.16	0.847	0.020	0.12
NN16-Ap10-3	1	16	1.79	0.77	0.814	0.020	0.30
NN16-Ap11-2	1	22	2.62	0.54	0.768	0.021	0.07
NN16-Ap12-1	2	22	8.00	1.93	0.681	0.047	0.46
NN16-Ap12-2	2	26	23.26	5.43	0.255	0.041	0.16
NN16-Ap12-3	2	19	2.25	0.32	0.793	0.026	0.12
NN16-Ap12-4	2	23	11.90	1.44	0.616	0.032	0.39
NN16-Ap12-5	2	22	0.48	0.09	0.839	0.018	0.11
NN16-Ap12-6	2	21	13.85	1.88	0.575	0.037	0.06
NN16-Ap13-1	1	4	16.39	9.95	0.300	0.100	0.04
NN16-Ap13-2	1	26	15.38	6.63	0.434	0.036	0.14
NN16-Ap14-1	1	1	0.81	0.38	0.854	0.026	0.67
NN16-Ap14-2	1	9	2.78	1.54	0.778	0.058	0.47
NN16-Ap15-1	1	9	4.42	1.78	0.733	0.073	0.23
NN16-Ap15-2	1	9	27.03	8.78	0.390	0.120	0.55

Table A-10: Concentrations of U and Th, and isotopic ratios of each spot in magnetite grains used to calculate U–Pb dates.

Spot	U (ppm)	Th (ppm)	$^{238}U/^{206}Pb$	2s	$^{207}Pb/^{206}Pb$	2s	rho
Chen2-Ap20-Mag-1	0	0	0.99	0.38	0.818	0.035	0.07

Chen2-Ap20-Mag-2	0	0	0.72	0.33	0.818	0.021	0.32
Chen2-Ap20-Mag-3	0	0	0.31	0.21	0.843	0.025	0.04
Chen2-Mag000-1	0	0	0.23	0.05	0.846	0.019	0.20
Chen2-Mag000-3	0	0	0.42	0.10	0.836	0.021	0.49
Chen2-Mag000-5	0	0	0.90	0.71	0.848	0.028	0.16
Chen2-Mag000-7	0	0	0.21	0.03	0.849	0.017	0.13
Chen2-Mag001-1	0	0	0.44	0.37	0.861	0.044	0.57
Chen2-Mag002-1	0	0	0.57	0.13	0.839	0.030	0.41
Chen2-Mag002-2	0	1	4.07	1.18	0.815	0.054	0.24
Chen2-Mag002-3	0	0	1.20	0.69	0.854	0.048	0.19
Chen2-Mag002-4	0	0	4.68	1.56	0.799	0.044	0.18
Chen2-Mag002-5	0	0	0.50	0.11	0.850	0.020	0.48
Chen2-mag16-1	0	0	3.71	2.24	0.760	0.049	0.36
Chen2-mag16-3	0	0	2.74	0.69	0.780	0.046	0.25
Chen2-mag16-4	1	4	16.08	1.37	0.411	0.041	0.26
Chen2-mag18-1	2	2	4.35	1.80	0.684	0.071	0.23
Chen2-mag18-2	0	0	3.28	1.15	0.841	0.081	0.26
Chen2-Mag19-1	0	1	0.11	0.02	0.840	0.018	0.34
Chen2-Mag19-2	0	0	0.05	0.03	0.847	0.018	0.36
Chen2-Mag19-4	0	0	0.17	0.09	0.842	0.018	0.30
Chen2-mag2-1	0	0	1.26	0.43	0.820	0.028	0.36
Chen2-mag2-2	0	2	1.33	0.58	0.822	0.020	0.37
Chen2-mag2-3	0	2	0.08	0.02	0.856	0.018	0.44
Chen3-Mag03-1	1	4	0.18	0.11	0.838	0.019	0.10
Chen3-Mag05-1	2	6	1.68	0.43	0.801	0.030	0.40
Chen3-Mag05-2	2	4	1.15	0.52	0.808	0.021	0.56
Chen3-Mag07-2	0	0	0.06	0.02	0.844	0.018	0.13
Chen3-Mag07-3	0	0	0.11	0.05	0.865	0.020	0.05
Chen3-ttn11-mag-1	0	0	2.50	2.35	0.861	0.076	0.21
Chen3-ttn12-mag-2	2	6	25.25	2.57	0.213	0.040	0.51
Chen3-ttn12-mag-3	0	1	5.05	1.82	0.755	0.052	0.36
EX17-Ap1_mag-1	1	1	3.75	1.16	0.757	0.029	0.56
EX17-Ap1_mag-2	0	0	11.87	2.55	0.608	0.042	0.34
EX17-Ap1_mag-3	1	0	2.11	0.40	0.790	0.027	0.39
EX17-Ap1_mag-6	0	0	5.80	2.11	0.678	0.072	0.57
EX17-Ap1_mag-7	0	0	4.91	2.08	0.783	0.054	0.56
EX17-Ap1_mag-8	0	0	2.48	0.99	0.840	0.028	0.48
EX17-Ap10_mag-1	1	1	4.56	1.39	0.724	0.032	0.58
EX17-Ap10_mag-2	1	0	8.74	0.71	0.668	0.021	0.39
EX17-Ap10_mag-3	1	0	8.39	0.98	0.656	0.023	0.34

EX17-Ap10_mag-4	0	0	7.95	1.00	0.622	0.029	0.24
EX17-Ap10_mag-5	1	0	9.28	0.83	0.617	0.029	0.42
EX17-Ap10_mag-6	1	0	4.77	0.37	0.722	0.025	0.27
EX17-Ap12_mag-1	0	0	1.65	0.59	0.778	0.031	0.52
EX17-Ap12_mag-2	0	0	1.21	0.41	0.803	0.026	0.40
EX17-Ap12_mag-3	1	1	5.29	0.72	0.723	0.029	0.41
EX17-Ap12_mag-4	0	0	10.54	3.84	0.558	0.072	0.13
EX17-Ap12_mag-5	0	0	16.46	2.36	0.494	0.043	0.17
EX17-Ap2_mag-1	0	0	5.80	1.28	0.712	0.028	0.33
EX17-Ap2_mag-10	3	3	12.51	1.86	0.511	0.046	0.26
EX17-Ap2_mag-2	2	2	7.76	1.28	0.655	0.035	0.57
EX17-Ap2_mag-3	1	1	9.35	0.39	0.613	0.020	0.43
EX17-Ap2_mag-4	1	1	8.56	0.52	0.637	0.020	0.39
EX17-Ap2_mag-5	1	0	9.78	0.74	0.592	0.017	0.28
EX17-Ap2_mag-6	1	1	2.87	0.42	0.799	0.024	0.61
EX17-Ap2_mag-7	1	1	5.34	0.49	0.712	0.017	0.37
EX17-Ap2_mag-8	1	1	6.80	0.51	0.685	0.020	0.36
EX17-Ap2_mag-9	4	3	22.00	1.49	0.308	0.023	0.54
EX19-Ap3-mag-3	0	0	1.15	0.20	0.891	0.091	0.15
EX19-Ap5-mag-5	0	0	1.04	0.32	0.992	0.072	0.47
EX19-Ap5-mag-6	0	0	0.17	0.07	0.866	0.021	0.28
EX19-Ap5-mag-7	0	0	0.51	0.67	0.883	0.048	0.29
EX19-Ap5-mag-8	0	0	5.67	2.40	0.894	0.037	0.16
NN01-massive – mag-10	0	0	3.61	3.56	0.629	0.092	0.18
NN01-massive – mag-11	0	0	8.27	6.94	0.664	0.029	0.10
NN01-massive – mag-13	0	0	2.47	2.04	0.788	0.060	0.28
NN01-massive – mag-14	0	0	3.25	0.70	0.742	0.024	0.26
NN01-massive – mag-3	0	0	8.84	3.05	0.518	0.049	0.17
NN01-massive – mag-4	0	0	6.59	1.01	0.659	0.050	0.12
NN01-massive – mag-6	2	0	8.84	3.97	0.762	0.018	0.49
NN01-massive – mag-7	0	0	2.37	0.90	0.769	0.037	0.63
NN01-massive – mag-8	0	0	4.93	1.99	0.783	0.050	0.20
NN01-massive – mag-9	0	0	4.35	1.55	0.722	0.038	0.55
NN01-random-mag-1	1	1	4.85	0.68	0.708	0.033	0.62
NN01-random-mag-10	0	1	6.99	1.15	0.689	0.034	0.58
NN01-random-mag-11	2	1	7.54	0.57	0.623	0.021	0.52
NN01-random-mag-12	3	3	4.60	0.17	0.714	0.016	0.47
NN01-random-mag-13	4	2	4.43	0.14	0.711	0.015	0.62
NN01-random-mag-14	0	1	5.63	0.98	0.674	0.033	0.49
NN01-random-mag-15	1	2	5.49	0.25	0.662	0.015	0.56

NN01-random-mag-16	1	1	9.57	0.44	0.607	0.019	0.51
NN01-random-mag-17	1	1	9.16	0.46	0.615	0.023	0.47
NN01-random-mag-18	0	1	3.02	1.17	0.718	0.036	0.64
NN01-random-mag-3	0	1	7.77	0.75	0.638	0.030	0.39
NN01-random-mag-4	1	1	1.76	0.16	0.749	0.016	0.34
NN01-random-mag-5	0	0	5.34	0.48	0.673	0.025	0.33
NN01-random-mag-6	3	1	6.76	0.30	0.656	0.015	0.41
NN01-random-mag-7	1	1	1.42	0.09	0.774	0.017	0.45
NN01-random-mag-9	0	2	7.10	0.82	0.668	0.022	0.41
NN02-Ap16-mag-1	26	0	30.78	1.14	0.065	0.003	0.52
NN02-Ap16-mag-2	82	0	28.26	0.65	0.127	0.003	0.48
NN02-Ap16-mag-3	49	1	17.09	0.47	0.393	0.009	0.38
NN02-Ap16-mag-4	0	0	0.19	0.12	0.848	0.020	0.09
NN02-Ap16-mag-5	0	0	0.12	0.04	0.849	0.018	0.15
NN02-Ap18-mag-15	5	1	15.37	1.06	0.419	0.018	0.53
NN02-Ap18-mag-8	0	0	1.06	0.80	0.830	0.024	0.12
NN02-mag-1	1	0	4.90	0.42	0.722	0.021	0.38
NN02-mag-2	4	0	25.96	1.18	0.180	0.025	0.13
NN02-ramdom-mag-3	0	0	3.45	1.87	0.920	0.046	0.10
NN03_m_2	0	0	2.22	1.19	0.826	0.057	0.15
NN03_m_5	0	0	7.25	0.90	0.674	0.019	0.05
NN03_m_8	1	1	6.67	4.89	0.580	0.131	0.27
NN03_t02_m_1	1	3	5.62	0.24	0.692	0.016	0.47
NN03_t02_m_2	1	4	2.55	0.25	0.753	0.019	0.44
NN03_t02_m_3	1	1	2.80	0.22	0.750	0.017	0.46
NN03_t02_m_4	0	1	2.92	0.45	0.768	0.018	0.59
NN03_t02_m_5	1	1	6.62	0.50	0.692	0.021	0.59
NN03_t02_m_6	1	1	7.59	0.25	0.635	0.015	0.37
NN03_t03_m_1_1	0	0	1.96	0.46	0.771	0.021	0.55
NN03_t03_m_10	2	2	2.85	0.15	0.788	0.016	0.59
NN03_t03_m_11	1	0	0.43	0.02	0.830	0.017	0.54
NN03_t03_m_12	1	1	4.35	2.27	0.709	0.041	0.67
NN03_t03_m_2_1	1	0	1.07	0.07	0.815	0.017	0.47
NN03_t03_m_3_1	0	0	13.70	2.08	0.549	0.038	0.22
NN03_t03_m_3	0	0	0.60	0.17	0.827	0.022	0.04
NN03_t03_m_4_1	0	0	4.05	0.39	0.791	0.020	0.53
NN03_t03_m_7	2	1	8.72	0.37	0.642	0.016	0.60
NN03_t03_m_8	0	0	1.72	0.48	0.780	0.027	0.62
NN03_t03_m_9	1	1	6.85	0.58	0.695	0.023	0.53
NN03_t05_m_2	0	0	2.33	0.70	0.816	0.028	0.18

NN03_t05_m_6	0	1	0.53	0.07	0.817	0.019	0.40
NN03-random-mag-13	0	0	1.15	0.39	0.822	0.067	0.14
NN03-random-mag-15	0	0	2.12	1.58	0.933	0.129	0.04
NN03-random-mag-21	0	0	14.24	9.50	0.445	0.138	0.05
NN03-Ttn1-mag-2	0	0	1.89	1.35	0.807	0.050	0.19
NN04_01_m01	1.23	6.59	5.43	0.69	0.727	0.021	0.49
NN04_01_m02	0.13	0.50	4.46	1.18	0.717	0.040	0.19
NN04_01_m03	0.43	1.02	13.70	2.27	0.548	0.034	0.34
NN04_01_m04	0.90	4.77	8.47	0.81	0.632	0.020	0.49
NN04_01_m05	0.79	3.59	3.64	0.22	0.729	0.018	0.32
NN04_29_m06	0.94	0.52	2.30	0.14	0.791	0.019	0.27
NN04_29_m07	1.71	4.47	7.08	0.40	0.666	0.019	0.67
NN04_29_m08	2.83	2.65	9.98	0.26	0.697	0.017	0.45
NN04_29_m09	2.00	5.65	11.78	0.58	0.580	0.015	0.39
NN04_29_m10	0.84	2.07	10.04	0.69	0.661	0.017	0.47
NN04_29_m11	1.80	4.07	13.68	0.43	0.543	0.015	0.25
NN04_29_m12	0.64	1.14	2.22	0.20	0.764	0.017	0.40
NN04_38_m13	0.29	1.53	2.84	0.46	0.755	0.019	0.13
NN04_38_m14	0.54	0.86	7.41	1.16	0.669	0.027	0.21
NN04_38_m15	0.94	1.18	10.26	0.57	0.632	0.017	0.36
NN04_38_m16	0.15	0.12	3.33	2.33	0.647	0.040	0.29
NN04_38_m17	0.22	0.41	1.30	0.27	0.766	0.021	0.11
NN04_42_m18	0.80	2.28	4.12	0.40	0.716	0.021	0.58
NN04_42_m19	0.38	0.51	2.87	0.29	0.755	0.019	0.21
NN04_42_m21	0.08	0.03	2.33	2.22	0.792	0.037	0.02
NN16--mag1-3	0	0	13.87	0.81	0.993	0.391	0.35
NN16--mag1-5	0	0	1.39	0.58	0.814	0.038	0.09
NN16--random-mag-2	0	0	9.86	1.78	0.814	0.275	0.44
NN16-Ap11-mag-4	0	0	0.02	0.01	0.865	0.018	0.08
NN16-Ap2-mag-1	0	0	2.27	1.37	0.796	0.032	0.03
NN16-Ap2-mag-2	0	0	1.45	0.48	0.815	0.038	0.20
NN16-Ap2-mag-3	0	0	0.19	0.09	0.836	0.022	0.46
NN16-mag5-1	0	0	4.14	1.97	0.835	0.117	0.26
NN50-Ap1-Mag-1	1	0	9.440	1.173	0.567	0.019	0.394
NN50-Ap1-Mag-10	3	1	10.428	0.376	0.546	0.013	0.581
NN50-Ap1-Mag-11	5	1	13.983	0.470	0.468	0.013	0.554
NN50-Ap1-Mag-12	8	3	10.194	0.238	0.539	0.012	0.525
NN50-Ap1-Mag-13	1	1	3.729	0.206	0.723	0.018	0.325
NN50-Ap1-Mag-14	1	1	5.989	0.468	0.686	0.016	0.242
NN50-Ap1-Mag-15	3	4	5.502	0.161	0.636	0.014	0.460

NN50-Ap1-Mag-16	1	2	4.163	0.358	0.698	0.016	0.618
NN50-Ap1-Mag-17	9	2	12.344	0.313	0.536	0.013	0.293
NN50-Ap1-Mag-18	9	2	12.374	0.607	0.535	0.013	0.536
NN50-Ap1-Mag-19	1	1	8.789	0.336	0.559	0.017	0.576
NN50-Ap1-Mag-2	2	1	8.973	0.568	0.597	0.019	0.442
NN50-Ap1-Mag-20	1	0	7.557	0.626	0.577	0.018	0.400
NN50-Ap1-Mag-4	4	3	9.880	0.304	0.553	0.013	0.470
NN50-Ap1-Mag-5	7	3	2.953	2.061	0.684	0.047	0.679
NN50-Ap1-Mag-6	4	3	9.160	0.298	0.602	0.015	0.414
NN50-Ap1-Mag-7	0	1	13.507	1.321	0.438	0.023	0.300
NN50-Ap1-Mag-8	2	2	11.978	0.410	0.524	0.014	0.514
NN50-Ap1-Mag-9	1	0	7.382	0.556	0.613	0.022	0.495
NN50-Ttn3_1-Mag-1	1	4	7.133	0.502	0.600	0.017	0.632
NN50-Ttn3_1-Mag-10	3	2	13.967	0.475	0.473	0.013	0.502
NN50-Ttn3_1-Mag-2	2	4	6.951	0.225	0.625	0.014	0.481
NN50-Ttn3_1-Mag-3	4	2	10.467	0.419	0.540	0.017	0.584
NN50-Ttn3_1-Mag-4	4	2	9.036	0.485	0.601	0.016	0.525
NN50-Ttn3_1-Mag-5	6	4	11.341	0.379	0.518	0.012	0.441
NN50-Ttn3_1-Mag-6	8	3	13.845	0.393	0.482	0.012	0.509
NN50-Ttn3_1-Mag-7	2	2	9.440	0.526	0.535	0.016	0.345
NN50-Ttn3_1-Mag-8	5	2	11.122	0.348	0.510	0.012	0.577
NN50-Ttn3_1-Mag-9	2	2	12.484	0.534	0.495	0.013	0.527
NN51a-Ap16-mag-1	2	2	10.01	0.42	0.567	0.015	0.58
NN51a-Ap16-mag-2	9	3	8.98	0.54	0.577	0.019	0.48
NN51a-Ap16-mag-3	5	3	10.77	0.28	0.547	0.015	0.50
NN51a-Ap16-mag-4	4	3	12.28	0.40	0.518	0.014	0.51
NN51a-Ap18-mag-1	4	1	12.13	0.38	0.473	0.015	0.38
NN51a-Ap18-mag-2	3	2	12.17	0.57	0.511	0.014	0.29
NN51a-Ap18-mag-3	0	1	8.37	1.57	0.581	0.035	0.40
NN51a-Ap18-mag-4	3	2	11.29	0.48	0.510	0.018	0.22
NN51a-Ap18-mag-5	3	2	9.20	0.23	0.559	0.015	0.57
NN51a-Ap18-mag-6	5	2	11.21	0.32	0.524	0.013	0.40
NN51a-Ap18-mag-7	1	1	6.12	0.36	0.664	0.020	0.37
NN51a-Ap18-mag-8	3	2	12.56	0.43	0.527	0.014	0.52
NN51a-Ap7-mag-1	5	2	11.63	0.34	0.547	0.013	0.43
NN51a-Ap7-mag-2	0	0	13.15	5.70	0.410	0.087	0.07
NN51a-Ap8-mag-1	4	1	4.64	2.95	0.613	0.035	0.64
NN51a-Ap8-mag-10	8	2	10.57	0.26	0.578	0.013	0.56
NN51a-Ap8-mag-2	3	2	10.84	0.32	0.554	0.014	0.45
NN51a-Ap8-mag-3	3	2	8.98	0.33	0.604	0.015	0.33

NN51a-Ap8-mag-4	1	0	22.78	2.28	0.223	0.022	0.24
NN51a-Ap8-mag-6	1	2	8.83	0.58	0.599	0.024	0.53
NN51a-Ap8-mag-7	3	2	7.47	0.22	0.631	0.015	0.47
NN51a-Ap8-mag-8	2	2	13.71	0.59	0.484	0.014	0.44
NN51a-Ap8-mag-9	3	2	11.35	0.53	0.527	0.015	0.58
NN51a-Ap9-mag-1	1	1	20.61	1.13	0.335	0.015	0.26
NN51a-Ap9-mag-2	1	1	13.65	1.13	0.440	0.019	0.26
NN51a-Ap9-mag-3	1	3	8.05	0.58	0.608	0.019	0.55
NN51a-Ap9-mag-4	6	3	9.83	0.30	0.576	0.013	0.54
NN51a-Ap9-mag-5	5	2	10.21	0.29	0.565	0.013	0.40
NN51a-Ap9-mag-6	0	1	15.01	2.32	0.398	0.040	0.14
NN52-Ttn1-Mag-1	3	5	12.696	0.985	0.465	0.024	0.474
NN52-Ttn1-Mag-10	1	2	16.894	0.519	0.413	0.017	0.269
NN52-Ttn1-Mag-11	1	2	12.326	0.620	0.534	0.016	0.454
NN52-Ttn1-Mag-12	2	2	12.029	0.541	0.532	0.016	0.560
NN52-Ttn1-Mag-2	1	0	16.805	0.650	0.468	0.017	0.275
NN52-Ttn1-Mag-3	1	1	13.726	0.861	0.498	0.020	0.423
NN52-Ttn1-Mag-4	12	11	14.954	0.677	0.556	0.017	0.481
NN52-Ttn1-Mag-5	2	3	9.880	0.869	0.550	0.020	0.596
NN52-Ttn1-Mag-6	1	2	14.013	0.478	0.466	0.018	0.384
NN52-Ttn1-Mag-7	1	1	11.438	0.757	0.558	0.018	0.438
NN52-Ttn1-Mag-8	2	4	12.883	0.571	0.496	0.019	0.436
NN52-Ttn1-Mag-9	2	7	8.756	0.542	0.593	0.021	0.207
NN52-Ttn3-Mag-1	2	5	8.817	0.815	0.622	0.025	0.471
NN52-Ttn3-Mag-2	2	7	11.563	0.453	0.547	0.014	0.617
NN52-Ttn3-Mag-3	1	2	15.251	0.685	0.470	0.021	0.519
NN52-Ttn3-Mag-4	1	1	15.860	0.772	0.425	0.017	0.617
NN52-Ttn3-Mag-5	1	1	9.997	0.549	0.566	0.017	0.262
NN52-Ttn4-Mag-1	1	3	11.995	0.553	0.544	0.013	0.595
NN52-Ttn4-Mag-10	2	3	16.277	1.294	0.403	0.026	0.444
NN52-Ttn4-Mag-11	2	4	8.087	0.515	0.560	0.016	0.472
NN52-Ttn4-Mag-12	2	4	9.167	0.592	0.614	0.017	0.317
NN52-Ttn4-Mag-13	1	3	14.289	0.719	0.482	0.018	0.506
NN52-Ttn4-Mag-2	2	6	12.190	0.607	0.514	0.022	0.479
NN52-Ttn4-Mag-3	1	3	10.851	0.685	0.528	0.017	0.297
NN52-Ttn4-Mag-4	1	2	13.089	0.915	0.511	0.023	0.533
NN52-Ttn4-Mag-5	1	1	10.322	0.662	0.566	0.021	0.593
NN52-Ttn4-Mag-6	1	3	8.726	0.400	0.588	0.015	0.516
NN52-Ttn4-Mag-7	2	6	10.318	0.373	0.564	0.018	0.473
NN52-Ttn4-Mag-8	2	4	12.509	1.017	0.514	0.020	0.528

NN52-Ttn4-Mag-9	2	5	8.139	0.497	0.608	0.017	0.528
NN54-Mag04-1	1	2	14.94	2.14	0.412	0.044	0.36
NN54-Mag04-2	0	0	6.31	2.53	0.782	~~0.128~~	~~0.07~~
NN54-Mag07-1	0	0	1.21	0.56	0.797	0.020	0.66
NN54-Mag07-2	0	0	3.60	0.45	0.754	0.023	0.25
NN54-Mag07-3	0	0	3.22	0.38	0.784	0.020	0.37
NN54-Mag07-4	0	0	2.60	0.43	0.775	0.022	0.43
NN54-Mag07-5	0	0	2.04	0.20	0.796	0.019	0.33
NN54-Mag5-1	1	1	11.80	2.16	0.611	0.055	0.33
NN54-Mag5-2	0	0	2.69	0.89	0.770	0.025	0.19
NN54-Mag5-3	0	0	1.99	0.35	0.807	0.020	0.42
NN54-Mag5-4	1	1	6.31	0.97	0.671	0.028	0.45
NN54-Ramdom-Mag-10	0	0	5.26	1.32	0.706	0.035	0.26
NN54-Ramdom-Mag-11	0	0	9.32	0.95	0.619	0.030	0.49
NN54-Ramdom-Mag-12	0	0	5.87	0.69	0.696	0.033	0.45
NN54-Ramdom-Mag-13	0	0	4.35	0.76	0.759	0.027	0.64
NN54-Ramdom-Mag-14	1	0	11.27	0.79	0.603	0.019	0.43
NN54-Ramdom-Mag-15	1	0	1.79	0.16	0.804	0.018	0.61
NN54-Ramdom-Mag-16	1	0	4.77	0.36	0.743	0.024	0.55
NN54-Ramdom-Mag-17	0	0	1.28	0.13	0.817	0.020	0.29
NN54-Ramdom-Mag-19	0	0	2.07	0.26	0.810	0.018	0.41
NN54-Ramdom-Mag-6	0	0	2.10	0.23	0.794	0.022	0.19
NN54-Ramdom-Mag-7	0	0	3.82	0.55	0.727	0.024	0.36
NN54-Ramdom-Mag-8	0	0	3.04	0.48	0.770	0.026	0.49
NN54-Ramdom-Mag-9	0	0	5.01	0.59	0.738	0.027	0.39
NN54-Random-Mag-1	0	0	3.83	1.05	0.752	0.030	0.31
NN54-Random-Mag-2	0	0	5.87	1.51	0.665	0.042	0.22
NN54-Random-Mag-3	0	0	5.88	1.23	0.757	0.036	0.30
NN54-Random-Mag-4	0	0	8.28	0.96	0.652	0.023	0.38
NN54-Random-Mag-5	0	0	6.64	2.10	0.707	0.049	0.45
NN54-Ttn3-Mag-1	1	2	2.55	0.44	0.761	0.021	0.17
NN56-Mag08-3	0	0	2.77	1.84	0.640	0.040	0.19
NN56-Mag12-1	1	3	7.53	1.01	0.603	0.039	0.39
NN56-Mag12-2	0	1	2.87	0.52	0.749	0.029	0.41
NN56-Ttn1-mag-1	0	0	1.28	1.21	0.737	0.043	0.31
NN56-Ttn1-mag-2	1	6	7.69	0.94	0.637	0.027	0.58
NN56-Ttn1-mag-3	1	5	3.91	0.42	0.710	0.020	0.54
NN56-Ttn1-mag-4	1	6	2.97	0.19	0.761	0.018	0.56
NN56-Ttn1-mag-5	1	6	6.72	0.41	0.643	0.017	0.60
NN56-Ttn1-mag-6	1	6	6.12	0.93	0.670	0.035	0.57

NN56-Ttn1-mag-7	0	1	13.79	3.14	0.468	0.040	0.33
NN56-Ttn11-mag-1	1	5	5.77	0.50	0.661	0.021	0.64
NN56-Ttn11-mag-2	1	1	5.41	0.92	0.671	0.028	0.58
NN56-Ttn11-mag-4	1	6	5.39	0.56	0.692	0.018	0.56
NN56-Ttn5-mag-2	1	0	8.18	1.76	0.592	0.039	0.59
NN56-Ttn5-mag-4	40	33	16.84	0.40	0.529	0.018	0.43
NN56-Ttn5-mag-5	1	5	2.97	0.42	0.725	0.021	0.63
NN56-Ttn5-mag-6	1	1	10.63	1.57	0.579	0.038	0.26
NN56-Ttn5-mag-7	16	16	20.81	0.75	0.446	0.016	0.43
NN56-Ttn5-mag-8	7	11	18.83	1.17	0.405	0.034	0.32
NN56-Ttn8-mag-1	2	6	7.33	0.83	0.612	0.032	0.49
NN56-Ttn8-mag-2	1	3	9.11	1.22	0.587	0.026	0.54
NN56-Ttn8-mag-3	31	15	19.52	0.65	0.468	0.017	0.45
NN56-Ttn8-mag-4	1	4	2.09	0.23	0.774	0.019	0.63
NN58-Ap6-Mag-1	0	0	0.276	0.192	0.860	0.036	0.354
NN58-Ap6-Mag-3	0	0	0.114	0.030	0.843	0.018	0.432
NN58-Random1-Mag-2	0	0	3.023	1.728	0.812	0.071	0.135
NN58-Ttn1-Mag-1	0	0	0.016	0.031	0.858	0.027	0.069
NN58-Ttn1-Mag-2	0	0	5.268	0.707	0.701	0.027	0.389
NN58-Ttn2-Mag-1	1	0	3.913	0.388	0.772	0.022	0.517
NN58-Ttn2-Mag-2	1	0	0.486	0.059	0.838	0.018	0.500
NN58-Ttn2-Mag-3	1	0	0.740	0.046	0.835	0.018	0.517
NN58-Ttn2-Mag-4	1	0	1.351	0.160	0.815	0.018	0.198
NN58-Ttn2-Mag-5	1	0	0.458	0.031	0.840	0.017	0.362
NN58-Ttn2-Mag-6	0	0	0.155	0.011	0.848	0.017	0.414
NN58-Ttn3-Mag-10	0	0	16.277	9.292	0.589	0.190	0.091
NN58-Ttn3-Mag-13	0	0	1.459	0.621	0.829	0.020	0.338
NN58-Ttn3-Mag-16	0	0	0.210	0.026	0.839	0.017	0.521
NN58-Ttn3-Mag-17	0	0	0.179	0.113	0.843	0.023	0.103
NN58-Ttn3-Mag-3	0	0	1.693	0.915	0.722	0.069	0.540
NN58-Ttn3-Mag-4	0	0	0.170	0.036	0.843	0.018	0.305
NN58-Ttn3-Mag-5	0	0	0.141	0.078	0.840	0.017	0.443
NN58-Ttn3-Mag-6	0	0	0.134	0.077	0.834	0.019	0.071
NN58-Ttn3-Mag-8	0	0	6.682	2.817	0.694	0.232	0.145
NN58-Ttn3-Mag-9	0	0	0.033	0.010	0.851	0.018	0.170

Table A-11: Concentrations of U and Th, and isotopic ratios of each spot in titanite grains used to calculate U–Pb dates.

Spot	**U (ppm)**	**Th (ppm)**	**$^{238}U/^{206}Pb$**	**2s**	**$^{207}Pb/^{206}Pb$**	**2s**	**rho**
Chen2-Ttn-2-1	43	260	24.27	3.39	0.325	0.050	0.38

Chen2-Ttn-2-2	47	150	33.67	1.42	0.146	0.018	0.16
Chen2-Ttn-3-1	53	220	38.23	0.92	0.074	0.003	0.13
Chen2-Ttn-3-2	56	150	39.43	0.91	0.062	0.003	0.35
Chen2-Ttn-3-3	90	242	39.18	1.04	0.102	0.005	0.10
Chen2-Ttn-4-1	49	140	37.27	1.20	0.107	0.014	0.03
Chen2-Ttn-5-1	79	273	41.15	0.99	0.056	0.003	0.38
Chen2-Ttn-5-2	265	563	41.95	1.02	0.060	0.004	0.19
Chen2-Ttn-6-1	68	269	27.87	0.73	0.315	0.009	0.53
Chen2-Ttn-8-1	50	217	29.41	2.41	0.252	0.048	0.26
Chen2-Ttn-8-2	115	195	37.76	1.08	0.111	0.005	0.20
Chen2-Ttn-8-3	90	204	40.23	0.99	0.068	0.003	0.47
Chen2-Ttn-9-1	188	101	40.45	0.97	0.070	0.002	0.25
Chen2-Ttn-9-2	84	150	38.55	1.08	0.095	0.009	0.21
Chen2-Ttn-9-3	197	103	39.92	1.02	0.063	0.003	0.28
Chen2-Ttn1-1	49	198	37.88	1.88	0.100	0.027	0.09
Chen2-Ttn10-1	40	147	10.87	7.09	0.517	0.087	0.59
Chen2-Ttn11-1	173	93	36.14	0.89	0.133	0.013	0.32
Chen2-Ttn12-1	78	320	39.00	1.09	0.076	0.007	0.11
Chen2-Ttn12-2	147	116	37.95	0.97	0.089	0.006	0.60
Chen2-Ttn13-1	41	247	19.65	3.30	0.436	0.060	0.48
Chen3-Ttn1-1	42	333	32.68	2.23	0.178	0.039	0.23
Chen3-Ttn1-2	54	428	37.12	0.87	0.079	0.005	0.47
Chen3-Ttn10-1	45	205	39.54	1.05	0.065	0.003	0.21
Chen3-Ttn10-2	50	213	40.63	0.94	0.052	0.002	0.12
Chen3-Ttn11-1	116	235	39.31	1.05	0.098	0.015	0.33
Chen3-Ttn11-2	56	233	36.74	1.03	0.085	0.008	0.39
Chen3-Ttn12-1	94	300	39.06	0.97	0.073	0.004	0.32
Chen3-Ttn14-1	32	144	40.13	1.05	0.058	0.004	0.20
Chen3-Ttn14-2	47	501	39.42	1.17	0.053	0.003	0.15
Chen3-Ttn15-1	32	461	39.64	0.99	0.051	0.004	0.26
Chen3-Ttn16-1	48	222	40.32	0.98	0.068	0.013	0.11
Chen3-Ttn16-2	318	476	40.95	0.92	0.054	0.002	0.51
Chen3-Ttn16-3	119	300	41.96	0.96	0.053	0.002	0.47
Chen3-Ttn16-4	43	169	40.52	1.04	0.061	0.003	0.19
Chen3-Ttn17-1	37	474	7.03	0.24	0.708	0.015	0.49
Chen3-Ttn17-2	57	207	16.05	0.48	0.503	0.012	0.61
Chen3-Ttn18-1	64	716	39.87	0.88	0.054	0.002	0.25
Chen3-Ttn18-2	62	374	39.28	0.94	0.057	0.003	0.39
Chen3-Ttn2-1	41	464	37.74	0.90	0.077	0.004	0.21
Chen3-Ttn21-1	75	479	39.67	1.11	0.055	0.006	0.08

Chen3-Ttn23-1	116	308	40.08	0.97	0.052	0.001	0.58
Chen3-Ttn4-1	126	311	38.54	1.02	0.057	0.002	0.25
Chen3-Ttn5-1	101	244	37.33	1.03	0.107	0.005	0.49
Chen3-Ttn6-1	48	370	24.57	5.09	0.327	0.091	0.31
Chen3-Ttn6-2	48	222	40.26	1.01	0.054	0.003	0.38
Chen3-Ttn6-3	65	289	40.29	1.10	0.056	0.002	0.41
Chen3-Ttn7-1	30	138	24.73	0.74	0.320	0.014	0.26
Chen3-Ttn8-1	171	532	40.23	0.98	0.058	0.003	0.31
Chen3-Ttn8-2	230	334	41.03	0.94	0.057	0.002	0.37
Chen3-Ttn9-1	43	111	39.11	1.06	0.052	0.002	0.31
Chen3-Ttn9-2	48	211	37.89	1.16	0.076	0.009	0.10
N16-Ttn23-1_1	23	125	21.55	0.86	0.399	0.020	0.32
N16-Ttn23-1	10	86	14.86	0.65	0.547	0.017	0.38
N16-Ttn26-1	27	135	36.19	1.42	0.105	0.023	0.20
N16-Ttn27-1	11	83	26.74	2.00	0.283	0.038	0.29
N16-Ttn27-2	72	276	34.45	1.19	0.186	0.013	0.24
NN01_t02_1	53	31	34.25	1.67	0.107	0.017	0.12
NN01_t02_2	36	23	34.36	1.68	0.107	0.010	0.33
NN01_t02_3	60	36	36.50	1.76	0.133	0.013	0.13
NN01_t02_4	199	72	39.75	1.18	0.098	0.007	0.19
NN01_t03	28	42	34.75	1.23	0.078	0.009	0.12
NN02-Ttn1-1	192	138	5.04	0.13	0.764	0.015	0.56
NN02-Ttn1-2	128	194	4.30	0.13	0.781	0.016	0.31
NN02-Ttn10-1	40	365	23.70	0.82	0.383	0.015	0.53
NN02-Ttn4-1	15	87	35.65	1.28	0.160	0.014	0.18
NN02-Ttn4-2	102	156	11.82	0.39	0.626	0.013	0.47
NN02-Ttn8-1	137	620	4.22	0.28	0.793	0.016	0.31
NN02-Ttn8-2	96	229	6.94	0.36	0.721	0.015	0.11
NN02-Ttn9-1	70	366	35.59	1.68	0.194	0.008	0.33
NN02-Ttn9-2	63	349	32.79	1.64	0.209	0.033	0.18
NN03_t02_1	53	389	30.03	2.77	0.228	0.042	0.30
NN03_t02_10	214	606	39.90	1.18	0.049	0.001	0.51
NN03_t02_11	49	268	38.08	1.10	0.066	0.003	0.22
NN03_t02_12	20	195	29.67	2.71	0.235	0.055	0.31
NN03_t02_13	159	1002	40.23	0.92	0.071	0.004	0.07
NN03_t02_14	254	1031	40.83	1.11	0.050	0.001	0.29
NN03_t02_15	31	194	38.31	1.11	0.097	0.007	0.17
NN03_t02_16	42	148	33.03	0.88	0.207	0.008	0.35
NN03_t02_17	48	130	39.98	1.00	0.072	0.003	0.22
NN03_t02_18	36	230	40.45	1.00	0.068	0.004	0.19

NN03_t02_19	40	62	30.77	0.93	0.246	0.013	0.23
NN03_t02_2	238	1481	39.26	0.91	0.068	0.003	0.22
NN03_t02_3	47	212	40.36	1.08	0.058	0.003	0.29
NN03_t02_4	44	242	38.40	1.15	0.088	0.005	0.22
NN03_t02_5	53	145	40.18	1.15	0.062	0.004	0.25
NN03_t02_6	61	394	40.00	1.01	0.056	0.003	0.09
NN03_t02_7	26	289	40.32	1.09	0.051	0.005	0.32
NN03_t02_8	84	521	40.54	0.92	0.048	0.001	0.29
NN03_t02_9	53	276	38.49	1.09	0.055	0.002	0.53
NN03_t03_1	44	99	37.95	1.10	0.090	0.006	0.20
NN03_t03_2	49	263	40.36	1.27	0.051	0.003	0.30
NN03_t03_3	100	383	39.17	1.22	0.055	0.003	0.30
NN03_t03_4	44	110	33.11	2.19	0.211	0.039	0.23
NN03_t03_5	63	270	41.29	1.24	0.052	0.002	0.33
NN03_t03_6	103	513	40.13	1.28	0.050	0.002	0.20
NN03_t03_7	68	307	37.52	1.02	0.114	0.005	0.24
NN03_t04_1	58	401	39.45	1.00	0.049	0.002	0.15
NN03_t04_2	238	1608	38.20	0.95	0.087	0.002	0.43
NN03_t04_3	47	83	41.41	1.11	0.052	0.003	0.13
NN03_t04_4	37	112	40.88	1.03	0.054	0.003	0.34
NN03_t04_5	41	45	41.63	0.99	0.053	0.002	0.23
NN03_t04_6	44	104	41.88	1.04	0.049	0.002	0.30
NN03_t04_7	19	216	39.65	1.28	0.052	0.003	0.19
NN03_t05_1	85	610	39.87	1.14	0.081	0.003	0.33
NN03_t05_2	62	275	41.00	1.19	0.051	0.002	0.19
NN03_t05_3	40	113	32.37	0.97	0.204	0.008	0.12
NN03_t05_4	47	302	40.58	0.99	0.060	0.006	0.10
NN03_t05_5	173	1014	32.41	0.84	0.229	0.010	0.23
NN03_t06_1	42	32	39.18	1.33	0.104	0.022	0.15
NN03_t06_2	60	439	39.97	1.36	0.073	0.011	0.05
NN03_t06_3	46	352	40.37	1.16	0.053	0.002	0.29
NN03_t06_4	59	417	39.22	0.83	0.092	0.003	0.23
NN03_t06_5	88	535	41.10	1.02	0.064	0.005	0.10
NN03_t06_6	110	570	40.27	1.08	0.068	0.010	0.27
NN04_05-08_1	41	159	38.28	0.98	0.050	0.002	0.26
NN04_05-08_10	28	95	37.65	1.16	0.056	0.003	0.37
NN04_05-08_2	33	96	36.94	1.31	0.065	0.003	0.41
NN04_05-08_3	26	81	38.14	0.90	0.052	0.003	0.23
NN04_05-08_4	27	83	38.07	0.89	0.047	0.003	0.28
NN04_05-08_5	42	121	36.54	0.98	0.067	0.006	0.16

NN04_05-08_6	27	81	38.67	1.13	0.049	0.002	0.33
NN04_05-08_7	36	130	39.42	1.03	0.048	0.002	0.36
NN04_05-08_8	956	284	39.82	1.10	0.050	0.001	0.47
NN04_05-08_9	26	84	38.51	1.02	0.053	0.003	0.33
NN04_09-11_1	36	136	34.86	1.04	0.129	0.009	0.27
NN04_09-11_2	28	87	37.81	0.98	0.075	0.007	0.12
NN04_09-11_3	28	84	37.58	0.96	0.069	0.003	0.25
NN04_09-11_4	22	68	35.45	1.40	0.124	0.021	0.18
NN04_09-11_5	24	70	37.61	1.25	0.080	0.007	0.12
NN04_12-17_1	28	75	35.84	1.12	0.104	0.014	0.11
NN04_12-17_2	27	74	38.43	1.31	0.065	0.005	0.18
NN04_12-17_3	29	90	37.48	0.98	0.066	0.003	0.33
NN04_12-17_4	34	129	38.02	1.03	0.059	0.003	0.19
NN04_12-17_5	26	84	38.46	1.03	0.053	0.002	0.22
NN04_12-17_6	27	88	38.05	1.08	0.057	0.003	0.32
NN04_12-17_7	33	132	38.12	1.00	0.048	0.002	0.25
NN04_12-17_8	31	110	38.65	1.08	0.052	0.002	0.45
NN04_18-24_1	25	63	37.38	1.22	0.065	0.004	0.31
NN04_18-24_10	19	28	38.34	1.19	0.052	0.003	0.22
NN04_18-24_11	34	52	38.52	1.08	0.048	0.002	0.19
NN04_18-24_12	23	26	38.68	1.08	0.063	0.002	0.42
NN04_18-24_2	38	110	38.40	1.02	0.062	0.005	0.13
NN04_18-24_3	37	112	37.94	1.10	0.074	0.005	0.22
NN04_18-24_4	39	111	38.14	0.95	0.076	0.005	0.28
NN04_18-24_5	37	110	37.34	0.88	0.081	0.006	0.13
NN04_18-24_6	26	64	38.36	1.17	0.069	0.008	0.10
NN04_18-24_7	47	98	39.40	0.96	0.050	0.003	0.32
NN04_18-24_8	37	82	31.11	1.00	0.179	0.013	0.19
NN04_18-24_9	20	29	39.22	1.12	0.052	0.004	0.11
NN04_25-28_1	25	86	37.15	0.93	0.066	0.004	0.26
NN04_25-28_2	52	150	38.14	0.98	0.060	0.003	0.19
NN04_25-28_3	46	147	35.17	0.87	0.098	0.007	0.23
NN04_25-28_4	33	121	37.06	0.90	0.068	0.003	0.31
NN04_25-28_5	29	89	37.36	1.04	0.067	0.003	0.30
NN04_25-28_6	25	85	37.44	0.98	0.074	0.005	0.12
NN04_25-28_7	34	122	35.15	0.97	0.100	0.006	0.08
NN04_25-28_8	27	90	38.57	0.97	0.053	0.002	0.43
NN04_29-33_1	44	165	38.79	0.92	0.050	0.003	0.25
NN04_29-33_2	536	835	39.22	0.92	0.050	0.001	0.47
NN04_29-33_3	140	255	30.30	2.02	0.205	0.032	0.01

NN04_29-33_4	41	38	34.66	1.15	0.130	0.010	0.26
NN04_35-37_1	17	22	38.17	1.43	0.061	0.008	0.07
NN04_35-37_2	19	26	37.89	1.05	0.054	0.003	0.17
NN04_35-37_3	22	25	37.89	0.86	0.083	0.005	0.31
NN04_35-37_4	19	25	39.45	1.08	0.050	0.004	0.14
NN04_35-37_5	122	60	37.71	1.09	0.056	0.001	0.40
NN04_38-41_1	16	27	39.86	1.15	0.057	0.004	0.12
NN04_38-41_2	21	29	37.74	1.10	0.086	0.006	0.24
NN04_38-41_3	20	29	35.10	1.28	0.065	0.004	0.07
NN04_38-41_4	352	319	37.57	0.88	0.087	0.007	0.09
NN04_38-41_5	310	389	38.57	0.91	0.056	0.002	0.57
NN04_38-41_6	14	23	34.13	1.35	0.140	0.007	0.38
NN04_38-41_7	44	41	32.39	0.99	0.157	0.009	0.07
NN04_Ttn34_1	29	85	38.01	1.15	0.116	0.006	0.28
NN04_Ttn34_2	28	84	38.04	0.88	0.051	0.003	0.17
NN04_Ttn34_3	44	77	21.70	0.57	0.438	0.013	0.40
NN04_Ttn42_1	28	74	13.85	0.55	0.571	0.014	0.57
NN04_Ttn42_2	28	73	37.37	0.88	0.077	0.007	0.08
NN04_Ttn42_3	28	72	38.88	1.21	0.052	0.002	0.31
NN04_Ttn42_4	25	56	39.18	1.06	0.053	0.004	0.15
NN04_Ttn42_5	27	62	37.66	0.98	0.064	0.005	0.17
NN04_Ttn42_6	31	50	35.97	1.59	0.123	0.028	0.04
NN04_Ttn42_7	28	66	38.08	1.10	0.053	0.002	0.30
NN16-Ttn14-1	54	309	39.18	1.11	0.050	0.003	0.20
NN16-Ttn14-2	16	140	39.67	1.19	0.054	0.007	0.16
NN16-Ttn14-3	285	854	38.02	0.83	0.103	0.003	0.33
NN16-Ttn14-4	181	345	39.60	1.00	0.051	0.002	0.53
NN16-Ttn15-1	112	383	38.51	0.95	0.076	0.004	0.15
NN16-Ttn15-2	139	699	38.64	1.07	0.063	0.005	0.22
NN16-Ttn16-1	16	153	22.83	3.21	0.361	0.070	0.40
NN16-Ttn16-2	24	166	37.19	1.03	0.111	0.011	0.10
NN16-Ttn17-1	159	675	40.18	1.03	0.052	0.002	0.22
NN16-Ttn17-2	306	488	39.97	1.00	0.050	0.001	0.44
NN16-Ttn18-1	28	282	39.02	1.13	0.052	0.003	0.33
NN16-Ttn18-2	36	285	39.87	1.08	0.054	0.003	0.29
NN16-Ttn19-1	56	292	39.40	1.04	0.051	0.003	0.20
NN16-Ttn19-2	14	96	38.14	1.24	0.095	0.007	0.10
NN16-Ttn28-1	261	940	40.77	1.11	0.053	0.002	0.35
NN16-Ttn28-2	97	370	39.82	1.08	0.053	0.003	0.35
NN16-Ttn28-3	462	1166	40.11	0.99	0.055	0.003	0.21

NN16-Ttn28-4	85	332	35.61	1.00	0.117	0.005	0.33
NN16-Ttn28-5	27	143	28.25	1.69	0.283	0.039	0.34
NN16-Ttn28-6	206	662	37.04	1.09	0.111	0.010	0.25
NN16-Ttn3-1	28	116	32.68	1.93	0.181	0.020	0.27
NN16-Ttn3-2	34	121	27.32	2.23	0.296	0.038	0.30
NN16-Ttn4-1	31	116	27.70	3.57	0.272	0.052	0.32
NN16-Ttn9-1	134	360	39.95	1.04	0.055	0.002	0.42
NN16-Ttn9-2	72	298	40.16	1.05	0.053	0.006	0.21
NN50_t02_1	58	23	22.57	1.40	0.355	0.013	0.54
NN50_t02_2	22	13	34.97	1.63	0.192	0.024	0.27
NN50_t02_3	33	22	34.60	1.59	0.107	0.020	0.20
NN50_t03_1	15	18	39.43	1.65	0.061	0.006	0.11
NN50_t03_2	31	27	27.06	0.83	0.292	0.008	0.34
NN51a-Ttn13	330	96	36.11	0.88	0.145	0.006	0.49
NN51a-Ttn18-1	39	36	32.37	0.86	0.212	0.011	0.36
NN51a-Ttn18-2	44	34	35.79	1.04	0.167	0.009	0.15
NN51a-Ttn18-3	74	48	35.54	0.93	0.109	0.007	0.22
NN51a-Ttn19-1	30	38	35.59	1.01	0.145	0.008	0.19
NN51a-Ttn19-2	40	56	39.89	0.96	0.056	0.003	0.17
NN51a-Ttn20-1	26	69	37.84	1.10	0.079	0.010	0.08
NN51a-Ttn20-2	43	142	39.02	1.00	0.076	0.005	0.18
NN51a-Ttn22-1	40	61	39.23	0.87	0.050	0.003	0.40
NN51a-Ttn22-2	317	148	40.24	0.99	0.050	0.001	0.39
NN51a-Ttn22-3	38	68	34.55	1.29	0.129	0.022	0.11
NN51a-Ttn22-4	219	129	41.63	0.93	0.051	0.001	0.31
NN51a-Ttn22-5	76	80	36.87	0.89	0.112	0.005	0.35
NN51a-Ttn22-6	168	243	41.14	0.96	0.051	0.002	0.51
NN51a-Ttn22-7	46	60	38.14	1.02	0.051	0.003	0.28
NN51a-Ttn27	41	23	36.40	0.87	0.078	0.007	0.60
NN51a-Ttn28-1	143	336	38.62	0.92	0.064	0.003	0.14
NN51a-Ttn28-2	45	131	34.14	0.99	0.144	0.007	0.18
NN51a-Ttn29	111	87	38.07	0.98	0.082	0.007	0.28
NN51a-Ttn31	94	197	36.05	1.02	0.114	0.006	0.48
NN51a-Ttn33	60	171	38.14	1.00	0.085	0.005	0.23
NN51a-Ttn34	395	205	38.48	0.85	0.060	0.002	0.55
NN51a-Ttn35	75	100	25.37	0.68	0.461	0.026	0.41
NN51a-Ttn36-1	50	84	39.89	0.96	0.047	0.003	0.30
NN51a-Ttn36-2	33	95	40.08	1.11	0.052	0.004	0.18
NN51a-Ttn5	74	29	25.25	0.97	0.389	0.021	0.33
NN51a-Ttn6	52	23	32.36	1.19	0.192	0.021	0.22

NN51a-Ttn7	202	104	23.87	0.88	0.432	0.013	0.36
NN51a-Ttn8	61	97	34.82	1.26	0.135	0.017	0.22
NN52_t01_1	39	137	38.12	1.55	0.063	0.008	0.34
NN52_t01_2	22	94	40.73	1.12	0.052	0.005	0.18
NN52_t01_3	24	101	41.36	0.99	0.047	0.002	0.20
NN52_t01_4	31	158	40.98	1.09	0.050	0.002	0.21
NN52_t01_5	361	362	39.81	1.11	0.075	0.003	0.41
NN52_t01_6	33	142	41.24	1.22	0.049	0.002	0.26
NN52_t03_1	28	129	41.53	1.13	0.050	0.003	0.17
NN52_t03_2	34	131	40.83	1.20	0.052	0.002	0.38
NN52_t03_3	88	163	37.20	1.02	0.063	0.003	0.33
NN52_t05_1	29	54	23.47	2.90	0.347	0.054	0.47
NN52_t05_2	22	48	40.32	1.17	0.051	0.003	0.31
NN52_t06_1	23	143	41.20	1.26	0.051	0.004	0.32
NN52_t06_10	29	206	40.14	1.27	0.065	0.004	0.28
NN52_t06_11	22	136	39.08	0.96	0.076	0.009	0.14
NN52_t06_12	26	175	40.97	1.25	0.053	0.003	0.27
NN52_t06_13	26	180	41.07	1.13	0.053	0.005	0.08
NN52_t06_14	22	135	41.02	1.13	0.048	0.004	0.13
NN52_t06_15	24	168	41.53	1.15	0.047	0.002	0.18
NN52_t06_16	130	250	41.84	0.90	0.054	0.002	0.23
NN52_t06_17	82	352	40.77	1.06	0.051	0.002	0.51
NN52_t06_2	24	146	38.64	1.17	0.083	0.006	0.27
NN52_t06_3	24	156	41.32	1.24	0.048	0.002	0.29
NN52_t06_4	29	186	40.27	1.17	0.052	0.004	0.08
NN52_t06_5	147	343	39.95	1.04	0.050	0.001	0.49
NN52_t06_6	33	237	40.32	1.23	0.064	0.002	0.35
NN52_t06_7	25	161	40.47	1.11	0.053	0.003	0.19
NN52_t06_8	71	327	38.83	0.88	0.065	0.003	0.44
NN52_t06_9	24	153	40.78	1.23	0.057	0.003	0.20
NN52_t07_1	27	163	41.72	1.19	0.048	0.003	0.18
NN52_t07_10	22	134	39.12	1.21	0.051	0.004	0.14
NN52_t07_11	21	118	39.70	1.08	0.057	0.004	0.14
NN52_t07_12	35	197	37.55	1.34	0.087	0.015	0.17
NN52_t07_13	39	245	40.83	1.19	0.053	0.002	0.31
NN52_t07_14	24	142	39.81	1.12	0.061	0.005	0.18
NN52_t07_15	29	175	40.18	1.17	0.056	0.002	0.28
NN52_t07_16	51	234	37.66	1.11	0.074	0.013	0.08
NN52_t07_2	27	185	41.70	1.11	0.049	0.003	0.09
NN52_t07_3	25	157	42.35	1.07	0.049	0.004	0.15

NN52_t07_4	24	149	41.29	1.19	0.050	0.003	0.19
NN52_t07_5	20	149	41.58	1.32	0.049	0.003	0.32
NN52_t07_6	22	151	41.44	1.38	0.053	0.003	0.19
NN52_t07_7	18	115	38.60	1.22	0.064	0.004	0.14
NN52_t07_8	23	136	40.83	1.25	0.052	0.003	0.46
NN52_t07_9	25	172	39.75	1.13	0.054	0.004	0.16
NN54-Ttn10-1	180	21	39.48	0.93	0.084	0.003	0.61
NN54-Ttn11-1	107	177	38.64	1.01	0.060	0.005	0.25
NN54-Ttn11-2	88	185	38.52	1.00	0.096	0.005	0.31
NN54-Ttn12-1	58	232	37.48	1.12	0.083	0.011	0.30
NN54-Ttn12-2	88	270	39.54	1.04	0.075	0.005	0.47
NN54-Ttn2-1	129	4	36.39	0.85	0.140	0.008	0.25
NN54-Ttn3-1	66	14	29.90	0.93	0.256	0.011	0.19
NN54-Ttn4-1	45	0	33.59	1.05	0.109	0.005	0.16
NN54-Ttn5-1	168	1	39.73	0.99	0.069	0.004	0.28
NN54-Ttn6-1	53	3	13.57	0.44	0.559	0.013	0.48
NN54-Ttn7-1	20	2	13.40	1.75	0.566	0.030	0.57
NN54-Ttn9-1	153	8	34.34	1.05	0.127	0.004	0.36
NN54-Ttn9-2	12	11	35.16	1.30	0.150	0.014	0.25
NN54-Ttn9-3	54	14	19.01	1.01	0.460	0.019	0.38
NN56-Ttn1-1	174	25	36.35	0.77	0.052	0.002	0.21
NN56-Ttn11-1	574	268	37.05	0.87	0.095	0.002	0.58
NN56-Ttn13-1	24	48	31.55	1.26	0.109	0.010	0.08
NN56-Ttn2-1	9	10	30.40	2.12	0.237	0.032	0.23
NN56-Ttn2-1_1	51	30	31.96	1.05	0.168	0.014	0.31
NN56-Ttn5-1	122	43	38.20	0.93	0.074	0.002	0.47
NN56-Ttn6-1	39	13	31.15	2.04	0.057	0.003	0.34
NN56-Ttn6-2	42	53	23.75	2.58	0.365	0.051	0.33
NN56-Ttn7-1	61	36	31.92	1.08	0.151	0.011	0.52
NN56-Ttn7-2	216	202	36.60	1.00	0.110	0.006	0.10
NN56-Ttn7-3	579	196	30.58	1.45	0.232	0.031	0.29
NN56-Ttn8-1	261	222	27.37	0.80	0.298	0.013	0.29
NN56-Ttn8-2	1011	824	32.58	0.71	0.190	0.004	0.44
NN56-Ttn9-1	13	8	20.70	0.76	0.399	0.019	0.17
NN58_t01_1	177	2	28.09	1.68	0.295	0.025	0.24
NN58_t01_2	60	1	34.60	1.49	0.163	0.017	0.27
NN58_t02_1	56	2	4.24	0.20	0.774	0.016	0.52
NN58_t02_2	28	0	6.15	0.33	0.730	0.016	0.56
NN58_t03_1	83	2	30.65	0.90	0.255	0.007	0.57
NN58_t03_2	26	1	34.33	1.17	0.203	0.010	0.31

NN58_t03_3	23	2	19.05	0.61	0.481	0.012	0.27
MJ_ttn1	32	1	38.04033	1.2	0.06813	0.01	-0.2
MJ_ttn2	48	2	37.58161	0.84	0.06178	0.01	0.02
MJ_ttn3	46	2	35.16503	0.94	0.07978	0.01	-0.1
MJ_ttn4	41	1	38.51859	0.95	0.06007	0.01	0.18
MJ_ttn5	43	2	38.99635	1.03	0.07322	0.01	0.13
MJ_ttn6	44	2	38.16612	0.94	0.079	0.01	-0.4
MJ_ttn7	40	1	39.87598	1.05	0.06668	0.01	0.17
MJ_ttn8	43	2	39.27326	1.05	0.06381	0.01	0.45
MJ_ttn9	44	2	40.40699	0.94	0.05754	0.01	-0.4
MJ_ttn10	32	1	38.94381	1.07	0.05055	0.01	0.19
MJ_ttn11	75	3	38.75399	0.75	0.05424	0	0.25
MJ_ttn12	35	1	39.57367	0.98	0.07967	0.01	-0.2
MJ_ttn13	34	1	40.17027	0.98	0.0625	0.01	0.16
MJ_ttn14	67	2	39.05738	0.73	0.07917	0.01	-0.1
MJ_ttn16	62	3	31.7989	0.93	0.19822	0.02	-0.6
MJ_ttn17	24	1	39.11572	1.48	0.08271	0.02	-0.6
MJ_ttn18	24	1	35.96589	1.81	0.15591	0.03	-0.8
MJ_ttn19	55	2	39.332	1.12	0.0691	0.01	-0.4
MJ_ttn20	73	3	39.81258	0.76	0.05466	0	0.19
MJ_ttn21	67	2	38.97973	0.87	0.05531	0	0.32
MJ_ttn23	34	1	39.80325	1.17	0.05258	0	-0.1
MJ_ttn24	30	1	36.40849	1.72	0.06821	0.01	0.24
MJ_ttn25	32	1	38.71027	1.04	0.05838	0.01	0.2
MJ_ttn26	32	1	38.49234	1.05	0.07297	0.01	-0.1
MJ_ttn27	29	1	36.04323	1.05	0.11485	0.01	-0.1
MJ_ttn30	33	1	39.26174	0.93	0.05142	0	0.21
MJ_ttn31	33	1	39.63252	1.05	0.05216	0	-0.2
MJ_ttn32	30	2	31.703	1.97	0.22319	0.04	-0.9
MJ_ttn33	133	5	39.16075	0.71	0.05358	0	-0
MJ_ttn35	75	3	39.502	0.97	0.06983	0	-0.2
MJ_ttn36	98	3	39.52931	0.69	0.05381	0	0.17
MJ_ttn37	48	2	38.23466	0.77	0.0577	0	0.03
MJ_ttn38	35	1	37.88199	1.01	0.07637	0.01	-0
MJ_ttn39	52	2	38.7729	0.81	0.04949	0	0.28
MJ_ttn40	32	1	37.32544	1.04	0.05237	0.01	0.17
MJ_ttn41	102	4	37.59757	0.67	0.04981	0	0.15
MJ_ttn42	75	3	37.18072	0.65	0.04866	0	0.06
MJ_ttn43	38	1	38.00365	1.12	0.05814	0.01	0.28
MJ_ttn45	163	6	39.0397	0.66	0.04883	0	0.49

MJ_ttn46	64	2	39.31383	0.88	0.05597	0	0.06
MJ_ttn48	34	1	38.6967	0.91	0.05459	0	0.02
MJ_ttn50	24	1	38.00435	1.09	0.05834	0.01	0.18
MJ_ttn51	21	1	38.01024	1.35	0.05253	0.01	0.07
MJ_ttn52	61	2	36.17005	1	0.04819	0	0.29
MJ_ttn53	77	3	38.54569	0.82	0.05421	0	0.33
MJ_ttn55	41	2	37.95173	0.95	0.0496	0.01	0.26
MJ_ttn56	40	3	24.38708	1.97	0.33619	0.04	-0.9
MJ_ttn57	23	1	37.34693	1.23	0.06652	0.01	-0.1
MJ_ttn58	30	1	37.14963	1.08	0.06378	0.01	0.09
MJ_ttn59	239	9	38.77139	0.66	0.051	0	0.26
MJ_ttn60	38	1	37.10942	0.97	0.05539	0	0.05
MJ_ttn61	44	2	39.30951	0.69	0.05196	0.01	0.08
MJ_ttn62	33	1	39.5575	0.83	0.05228	0	0.1
MJ_ttn63	37	1	38.07662	0.91	0.05449	0	-0.1
MJ_ttn64	43	2	38.49807	0.88	0.05898	0.01	0.25
MJ_ttn65	31	1	36.77082	1.15	0.08734	0.01	-0.5
MJ_ttn66	35	2	33.28494	1.55	0.14643	0.03	-0.7
MJ_ttn67	48	2	37.23871	1.02	0.08601	0.01	-0.4
MJ_ttn68	32	1	37.623	0.86	0.07462	0.01	-0.1
MJ_ttn69	40	1	40.32149	1.13	0.05166	0.01	0.17
MJ_ttn70	26	1	34.72124	1.08	0.10866	0.01	0.01
MJ_ttn71	75	3	39.50263	1.01	0.06788	0.01	-0.5
MJ_ttn72	280	10	37.65837	0.55	0.05136	0	-0
MJ_ttn73	32	2	31.94896	1.57	0.17334	0.03	-0.7
MJ_ttn74	85	3	38.73637	0.89	0.05621	0	0.49
MJ_ttn75	51	2	38.6049	0.93	0.05184	0	0.17
MJ_ttn76	39	1	39.73729	1.01	0.05375	0.01	-0
MJ_ttn77	53	2	34.18904	1.15	0.11607	0.01	-0.3
MJ_ttn78	72	3	35.9562	0.83	0.06395	0.01	0.17
MJ_ttn79	24	1	36.22128	1.48	0.09721	0.01	-0.5

References

Jicha, B.R., Singer, B.S., and Sobol, P., 2016, Re-evaluation of the ages of 40Ar/39Ar sanidine standards and supereruptions in the western U.S. using a Noblesse multi-collector mass spectrometer: Chemical Geology, v. 431, p. 54–66, doi:10.1016/j.chemgeo.2016.03.024.

Min, K., Mundil, R., Renne, P.R., and Ludwig, K.R., 2000, A test for systematic errors in 40Ar/39Ar geochronology through comparison with U/Pb analysis of a 1.1-Ga rhyolite: Geochimica et Cosmochimica Acta, v. 64, p. 73–98, doi:10.1016/S0016-7037(99)00204-5.

Ross, J., 2019, NMGRL/pychron v18.2:, doi:10.5281/zenodo.3237834.